Surface Wave Tomography Across Europe-Mediterranean and Middle East Based on Automated Inter-station Phase Velocity Measurements

Amr Mohammed Mahmoud Elsayed El-Sharkawy

Dissertation

in the fulfilment of the requirements for the doctoral degree
of the Faculty of Mathematics and Natural Sciences
at Christian-Albrechts University, Kiel, Germany

February 2019

First examiner: Prof. Dr. Thomas Meier
Second examiner: Prof. Dr. Sergei Lebdev

Date of the oral examination: February 26^{th}, 2019
Date of publication approval: February 26^{th}, 2019

I would like to dedicate this thesis to my loving parents and the God’s endowment to me "my best friend ever Dr. Mona Hamada" . . .

Declaration

I hereby declare that except where specific reference is made to the work of others, the contents of this dissertation are original and have not been submitted in whole or in part for consideration for any other degree or qualification in this, or any other university. This dissertation is my own work and contains nothing which is the outcome of work done in collaboration with others, except as specified in the text and Acknowledgements. Moreover, I confirm that the preparartion of this thesis subjected to the rules of Good Scientific Practice of the German Research Foundation. I also confirm that I have not been subjected to the withdrawal of any academic degree.

Amr Mohammed Mahmoud Elsayed El-Sharkawy
February 2019

Acknowledgements

Above all I thank God Almighty for blessing me to complete this thesis and taking it out in this form. Few words are not enough to acknowledge all the people who supported me to work effeciently on my PhD project and continuously encouraged me through out the writing process of the manuscript. At the outset, Iwould like to express my sincere gratitude to my supervisor Prof. Dr. Thomas Meier for his continuous support, scientific discussions and also for sharing his experience with us which made things go smoother but in the right direction. His insights to streamlining the implementation of my working plans are highly appreciated in every way. I am grateful for his patience, instant guidance and supervision both on the technical and personal levels. He tought me that a critical thinking is important to be a scientist. I understood from him the significance of 1 %. For me if I achieve 99 %, it is more than satisfactory but I learnt from him "why not 100 %". Sometimes he become little bit strict but now I understood that it was required to achieve high standards.

I especially thank Prof. Dr. Sergei Lebedev, from Dublin Institute for Advanced Studies, Dublin, Ireland, for his collaboration and support during my entire PhD tenure, though he was not reachable personally but he always replied promptly whenever I need help. Without his codes and help I would not be able to obtain high resolution phase velocity maps. I would like to thank my colleague Dr. Luigia Cristiano. I was able to obtain her immediate help and support, share ideas and discuss results. I would like to thank my colleague Dr. Christian Weidle for his useful comments and discussions during this study. All together, I would like to thank all the group members of Prof. Dr. Thomas Meier for their support during my PhD time and I also would like to thank all members of Institute of Geosciences, in Kiel, who supported me one way or other in successful completion of the thesis. Since more than couple of years we are collaborating with scientists from different countries e.g., France (Prof. Dr. Lapo Boschi, Institut des Sciences de la Terre, Paris) and Ireland (Prof. Dr. Sergei Lebedev, Dublin Institute) to study specific aspects of my work in greater details. This resulted in a submitted scientific papers to a peer-reviewed journals. In addition, an on-going collaboration with scientists from other institutes in Germany e.g., Prof. Dr. Christian Hübscher from Hamburg University and Prof. Dr. Heidrun Kopp from GEOMAR

Helmholtz-Centre for Oceanography, Christian-Albrechts University in Kiel to deeply study the joint interpretations of different geophysical data sets. I a thankful to them all for the continuous support and cooperations.

Special thanks and gratitude go to my best friend and colleague ever "Dr. Mona Hamada" for her support, discussions, feedback, patience and continuous encouragement enabled me to complete this work, I alwasy appreciate the feedback offered by her. There are no proper words to say thanks to Mr. Amr Hegazy for his continuous support, I am deeply grateful to him. I thank to my lovely young friends Hanan- and Haneen Amr Hegazy who are the pride and joy of my life. I love them more than anything.

Deep gratitude is given to My Father, My Mother, My Sister "Doaa", my brothers "Dr. Waleed and Moamen" and all my family who gave and assigned me all the ways and possibilities to provide this study in this way.

My sincere thanks go to Prof. Dr. Hatem Hamdy Odah, president of the National Research Institute of Astronomy and Geophysics for his great efforts to offer all the possible facilities to complete this work. I would like to express my gratitude and appreciation to the people at the Egyptian National Seismological Network (ENSN) Lab., Seismology Department, National Research Institute of Astronomy and Geophysics (NRIAG) for providing us with the waveform data and other facilities.

Abstract

The Alpine-Mediterranean mobile belt is, tectonically, a highly complicated and active region. Since the early Tertiary, a series of collisions between Gondwana-derived continental microcontinents and Eurasia have shaped the Mediterranean geology due to the closure of the intervening ocean basins. The present day stress field is controlled by the Africa-Eurasia convergence, subduction in the Hellenic, Cyprus, and Calabrian arcs, the collision between the Arabia and Eurasia and the displacement of the Anatolian-Aegean microplate. Such complex subduction events and associated collisions, resulted in mountain building and plateau formation, magmatism, escape tectonics, lithospheric deformation and opening of back-arc basins. Despite the numerous studies that have attempted to characterize the lithosphere-asthenosphere structure in the Mediterranean, there are still many controversial issues such as, the variability of lithospheric structure underneath the Mediterranean, the age, nature and distribution of the oceanic lithosphere, the presence and geometry of the subducting slabs and slab fragments e.g. in the western Mediterranean, the Alps, the Dinarides, they Apennines, the Hellenic arc, Cyprus, and beneath Anatolia.

Seismic tomography is an imaging tool which allows to construct 3-D models of the Earth's internal structure from observables of seismic waves. Surface wave tomography can be performed using earthquakes and/or ambient noise data and is sensitive to isotropic as well as anisotropic 3-D shear-wave velocity structure in broad depth ranges sampling the crust and the lithosphere-asthenosphere structure. In this study, surface wave tomography is performed to characterize the structure of the lithosphere-asthenosphere underneath the Mediterranean basin. We utilize a large database consists of $\sim$ 3800 teleseismic earthquakes recorded by $\sim$ 4500 broadband seismic stations provided by IRIS and EIDA in a combination, for the first time, with waveform data from the Egyptian National Seismological Network (ENSN) in order to ensure a good path coverage especially for the eastern Mediterranean. An automated algorithm for inter-station phase velocity measurements is applied to obtain Rayleigh and Love fundamental mode phase velocities from this database ($\sim$ 3.5 millions of waveforms). Path average dispersion curves are obtained by averaging the smooth parts of single-event dispersion measurements. We calculated new high resolution Rayleigh and Love

wave phase velocity maps using an unprecedentedly large number (200.000) of fundamental mode dispersion curves in a broad period range from 8 s to 350 s. The phase velocity maps provide a local phase velocity dispersion curve for each geographical grid node of the map. In order to relate the local dispersion curves to 1-D velocity models as function of depth, the Particle Swarm Optimization (PSO) algorithm has been developed and implemented. In our implementation we newly allowed for random local search in order to speed up the convergence of the entire swarm towards the global best position. Moreover, a random excursion to best position of the other particles is also implemented in order to ensure the exploration of the entire model space.

Taking the eastern Mediterranean as a special case, we aim to determine the nature of the crust (oceanic or deformed continental) underlies its individual basins (e.g., Levant basin in the eastern most bank, and the Ionian Sea in the western most bank), as well as examining the variability of their crustal and mantle lithospheric structures. In this regard, broad band average local phase-velocity dispersion curves for the Levant Basin and the Ionian Sea have been constructed and inverted individually for 1-D shear wave velocity models as function of depth using the newly elaborated Particle Swarm Optimization (PSO) algorithm. To help minimizing the trade-offs between the crustal velocities, mantle velocities and the crustal thickness, we constrained our inversion with accurate local P-wave initial models. The P-wave velocity models have been calculated from two seismic refraction profiles recently recorded at the Levant Basin and the Ionian Sea. The results indicate a Moho depth of about 22 km and 16 km beneath the Levant and the Ionian Basin, respectively. The thickness of the crystalline part of the crust at the Levant basin is $\sim$ 10 km, whereas it is of $\sim$ 6 km beneath the Ionian Sea, overlain by a thick pile of sediments at both locations. As a proxy, the Vp/Vs ratio is used to identify the nature of the crust. Beneath the Levant basin, a ratio of $<$ 1.8 is obtained pointing to a stretched continental crust, whereas the $>$ 1.8 value at the Ionian Sea indicates its oceanic nature. In the upper mantle, a shallow asthenosphere is highly pronounced beneath the Levant Basin with $\sim$ 70 km of LAB depth. On the other hand, anomalously higher shear-velocities beneath the Ionian Sea indicates a very thick oceanic lithosphere. Based on our model for the upper mantle of the Ionian Sea we show that, on average, the Ionian oceanic lithosphere has continued to cool well beyond the 80 Ma age, contrary to the "plate model" prediction, and is now extremely thick, over 200 km. This may indicate the applicability of the half-space cooling model for the very old oceanic lithosphere in the Ionian Sea.

Furthermore, to shed light on the lithosphere-asthenosphere system underneath the entire Mediterranean region, we constrcted a 3-D shear wave velocity model down to depth of 300 km. The local dispersion curve for each node underneath the Europe-Mediterranean

region is inverted for 1-D shear wave velocity model, with inter-knot spacing of 30 km. The resulted 1-D models are then combined to construct the 3-D velocity model. The obtained lateral resolution in Europe and the northern Mediterranean is better than 100 km, otherwise it is 150 km elsewhere. The resulted model shows significant variations in shear wave velocities both horizontally and vertically. High velocity anomalies have been imaged underneath western Europe indicating its thick continental mantle lithosphere as well as beneath the Eastern European craton down to 250 km depth. Moreover, a large high velocity feature covers the eastern Mediterranean region from beneath the Herodotus basin in the East towards the Ionian sea in the west indicating a rather uniform, very thick oceanic mantle lithosphere down to depth of > 200 km. The subducted mantle lithospheric slabs have been imaged as downgoing high velocities underneath the Alboran basin, the central and eastern Alps, northern Apennines, Dinarides. The African subducting lithosphere beneath both the Hellenic and Cyprus arcs are also imaged clrealy. Shallow asthenosphere has been imaged underneath the western Mediterranean, central European asthenosphere and the Pannonian basin. The revealed low velocities beneath Anatolia and the middle East indicating overall thin lithosphere and shallow asthenosphere which correlates very well with the distribution of the Cenozoic volcanism and the surface uplift in this area. This might partly explain its high topography. In central northern Anatolia, from 160 km and downward a N-S trending high velocity anomaly in the upper mantle is detected.

Zusammenfassung

Aus tektonischer Sicht ist der Alpen-Mittelmeer-Gürtel eine komplizierte und aktive Region. Seit dem frühen Tertiär wurde die Geologie des Mittelmeers infolge von Kollisionen zwischen Gondwana-kontinentalen Mikrokontinenten und Eurasien aufgrund der Schließung der dazwischen liegenden Meeresbecken entwickelt. Das heutige Spannungsfeld wird durch die Konvergenz zwischen Afrika und Eurasien, die Subduktion in den hellenischen, zyprischen und kalabrischen Bögen, die Kollision zwischen Arabien und Eurasien und die Verschiebung der anatolisch-ägäischen Mikroplatte kontrolliert. Solche komplexen Subduktionsereignisse und damit verbundene Kollisionen führten zu Gebirgsbildung und -plateaubildung, Magmatismus, Extrusion, Lithosphärische Verformung und von Backarc-Öffnung. Trotz zahlreicher Studien, die versucht haben, die Lithosphären-Asthenosphären-Struktur im Mittelmeerraum zu charakterisieren, gibt es immer noch viele kontroverse Themen wie die Variabilität der lithosphärischen Struktur unter dem Mittelmeerraum, das Alter, die Natur und die Verbreitung der ozeanischen Lithosphäre, die Präsenz und Geometrie der subduzierenden Platten und Plattenfragmente, z.B., im hellinischen Bogen Zypern, den Alpen, den Dinariden, dem Apennin, im westlichen Mittelmeerraum und unter Anatolien.

In dieser Arbeit wird eine Oberflächenwellentomographie durchgeführt, um die Struktur der Lithosphäre-Asthenosphäre unterhalb des Mittelmeerbeckens zu charakterisieren. Wir verwenden einen Datensatz, der aus $\sim$ 3800 teleseismischen Erdbeben besteht, die von $\sim$ 4500 seismischen Breitbandstationen daten. Erstmals Daten des ägyptischen nationalen seismologischen Netzwerks (ENSN) aufgezeichnet wurden und eine gute Abdeckung speziell in den östlichen Mittelmeerraum gewährleisten. Ein automatisierter Algorithmus wird angewendet, um die Phasengeschwindigkeiten der Rayleigh- und Love-Grundmode zwischen den Stationen aus großen Datenmengen ($\sim$ 3,5 Millionen Wellenformen) zu bestimmen. Wir berechneten neue hochauflösende Rayleigh- und Wellenphasengeschwindigkeitskarten unter Verwendung einer beispiellos großen Anzahl (200.000) von Grundmodendispersionskurven in einem breiten Periodenbereich von 8 s bis 350 s. Die Phasengeschwindigkeitskarten stellen eine lokale Phasengeschwindigkeitsdispersionskurve für jeden geographischen Gitterknoten der Karte bereit. Um die lokalen Dispersionskurven in 1-D Geschwindigkeitsmodellen zu invertieren, wurde ein neue Inversionsauszatz auf Basis des Particle Swarm Optimization (PSO) Algorithmus entwickelt und implementiert. Bei unserer Implementierung haben wir eine zufällige lokale Suche zugelassen, um die Annäherung des gesamten Schwarms an die global beste Position zu beschleunigen. Darüber hinaus wird eine zufällige Abweichung zur besten Position der anderen Partikel implementiert, um die Erkundung des gesamten Modellraums sicherzustellen.

Mit dem Ziel zu bestimmen, welche Art von Kruste (ozeanisches oder deformiertes kontinentales) den einzelnen Becken des östlichen Mittelmeerraums (z. B. Levante-Becken im östlichsten Ufer und des Ionischen Meeres im westlichsten Ufer) zugrunde liegt, sowie Untersuchung der Variabilität der Mantellithosphäre konstruierten wir breitbandige mittlere Phasengeschwindigkeits-Dispersionskurven für das Levante-Becken und das Ionische Meer. Die lokalen Dispersionskurven werden dann für 1-D-Scherwellengeschwindigkeitsmodelle unter Verwendung des neu entwickelten Particle Swarm Optimization (PSO) -Algorithmus einzeln invertiert. Um den Kompromiss zwischen den Krustengeschwindigkeiten, den Mantelgeschwindigkeiten und der Krustenstärke zu minimieren, haben wir unsere Inversion mit genauen lokalen P-Wellen-Anfangsmodellen eingeschränkt. Die Geschwindigkeitsmodelle der P-Welle wurden aus zwei seismischen Refraktionsprofilen berechnet, die kürzlich im Levante-Becken und im Ionischen Meer aufgenommen wurden. Die Ergebnisse zeigen eine Moho-Tiefe von etwa 22 km bzw. 16 km unterhalb der Levante bzw. des Ionischen Beckens. Die Dicke des kristallinen Teils der Kruste im Levant-Becken beträgt 10 km, während er 6 km unter dem Ionischen Meer liegt und an beiden Standorten von einem dichten Sedimenthaufen überlagert wird. Als Proxy wird das Vp/Vs-Verhältnis verwendet, um Unterschiede der Komposition der Kruste zu bestimmen. Unterhalb des Levante-Beckens wird ein Verhältnis von <1,8 erhalten, das auf eine ausgedehnte kontinentale Kruste hinweist, während der Wert > 1,8 am Ionischen Meer seine ozeanische Natur anzeigt. Im oberen Mantel ist unter dem Levante Basin eine flache Asthenosphäre mit einer Tiefe von 70 km LAB stark ausgeprägt. Andererseits weisen anomal höhere Schergeschwindigkeiten unter dem Ionischen Meer auf eine sehr dicke ozeanische Lithosphäre hin. Ausgehend von unserem Modell für den oberen Mantel unter dem Ionischen Meer zeigen wir, dass sich die ionische ozeanische Lithosphäre im Gegensatz zu den Vorhersagen über das "Thermal Plate Cooling" -Verfahren über das 80-Ma-Alter hinaus deutlich abgekühlt hat und jetzt extrem dick ist, über 200 km. Dies könnte auf die Anwendbarkeit des Halbraumkühlungsmodells für die sehr alte ozeanische Lithosphäre im Ionischen Meer hindeuten.

Um das Lithosphären-Asthenosphären-System unterhalb des gesamten Mittelmeerraums zu beleuchten, haben wir ein 3D-Modell der Scherwellengeschwindigkeit bis zu einer Tiefe von 300 km berechnet. Dabei wurde die lokale Dispersionskurve für jeden Knoten unterhalb des Untersuchungsgebiets in ein 1-D-Scherwellengeschwindigkeitsmodell invertiert, wobei der Abstand zwischen den Knoten 30 km beträgt. Die resultierenden 1-D-Modelle werden dann kombiniert, um das 3-D-Geschwindigkeitsmodell zu erstellen. Das erhaltene Modell zeigt sowohl horizontal als auch vertikal erhebliche Schwankungen der Scherwellengeschwindigkeit. In West- und Osteuropas wurden positive Anomalien Varationen, was auf die dicke kontinentale Mantellithosphäre unter dem osteuropäischen Kraton bis in

eine Tiefe von 250 km hindeutet. Darüber hinaus deckt ein großes Hochgeschwindigkeitsanomalie den östlichen Mittelmeerraum vom Herodotus-Becken im Osten zum Ionischen Meer im Westen ab, was auf eine gleichförmige, sehr dicke ozeanische Mantel-Lithosphäre bis zu einer Tiefe von> 200 km hindeutet. Die subduzierten Mantellithosphärenplatten wurden als abwärts gerichtete hohe Geschwindigkeiten unter dem Alboran-Becken, den Zentral- und Ostalpen, dem nördlichen Apennin und den Dinariden abgebildet. Die afrikanische subduzierende Lithosphäre unter den hellenischen und zyprischen Bögen wird ebenfalls direkt abgebildet. Eine flache Asthenosphäre wurde unter dem westlichen Mittelmeerraum, der mitteleuropäischen Asthenosphäre und dem pannonischen Becken abgebildet. Die aufgedeckten niedrigen Geschwindigkeiten unter Anatolien und dem Nahen Osten deuten auf eine insgesamt dünne Lithosphäre und flache Asthenosphäre hin, die sehr gut mit der Verteilung des känozoischen Vulkanismus und der Oberflächenerhöhung in diesem Bereich korreliert. Dies erklärt zum Teil die hohe Topographie. Im zentralen Nordanatolien wird ab 160 km eine N-S-Tendenz mit hoher Geschwindigkeit im oberen Mantel festgestellt.

Table of contents

List of figures

List of tables

Chapter 1

Introduction

I cannot help feeling that seismology will stay in the place at the center of solid earth science for many, many years to come. The joy of being a seismologist comes to you, when you find something new about the earth's interior from the observation of seismic waves obtained on the surface, and realize that you did it without penetrating the earth or touching or examining it directly.

Keiiti Aki, presidential address to the Seismological Society of America, 1980

1.1 Motivation

From tectonic perspective and as a highly variable and complicated mobile belt, the Alpine-Mediterranean has become, since decades, a source of inspiration for wide range of geo-scientists to understand the different geodynamic processes at various scales. It acts as a natural laboratory to deeply investigate the driving forces of tectonic deformation within a complex, active mobile belt. Generally, the Africa-Eurasia convergence since the early Tertiary forced fragements of oceanic and contenintal nature to interact. The distribution of the oceanic lithosphere in the Mediterranean is highly variable. The oldest oceanic lithosphere preserved in-situ is located underneath the Ionian Sea (230-280 Ma, Müller *et al.* 2008) and the Herodutus Basin (340 Ma, Garnot 2016), whereas a recently formed as a result of the counter-clockwise rotation and separation of the Corsica-Sardinia block from the European mainland, the quaternary-aged oceanic lithosphere underneath the Ligurian Sea (Malinverno & Ryan 1986; Faccenna *et al.* 2004; Müller *et al.* 2008). Several studies

revealed that different tectonic events invoked the closure of the Tethys ocean, the subduction of the oceanic lithosphere and the formation of orogenic belts in the Mediterranean basin underneath Anatolia, the Hellenic arc, the Dinarides, the Carpathians, the Alps, the Apennines, Calabria, the Pyrenees and the Alboran (Jolivet *et al.* 2009; Faccenna *et al.* 2007, 2014). Knowledge of the Earth's lithosphere-asthenosphere system is fundamental for the understanding of processes observed at the surface such as intraplate volcanism, seismicity, surface erosion, plate motions, the contribution of mantle convection to the surface tectonics and uplifting of the orogenic belts and its relation to the mantle lithosphere delamination processes. The lithosphere and the underlying asthenosphere of the Europe-Mediterranean region have been the topic of plenty of studies, however there are still many controversial issues such as the presence and geometry of the subducted slabs and slab fragments e.g. in the Alps, the Dinarides, the Apennines, in the western Mediterranean and beneath Anatolia. Moreover, the nature and thickness of the crust and the mantle lithosphere in the eastern Mediterranean are still debated. There is continuing debate on whether the thickness of the oceanic lithosphere reaches a maximum at around 80 Ma of the lithospheric age (the "thermal plate cooling model") or whether, it increases continuously with increasing the lithospheric age according to the "half-space cooling model" (e.g., Davis & Lister 1974; McKenzie *et al.* 2005).

The data availability has been always among the major challenges of observational seismology. We generally rely on earthquake sources, which are not distributed regularly in either time or space. The increasingly dense coverage of Europe-Mediterranean with broadband seismic stations enables to investigate its crust and mantle lithospheric structure in greater details, provided that velocity structural information can be obtained effectively from the huge volumes of surface wave data. Interpreting surface wave dispersion measurements provides an important tool for obtaining the shear wave velocity variation at lithsopheric depths as they exhibit distinctive observational characteristics in different tectonic provinces. Shield areas have the highest values of shear wave velocities with depth and a relatively weak mantle low-velocity zone. On the other hand, rift areas have much lower upper-mantle shear wave velocities and a very pronounced low velocity zone (Kovach, 1987). In this study, surface wave tomography is applied to an unprecedentedly large number of fundamental mode dispersion curves to obtain new high resolution Rayleigh and Love wave phase velocity maps. For the first time, broad band waveform data, from the Egyptian National Seismological Network (ENSN) have been combined with the available data from IRIS and WebDC in order to ensure a good path coverage for the region with the aim to determine what type of crust (oceanic or deformed continental) underlies the individual basins of the eastern Mediterranean, how shear wave velocities vary in the lower crust and upper mantle through

the region, and whether the Vp/Vs ratio is indicative of lithospheric deformation. In addition, a high resolution 3-D Rayleigh wave velocity structure of the lithosphere-asthenosphere system underneath the entire Mediterranean including the Alps and the adjacent regions are investigated in order to deeply study the active processes driven by the subduction processes and mantle flow.

1.2 Seismic Tomography

Knowledge of the Earth's interior is fundamental for a deeper understanding of the regional tectonics and geodynamic processes. But the direct inspection of the structure of the Earth's interior remains nearly fictitious. Therefore indirect observations are used to gain information on the Earth's crust and mantle. Seismic tomography is a technique for imaging the earth's subsurface characteristics and the current state of seismic velocities within the structure of the Earth's interior on various scales. The Earth's interior is hetereogenous, broadly layered, therefore seismic wavelets are subjected to be refracted and reflected across Earth's interfaces. When an earthquake occurs, the time for a seismic wave to arrive at a seismic station can be used to measure the velocities along the ray path of the wave. Using arrival times of different seismic waves, seismologists can define slower and faster regions deep in the Earth. Since earthquakes are the main source of data, the quality of tomographic images depends on the spatial and temporal occurrence distributions of earthquakes. Generally, seismic tomography is often compared to a computerized auxialary tomography (CAT) scan in medicine. The CAT scan uses computers to generate a 3-D image of the human body from many flat X-rays. Seismic tomography uses the same principles as CAT scan, except travel-time difference is observed rather than the X-rays attenuation (i.e., reduction in intensity and amplitude of X-rays that pass through the body). However, it is worth noticing that seismic tomography is much more complicated than the medical inversion. This is due to several factors include: ray path coverage, the sparse distribution of seismic sources and stations, errors in earthquakes locations, picking and timing errors in the data.

Primary, secondary and surface waves can be used for producing tomographic models of different resolutions based on seismic wavelength, frequency content, and the distribution of the seismic stations and ray path coverage. P- and S-wave arrival times of phases traveling through the Earth's crust, mantle and core have been used by many authors to derive global P-wave and shear wave velocity models (e.g. Zhou 1996; van der Hilst *et al.* 1997; Obayashi & Fukao, 1997; Bijwaard *et al.* 1998; Kennett *et al.* 1998; Bijwaard & Spakman 2000; Boschi & Dziewonski 2000; Zhao 2001; Piromallow & Morelli 2003; Wortel & Spakman

2004; Lei & Zhao 2006; Schaeffer & Lebedev 2013). Local earthquake tomography (LET) is another common tool for imaging subsurface structure in seismically active areas. It needs to accurately define the spatial locations and origin time of the earthquake hypocenters as part of the image reconstruction. On contrary, teleseismic tomography has been used extensively to map the structure of the crust and lithosphere on different scales ranging from tens of kilometers to hundreds of kilometers. Wide-angle tomography exploits refraction and wide-angle reflection data in order to constrain variations in seismic structure of the crust.

Surface wave signals are considered the strongest arrivals on the teleseismic seismograms providing some of the best constraints on the earth's structures. Their large amplitudes with relatively low attenuation and long propagation paths provided significant contribution to our knowledge of the Earth's crust and upper mantle structure. Their high sensitivity to velocities variations with depth provide a proxy for determining the shear wave velocity variation in the Earth interior as they exhibit distinctive observational characteristics in different tectonic provinces. Surface wave tomography has now become a powerful tool for studying the lateral heterogeneities of the Earth's crust and upper mantle (e.g. Woodhouse & Dziewonski 1984; Tanimoto & Anderson 1985; Nataf, Nakanishi & Anderson 1986; Nolet 1987; Levshin *et al.* 1989; Montagner & Tanimoto 1990; van der Lee & Nolet 1997; Shapiro & Ritzwoller 2002; Boschi *et al.* 2004; Schäffer & Lebedev 2013). 1-D velocity models have been obtained along great circle paths using the surface wave dispersion measurements whereas long period surface waves have been used mainly for calculating two-dimensional (2-D) isotropic and azimuthally anisotropic maps of surface wave velocity variations in the mantle (Knopoff 1972; Levshin *et al.* 1989; van der Hilst *et al.* 1997; Lebedev *et al.* 2006, 2013; Meier *et al.* 2016). Such tomographic maps represent the spatial distribution of the phase or group velocity averages at each location on the map and summarize large volumes of surface wave dispersion information (Levshin *et al.* 2001).

Traditional surface wave tomography is based upon the Jordan-Wenzel-Kramers-Brillouin (JWKB) ray theory: a high frequency approximation, which is valid if only if the lateral length scales of the heterogeneities are larger than the characteristic wavelength of the seismic waves. in finite-frequency tomography, surface wave phase delays are sensitive not only to heterogeneities along the source-receiver great circle ray, but also to anomalies that are off the reference ray. The first trial to account for finite-frequency effects in surface wave tomography has been performed by Yomogida and Aki (1987). They introduced an *ad hoc* sensitivity within the first Fresnel zone scaled exponentially to the phase delay between the great circle ray and the detoured scattering path. Meier *et al.* (1997) proposed a two-step surface wave tomographic method, in which JWKB waveform modelling is first used to

obtain a preliminary 1-D S-wave velocity model along the source-receiver distance, then the remaining residuals are inverted based on the Born scattering approximation.

The rapid growth in the number of seismic stations in recent years and the availability of seismic waveforms data resulted in large volumes of high quality surface wave broadband data. In this study, we utilize large volumes of data in an effort to image the lithospheric and sublithospheric structure in great detail with increasing resolutions. Very broad band phase velocity dispersion measurements from earthquake recordings within the period range from 8 s to 350 s yield information about the middle to lower crust, the mantle lithosphere as well as the asthenosphere. An algorithm for the automatic determination of the phase velocities is applied to such large number of waveforms recorded at any station pair along the same great circle path. The single-event measurements for each inter-station path are averaged in order to obtain average dispersion curve represents the structure between the two station. Then, we derive phase-velocity maps from such large database of path-averaged dispersion curves using the ray theory formulation. The resolution of the maps depends on the ray path coverage of our database. We quantify the resolution using synthetic data inversions. We define a "checkerboard" input phase velocity map corresponding to anomalies extending a few hundred km laterally and compute the corresponding synthetic phase anomalies. No noise is added to the data. We invert the resulting synthetic data through an application of the same tomography algorithm that we use on real observations, including the regularization scheme and smoothing. Phase velocity maps obtained from dispersive surface waves correlate very well with the main tectonic belts and geologic units providing better constraints on their geometry and the relation to the regional tectonics (Levshin *et al.* 1994; Ritzwoller *et al.* 2002).

1.3 Structure of the thesis

Directly after the introduction chapter, the main body of the thesis is presented in another three chapters as following:

Chapter Two gives a brief introduction to the properties of surface waves and the various methods to measure surface waves. This is followed by the application of an automated algorithm for inter-station phase velocity measurements to a large and heterogeneous dataset to obtain Rayleigh and Love fundamental mode phase velocities. We utilize a database consisting of $\sim$ 3800 teleseismic earthquakes recorded by $\sim$ 4500 broadband seismic stations provided by IRIS and EIDA in a combination, for the first time, with waveform data from the Egyptian National Seismological Network (ENSN) in order to increase the path coverage

especially for the Eastern Mediterranean. Path average dispersion curves are obtained by averaging the smooth parts of single-event dispersion measurements. We finally calculate maps of Rayleigh and Love wave phase velocities at different periods ranging from 8 s to 350 s using surface wave tomography. Details about the tomographic inversion of average phase velocities is provided including the basic formulations for tomographic inversion. The effect of regularization on the tomographic maps is checked by testing range of damping values and optimal damping parameters for this data set are suggested with the help of "L" curve test aided by visual inspection of the phase velocity maps at different damping values. The resolution of the isotropic phase velocity maps is evaluated using the help of checkerboard test with various block sizes of the anomalies. Finally, qualitative interpretations of the different features on the isotropic and azimuthally anisotropic phase velocity maps are discussed.

Chapter Three aims to determine what type of crust underlies the individual basins in the Eastern Mediterranean, how shear wave velocities vary in the lower crust and upper mantle through the region, and whether the Vp/Vs ratio is indicative for the nature of the crust. In this chapter, phase velocty maps for the Eastern Mediterranean are presented. In an effort to examine the variability of the crust and the mantle lithospheric structure underneath the Eastern Mediterranean, we constructed average broad band local phase-velocity dispersion curves specifically at the Levant Basin (representing deformed continental lithosphere) and at the Ionian Sea (as oceanic lithosphere). Each local dispersion curve is inverted individually for 1-D shear wave velocity model using a newly implemented Particle Swarm Optimization (PSO) algorithm. Details about the newly elaborated inversion algorithm including the parametrization and regularization are given in this chapter. In order to minimize the trade-off between the crustal, mantle velocities and the crustal thickness, we constrained our inversions with accurate local P-wave initial models from seismic refraction data.

Chapter Four provides a general overview about the existing models of the Mediterranean in addition, it introduces a new high resolution 3-D Rayleigh wave velocity model of the lithosphere-asthenosphere system underneath the entire Mediterranean including the Alps and the adjacent regions. The newly implemented Particle Swarm Optimization (PSO) algorithm is also applied to all the local dispersion curves which are constructed from the phase velocity maps to be is inverted individually for 1-D velocity models. The resulting 1-D models are then combined to construct the 3-D velocity model. Details about the obtained 3-D model which shows significant variations in shear velocities both horizontally and vertically.

Chapter Five summerize the main results and outcome of the study. An outlook on future working directions is also presented.

References

Bijwaard, H. & Spakman, W. 2000. Non-linear global P-wave tomography by iterated linearized inversion. Geophys. J. Int., 141, 71-82.

Bijwaard, H., Spakman, W., & Engdahl, E. R. 1998. Closing the gap between regional and global tomography. J. Geophys. Res., 103, 30005 - 30078.

Boschi, L. and Dziewonski, A. M., 1999. High- and low-resolution images of the Earth's man- tle: Implications of different approaches to tomographic modeling. J. Geophys. Res., 104(B11), 25,567–25,594.

Boschi, L. & Dziewonski, A. M., 2000. Whole Earth tomography from delay times of P, PcP and PKP phases: Lateral heterogeneities in the outer core and radial anisotropy in the mantle? J. Geophys. Res., 105(B6), 13,675–13,696.

Boschi, L., Ekström, G., & Kustowski, B., 2004. Multiple resolution surface wave tomography: the Mediterranean basin. Geophys. J. Int., 157, 293–304.

Davis, E.E., Lister, C.R.B., 1974. Fundamentals of ridge crest topography. Earth Planet. Sci. Lett. 21, 405 - 413.

Jolivet, L., C. Faccenna, and C. Piromallo, 2009, From mantle to crust: Stretching the Mediterranean, Earth Planet. Sci. Lett., 285(1–2), 198–209, doi:10.1016/j.epsl.2009.06.017.

Kennett, B. L. N., Widiyantoro, S., and van der Hilst, R. D., 1998. Joint seismic tomography for bulk sound and shear wave speed in the Earth's mantle. J. Geophys. Res., 103, 12469-93.

Koulakov, I., Kaban, M., Tesauro, M. & Cloetingh, S., 2009. P- and S- velocity anomaly in the upper mantle beneath Europe from tomographic inversion of ISC data. Geophys. J. Int. 179, 345 - 366.

Lei, J. and Zhao, D. (2006). Global P-wave tomography: On the effect of various mantle and core phases. Phys. Earth Planet. Int., 154, 44-69.

Levshin, A. L., Ritzwoller, M. H., & Ratnikova, L. I., 1994. The nature and cause of polarization anomalies of surface waves crossing northern and central Eurasia, Geophs. J. Int. 117, 577 - 590

Lippitsch, R., Kissling, E. & Ansorge, J. 2003. Upper mantle structure beneath the Alpine orogen from high-resolution teleseismic tomography. J. Geophys. Res. 108, B82376.

Mckenzie, D., Jackson, J.A., Priestley, K., 2005. Thermal structure of oceanic and continental lithosphere. Earth Planet. Sci. Lett. 233 (3-4), 337–349.

Piromallo, C. & Morelli, A., 2003. P wave tomography of the mantle under the Alpine-Mediterranean area. J. Geophys. Res. 108, B22065.

Nolet, G., (ed.), 1987. Seismic tomography, Kluwer, Dordrecht.

Ritzwoller, M. H. & Levshin, A. L., 1998. Eurasian surface wave tomography: Group velocities. J. Geophys. Res., 103(B3), 4839 - 4878.

Ritzwoller, M. H., Barmin, M. P., Villasenor, A., Levshin, A. L., & Engdahl, E. R., 2002. Pn and Sn tomography across Eurasia to improve regional seismic event locations. Tectonophysics 358: 39–55.

Schaeffer, A.J., Lebedev, S., Becker, T.W., 2016. Azimuthal seismic anisotropy in the Earth's upper mantle and the thickness of tectonic plates. Geophys. J. Int. 207, 901–933.

Spakman, W. & Nolet, G. 1988. Imaging algorithms: Accuracy and resolution in delay time tomography. In: Vlaar NJ, Nolet G, Wortel M, and Cloetingh S (eds.) Mathematical Geophysics: A Survey of Recent Developments in Seismology and Geodynamics, pp. 155–188. Dordrecht, The Netherlands: D Reidel.

Spakman, W. 1991. Delay time tomography of the upper mantle below Europe, the Mediterranean, and Asia Minor. Geophys. J. Int. 107, 309 - 332.

Spakman, W., van der Lee, S. & van der Hilst, R. 1993. Travel-time tomography of the European Mediterranean mantle. Phys. Earth Planet. Inter. 79, 3 - 74.

Spakman, W. & Wortel, R., 2004. in The TRANSMED Atlas, The Mediterranean Region from Crust to Mantle (eds Cavazza, W., Roure, F. M., Spakman, W., Stampfli, G. & Ziegler, P.A.) 31–52 (Springer, 2004).

Trampert, J. & Woodhouse, J.H., 1995. Global phase velocity maps of Love and Rayleigh waves between 40 and 150 s period, Geophys. J. Int., 122, 675 - 690.

Trampert J & Woodhouse JH .2003. Global anisotropic phase velocity maps for fundamental surface waves between 40 and 150s. Geophys. J. Int., 154, 154 - 167.

Wang, Z. & Dahlen, F. A., 1995. Validity of surface-wave ray theory on a laterally heterogeneous earth, Geophys. J. Int., 123(3), 757 - 773.

van der Lee, S. & Nolet, G., 1997. Upper mantle S velocity structure of North America. J. Geophys. Res., 102, 22815 - 22838.

Yanovskaya, T. B. & Ditmar, P. G., 1990. Smoothness criteria in surface wave tomography. Geophys. J. Int. 102, 63 - 72.

Yao, H., Van Der Hilst, R. D., & De Hoop, M. V., 2006. Surface-wave array tomography in SE Tibet from ambient seismic noise and two-station analysis i. phase velocity maps, Geophysical Journal International, 166(2), 732 - 744.

Yoshizawa, K. & Kennett, B. L. N., 2002. Determination of the in uence zone for surface wave paths. Earth 440 - 453.

Zhao, D., 2001. Seismic structure and origin of hotspots and mantle plumes. Earth Planet. Sci. Lett., 192, 251–265.

Zhou, H. W., 1996. A high resolution P wave model of the top 1200 km of the mantle. J. Geo- phys. Res., 101, 27,791–810.

Chapter 2

Surface wave tomography: determination of isotropic and azimuthally anisotropic phase velocity maps

2.1 Properties of surface waves

The higher frequency part of a seismic wave generated by an earthquake is usually dominated by the arrivals of P and S waves, with later arrivals often caused by multipathing and scattering as a result of heterogeneous structure. However, most broadband seismograms are dominated by large, longer period (lower frequency) waves that arrive after the P and S waves. These waves are called surface waves, and propagate along the surface of the Earth. Surface waves arise from the interaction of elastic waves with the free surface, and are composed of P and S waves in a linear combination (Rayleigh 1885; Love 1911; Liu & Fan 2012; Vinh & Rudzki 1912; Shearer 2009). They are generally the strongest arrivals recorded at teleseismic distances and they provide some of the best constraints on Earth's shallow structure (Brune 1969; Dorman 1969; Knopoff 1972; Levshin *et al.* 2001). Their waveforms are more complicated than body waves. Rather than a sharp onset, a wave packet is observed that is similar to a Gaussian packet. Due to geometrical spreading the energy carried by surface waves spread out in two directions and decays less with distance ($\sim \frac{1}{r}$), where r is the distance. This is in contrast to body waves that spread out in three directions and their energy decays with $\sim \frac{1}{r^2}$. That's why surface waves are recorded with larger amplitudes

and at larger distances. They travel slower than body waves and their velocities are strongly frequency dependent. Surface waves are dominant waves on the seismograms, and for large earthquakes they can circle the globe many times. Constructive interference among these circulating surface waves and body waves reverberations, forms the normal modes or free oscillations of the Earth (Dziewonski & Romanowicz, 2007). In other words, surface waves can be understood as a superposition of free oscillations or body waves (Kennett, 1976). There are two types of surface waves that propagate along Earth's surface: Rayleigh waves and Love waves.

2.1.1 Rayleigh waves

The mathematical treatment of surface wave propagation is complex but Rayleigh waves can be thought of as arising from the constructive interference of multiply reflected P-waves and the vertically polarized (SV) shear waves at the free surfaces and produce elliptical retrograde particle motion (Rayleigh, 1885; Kennett, 1976; Shearer, 2009; Kolinsky *et al.* 2010). Following Shearer (2009), the wave equation of a plane P-wave, propagating in +x direction is given by

$$u = Ae^{-i\omega(t-ps-\eta z)}, \tag{2.1}$$

where p is the horizontal slowness, $\eta = \sqrt{\frac{1}{c^2} - p^2}$ is the vertical slowness and c is the P-wave velocity.

The wave equation can be written in the form of potentials, where ϕ is the scalar potential, which represents a P- wave and ψ is vector potential for the S wave.

$$u = \nabla\phi + \nabla x\psi, \quad \nabla.\psi = 0 \tag{2.2}$$

The ψ_y is the only part of ψ that produces the SV motion for plane wave propagtion in the x direction. Considering plane wave solutions for the plane wave for ϕ and ψ_y, this gives:

$$\phi = Aexp^{-i\omega(t-px-\eta_\alpha z)}, \tag{2.3}$$

$$\psi_y = Bexp^{-i\omega(t-px-\eta_\beta z)}, \tag{2.4}$$

where A and B are the amplitudes of P and SV waves respectively. The vertical slowness η for P and SV waves can be written as

$$\eta_\alpha = \sqrt{\frac{1}{\alpha^2} - p^2}, \tag{2.5}$$

$$\eta_\beta = \sqrt{\frac{1}{\beta^2} - p^2}, \tag{2.6}$$

Assuming that both P and SV have same horizontal slowness, the ray parameter p is constant and y component of the displacement and its partial derivatives are zero for P/SV plane wave. Therefore, the P-wave displacements of x and z components can be written as following

$$u_x^P = \partial_x \phi = pAi\omega A e^{-i\omega(t-px-\eta_\alpha z)}, \tag{2.7}$$

$$u_z^P = \partial_z \phi = \eta_\alpha Ai\omega A e^{-i\omega(t-px-\eta_\alpha z)}, \tag{2.8}$$

The SV displacements can also be written as

$$u_x^S = -\partial_z \psi_y = -\eta_\beta Bi\omega e^{-i\omega(t-px-\eta_\beta z)}, \tag{2.9}$$

$$u_z^S = \partial_x \psi_y = pBi\omega e^{-i\omega(t-px-\eta_\beta z)}, \tag{2.10}$$

In case of the boundary condition at the free surface is equal to zero (Z = 0), then the normal and shear tractions must vanish: $\tau_{xz} = \tau_{zz} = 0$.

$$\tau_{xz} = \mu(\partial_z u_x + \partial_x u_z), \tag{2.11}$$

$$\tau_{zz} = \lambda(\partial_x u_x + \partial_z u_z) + 2\mu\partial_z u_z. \tag{2.12}$$

Solving the above the equations by substituting (2.7)-(210) into (2.11) and (2.12), we obtain

$$\tau_{xz}^P = -A(2\mu p\eta_\alpha)\omega^2 e^{-i\omega(t-px-\eta_{alpha}z)}, \tag{2.13}$$

$$\tau_{zz}^P = -A\left[(\lambda+2\mu)\eta_\alpha^2) + \lambda p^2\right]\omega^2 e^{-i\omega(t-px-\eta_{alpha}z)}, \tag{2.14}$$

$$\tau_{xz}^S = -B\mu(p^2-\eta_\beta^2)\omega^2 e^{-i\omega(t-px-\eta_{beta}z)}, \tag{2.15}$$

$$\tau_{zz}^S = -B(2\mu\eta_\beta p)\omega^2 e^{-i\omega(t-px-\eta_{beta}z)}. \tag{2.16}$$

The requirements for the free surface are

$$\tau_{xz} = \tau_{xz}^P + \tau_{xz}^S = 0, \tag{2.17}$$

$$\tau_{zz} = \tau_{zz}^P + \tau_{zz}^S = 0. \tag{2.18}$$

By substituting (2.13) - (2.16) into (2.17) and (2.18) at $z = 0$, and terminating the common terms we get

$$A(2p\eta_\alpha) + B(p^2 - \eta_\beta^2) = 0, \tag{2.19}$$

$$A\left[(\lambda + 2\mu)\eta_\alpha^2 + \lambda p^2\right] + B(2\mu\eta_\beta p) = 0. \tag{2.20}$$

By substituting $\lambda + 2\mu = \rho\alpha^2$, $\mu = \rho\beta^2$ and $\lambda = \rho(\alpha^2 - 2\beta^2$, the equations for τ_{zz} can be written in terms of P and S velocities as following

$$A\left[2p\eta_\alpha\right] + B\left[p^2 - \eta_\beta^2\right] = 0, \tag{2.21}$$

$$A\left[\alpha^2(\eta_\alpha^2 + p^2) - 2\beta^2 p^2\right] + B\left[2\beta^2\eta_\beta p\right] = 0. \tag{2.22}$$

These equations describe P - SV boundary condition at free surface, where p is the horizontal slowness. Recalling the vertical slowness is given by $\eta_\alpha = \sqrt{\frac{1}{\alpha^2} - p^2}$ and $\eta_\beta = \sqrt{\frac{1}{\beta^2} - p^2}$, where $p > \beta^{-1} > \alpha^{-1}$ and η_α and η_β are imaginary. From equation (2.1) if we factor out the depth dependence, we get

$$u = Ae^{i\omega\eta z}e^{-i\omega(t-px)}. \tag{2.23}$$

In case that η is imaginary, it will lead to real values in exponent. This will result in evanescent waves. Evanescent are inhomogeneous waves and their amplitudes decay or grow exponentially with depth. The equations 2.21 and 2.22 can be written in the form

$$\begin{bmatrix} (2p\eta_\alpha) & (p^2 - \eta_\beta^2) \\ \alpha^2(\eta_\alpha^2 + p^2) - 2\beta^2 p^2 & B\left[2\beta^2\eta_\beta p\right] \end{bmatrix} \quad \begin{bmatrix} A \\ B \end{bmatrix} = 0. \tag{2.24}$$

For a homogeneous wave, the vertical slowness has real values. There is no dispersion in this case. The non trivial solution only occurs only if the determinant of the coefficient matrix is equal to zero, that is, when

$$(p^2 - \eta_\beta^2)\left[\alpha^2(\eta_\alpha^2 + p^2) - 2\beta^2 p^2\right] - 4\beta^2 p^2\eta_\alpha\eta_\beta = 0. \tag{2.25}$$

By substituting the values of η_α and η_β, the above equation can be written in terms of ray parameter p, P, and S velocities:

$$(2p^2 - \frac{1}{\beta^2})^2 + 4p^2(\frac{1}{\alpha}^2 - p^2)^{\frac{1}{2}}(\frac{1}{\beta}^2 - p^2)^{\frac{1}{2}} = 0. \tag{2.26}$$

To simplify this equation further we take β^2 common and for the imaginary values of η_α η_{beta} ($p > \beta^{-1} > \alpha^{-1}$), this can be written as:

$$(2p^2 - \frac{1}{\beta^2})^2 - 4p^2(p^2 - \frac{1}{\alpha}^2)^{\frac{1}{2}}(p^2 - \frac{1}{\beta}^2)^{\frac{1}{2}} = 0. \tag{2.27}$$

This equation is the Rayleigh equation. It depends upon P-wave velocity, α, and S-wave velocity β. The roots of the equation give the Rayleigh wave velocity, which propagates over an isotropic and elastic surface defined on the half surface (y $\geq$ 0). The phase velocity is $c = \frac{1}{p}$, and its value is slightly less than β. The value of $c = 0.92\beta$ for Poisson solid.

2.1.2 Love waves

Love wave (LQ or G) results from the constructive interference of the horizontally polarized (SH) shear waves at the free surface. It requires a velocity structure that varies with depth to exist. Unlike the Rayleigh wave, it can not exist in a uniform half-space (Dziewonski & Romanowicz, 2007). This is because the free-surface stress condition is incompatible with the propagation of an SH-type surface wave in the medium. According to Shearer (2009), the simplest circumstance for Love wave to propagate is the presence of a layer (with shear velocity β_1) overlying a half-space (with shear velocity β_2) (Shearer 2009). Therefore, if the shear wave velocity increases with the depth, it forms a wave guide, where *SH* waves are trapped. In this case a plane wave will turn at the depth where $\beta = \frac{1}{p}$, where p is the horizontal slowness the wave will propagate with along the surface. The dispersion equation for Love waves (Lay & Wallace, 1995b, chapter 4) can be written as

$$\tan(\omega\eta_{\beta 1}H) = \frac{\mu_2\eta_{\beta 2}}{i\mu_1\eta_{\beta 1}} = \frac{\mu_2\hat{\eta}_{\beta 2}}{\mu_1\eta_{\beta 1}}. \tag{2.28}$$

Taking into account a post critical situation where $c = \frac{1}{p} < \beta_2$ will yield $\eta_{\beta_2} = i\eta_{\beta_2}$ and $\hat{\eta}_{\beta 2}$ is real. The above equation gives a condition related to ω and c which must be satisfied. The velocityof the wave depends upon ω and c. Rewriting above equation gives

$$2H\omega\sqrt{\frac{1}{\beta_1^2} - \frac{1}{c^2}} - 2\pi n = 2\tan^{-1}\left[\frac{\mu_2\sqrt{\frac{1}{c^2} - \frac{1}{\beta_2^2}}}{\mu_1\sqrt{\frac{1}{\beta_1^2} - \frac{1}{c^2}}}\right] \tag{2.29}$$

or

$$\tan(H\omega\sqrt{\frac{1}{\beta_1^2}-\frac{1}{c^2}}) = \frac{\mu_2\sqrt{\frac{1}{c^2}-\frac{1}{\beta_2^2}}}{\mu_1\sqrt{\frac{1}{\beta_1^2}-\frac{1}{c^2}}}. \tag{2.30}$$

This equation represents the dispersion equation for Love waves, where H is the layer thickness, 2π is the phase shift, c is the phase velocity and ω is the angular frequency. The condition to ensure that all the terms are real is, $\beta_1 < c < \beta_2$. In order to solve this equation for the unknown phase velocity, we introduce the variable $\zeta = H\sqrt{\frac{1}{\beta_1^2}-\frac{1}{c^2}}$. This gives

$$\tan(\omega\zeta) = \frac{\mu_2}{\mu_1}\frac{\sqrt{H_2(\beta_1^{-2}-\beta_2^{-2}-\zeta^2)}}{\zeta}. \tag{2.31}$$

To determine where solutions exist, we can plot each function on either side of the equality sign. A finite number of solutions for the phase velocities exist, depending on ω, β_1, β_2, and H. Where the two curves intersect, we get a value for ζ, and hence for the phase velocities. The solutions are called modes; for a given frequency, there are several modes, each propagate with different apparent velocity.

2.1.3 Dispersion characteristics of surface waves

Seismic surface waves are dispersive; their propagation velocities change as a function of their frequency. In other words, individual harmonic components of the surface wave seismogram (individual modes) propagate over the globe at different velocities. In case of normal dispersion, lower frequencies have longer wavelengths - as the velocity is the product of the frequency and wavelength - and penetrate deeper in to the Earth. Since the velocity generally increases with depth, lower frequencies pass through the Earth with higher velocities. When the velocity varies as a function of frequency, surface wave is dispersed. Consequently surface wave signals disperse, as they travel away from their source, the faster waves arriving first and the slower waves becoming progressively delayed (Tromp & Dahlen, 1992; Levshin, 2001). Surface wave dispersion studies have been applied to understand the interior structure of the Earth started since the 1920s (e.g., Love, 1911; Rudzki, 1912; Gutenberg, 1924,1926; Jeffreys, 1928, 1936; Stoneley, 1932; Newlands, 1950; Haskell, 1953; Press, 1956; Ewing *et al.* 1957; Gutenberg & Richter, 1963; Dzeiwonski, 1971; Knopoff, 1972, 1983; Nolet, 1987; Sneider, 1993; Trampert & Woodhouse, 2003; Meier *et al.* 2004; Endrun *et al.* 2008; Lebedev *et al.* 2009, 2010, 2013; Goes *et al.* 2012; Nita *et al.* 2016 and many others).

Theoretical examinations of surface waves have been studied by Love (1911) and Rudzki (1912). The transmission of Rayleigh waves in a heterogeneous medium with a constant density and with a rigidity varying linearly with depth has been investigated by Stoneley (1932). Newlands (1950) discussed in greater detail Rayleigh waves in a heterogeneous medium consisting of two-layers. The matrix formulation of Thomson (1950) had been applied to the dispersion of surface waves on multilayered media (Haskell, 1953). Anderson (1961) investigated further the dispersive characteristics of transversely isotropic media. Crampin (1970) extended the Thomson-Haskell matrix formulation to anisotropic layers. Coste (1997) approximated dispersion formula for Rayleigh waves in a layered medium. A relation for the effective Rayleigh wave phase velocities in a vertically heterogeneous isotropic elastic half-space has been derived by Lai *et al.* (2014).

In a homogeneous isotropic half-space the surface waves are non dispersive. But when different frequency components travel at different phase velocities, pulse shapes will not stay the same as they travel but will become dispersed as the frequencies separate (Shearer, 2009). This results in interference effects that eliminate the wave energy except at particular times defined by the group velocity of the wave. The simplest case to explore the phenomenon of the dispersion further is to consider the net effect of two harmonic waves with slightly different frequencies and wave numbers. The sum of two harmonic waves with particular wave numbers k_1 and k_2 and frequencies ω_1 and ω_2 can be wriiten as:

$$u(x,t) = \cos(\omega_1 x - k_1 x) + \cos(\omega_2 x - k_2 x), \tag{2.32}$$

where ω is the angular frequency and k is the wave number. Both can be written in terms of the differences from their average values ω and k:

$$\omega_1 = \omega - \sigma\omega, k_1 = k - \sigma k, \tag{2.33}$$

$$\omega_2 = \omega - \sigma\omega, k_2 = k - \sigma k, \tag{2.34}$$

By substituting and adding the two cosines and simplifying, we obtain

$$\begin{aligned} u(x,t) &= \cos(\omega t - \sigma\omega t - kx + \sigma kx) + \cos(\omega t + \sigma\omega t - kx - \sigma kx) \\ &= \cos\left[(\omega t - kx) - (\sigma\omega t - \sigma kx)\right] + \cos\left[(\omega t - kx) + (\sigma\omega t - \sigma kx)\right] \\ &= 2\cos(\omega t - kx)\cos(\sigma kx - \sigma\omega t), \end{aligned} \tag{2.35}$$

To solve equation this equation we used the trigonometric identity $cos(A+B)+cos(A-B) = 2cosAcosB$. Therefore, the sum of the two harmonic waves is a product of two cosine

functions. Both correspond to propagating harmonic waves. Because $\sigma\omega$ is less than ω, the second term has a lower frequency, and varies more slowly with time than the first. In a similar way, because σk is less than k, the second term varies more slowly in space. Therefore, we have a carrier wave with angular frequency ω and wave number k, on which a slower varying envelope with angular frequency $\sigma\omega$ and wave number σk is superimposed. Both travels with different velocities. The carrier wave is called phase velocity and refers to the velocity of a monochromatic wave or the velocity at which the peaks and troughs at a given frequency move along the surface, whereas the envelope wave is called group velocity and refers to the velocity at which the wave energy propagate. The group velocity U can be written as

$$U = \frac{d\omega}{dk}, \tag{2.36}$$

as $\omega = ck$, therefore the group velocity can be also written as

$$U = \frac{d\omega}{dk} = \frac{dck}{dk} = c + k\frac{dc}{dk} = (1 - k\frac{dc}{d\omega})^{-1}, \tag{2.37}$$

The phase velocity of both Rayleigh and Love increases with period. From this equation, it can be seen that, group velocity is dependent upon phase velocity. As $\frac{dc}{d\omega}$ is negative in equation 2.37, this shows that group velocity is less than phase velocity *($U < c$)* (Shearer, 2009). In case of the phase velocity changes is zero, the group and phase velocities are the same. Generally the phase velocity is increasing with period, and decreasing with frequency. Rayleigh wave dispersion curves include a phase velocity increase from about 2 to 3 $km.s^{-1}$ at short periods below 10 s to about 4 $km.s^{-1}$ at intermediate periods (20 - 50 s). Another strong increase to more than 5 $km.s^{-1}$ occurs at periods longer than 100 s (Dziewonski & Romanowicz, 2007; Shearer, 2009; Bartzsch *et al.* 2011; Lebedev *et al.* 2013). On the other hand Love wave phase velocities are higher than Rayleigh wave phase velocities for periods lower than about 120 s and show a steadier increase with period (Dahlen & Tromp 1998; Dziewonski & Romanowicz, 2007; Lebedev *et al.* 2013; Soomro *et al.* 2016; Kästle *et al.* 2018). At very long periods Love wave phase velocities are normally lower than Rayleigh wave phase velocities.

Group velocitits tend to change more significantly with structure at depth but the error in their meaurements are also larger than those of phase velocity. On the other hand, source effects on group velocity are relatively small and are usually ignored. Due to their long wavelengths, they sample the deeper structure of the Earth and they provide some of the best constraints on the Earth‘s crust and upper mantle structure. In general, destructive interference of the upgoing and downgoing reflected waves will occur, except at certain

discrete frequencies ω and n multiples of it (with n as an integer). The values of ω given for n = 0 are termed the fundamental modes while larger values of n define the higher modes or overtones (Dzeiwonski, 1984 and van der Lee & Nolet, 1997).

2.1.4 Surface wave methods

2.1.4.1 Single-station approach

The single-station method is a classical technique for analysing long-period Rayleigh and Love waves recorded on digital seismic networks (Brune, Nafe & Oliver 1960). Such measurements are used to study the lateral variations of surface wave velocities on a regional scale structure (Dzeiwonski 1969; Nakanishi & Anderson 1984; Knopoff 1972; Levshin 1995; Trampert & Woodhouse, 1995; Ritzwoller *et al.* 1995; Ritzwoller & Levshin, 1998; Pasyanos *et al.* 2011; Foster *et al.* 2014). Earthquake source parameters including origin time, source location, source mechanism and source finiteness are required when measuring the single-station velocities (Brune, Nafe & Oliver, 1960; Brune, 1962; Levshin, 1992). These components are highly affecting the initial phase of the surface wave which is used to calculate the single-station surface wave velocities. Both surface wave observables: phase and group velocities can be measured using the single-station method as following:

i) Phase velocity measurements: The single-station methods measure the phase accumulated over the entire ray path from source to receiver (e.g. Trampert & Woodhouse 1995). The observed phase ϕ_i can be written as

$$\phi_i = \omega t_0 - \frac{\pi}{4} + \phi_s - \frac{\omega l_i}{C_i} + \frac{(i-1)\pi}{2} - \phi_f - \phi_r + 2N\pi, \tag{2.38}$$

where ω is the angular frequency, t_0 is the starting time of the group velocity window, $-\frac{\pi}{4} + \phi_s$, is the initial phase at the source, l_i is the length of surface wave path, the term $\frac{(i-1)\pi}{2}$ comes from the polar phase shifts (Brune, Nafe & Alsop 1961) at the pole and antipole, ϕ_f is the phase delay due to finite source process, ϕ_r is the instrumental phase delay, $2N\pi$ is the ambiguity of the phase. From those equations, the apparent phase velocity along the entire surface wave path can be defined as

$$C_i = \frac{\omega l_i}{-\phi_i} + \omega t_0 + \frac{\pi}{4} + \phi_s + \frac{(i-1)\pi}{2} - \phi_f - \phi_r + 2N\pi, \tag{2.39}$$

Frequency dependence of the ellipticity advocated by (Dahlen, 1976; Dziewonski & Sailor, 1976). Foster *et al.* (2014) extended the single-station method by introducing a correction of the propagation direction with the help of dense mini arrays. Plenty of studies have been using single-station measurements to calculate the phase velocities for different parts of the globe (Lee & Solomon 1979; van der Lee & Nolet 1997; Ekström *et al.* 1997; Godey *et al.* 2003; Carannante & Boschi 2005; van der Lee & Frederiksen 2005; Lebedev *et al.* 2006; Marone *et al.* 2007; Nettles & Dziewonski, 2008; Pollitz & Snoke, 2010; Yuan *et al.* 2011; Foster *et al.* 2014).

ii) Group velocity measurements: The earlier group velocity single station measurements were carried out by Gutenberg (1924) and Ewing and Press (1950). They measured group travel time from source to stations as function of periods in time domain. Landisman *et al.* (1969) introduced time frequency analysis for single station method. This method was improved by (e.g. Levshin *et al.* 1989; Ritzwoller & Levshin, 1998; Vdovin *et al.* 1999; Pasyanos *et al.* 2007). According to Nakanishi and Anderson (1984), the group velocity U_i is calculated by using the formula:

$$U_i = l_i(t_g + \frac{d\phi_s}{d\omega} - \frac{d\phi_f}{d\omega} - \frac{d\phi_r}{d\omega}), \tag{2.40}$$

where l_i is the length of surface wave path, i.e., source-receiver distance, t_g is the arrival time of the wave group at the centre angular frequency ω on the seismogram, ϕ_s is the directional part of the initial phase at the source, ϕ_f phase delay due to finite source process, ϕ_r is the instrumental phase delay. The group arrival time t_g is calculated by analysing a moving window with a specific width that may be determined empirically (Landisman, Dzeiwonski & Sato, 1969). Then the effect of the source orientation $\frac{d\phi_s}{d\omega}$ is taken into account. Such effect on the Rayleigh wave group velocity measurements has been estimated by Knopoff and Schwab (1968).

2.1.4.2 Inter-station phase velocity approach

The inter-station method (Sato 1955) is often used for regional surface wave tomography and local scale interstation measurements of phase velocity (e.g. Meier *et al.* 2004; Yao *et al.* 2006; Zhang *et al.* 2007; Endrun *et al.* 2008). The advantage of this method lies in the minimzing the effect of wave propagation from the source to the receiver as well as canceling out the error of source mechanism and source location. Brilliant and Ewing (1954) measured Rayleigh wave phase differences between stations in the time domain. This helped

to eliminate the shifts in the phase due to the propagation of the fundamental modes from the source to the first station. In order to diminish the influence of the source on phase-velocity measurements, Toksöz and Ben-Menahem (1963) measured phase velocities in the frequency domain using successive passages of surface waves at a single station. Moreover, McEvilly (1964) measured the phase difference between two stations in the frequency domain for both Love and Rayleigh waves. According to Meier *et al.* (2004), considering the ray theory is valid and that surface waves propagate along the exact great-circle, the phase velocity curve is computed from the phase difference $\phi(\omega)$ that could be extracted from the complex spectrum $\varsigma(\omega)$ of filtered and weighted cross-correlation function of the fundamental mode surface waves between the two recording stations as following:

$$\phi(\omega) = arctan\frac{\Im\{\varsigma(\omega)\}}{\Re\{\varsigma(\omega)\}} + 2n\pi, \tag{2.41}$$

where n is an integer describing the number of cycles the surface wave has undergone in it's travels. A suite of potential phase velocity curves is computed for several possible values of n and the appropriate dispersion curve is chosen from this suite by comparison with initial model because of the ambiguity in the phase. The average phase velocity $c(\omega)$ at the frequency ω due to the velocity structure between the two recording stations can be expressed by:

$$c(\omega) = \frac{\omega\Delta}{\phi(\omega)}, \tag{2.42}$$

where Δ is the distance between the wave fronts originating at the source and arriving at the two recording stations (the difference in epicentral distances). This method has been widely applied using local and regional networks (e.g. Endrun *et al.* 2004, 2008, 2011; Meier *et al.* 2004; Prindle & Tanimoto 2006; Lebedev *et al.* 2006, 2009; Yao *et al.* 2006; Deschamps *et al.* 2008; Darbyshire & Lebedev, 2009; Beghein *et al.* 2010; Yoshizawa & Ekström, 2010; Adam & Lebedev, 2012; Agius & Lebedev, 2013; Foster *et al.* 2014; Soomro *et al.* 2016). General speaking, the inter-station dispersion curves proved to be highly effective data as input for surface wave tomography (Adam & Lebedev 2012). Generally, It can provide phase velocity disperion curves in a very broad frequency band compared to the single station measuremnts, especially at higher frequencies (Lebedev *et al.* 2006). Moreover, this method is well suited for networks with variable inter-station distances ($\sim$50 km to 1000 km) and large volumes of data sets. For regional networks (where the inter-station distances $\sim$100 km), the period range may span from $\sim$10 seconds to 200-400 seconds. Using local networks with finer station spacing $\sim$10 km, phase velocities may be obtained for periods as low as 3.0 s (Endrun *et al.* 2004). Compared to the more commonly used single-station

geometries, the inter-station measurements have the advantage of a closer spacing between the stations providing higher lateral resolution.

2.1.4.3 Ambient noise tomography

Ambient noise tomography has become a valuable method to extract surface waves signal from continuous seismic recordings to provide both small scale as well as large scale tomographic images of the Earth crust and shallow uppermost mantle (Boschi & Ekström 2002; Sabra *et al.* 2005; Shapiro *et al.* 2005; Yao *et al.* 2006; Lin *et al.* 2007; Bensen *et al.* 2008; Stehly *et al.* 2009; Fry *et al.* 2010; Verberke *et al.* 2012; Mocquet *et al.* 2014; Qorbani *et al.* 2015). Cross-correlating continuous recordings of seismic signals (ambient noise) allows for estimating short and intermediate periods (< 50 s) surface wave velocities (Stehly *et al.* 2006, 2009) which is complementary to the period range of teleseismic surface waves, and allowing to better imaging the lithosphere-asthenosphere system (Kästle et al 2016, 2018). As noted by Shapiro and Campillo (2004), the cross-correlation of seismic ambient signal recorded at two different stations approximates the Green function associated with a point source acting at one of the stations location, and a receiver deployed at the other's location. Such empirical Green function can then be analyzed in different ways, with the ultimate goal of obtaining information about Earth's structure at various depths between the two stations. Most authors either extract group velocity from its envelope (e.g., Ritzwoller *et al.* 2001; Shapiro *et al.* 2005; Stehly *et al.* 2006, 2009) or measure the phase velocity (e.g., Lin *et al.* 2008; Yao and van der Hilst, 2009; Ekström *et al.* 2009). Inverting the entire ambient-noise waveform have been introduced by (Tromp *et al.* 2010; Basini *et al.* 2012).

While measuring the ambient noise group velocitis is widely recognized, measuring the phase velocity is more elusive. Phase and group velocity measurements are only valid under certain conditions such as a uniform distribution of noise sources in space and time, a laterally homogeneous medium velocity, and far-field sources. As these conditions are not strictly met in practical situations, errors in the measured phase velocity are to be expected (Tsai 2009; Yao & Van Der Hilst 2009; Tsai & Moschetti 2010). Correcting for such errors is not an easy task due to the complexity of these effects. Therefore, it is important to validate data obtained from ambient-noise analysis by comparison with equivalent measurements obtained from earthquake observations (Yao *et al.* 2008; Ritzwoller *et al.* 2011; Kästle *et al.* 2016). Following the theoretical formulation of Tsai and Moschetti (2010), Boschi *et al.* (2013) derived different approaches to measure inter-station surface wave phase velocity and applied them on the same dataset of (Verbeke *et al.* 2012). One approach of them is based on time-domain cross-correlation, and is implemented using a far-field approximation of the

wavefield equation. The other is based on frequency domain cross-correlation, and on finding the roots of the real part of the cross-correlation spectrum. Kästle *et al.* (2016) improved the algorithm is the 'frequency domain' approach employed by Boschi *et al.* (2013) based on the ideas of Aki (1957) and Ekström *et al.* (2009). In this approach, the zero crossings of the real part of the cross-correlation spectrum are evaluated to derive the phase-velocity dispersion measurements. This means that the Green function's amplitude does not have to be reconstructed, which is the case when phase is to be determined by analysis of time-domain traces (Bensen *et al.* 2007; Lin *et al.* 2008; Verbeke et al.2012). They validated their ambient-noise observations by comparison with earthquake-based ones.

Ekström *et al.* (2009) introduced another method for phase velocity dispersion curve computation using the Bessel function approximation of the measured spectra. An advantage of this approach with respect to the previous ones was that it avoided the limitation given by short inter-station distances with respect to wavelengths. Another method was proposed by Lin *et al.* (2009) in which each station was considered as an effective source of the seismic noise and the other stations were used to recover the wavefronts of the propagating noise signal. They estimated phase velocity variations and the azimuth of the propagation. Although surface waves emerge from long-term waveform cross correlation of ambient noise, body wave reconstruction from regional and teleseismic earthquakes as well as from ambient noise has been demonstrated by several studies (e.g. Landes *et al.* 2010; Nakata *et al.* 2014, 2015; Oliver *et al.* 2015).

2.2 Data set

We utilize a large database consists of more than 4000 seismic events recorded by more than 4500 broad band seismic stations distributed within the region between latitudes -60° to 100° eastward and longitudes -70° to 85° northward, provided by the European Integrated Data Archive (WebDc/EIDA) and IRIS. Moreover, for the first time, data from the Egyptian National Seismological Network (ENSN), recorded by up to 25 broad band seismic stations, are also included in the analysis. The reviewed catalog by the international seismological centre (ISC) is used for select regional and teleseismic earthquakes with specific criteria. We searched for stations with inter-station distances ranges from 0.45° and 30° as well for all events in the period from 1990 to 2015 which have an epicentral distances ranges between 2.7° and 120°, a minimum magnitude of 4 - 6 Mw (increasing linearly with the epicentral distance) and a maximum depth of 100 km. Furthermore, the backazimuth of the selected

Table 2.1 Selection criteria for the processed events

Criteria	Values
Min. epicentral distance (°)	2.7
Max. epicentral distance (°)	120
Max. considered depth (km)	100
Deviation from great circle path	7.0
Min. magnitude at min. distance	4.0
Min. magnitude at max. distance	6.0
Min. inter-station distance (°)	0.45
Max. inter-station distance (°)	30.0

events must lie within 7° from the azimuth of the great circle connecting the two recording stations.

Figure (2.1) shows an orthographic projection of all the events which met the selection criteria. An automated routine based on ObsPy (Beyreuther *et al.* 2010) is used to retrieve the waveform data via the European Integrated Data Archive (EIDA) infrastructure. On the other hand, we developed another Obspy routine to extract the desired waveforms from the Egyptian seismic stations. Using this routine, we were able to prepare the Egyptian data for the analysis. Such preparations include extracting specific times windows, re-sampling, rotation, and correction for the different instrument responses.

Approximately 8.0 millions waveforms have been requested through the Arclink interface of WebDC (http://www.webdc.eu) for all the possible station combinations. In total, we downloaded more than 3.5 millions waveforms of all the requests. Figure (2.2) shows a color-coded distribution of the seismic stations within th considered region.

The color indicates the number of downloaded events per each individual station from the international seismic networks as well as the extracted events from the Egyptian National Seismological Network. The number of processed events per each station-pair (Fig. 2.3) is greater for station pairs with an NE to SE and E-W azimuths, due to the high rate of seismic activity in Eastern Asia. For paths with a more northerly azimuth, there are significantly fewer events, with moderate event rates in eastern Mediterranean and the northeastern Pacific. Including the Egyptian staions helps alot to enhance the azimuthal path coverge of the Eastern Mediterranean compared to the previous surface wave studies (Bourova *et al.* 2005; Karagianni *et al.* 2002, 2005).

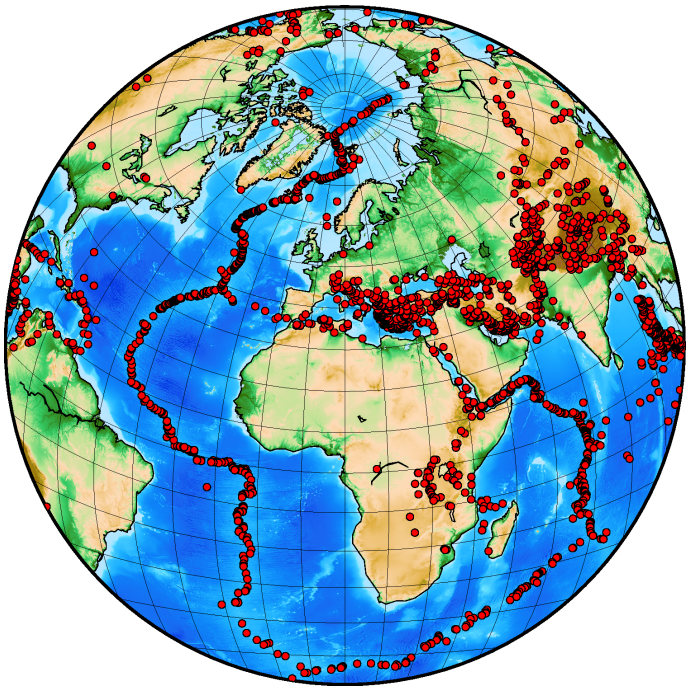

Fig. 2.1 The distribution of the seismic evenets used in this study.

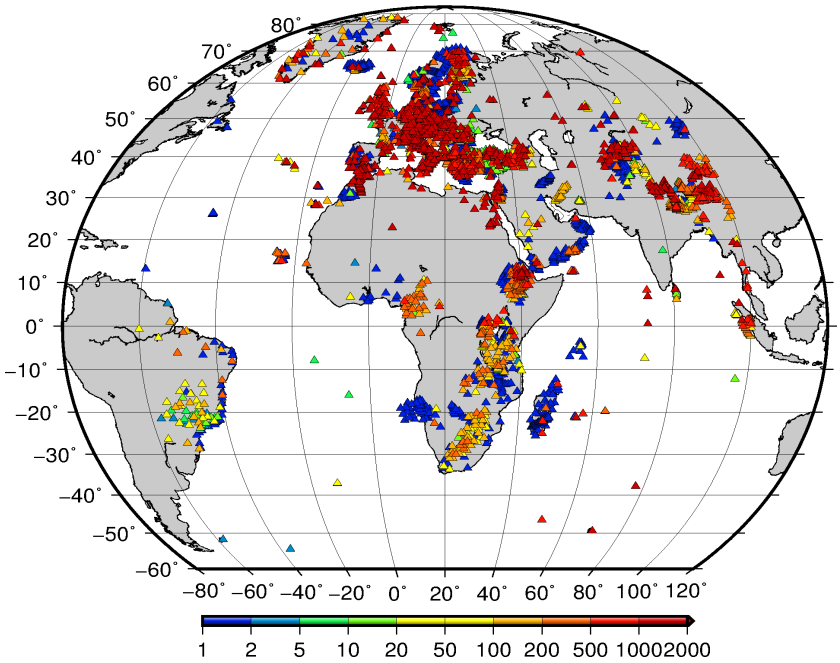

Fig. 2.2 Seismic stations distribution within and around the study region. The color of each station represent the number of available waveforms for each single station.

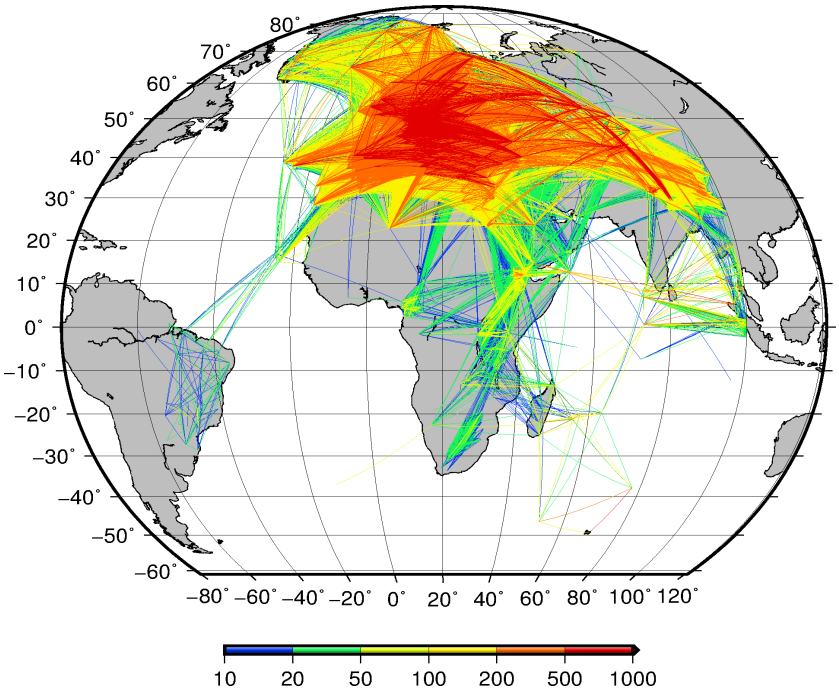

Fig. 2.3 The ray path coverage. The color represents the number of events recorded by each station pair located on the same great circle path.

2.3 Automated inter-station phase velocities

The distribution of broad band seismic stations in the study area (Fig. 2.2) is highly uneven. The dataset shows a heterogeneous instrumentations and different times of deployments. This results in a large amount of waveforms. The best coverage in terms of density and bandwidth is achieved in Europe and the Mediterranean. Array methods can only be applied to small regions and limited time periods. The inter-station measurements, in contrast, are well suited to determine phase velocities of fundamental modes from large available data volumes (Yang *et al.* 2007). Previous applications of broad-band inter-station cross-correlation measurements of phase velocities using earthquake data have been limited to relatively local studies because of the substantial burden of the manual data processing (Zhang *et al.* 2007; Roux *et al.* 2011; Polat *et al.* 2012).

In this section, a new implementation of the automated inter-station phase velocity measurements (Soomro *et al.* 2016) is utilized to obtain Rayleigh and Love dispersion curves by cross-correlating the seismograms for each station pair approximately located on the same great-circle path. This involves two sub-processes. Firstly, we employ an elaborated filtering and windowing scheme to enhance the target signal and makes possible a significantly broader frequency band of the measurements, compared to previous implementations of the method.

The selection of acceptable phase-velocity measurements for each event is performed in the frequency domain, based on a number of fine-tuned quality criteria including a smoothness crieteria (Soomro *et al.* 2016). Plenty of single-event dispersion curves are calculated from from both propagation directions, when possible. Secondly, path-average dispersion curves are obtained by averaging the smooth parts of single-event measurements to obtain robust, broad-band dispersion curves representing the structure between the considered stations with the error estimates. This automated implementation of the inter-station method is well suited for the analysis of large databases from hetereogeneous distribution of seismic stations.

2.3.1 Single-event phase velocity measurements

The newly developed automated inter-station algorithm (Meier *et al.* 2004; Soomro *et al.* 2016) is applied to measure the fundamental mode Rayleigh and Love wave phase velocities along all the inter-station paths crossing the region. Using this algorithm, the phase velocities are calculated from the phase difference of the fundamental mode at the two recording stations which are approximately located on the same great-circle path. The phase difference is mainly caused by the heterogeneous structure along the inter-station path (De Vos *et al.* 2013) and can be determined from the weighted and filtered cross-correlation of fundamental mode waveforms with it's Fourier transformation (Soomro *et al.* 2016), with the advantage of a closer spacing, providing a higher lateral resolution. This automated method has been designed to obtain smooth, path-average fundamental mode dispersion curves from large inhomogeneous data sets recorded by permanent and temporary stations. It's main characteristics can be summerized as follows: (a) solution of the 2π ambiguity by picking the correct 2π branch on which the measurements should be performed, (b) the automated determination of the frequency range of reliable measurements, (c) selecting the smooth segments of the dispersion curve and the rejection of rough perturbations, (d) the detection of quality problems caused by wrong response information or timing problems and (e) the rejection of outliers and the very small segments of the dispersion measurements.

Following Soomro *et al.* (2016), the Fourier transform of the fundamental mode waveform *U(t)* may be formulated as:

$$U_0(\omega) = |U_0(\omega)|exp(i\phi_0(\omega)) \simeq |U_0(\omega)|exp\left(-i\int_0^{\Delta} k(\omega,s)\,ds\right) \tag{2.43}$$

where $\phi(\omega)$ is the phase spectrum of the fundamental mode, $k(\omega,s)$ is the frequency dependent wave number along the path and Δ is the epicentral distance. By cross-correlating the

Fourier transform *U(t)* of the fundamental mode waveforms $\rho_0(t)$, the phase difference can be calculated as:

$$F\{\rho_0(t)\} = |U_{01}(\omega)||U_{02}(\omega)|exp(i\phi_0(\omega)) \tag{2.44}$$

$$\phi(\omega) = \phi_{01}(\omega) - \phi_{02}(\omega) \simeq k(\omega)(\Delta_2 - \Delta_1) \tag{2.45}$$

where $\phi_{01}(\omega)$ and $\phi_{02}(\omega)$ are the phase spectra of the fundamental modes at two stations and $(\Delta_1$ and $\Delta_2)$ are the epicentral distances for station 1 and station 2, respectively. As a result, the uncorrelated noise has less effect on cross-correlation function and the contibution of the large amplitude fundamental mode to the cross correlation function is enhanced. This is followed by a time-frequency analysis in order to obtain $\rho(\omega_n,t)$ in the frequency-time domain. The cross-correlation function is then filtered with a set of frequency-dependent Gaussian band-pass filters in order to enhance the time-frequency resolution (Soomro *et al.* 2016). To suppress effects from other signals, e.g., uncorrelated noise and higher modes, a Gaussian windowing is applied in the time domain (Wielandt 1987; Meier *et al.* 2004; Soomro *et al.* 2016). The width of the window is increasing linearly as a function of frequency.

According to Meier *et al.* (2004) the time windows are placed around the maximum of the filtered cross correlation function with the aim to extract the fundamental mode contribution and reduce both the higher modes contributions as well as the uncorrelated noise effect. Finally, the resulted cross correlation function $\rho_\omega(\omega_n,t)$ is appoximately equal to the filtered cross correlation function of the fundamental mode $\rho_0(\omega_n,t)$. In the frequency domain, the fundametal mode phase difference between the two recording stations can be then calculated and the phase velocity can be measured as follows:

$$c(\omega) = \frac{\omega(\Delta_2 - \Delta_1)}{\phi(\omega) + 2n\pi}, \tag{2.46}$$

An example of the automated determination of the single-event phase velocities from the cross-correlation function is shown in figure (2.4). The vertical component waveforms of the teleseismic event of 25-Aug-2001, 5.9 M_w at the two recording stations (GVD and WDD) as well as their corresponding time-frequency representations are shown on the top panel of the figure. The group arrival of the fundamental mode Rayleigh wave clearly emerges as a ridge across the time-frequency map. At higher frequencies above 60 mHz, both waveforms are strongly scattered due to the effect of the crustal structure heterogeneities along the wave propagation path. The cross-correlation function associated with the amplitude of it's time-frequency representations are plotted on the bottom left panel. It is clear that the dispersion can be highly reduced using the cross-correlation. In the bottom right, a bundle of candidate phase-velocities due to the 2π ambiguity (blue lines), plotted together with the

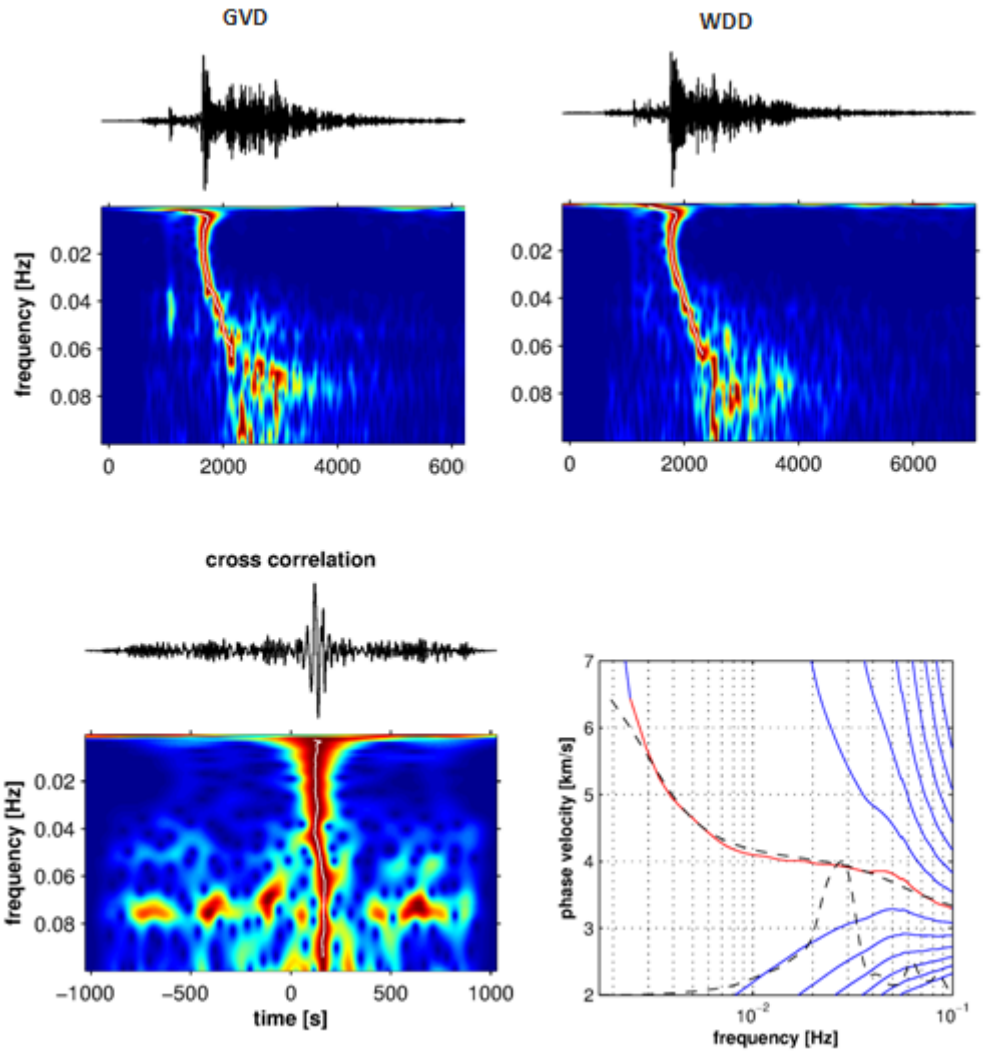

Fig. 2.4 Automated inter-station single-event Rayleigh phase-velocity measurement for the station pair GVD-WDD

reference model (dashed black); red line: is the automatically selected smooth segment of the curve that is accepted as the dispersion measurement representing the structure between the considered stations.

For the automated selection of the smooth parts of the dispersion curves, Soomro *et al.* (2016) introduced three main criteria include:

i) Background model criterion: in which the correct 2π branch has to be identified by comparing it to a reasonable background model. From figure (2.4), the 2π branches are close to each other at higher frequencies. With decreasing the frequencies, they are

strongly divergent. This enables the identification of the correct branch easily at lower and intermediate frequencies. At higher frequencies, the neibouring branches are also tested. An emperically-defined threshold ($th_{\Delta C}$ = 15 %), representing the difference between the measured phase velocities $C(\omega_i)$ and the those for background model $C_o(\omega_i)$. This can be defined as following:

$$|\frac{C(\omega_i) - C_o(\omega_i)}{C_o(\omega_i)}| \times 100 < th_{\Delta C}; \tag{2.47}$$

The portions of the curve that exceed this threshold are rejected. The acceptable phase velocity curve is the closest one to the background model, especially at intermediate and lower frequencies. A global 1D model would be sufficient for the 2π branch indentification, neverthelss in our case we used a path-specific reference model. For each station-pair, a path-average reference model has been calculated through a 3D model consists of CRUST1.0 (Laske *et al.* 2013) and PREM (Dziewonski & Anderson 1981). Such path-specific reference models accounts for the first order structural variations like the Moho depth and the sedimentary basin along the paths. Preferably is to keep this parameter as loose as possible in order to allow for sufficient variations from the background model.

ii) Smoothness criterion: in order to ensure a certain degree of smoothness on the accepted phase velocity measurements, the phase velocity perturbations are evaluated by calculating the first partial derivative of the measured phase velocity with repect to frequency and comparing it with the corresponding value of the background model. Then a summation of the absolute values of the derivative deviation from the reference model over a moving window in the frequency domain is performed (Soomro *et al.* 2016). The frequency range of the summation is increasing linearly with frequency, to account for the greater first derivative of the phase velocities at lower frequencies. Consequently, a frequency independent threshold is applied (in our case is equal (th_S = 0.055). This can be defined by multiplying the smoothed first derivative by the considered frequency range (Δf) over which the summation is done.

$$S(\omega_i) = \sum_{\omega_i=\omega_i-d(\omega_i)}^{\omega_i+d(\omega_i)} |\frac{C'(\omega_j) - C'_o(\omega_j)}{C_o(\omega_j)}| \times \Delta f < th_S, \tag{2.48}$$

iii) Length of the accepted segment: very short portions of the the dispersion curves are useless and may be errorneous especially at higher frequencies where deviations in the phase velocity from the background model may be greater, due to lateral heterogeneities and crustal wavefield complexities. In order to avoid such too short segments, We apply the length criterion as introduced Soomro et la., (2016). It is a frequency-dependent, relaxed at longer

periods and more stricter at short period. For more details on the choice of the smoothness parameter and the other parameters, see Soomro *et al.* (2016).

2.3.2 Automatic averaging of individual measurements

Measureing the path-average dispersion curve from a bundle of single-event dispersion curves helps to obtain a single, robust broadband inter-station curve representing the structure between the considered two stations (Meier *et al.* 2004; de Vos *et al.* 2013; Soomro *et al.* 2016). They showed that averaging the phase velocity measurements from multiple single-event curves from both propagation directions is partly compensates for effects from regions far from the inter-station area and helps to increase the inter-station sensitivity. Therefore, after obtaining a bundle of smooth single-event dispersion measurements, in a further process we follow the automated averaging scheme (Soomro *et al.* 2016) to obtain a unique very broad band and more accurate dispersion curve sampling the given inter-station path. Figure (2.5) shows an example of the automated calculations of the individual inter-station measurements for $\sim$ 25 years of data recorded by the station-pair (GVD-WDD). In total, more than 1020 seismic events from both propagation directions were processed. The station pair locations (red triangles) are shown on the map in figure (2.5a). The processed events are plotted in red and black representing the different propagation directions.

In the averaging procedure, some selection criteria are applied (Soomro *et al.* 2016). They include (a) the outliers rejection (in our case, 10 % outermost values are rejected), (b) at each frequency a minimum number of measurements is needed (here, 5), (c) the mean phase velocity and standard deviation are calculated separately for the two directions, (d) calculation of the standard deviations for the averaged curves and (e) the length criteria is applied to the resulting path-average curve. This resulted in $\sim$ 750 acceptable single-event dispersion curves. The measurements for the two different propagation directions which are plotted in black and red curves (Fig. 2.6b). Obviously, the measurements are highly mutually consistent for the two different propagation directions. The same dispersion measurement are plotted on top of each other in figure (2.6c) after the rejection of the 10 % of the outliers. The resulted path-average dispersion curve and its standard deviation, after outlier rejection are shown on figure (2.6d).

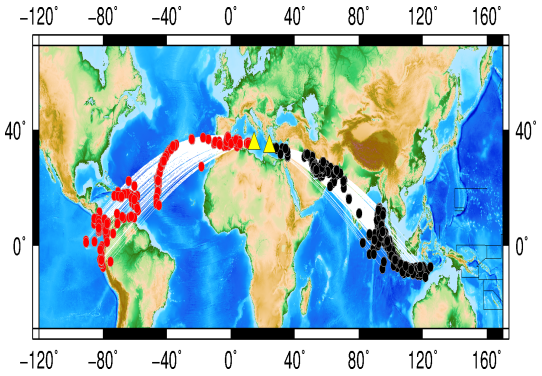

(a) Map shows the processed events

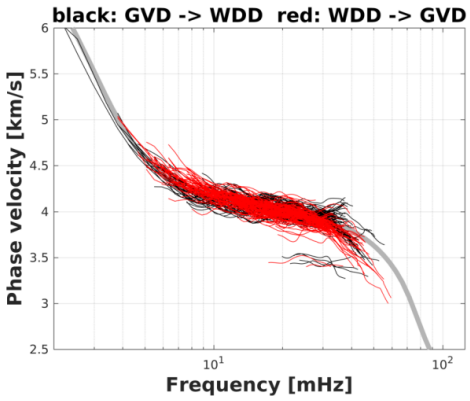

(b) All selected individual measurements

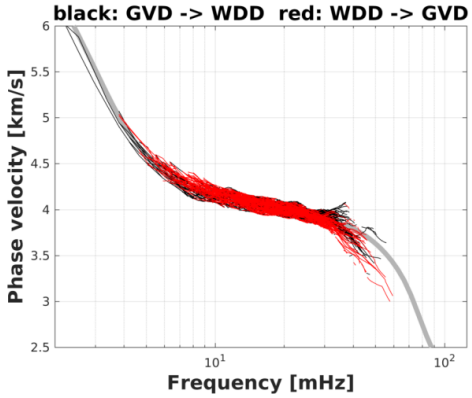

(c) The same as (b) without the outliers

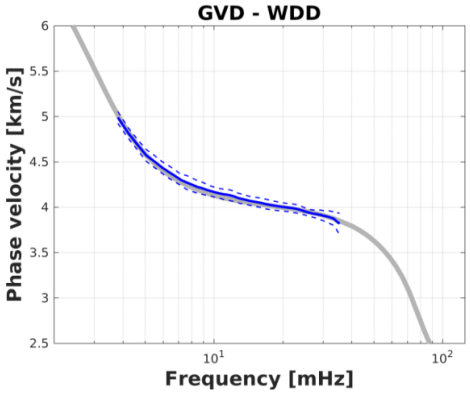

(d) Average dispersion curve and standard deviation

Fig. 2.5 Automated averaging of individual inter-station dispersion measurements for the station-pair GVD-WDD

2.3.3 Effect of Off-great-circle propagation on the phase velocities

Assuming that ray theory is valid and a wave propagating exactly along the great-circle path connecting an earthquake and two recording stations, the phase difference between the stations is then mainly caused by the structure along the interstation path and the effect of the unknown three dimensional Earth structure far from the inter-station path could be diminished (De Vos *et al.* 2013). This condition seems to be difficult to achieve on real Earth due to deviations of the wave propagation caused by lateral heterogeneities and crustal complexities.

Several studies dealt with the effect of off-great-circle propagation on the surface waves. Array analysis of 20-100 s period waves in the French Alps (Cotte *et al.* 2000) showed that the deviations may be greater than 30°. Levshin *et al.* (1994) studied the polarization anomalies

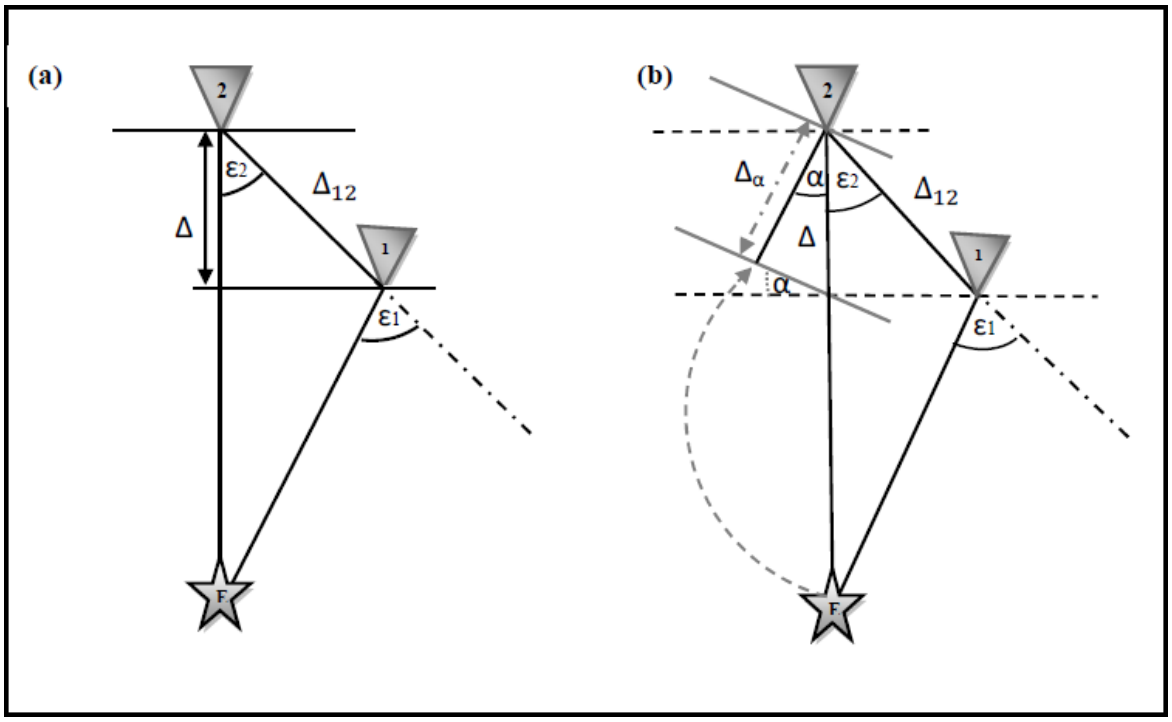

Fig. 2.6 Source-receiver geometry for the two-station measurements. a) In absence of off great-circle path propagation. b) In presence of off great-circle path propagation. The distance between the two stations is denoted by Δ_{12}, ε_1 is the angle between the proposed great-circle connecting the two stations and the event and the actual great-circle connecting the event and the first station, ε_2 is the angle between the inter-station path and the great-circle path and Δ and Δ_α are the difference in epicentral distances in the absence and presence of off path propagation, respectively, and α represents the deviation angle from the great-circle path.

observed in the former Soviet Union for surface waves crossing northern and central Eurasia, and showed how a regional structure showing lateral hetereogenities in the crust and upper mantle can cause large deviations from the great-circle propagation. According to Alsina and Snieder (1996), based on beam-forming analysis of data from a temporary array in the Netherlands, Germany and Belgium, they measured off-path propagation up to 30° at 40 s period and also showed that the waves propagated through the Tornquit-Teisseyre Zone had large deviations. In contrast, a smaller deviations from the great-circle-path were observed in the Iberian Peninsula (Alsina *et al.* 1993). In the following we are showing how the off-path propagation can bias the phase velocity measurements. The source-receiver geometry for the inter-station phase velocity measurements is shown in the diagram in figure (2.6). The distance between the two stations is denoted by Δ_{12}, ε_1 represents the angle between the proposed great-circle connecting the two stations and the event and the actual great-

circle connecting the event and the first station and ε_2 is the angle between the great-circle contecting the two stations and the great-circle-path to the second station, where $\varepsilon_2 = \varepsilon_1$ have to be small and very close to zero.

In the ideal case where $\varepsilon_2 = \varepsilon_1 = 0$, the phase velocity between the two stations $c_{12}(\omega)$ can be calculated by substituting Δ by Δ_{12} in equation (2.42), where the distance between the wavefronts at the two recording stations is the same as the inter-station distance:

$$c_{12}(\omega) = \frac{\omega \Delta_{12}}{\phi(\omega)}. \tag{2.49}$$

How large would the error be in the phase velocity measurements, if we would use equation (2.48) instead of equation (2.42) (i.e., in case that the epicenter is not located on the great-circle connecting the two recording stations). This can be estimated from the ratio R_1 between the phase velocity measurements from (eq. 2.48) and (eq. 2.42), respectively assuming a plane wave at the surface of half-space, where $\Delta = \Delta_{12} \cos \varepsilon_2$:

$$R_1 = \frac{c_{12}(\omega)}{c(\omega)} = \frac{(\omega)\Delta_{12}}{\phi(\omega)} / \frac{(\omega)\Delta}{\phi(\omega)}, \tag{2.50}$$

$$R_1 = \frac{1}{cos\varepsilon_2}. \tag{2.51}$$

Consequently using the inter-staion distance instead of the epicentral distance will bias the estimated the inter-station phase velocities towards higher values. Indeed, the effects of lateral heterogeneity in the Earth especially in the lithosphere induce refraction and diffraction of the long-period surface waves. It has long been known that the lateral refraction of long-period surface waves by heterogeneity in the mantle may be significant. Evernden (1954) was among the first authors who claimed that there is a measurable off-great-circle propagation even for long-period surface waves. Such effects are strong at continental margins, where the crustal thickness changes considerably. The presence of the lateral heterogeneity in addition to the finite frequency content of the seismic surface waves makes the application of the inter-station method more complicated. Deviations from great-circle propagation can be very difficult to be estimated due to the complexity of the wavefield. In such cases, polarization analysis or array mesurements is needed. In the simple case as in figure (2.6b), the effect of off-great-circle propogation on the inter-station phase velocity measurements will be estimated quantitatively in order to know to which extent the error in the measurements due to this effect can be. Figure (2.6.b) shows the case in presence of off-great-circle propagation, where (α) represents the deviation angle from the great-circle-path and Δ_α is the distance

between the wave fronts originating at the source and arriving at the two stations according to the off-path propagation. Now, the phase velocity along Δ_α can be expressed as:

$$c_\alpha(\omega) = \frac{\omega\Delta_\alpha}{\phi(\omega)}, \tag{2.52}$$

where $\Delta_\alpha = \Delta \cos\alpha$, and consequently the ratio R_2 at frequency ω between $c(\omega)$ (eq. 2.42) and $c_\alpha(\omega)$ (eq. 2.51) can be written as:

$$R_2 = \frac{c(\omega)}{c_\alpha(\omega)} = \frac{\omega\Delta}{\phi(\omega)} \Big/ \frac{\omega\Delta_\alpha}{\phi(\omega)}, \tag{2.53}$$

$$R_2 = \frac{1}{cos\alpha}. \tag{2.54}$$

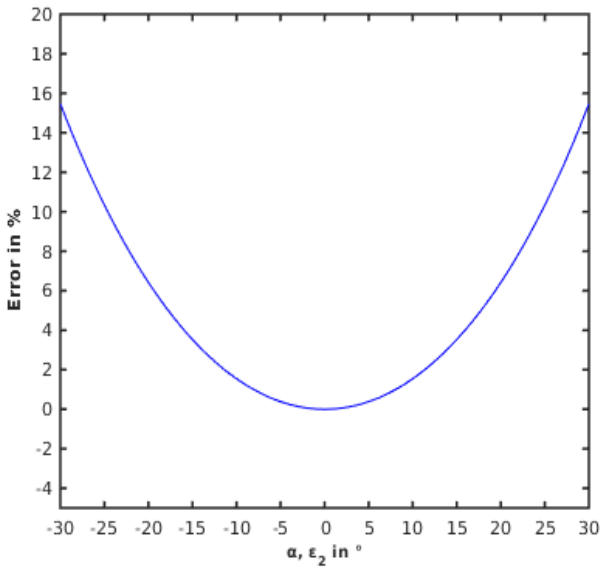

Fig. 2.7 The relative error in the phase velocity measurements as function of the off-great -circle propagation.

Clearly there is a similarity between the equation (2.50) and equation (2.53), nevertheless, they are accounting for two different cases as shown in figure (2.7). It shows the relation between the deviation angle in degrees from the great-circle path on the horizotal axis and the expected error in % of the measured phase velocity on the vertical axis, in case of prescence of off-path propagation (the true propagation path of the phase originated at the source and recorded at the two stations). Although the source-station geometry is accounted for correctly, tt is became clearer that the less the deviation angle from the great-circle-path, the less the error in phase velocity measurements. If the angle between the great circle connecting the

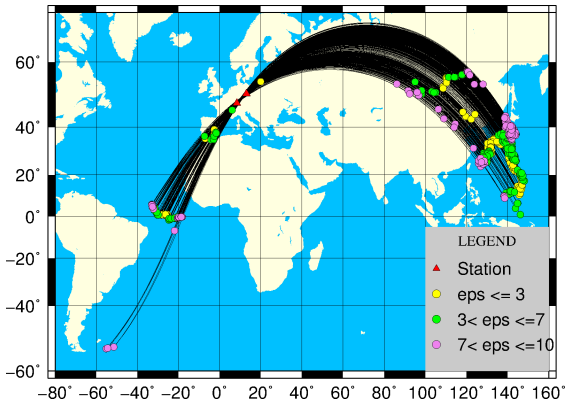

(a) Map shows the processed events

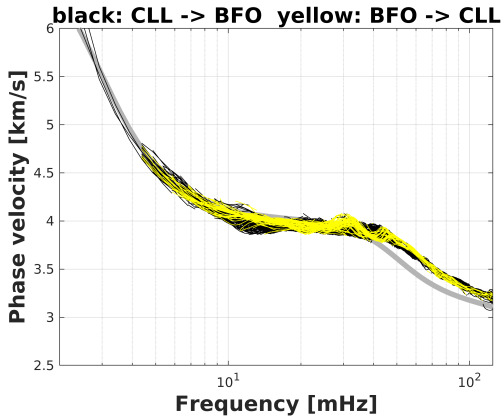

(b) Single-event measurements ($0° \leqslant \varepsilon \geqslant 3°$)

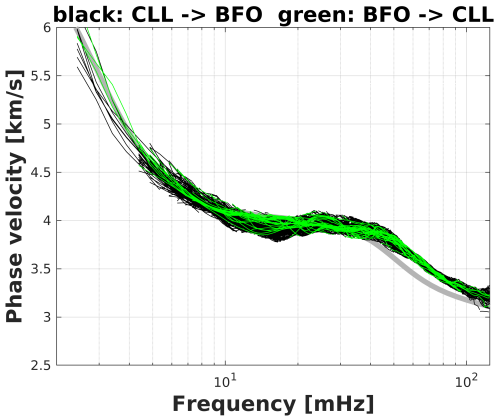

(c) Single-event measurements ($3° < \varepsilon \geqslant 7°$)

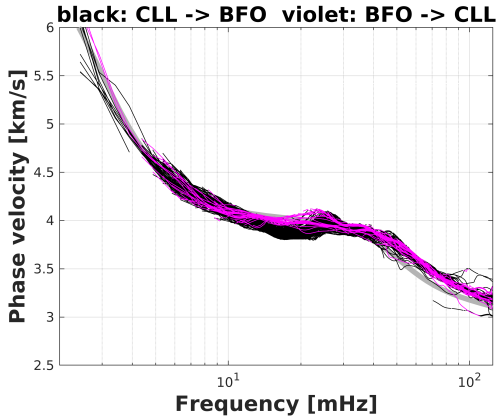

(d) Single-event measurements ($7° < \varepsilon \geqslant 10°$)

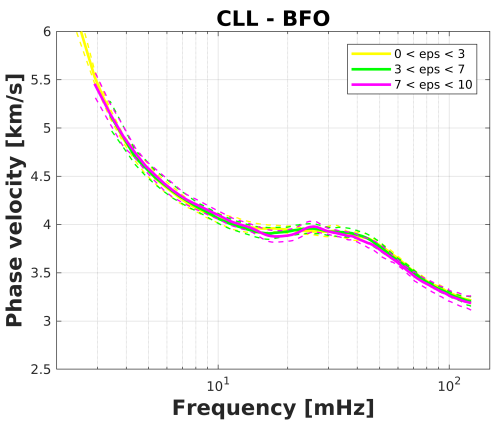

(e) Average dispersion curve from three datasets

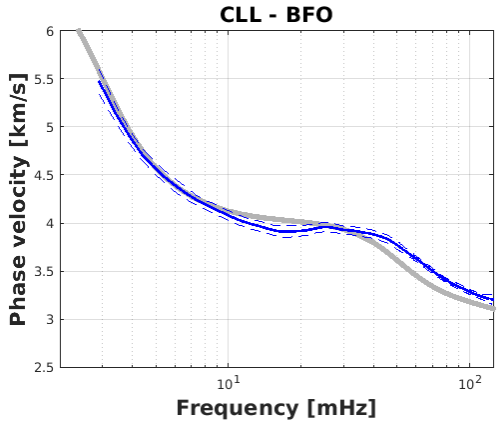

(f) Overall average curve and standard deviation

Fig. 2.8 Comparison of the automated phase-velocity measurements for three subsets of events with different backazimuthal deviation from the inter-station great-circle (station pair BFO-CLL). The evente are classified into three categories based on the off-great-circle propagations. The yellow, green and magenta circles represents the events from $0° \leqslant \varepsilon \geqslant 3°$, $3° < \varepsilon \geqslant 7°$ and $7° < \varepsilon \geqslant 10°$ respectively.

two stations and the great circles through the stations and the epicentre is smaller than 7°, then the standerd error in phase velocity measurements ranges from less than 1%, on both of the propagation directions.

A typical choice of the great-circle deviation angle is $5^\circ - 10^\circ$ is commonly applied and allows for robust dispersion measurements (e.g. Endrun *et al.* 2008; Adam & Lebedev 2012). To verify that this assumption does not introduce a systematic error in dispersion measurements of real, non-planar surface waves, we categorized measurements from events with different values of great-circle deviations. Figure (2.8) shows an example of the automated calculations of the individual inter-station measurements for $\sim$ 25 years of data recorded by the station-pair (CLL - BFO). In total, more than 1520 seismic events from both propagation directions were processed. The events are classified in to three categories based on the deviation angle (ε) from the great-circle-path. The yellow, green and magenta circles represents the events from $0^\circ \leqslant \varepsilon \geqslant 3^\circ$, $3^\circ < \varepsilon \geqslant 7^\circ$ and $7^\circ < \varepsilon \geqslant 10^\circ$ respectively. The events and recording stations locations (red triangles) are shown on the map in figure (2.8a). This resulted in total $\sim$ 1150 acceptable single-event dispersion curves. The measurements for the three categories (figures 2.8b, c and d) are highly consistent. A choice of $0^\circ \leqslant \varepsilon \geqslant 3^\circ$ reduces the number of events by, roughly, a factor of three, with the remaining individual dispersion measurements (Fig. 2.8b) overall smoother than those for the events in the range of the two other categories (Fig. 2.8c and d). However, after the calculation of the average dispersion curve for each subset, the resulting phase velocity curves are barely distinguishable (Fig. 2.8e), with slightly larger standard deviations when ε is increased.The overall path-average dispersion curve and it's standard deviation from the three subset is shown in figure (2.8f).

2.3.4 Evaluation of the data quality

As discussed previously, this method is applied to very large dataset (Fig. 2.2) to obtain the inter-station fundamental mode Rayleigh and Love wave phase velocities. Ranging between tens to more than thousand of single-event dispersion curves for each station pair are considered to obtain robust, broad-band path-average dispersion curves representing the structure between the considered stations with the error estimates. Altogether resulted in unprecedented number of Rayleigh and Love wave phase velocity curves. The total amount of Rayleigh wave measurements is about 200.000, whereas for Love wave measurements is about 50 % of the number of Rayleigh measurements (115.000 curves). This is may be due to the higher effect of noise on the transverse commponent compared to the vertical and the radial ones.

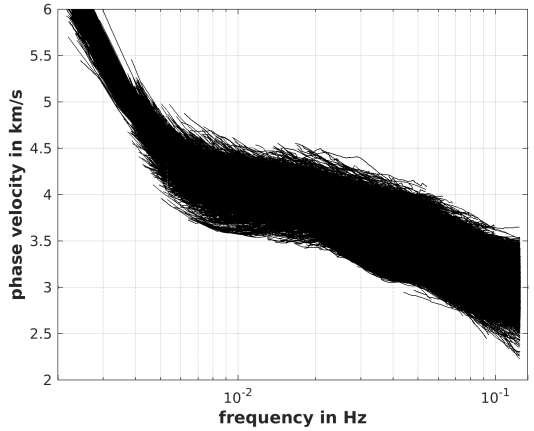

(a) path-averaged Rayleigh phase velocities

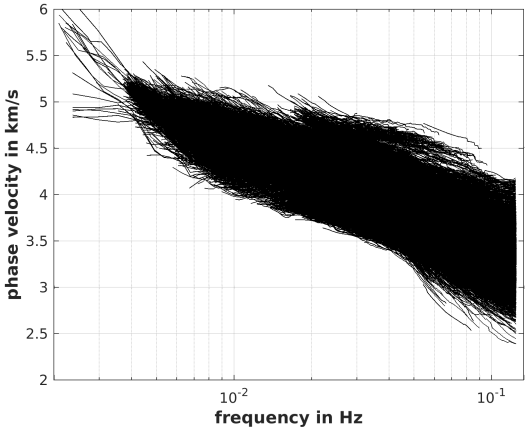

(b) path-averaged Love phase velocities

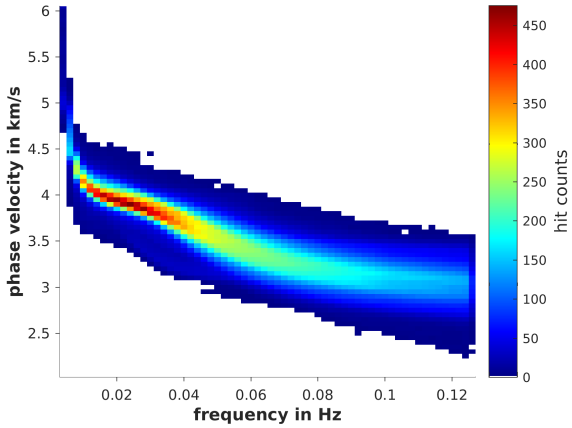

(c) 2D histogram for Rayleigh data

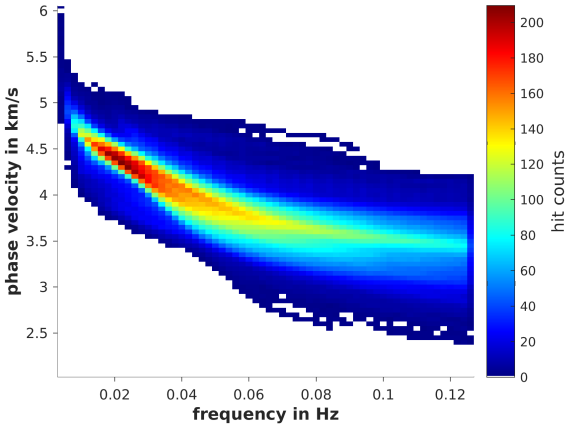

(d) 2D histogram for Love data

Fig. 2.9 Path-averaged dispersion curves plotted on top of each other and the corresponding 2-D histograms of all automatically measured Rayleigh and Love phase-velocity curves of the entire data set.

The path-averaged dispersion measurements (phase velocity as function of frequency) are plotted on top of each other for both Rayleigh and Love waves in figure (2.9a) and (2.9b), respectively. The corrsponding 2-D histograms of the entire phase velocity data set are also shown (Figs. 2.9c and d). Generally, the 2D histograms show very broad frequency band (125 - 2.90 mHz or 8 - 350 s) in which the measurements have been obtained. Most of Rayleigh waves measurements are in the 10 - 80 mHz frequency band, whereas Love wave measurements are in the range of 10 - 60 mHz. The number of the measurements at higher frequencies decreases gradually. This is owing to the strong lateral heterogeneities and crustal complexities that may bias the measurements. Thousands of measurements have been obtained at periods shorter than 10 seconds. At the lower frequencies, the number

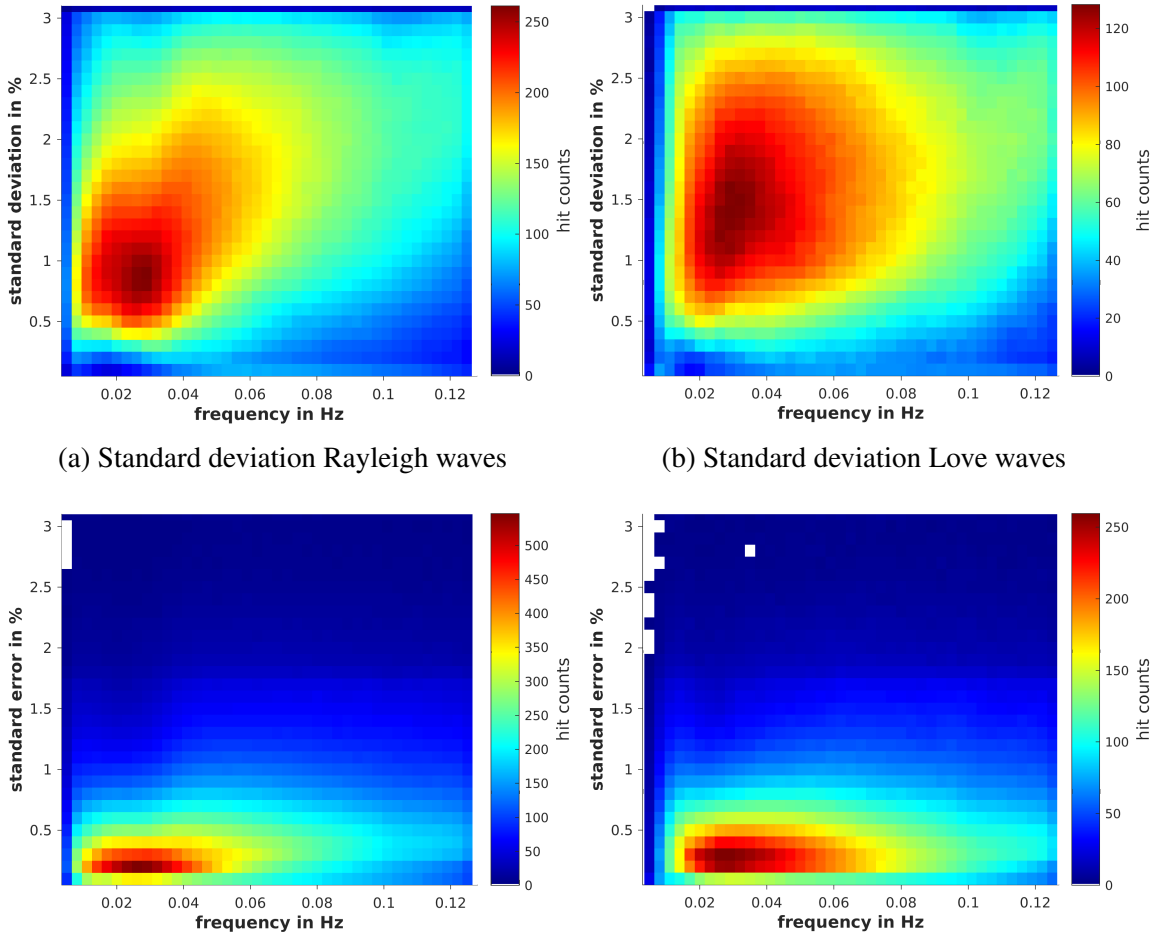

(a) Standard deviation Rayleigh waves

(b) Standard deviation Love waves

(c) Standard error Rayleigh waves

(d) Standard error Love waves

Fig. 2.10 Standard deviations and standard errors as a function of frequency for all automatically measured Rayleigh and Love phase-velocity curves of the entire data set.

of Love wave measurements is also decreasing and this may be due to the interference bewteen the higher modes (overtones) and the fundamental mode (Schäffer and Lebedev 2015). It also could be due to the contamination of the horizontal component with Rayleigh waves. The standard deviation and the standard error as a function of frequency and the inter-station distance are both for Rayleigh and Love waves are shown on figures (2.9) and (2.10), respectively. The standard deviation values are decreasing with increasing the inter-staion distances for both Rayleigh and Love waves.

Altogether, our measurements have a standard deviations less than 3 % for the frequency and less than 2.5 % for interstation distances. Considering this large phase-velocity dataset, we noticed that for the majority of the measurements the standard error (i.e., the standard

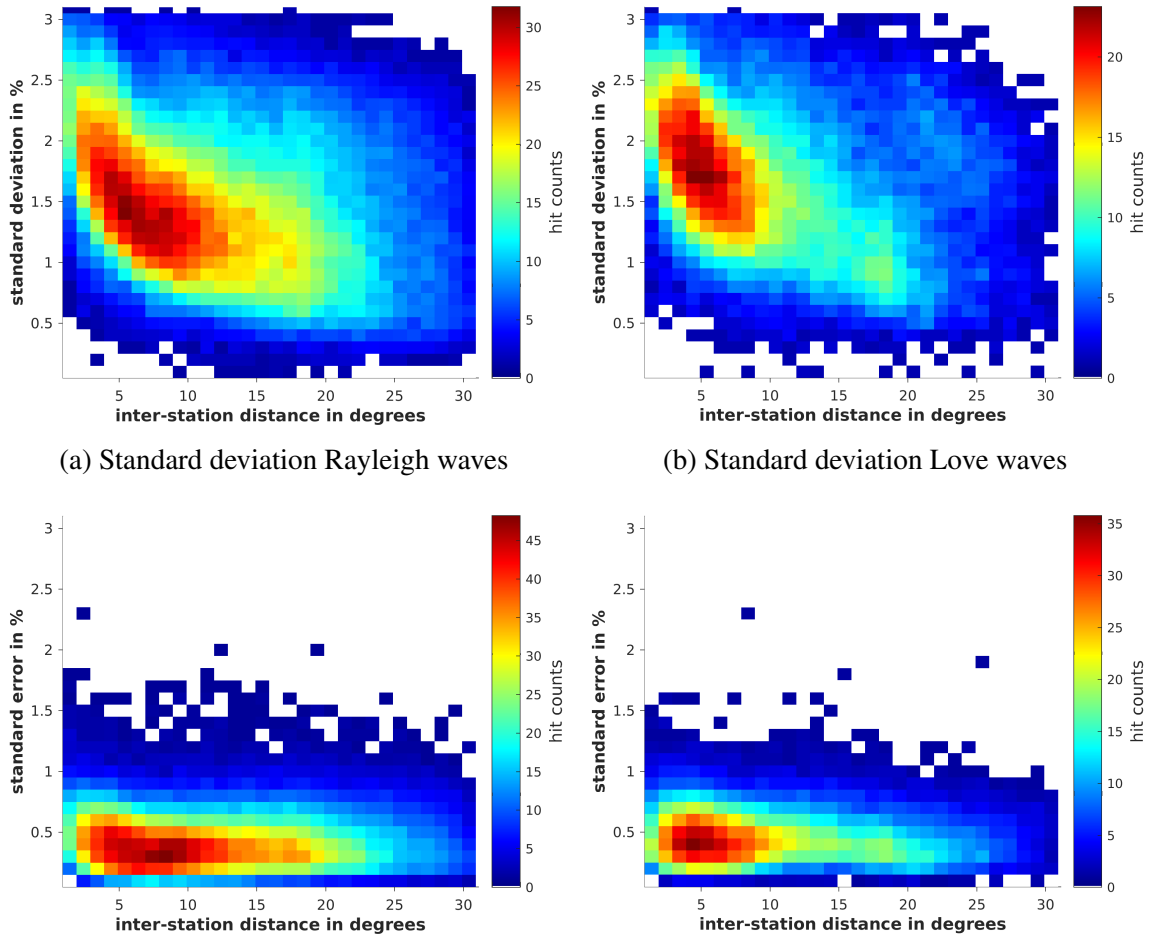

(a) Standard deviation Rayleigh waves

(b) Standard deviation Love waves

(c) Standard error Rayleigh waves

(d) Standard error Love waves

Fig. 2.11 Standard deviations and standard errors as a function of inter-station distance for all automatically measured Rayleigh and Love phase-velocity curves of the entire data set.

deviation of the mean) is much lower (less than 1 % for the frequency and less than 0.7 % for the inter-station distance.

The automated inter-station phase velocity method (Soomro *et al.* 2016) allows for a real assessment of the effect of the different parameters on the final average path-average phase velocity curves. Biases and very rough perturbations in the individual phase velocity measurements may occur due to the contamination of random noise, which is expected to be taken out by the averaging procedure, or due to the interference between the higher modes and the fundamental model (Meier *et al.* 2004 & Soomro *et al.* 2016). Moreover, the phase velocity measurements can also be affected by the non-plane waves created from lateral heterogeneities and crustal complexities. Wielandt (1993) reported that positive or negative biases in the phase velocity measurements can be introduced not only by the medium but also

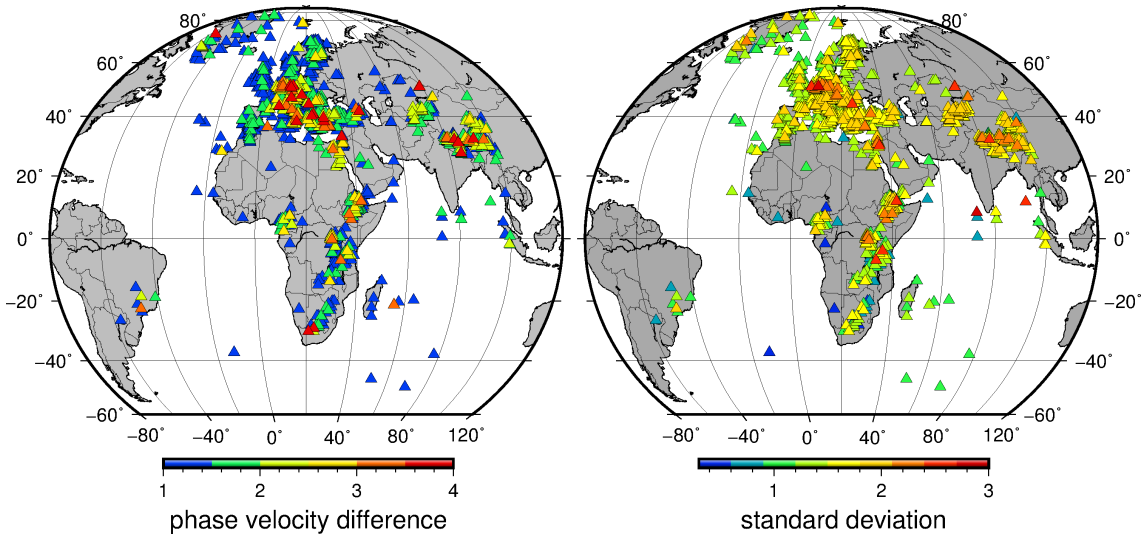

(a)

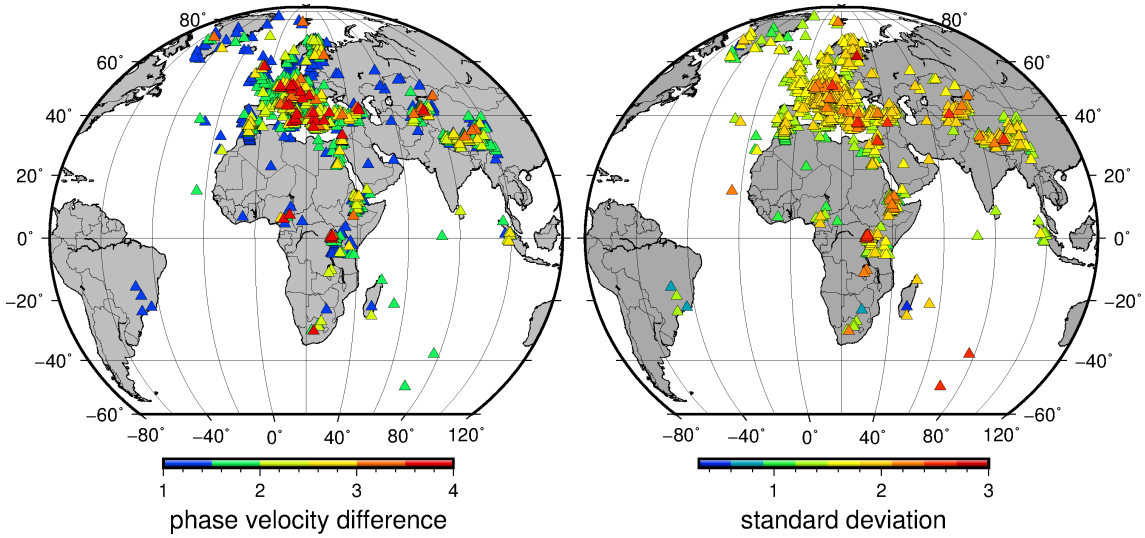

(b)

Fig. 2.12 The frequency-averaged phase velocity difference between the two propagation directions (*left*) and the average standard deviation (*right*) per each station of the Rayleigh wave (a), Love wave (b) phase velocity dataset.

by the non-plane wavefield geometries especially on the distribution of amplitudes around the point of observation. Such effects can be clearly seen as pumbs or cusps on the single-event dispersion measurements that are usually rejected by the automated selection criteria as introduced in Soomro *et al.* (2016). That is why selecting the smoothness parameter should be done very carefully. On the other hand, there are other technical issues that could strongly affect the quality of the data such as wrong instrument response, timing problems, or wrong polarities. According to Weidle *et al.* (2013) the average phase velocity deviations from the

background model and the degree of consistency between the average phase velocities of both propagation directions may allow to identify stations that have data quality issues. Averaged over all frequencies, phase velocity difference between the two propagation directions (*left*) and the average standard deviation (*right*) of the entire dataset of Rayleigh and Love phase velocities are shown on figures (2.12a) and (2.12b), respectively. Stations with large values of phase velocity difference and standard deviation may suffer from data quality issues. For example, the higher values of difference in the velocities measured in both propagation directions may be related to wrong instrument responses (Weidle *et al.* 2013). As a result we rejected $\sim 20(\%)$ of the total number of the stations as an additional quality control crietria in order to ensure obtaining a reliable fundamental mode dispersion curves, that can be used as input for further studies like surface wave tomography. Figure 2.13 shows the phase velocity difference between the different propagation directions and the standard deviation for each station after the rejection of 20% the errorneous stations with the corresponding 1D histograms.

2.4 Determination of phase velocity maps from inter-station phase velocities

Surface wave inverse problem consists mainly of two parts; linear and nonlinear (Barmin *et al.* 2001). A nearly linear part is to calculate 2-D dispersion maps and a non-linear part in which the dispersion maps are used to estimate Earth structure. This section deals with the former part which is termed as surface wave tomographic inversion. Generally, there are some surface wave algorithms that have been designated to directly linearize the relation between the seismic waveforms and an Earth model (e.g., Nolet 1987; Snieder 1988; Marquering *et al.* 1996 and some others), in which they calculate the Earth model iteratively without calculating the dispersion maps. On the other hand, calculating the dispersion maps has it's own advantages. Such as summarizing large numder of dispersion measurements which is still remain closer to the data than the structural models and can be utilized either alone as an input for obtaining the shear velocity models or jointly inverted with different geophysical datasets (Levshin *et al.* 2001). Moreover, they are applicable to extract surface wave information from noisy records. There are large number of surface wave tomographic techniques that are available and currently in use by different researchers around the world (Li & Romanowicz 1995, 1996; Marquering *et al.* 1996; Meier *et al.* 1997; Yoshizawa & Kennett 2002; Zhou *et al.* 2006). But they are different in several ways, such as the theoretical assumptions, model parameterization, the model geometry (cartesian &

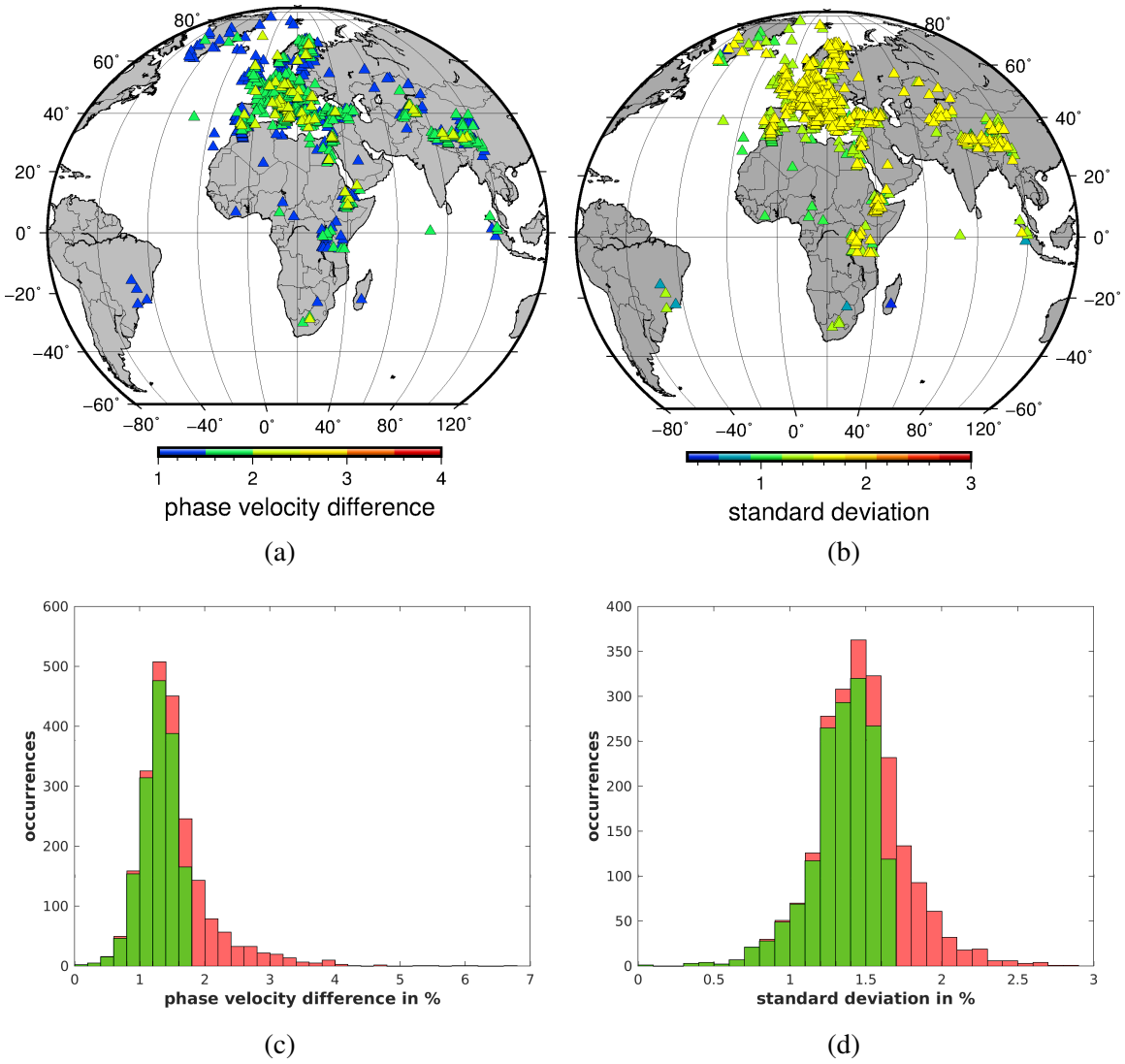

Fig. 2.13 The standard deviation and the phase velocity difference between the different propagation directions for each station after the rejection of 20% the erroneous stations with the corresponding 1D histograms. The red part represents the 20 % rejection of the outliers

spherical), the regularization and damping, and the possibilty of calculating the azimuthal anisotropy simultaneously with the isotropic velocities.

We use ray theory to invert, simultaneously, fundamental mode surface wave phase velocity measurements ($\sim$ 200.000 curves) made at very broad period range for both Rayleigh (8 - 350 s) and Love waves (8 - 250 s) following Deschamps *et al.* (2008), in order to calculate a frequency-dependent 2-D phase velocity maps. The 2-D tomographic maps show in principal the spatial distribution of the phase velocity at each geographical grid point on the map which in turn can be used as input for estimating the shear velocity structure of the

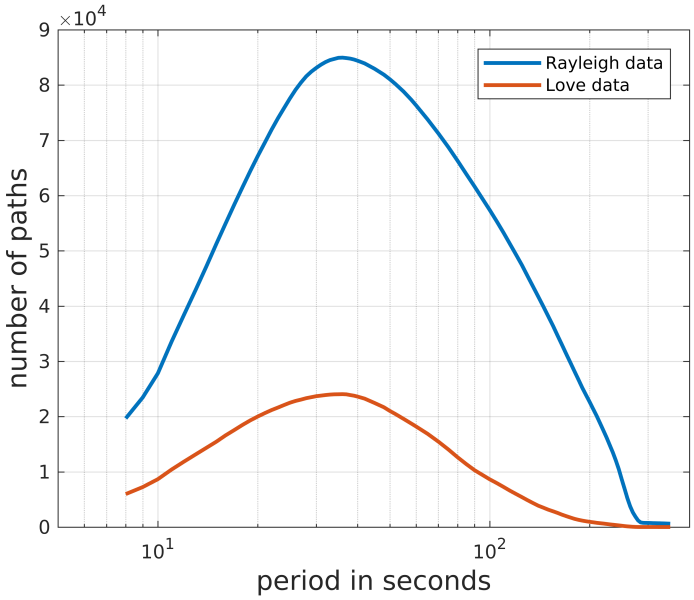

Fig. 2.14 Histogram shows no. of paths as function of period for Rayleigh and Love wave. There is a peak around ∼40 - 60 sec s with more than 90000 measurements for Rayleigh waves and 25000 measurements for Love waves.

crust, the lithospheric mantle, and asthenosphere. The inter-station dispersion curves depend, in principal, on the sensitivity of Earth's structure along the inter-station areas. This is used to constrain the distribution of phase velocity anomalies with respect to a regional average phase velocity values. Figure (2.14) shows the number of inter-station paths for both Rayleigh (blue) and Love (red) data as a function of period. At periods of 8 seconds, the number of measurements is more than 20000 and 8500 paths for Rayleigh and Love measurements, respectively. The number of the measurements reaches it's peak value within the period range from 30 to 70 seconds with more than $\sim$ 85000 and $\sim$ 25000 of Rayleigh and Love measurements, respectively. Figure (2.15) shows the azimuthal ray path coverage of the area based on the number of the crossing inter-station paths. The color-coded background represents the number of crossing paths per 1° x 1° cells at period of 60 seconds. Genreally speaking, for Love dataset we have approximately one-third of Rayleigh wave measurements.

Each measured interstation dispersion curve contains the average perturbations of the phase velocity ($\delta C_i(\omega)$) and the error in the measurements ($\Delta C_i(\omega)$) at each point with latitide (θ) and longitude (ϕ) along the considered inter-station path. This can be expressed as:

$$\delta C_i(\omega) \pm \Delta C_i(\omega) = \int_\theta \int_\phi K_i(\omega,\theta,\phi)\delta C(\omega,\theta,\phi) d\phi d\theta \tag{2.55}$$

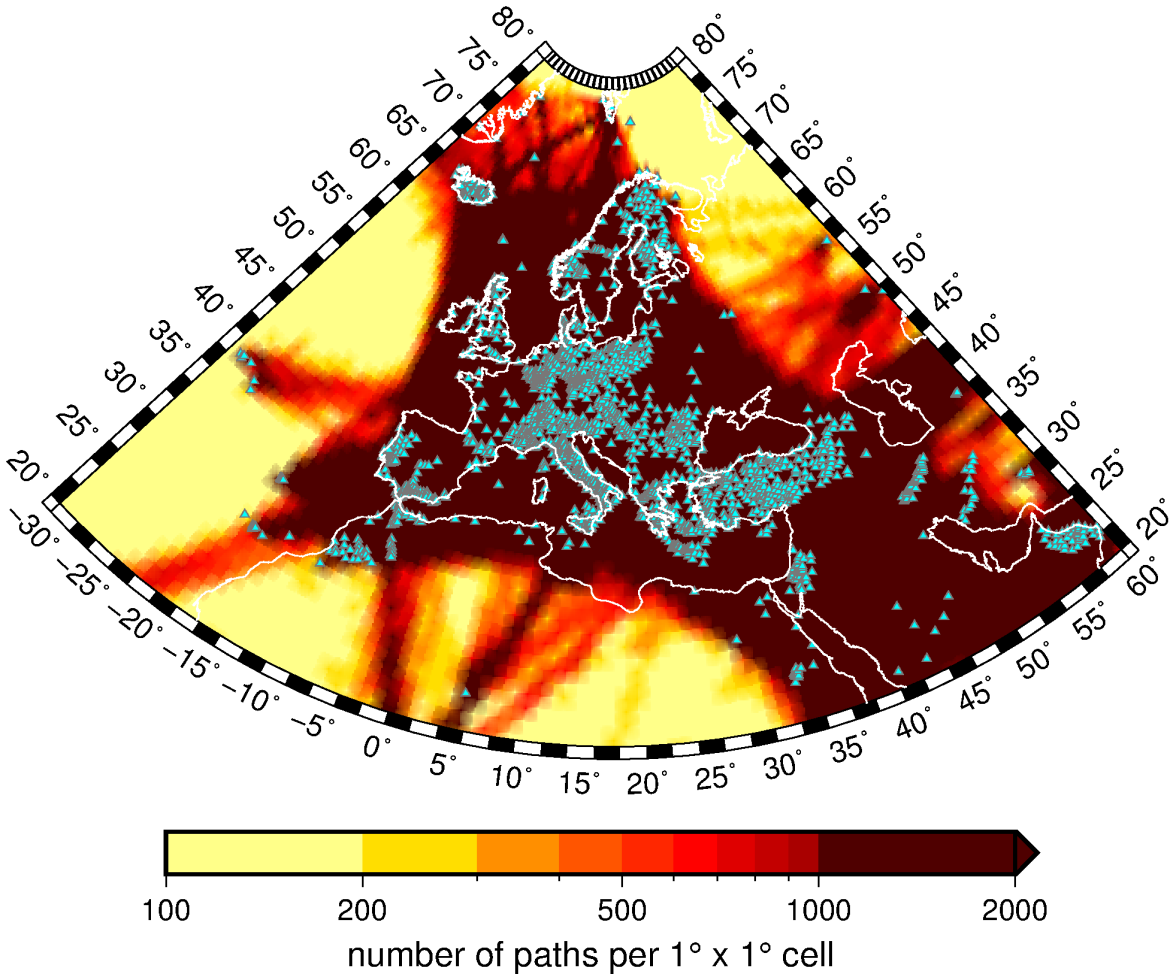

Fig. 2.15 Ray path density coverage of the surface wave tomography. Color-coded is the number of paths per 1° x 1° cells at period of 60 seconds. Cyan triangles indicate the seismic stations icluded in the anaylsis. Central Europe and the Mediterranean are mostly very well covered.

where ω is the angular frequency and $K_i(\omega, \theta, \phi)$ defines the sensitivity kernel (area) for the ith station pair.

Surface wave dispersion measurements have been shown to change with azimuth (Forsyth, 1975; Suetsugu and Nakanishi, 1987). Tanimoto and Anderson (1984, 1985) were the first to map the azimuthal variations of Rayleigh and Love wave dispersion at very long periods (100 - 250 sec.) They showed that the fast propagation direction correlates with the direction of mantle flow. Such variations of phase and group velocities with azimuth is called azimuthal anisotropy. The mathematical expressions for the azimuthal dependence of Rayleigh and Love waves in an anisotropic medium were firstly introduced by Smith and Dahlen (1973). They defined the anisotropic part by using the 2ψ and 4ψ contributions to

the phase velocity devations which in principal account for the π- and $\frac{\pi}{2}$-periodic variations where ψ is the local ray path azimuth. The 4ψ anisotropy can not be neglected and should be accounted for in the tomographic inversion (Montagner & Tanimoto 1991; Trampert & Woodhouse 2003). Darbyshire and Lebedev (2009) argued that including the anisotropy in the tomographic inversion helps to improve the solution significantly and they showed that the variance reduction of the data is improved by $\simeq 25\%$. Consequently, neglecting the anisotropy contributions may result in an overestimated velocity variations.

In order to isolate the isotropic and anisotropic contributions to the Rayleigh and Love wave phase velocity anomalies, we simultaneously invert for regional variations of these contributions with respect to a regional average velocity at each independent period. The total phase velocity anomaly is given by:

$$\delta C(\phi,\theta) = \delta C_{iso}(\phi,\theta) + \delta C_{2\psi}(\phi,\theta) + \delta C_{4\psi}(\phi,\theta) \tag{2.56}$$

where δC_{iso} represents the isotropic anomalies and $\delta C_{2\psi}$ and $\delta C_{4\psi}$ represent the the 2ψ- and 4ψ-anisotropy which are defined as:

$$\delta C_{2\psi}(\phi,\theta) = A_{2\psi} cos(2\psi) + B_{2\psi} sin(2\psi), \tag{2.57}$$

$$\delta C_{4\psi}(\phi,\theta) = A_{4\psi} cos(4\psi) + B_{4\psi} sin(4\psi), \tag{2.58}$$

where $A_{2\psi}$ and $B_{2\psi}$ and $A_{4\psi}$ and $B_{4\psi}$ are the four anisotropic terms defined for each latitide (θ) and longitude (ϕ). The amplitude (Λ) and the fast propagation direction of the wave (Θ) are given by:

$$\begin{cases} \Lambda_{2\psi} = \sqrt{A_{2\psi}^2 + B_{2\psi}^2} \\ \Theta_{2\psi} = \frac{1}{2}\arctan\left(\frac{B_{2\psi}}{A_{2\psi}}\right) \end{cases} \textit{and} \begin{cases} \Lambda_{4\psi} = \sqrt{A_{4\psi}^2 + B_{4\psi}^2} \\ \Theta_{4\psi} = \frac{1}{2}\arctan\left(\frac{B_{4\psi}}{A_{4\psi}}\right) \end{cases} \tag{2.59}$$

Therefore, we invert our dispersion measurements for five parameters, the isotropic and four anisotropic coefficients. The inter-station sensitivity areas (Eq. 2.54) are very complex (Chevrot & Zhao 2007). Including all the possible inter-station measurements in the inversion helps to improve the sensitivity at intermediate and long wavelength structures. The sensitivity areas $K(\theta,\phi)$ are evaluated at knots of a dense integration grid (Lebedev & van der Hilst, 2008). Following Wang and Dahlen (1995) we computed a global triangular grid of knots with equal inter-knot spacing. In this study, the knot spacing for this grid is generally chosen to be 10 Km, sufficiently small for an accurate integration over the approximate sensitivity kernels. The grid knots surrounding any particular knot form a hexagon shape. The area

of these hexagons around each knot is calculated. The sensitivity areas $K(\theta,\phi)$ is then calculated at each grid knot and multiplied with the surrounding hexagon area. This results in the weight of each knot in the integral over the sensitivity area. The sensitivity kernels were approximated by paths of finite width. In the calculations, we varied the ray path width between 50 and 300 km. There were some differences in the shape and the strengthes of some of the anomalies. That's why, we defined a period-dependent ray path width that increasing linearly with longer periods based on intensive testing. For the model we constructed also a triangular grid similar to that of the integration grid but with a larger interknot spacing according to the inter-station distances and ray path coverage in the considered area. An interknot spacing of 30 km is chosen due to the large dataset we obtained. The smaller spacing, indeed, leads to better variance reduction and an increase of the detailed small scale features. The same shell of knots is used at all periods. The isotropic and the azimuthally anisotropic phase velocity perturbations are unknown. Such perturbations in the phase velocities are computed at the location of the model grid knots by integrating over the neighbouring integration grid knots.

At more than 100 selected periods sampling our broad period range (8 to 350 seconds), we build a system of linear equations by combining Eq. (2.54) obtained from all possible dispersion measurements from different station combinations. To solve this system of linear equation we use the least square techniques LSQR (Paige & Saunders 1982) with a standard mean of regularization including lateral smoothness and a small amout of norm damping. For each individual period (Deschamps *et al.* 2008), we solve Eq. 2.55 as:

$$\mathbf{d} = G.\mathbf{m} \tag{2.60}$$

where $\mathbf{d}$ is the vector that contains the path-average phase velocity anomaly measured on the dispersion curve at the considered period, $\mathbf{m}$ is the model vector that contains the five terms (C_{iso}, $A_{2\psi}$, $B_{2\psi}$, $A_{4\psi}$ and $B_{4\psi}$) and G is the sensitivity matrix which contains the coefficients that link the data and the model. Assuming that $\mathbf{N}$ is the number of paths at each period and $\mathbf{M}$ is the number of knots, the transposed data and model vectors can be given as:

$$\mathbf{d^T} = \left(\overline{\delta C_1} \ldots \overline{\delta C_N}\right) \tag{2.61}$$

and

$$\mathbf{m^T} = \left(\delta C_{iso,1} \ldots \delta C_{iso,M} \quad A_{2\psi,1} \ldots A_{2\psi,M} \quad B_{2\psi,1} \ldots B_{2\psi,M} \quad A_{4\psi,1} \ldots A_{4\psi,M} \quad B_{4\psi,1} \ldots B_{4\psi,M}\right) \tag{2.62}$$

respectively. The sensitivity matrix $\boldsymbol{G}$ consists of five sub matrices and can be given as:

$$\mathbf{G} = \begin{pmatrix} \mathbf{G}_{iso} & \mathbf{G}_{C2\psi} & \mathbf{G}_{S2\psi} & \mathbf{G}_{C4\psi} & \mathbf{G}_{S4\psi} \end{pmatrix} \tag{2.63}$$

where,

$$\mathbf{G}_{iso} = \begin{pmatrix} K_{11} & \dots & K_{1M} \\ \dots & \dots & \dots \\ K_{N1} & \dots & K_{NM} \end{pmatrix},$$

$$\mathbf{G}_{C2\psi} = \begin{pmatrix} a_1K_{11} & \dots & a_1K_{1M} \\ \dots & \dots & \dots \\ a_NK_{N1} & \dots & a_NK_{NM} \end{pmatrix}, \mathbf{G}_{S2\psi} = \begin{pmatrix} b_1K_{11} & \dots & b_1K_{1M} \\ \dots & \dots & \dots \\ b_NK_{N1} & \dots & b_NK_{NM} \end{pmatrix},$$

$$\mathbf{G}_{C4\psi} = \begin{pmatrix} c_1K_{11} & \dots & c_1K_{1M} \\ \dots & \dots & \dots \\ c_NK_{N1} & \dots & c_NK_{NM} \end{pmatrix}, \mathbf{G}_{S4\psi} = \begin{pmatrix} d_1K_{11} & \dots & d_1K_{1M} \\ \dots & \dots & \dots \\ d_NK_{N1} & \dots & d_NK_{NM} \end{pmatrix}.$$

In these matrices, the K_{ij} are the weights of path i for knot j (i.e, the sensitivity areas), and the azimuthal dependence is accounted for by the constants $a_i = cos(2\psi_i)$, $b_i = sin(2\psi_i)$, $c_i = cos(4\psi_i)$ and $d_i = sin(4\psi_i)$. ψ_i is the azimuth of the path i. Generally the differential sensitivity areas of the inter-station measurements are complex (Chevrot & Zhao, 2007). Diffraction of surface waves due to the Earth's small scale hetereogenities affects it's sensitivity to resolve Earth's structures. Considering all the possible inter-station dispersion combinations will improve the sensitivity to intermediate and long wavelength structures. In this regard, smoothing the sensitivity areas is more likely to make them more robust. We define the senstivity areas in the same way at all frequencies considering a period-dependent ray path widths along interstation great-circle paths. Both the isotropic and azimuthally anisotropic terms are smoothed and damped independently. Selecting a proper smoothing and damping values is always subjective. We defined our preferred model as a compromise between model smoothness and ability to explain observed data (variance reduction). This is given in the next sub-section.

2.4.1 Effect of regularization on tomographic inversion

In surface wave tomographic inversions, regularization means applying some constraints explicitly on the estimated model during the inversion. Generally, it involves the application of some constraints on model amplitude and the perturbations of the velocities from a reference value and their spatial variations in order to increase the inversion stability. The strength of regularization of the tomographic models may vary in an adaptive way taking

into account data quantity, quality and the area under investigation. Sieminski et la., (2004) showed that together with a dense ray path coverage, a physically based regularization can overcome the shortcomings of regional surface wave tomography based on ray theoritical approximation in considering the finite frequency effects. Under such conditions, detection of lateral heterogeneities with length scales smaller than the wavelength of the dataset is possible. Smoothing and damping are standard means of regularizing a tomographic inversion. Such parameters affect overall the tomographic maps. Oversmoothing results in a smooth phase velocity maps with low resolution, whereas undersmoothing may introduce some artifacts due to noise or data errors (Darbyshire & Lebedev, 2009). With small effect of the norm damping, we applied two types of smoothness. At first the lateral smoothing, which is used to penalizes the second lateral derivative of the phase velocity distribution (Deschamps *et al.* 2008) by minimizing the perturbation difference at each knot with the average value of the six nearest neighbors. This type of damping is suitable to retrieve regular gradients as the small scale local anomalies are averaged out. The second type of smoothness is the gradient damping, in which the difference between each two neighbouring knots is penalized (Darbyshire & Lebedev, 2009). It's a process similar to taking the first partial derivative of the anomaly distribution. According to Menke and Abbott (1990) the choice of smoothingdamping parameters can be done by examining the trade-offs between model resolution and the model roughness which is defined as the average difference between the perturbations at a certain grid knot and those at it's nearest-neighbour grid knots.

We aim to explain with our models over half of the signal given by the measurements. That is, the remaining variance should be less than 0.5. If the variance reductions are too small (remaining variance too high), this means that the measurements are highly mutually inconsistent may be due to the contaminating noise in the data (dispersion curves). To improve on this, we performed the outliers rejection procedure. Strictly speaking, this is not outliers removal but selection of the most mutually consistent data. We tried removing 5% , 15% , 25% , 35% and 50% outliers and everytime we visually checked the resulted models. It is worth to be mentioned that we did the outliers removal based on weakly regularized models (small smoothing and damping coefficients). At the end we removed 15% of the outliers at all periods. Then, we performed a series of inversion tests systematically in order to pick the optimal smoothness values and obtain meaningful results. This includes systematic variation of the lateral smoothing and the gradient damping while keeping the norm damping small. The isotropic and anisotropic smoothness terms were varied in the range from 0.1 to 1.0, respectively. For each isotropic damping value we varied anisotropic damping values from 0.1 to 1 and vice-versa. This forms a matrix of 100 elements (10 rows 10 columns). Each row of the matrix represents different isotropic damping values at particular anisotropic damping

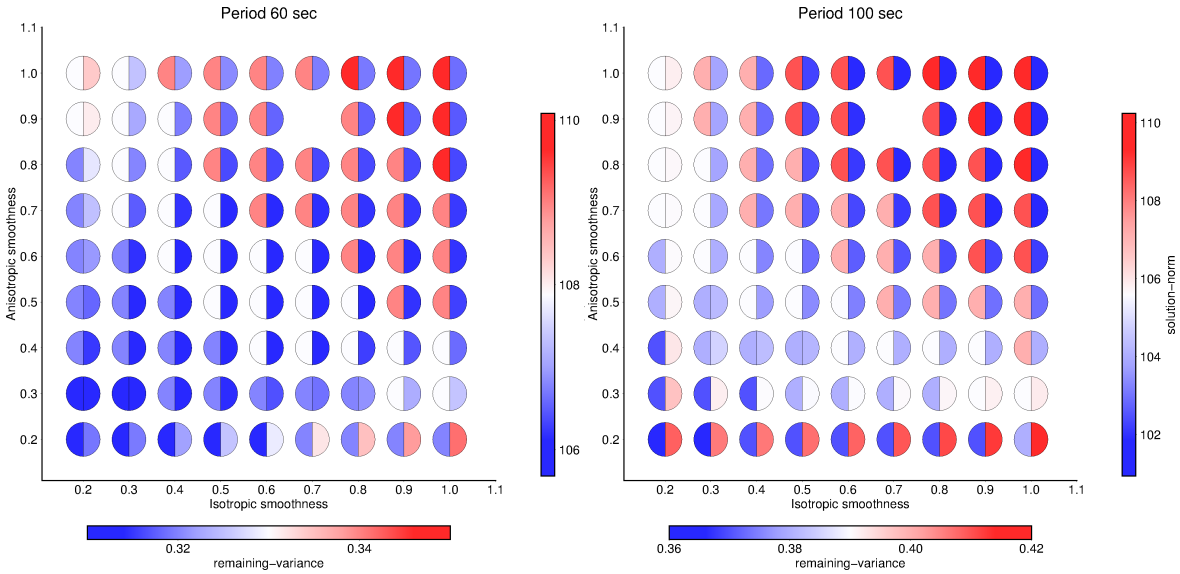

(a) Period of 60 seconds (b) Period of 100 seconds

Fig. 2.16 Assessment of optimal regularization parameters: Left and right half circles show data variance and model norm, respectively, for various combinations of isotropic and anisotropic damping parameters for 60 s (left) and 100 s (right).

value. Similarly every column represents different values of anisotropic damping at particular isotropic damping.

For each damping values we have plotted a pie wedge plot representing the results of the inversion using these values to smooth the model (Fig. 2.16), the left half circle shows the value of the data variance (remaining variance) and right half circle shows the model norm values. It can be seen that in the lower left part of the plot the value of data variance is low and solution value is high and vice-versa at the upper right part. These values are not acceptable and may give rise to artifacts and unexplained anomalies on the maps. On the other hand, our preferred values forms a kind of L Curve, a compromise between the isotropic and anisotropic values that could be used as a starting values for an inversion with a preliminary acceptable results. Generally, this is very useful test in defining a range of damping parameters (isotropic and anisotropic) by narrowing down the models to be visually checked. Indeed we carefully checked all the models from all the tests. The visual inspection of the model also confirms that a high damping values results in models with less resolution and the low damping results in smaller anomalies and artifacts that do not explain the model efficiently. Therefore, with the help of this test we can pick acceptable values of the smoothness parameters.

With such intensive tests, it became very clear that smoothing coefficients should be different at different periods so as to retrieve the same-scale structure. As the number of the paths is period-dependent (Fig. 2.14), therefore the fewer the paths we have the smaller smoothing coefficients we should use considering the scale of the structure to be retrieved at each specific period. Figure (2.16) shows the assessment of the optimal regularization parameters for various combinations of isotropic and anisotropic damping parameters at two different periods 60 (left) and 100 seconds (right). In general, the smoothness values increase with increasing the long periods. In figure (2.17) we show phase velocity maps with different smoothing values for the isotropic part (low, intermediate and high damping values) while keeping the ansiotropic part fixed. On the other hand we show the damping effect when fixing the isotropic part and varying the anisotropic part in figure (2.18). When introducing a high isotropic damping, the isotropic signal leaked to anisotropic part and similar effect of leakage in isotropic part is observed as well when overdamping the anisotropic part. With low value of damping parameters, errors in dispersion measurements may dominate the resulting phase velocity maps. High damping parameters in one hand decrease the resolution and on the other hand they provide a dominant feature for a particular region.

2.4.2 Selection of the ray path width of surface waves

In presence of strong lateral heterogeneities, ray theory appoximation tends to breakdown when the scale length is comparable or less than the wavelength of the waves. A good path coverage and a physically regularized inversion can overcome this issue. On the other hand, taking into account the finite path width of surface wave ray paths can also play a role in enhancing the senstivity areas in the inversion. An empirical condition for the validity of surface wave ray theory has been introduced by Wang and Dahlen (1995) in order to be valid in presence of strong lateral hetereogenities. They calculate the phase, arrival angle and and purturbations amplitude using the Jordan-Wenzel-Kramers-Brillouin (JWKB) approximation and compared them with those from coupled-mode theory. For this condition they assume that the width of the first Fresnel zone should be much smaller than the scalelength of lateral heterogeneity. Consequently, it is possible to assign a finite path width to each interstation path to approximate a broad sensitivity area (kernel) in the inversion. Based on the high frequency approximation of the geometrical ray theory, the influence area of a surface wave ray path propagating along the great circle path looks like a delta function. However, the real surface waves with finite frequency should sample a finite region around a ray path. According to Cerveny and Soares (1992), this ray with finite width can be termed a physical ray width. Recently, Yoshizawa and Kennett (2002) approximately defined this influence

zone (i.e, the physical ray path width) around the propagation path for a surface wave by investigating the Fresnel zones for a given frequency range. They stated that such influence zone, over which surface waves are coherent in phase, is identified as approximately one-third of the width of the first Fresnel zone. Empirically they showed that the typical width of physical rays for a 40 s Rayleigh wave with epicentral distances of 3000 km is around 200 km. Moreover, if two physical rays are crossing, the diagonal spread of the crossover region should be slightly larger than the width of the in fluence zone of the rays.

Here we performed extensive inversion tests with different values of the ray path widths. Ranging from zero-width rays to more 300 km. Indeed the results show phase velocity maps that are in principal remain qualitatively similar. Careful visual inspection of the maps shows that the anomaly distributions became more robust as the path width increases, however too large path width slightly biases the amplitudes of the anomalies. Figure (2.18) shows the 100 seconds isotropic rayleigh wave velocity map as an example of the inversion using different values of the ray path width (0, 50, 100 and 150 km). The values of maximum and average isotropic anomalies indicates a systematic change in the results as a consequence of finite path width. Moreover, a decrease in variance reduction as the path width increases is obtained which in general results in enhancing the final solution of the inversion problem. Basically, we developed a period-dependent path width strategy for our inversion, in which the path width increases linearly towards longer periods ranging from 50 km to more than 400 km at periods longer than 300 seconds.

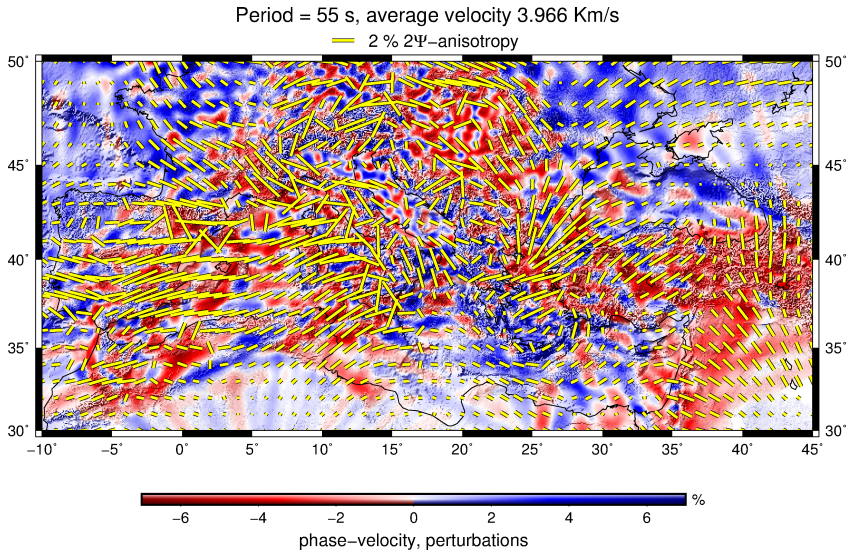

(a) Low damping of the isotropic term.

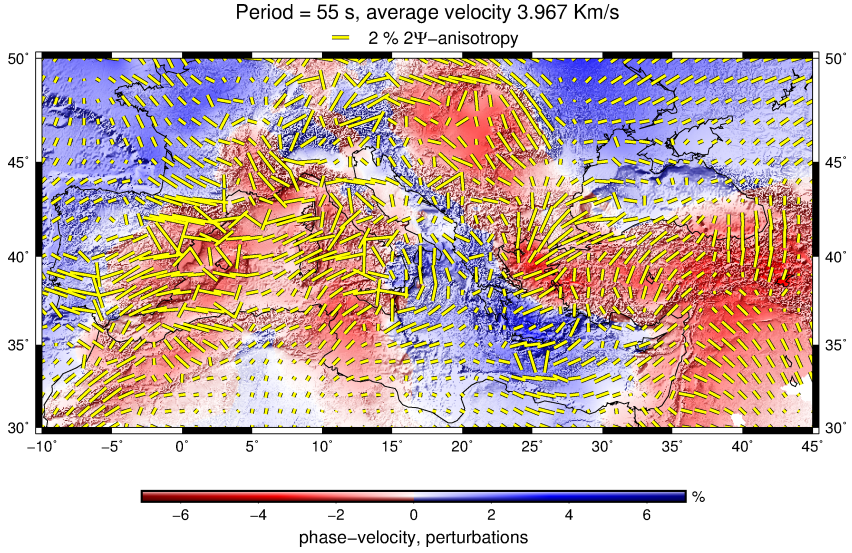

(b) Intermediate damping of the isotropic term.

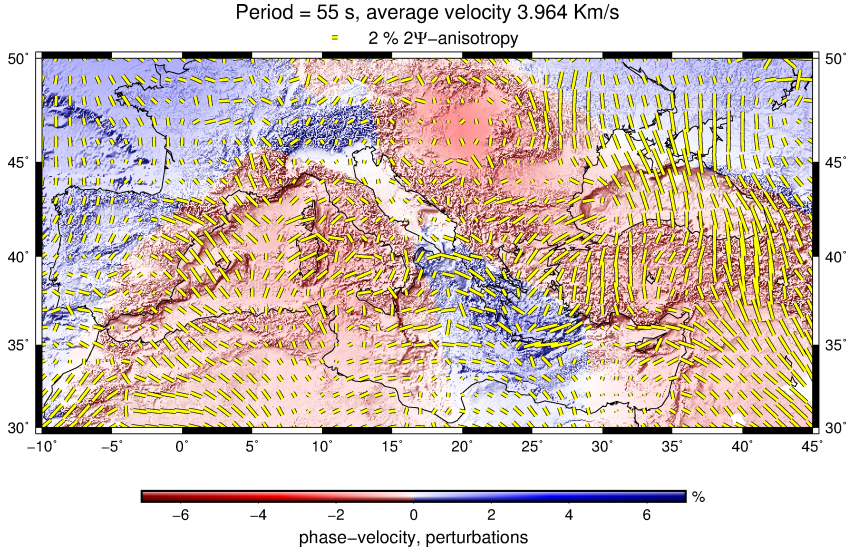

(c) High damping of the isotropic term.

Fig. 2.17 Effect of varying isotropic damping on Rayleigh wave phase velocity maps. Anisotropic damping values are fixed.

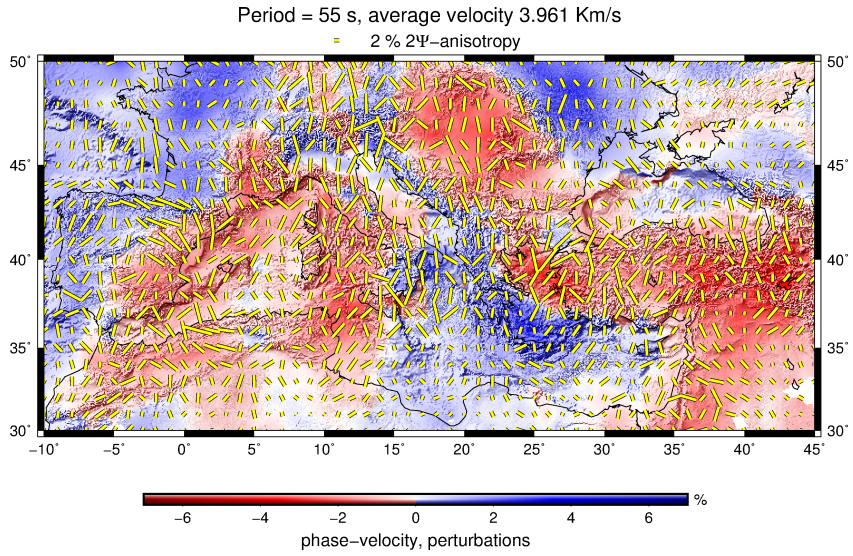

(a) Low damping of the anisotropic terms (2ψ and 4ψ).

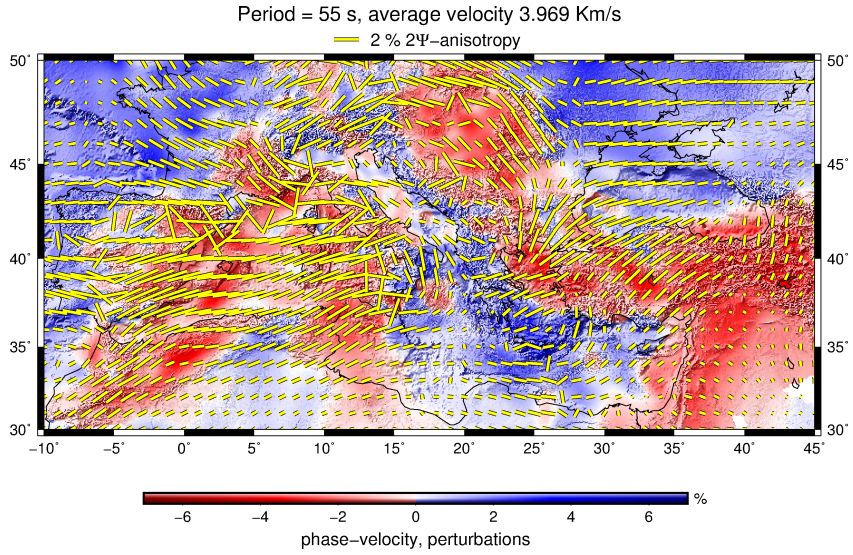

(b) Intermediate damping of the anisotropic terms (2ψ and 4ψ).

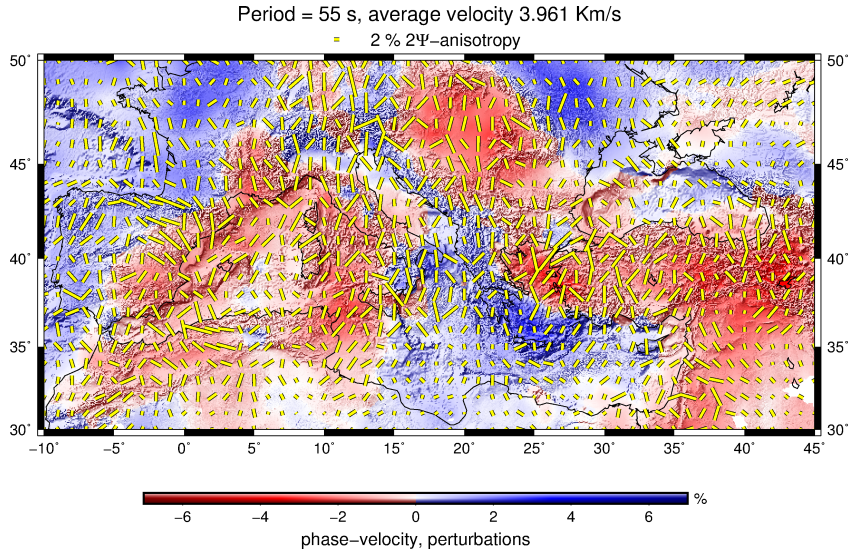

(c) High damping of the anisotropic terms (2ψ and 4ψ)

Fig. 2.18 Effect of varying anisotropic damping on Rayleigh wave phase velocity maps. Isotropic damping values are fixed.

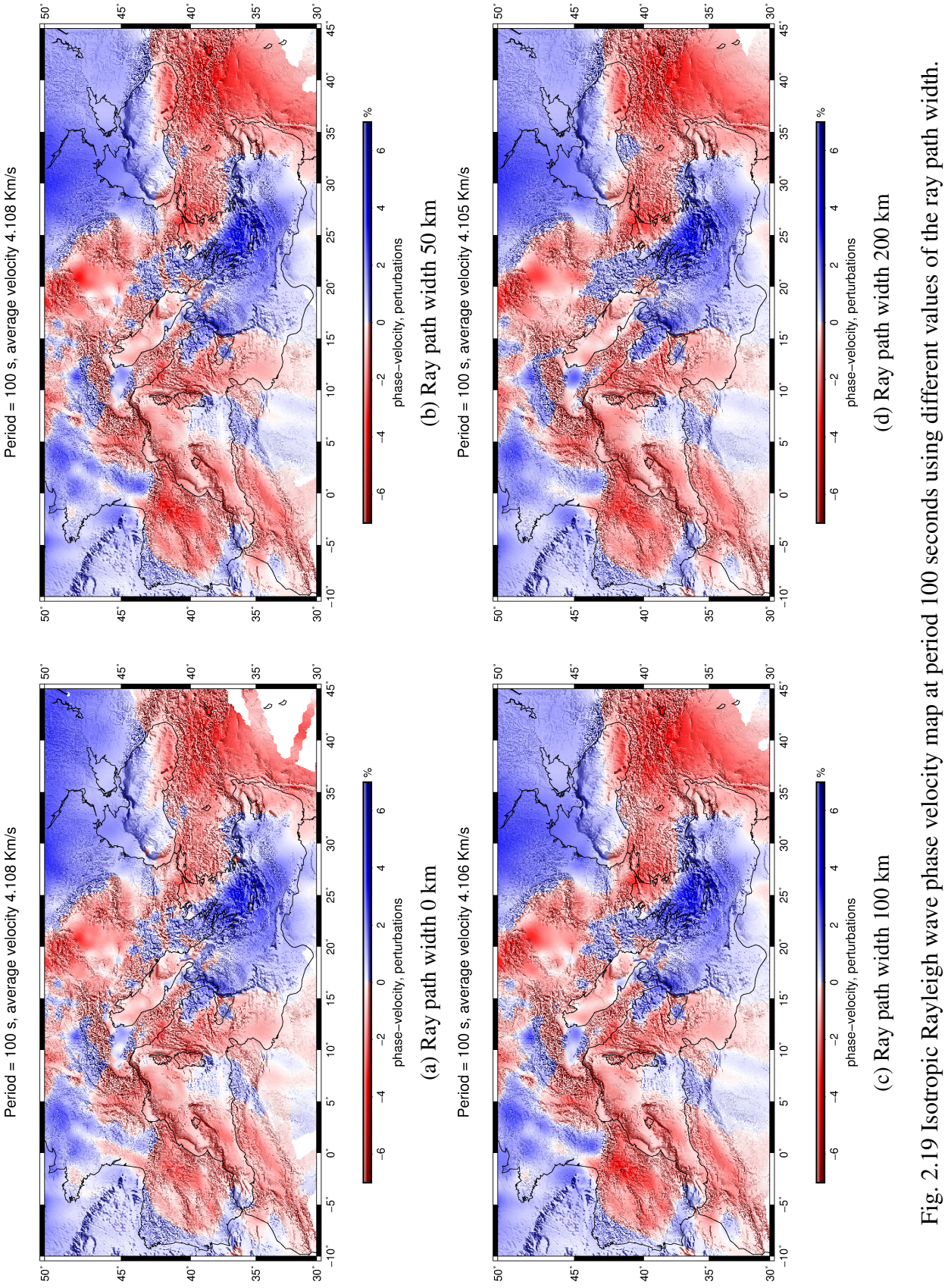

(a) Ray path width 0 km (b) Ray path width 50 km

(c) Ray path width 100 km (d) Ray path width 200 km

Fig. 2.19 Isotropic Rayleigh wave phase velocity map at period 100 seconds using different values of the ray path width.

2.5 Resolution tests

Seismic tomography has become an essential technique for mapping the internal structure of the Earth at local, regional and global scales (e.g. Dziewonski & Woodhouse 1987; Spakman 1988; Montagner & Tanimoto 1991; Evans & Achauer 1993; Fichtner 2011; Darbyshire & Lebedev 2009). However, estimating the reliability of the tomographic maps and knowing how close they are to the actual internal structure of the Earth are still a challenge. Nowadays, the most commonly used test is create model from a synthetic tests. This is called checkerboard test, which consists of a regular alternating pattern of positive and negative anomalies (e.g., positive and negative velocity perturbations relative to reference values) along each spatial dimension of the model. Inverting such synthetic data provides insight about the smearing effect of the model. The checkerboard test was first introduced by Spakman and Nolet (1988) and rapidly became very popular due to it's relative ease of interpretation. Here, we carried out checkerboard test and the size of checkers was varied from 100 to 300 km. Figures 2.20 and 2.21 show the results of the checkerboard test at different periods 12, 30, 60 and 100 seconds which represent lower crust, mantle lithosphere and asthenosphere. Despite of some smearing effects and amplitude damping, the inverted anomalies are generally well-defined at the central part of the study area including the central Mediterranean and Europe. The location and size of synthetic anomalies is recovered sufficiently in most cases.The resolution at periods from 30 to 60 s reaches its peak and slightly decreases at lower and higher periods. Results at the edges of our model have to be interpreted with more caution. Smearing on the checkerboards occurs in areas with less path crossings, for example in the southern Mediterranean. Alltogether we conclude that the overall the lateral resolution is about $\sim$ 150 km except for the central part of the study area which is characterized by the highest path coverage, it shwos approximately 100 km lateral resolution.

2.6 Discussion of the results

Analysis of phase velocity lateral variations is widely used tool for evaluating the different tectonic features present in the different regions. Phase velocity is related to crustal and upper-mantle structures, with a depth dependence that varies with periods and wave type. Shorter periods carry information on shear-wave velocity anomalies at shallow depths, whereas longer periods sample deeper into the Earth's upper mantle (e.g., Boschi and Ekström, 2002). Love waves are sensitive to shallower structures than Rayleigh waves at the same period.

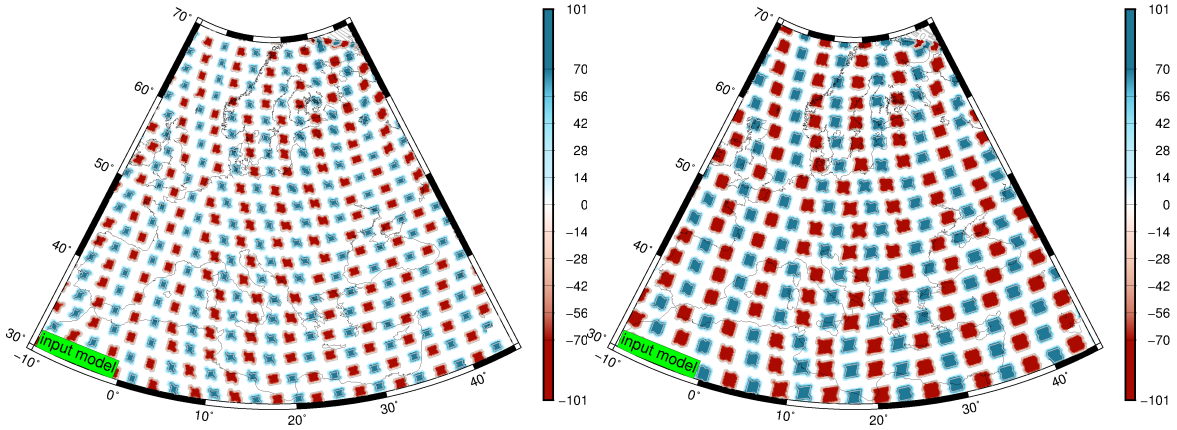

(a) Input model with 100 km block size

(b) Input model with 150 km block size

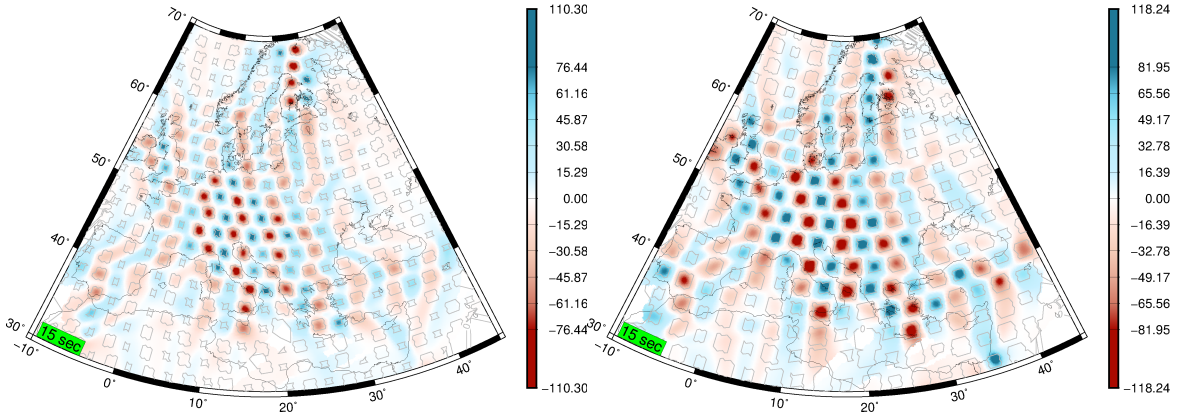

(c) Recovered model (100 km block size) at 15 sec (d) Recovered model (150 km block size) at 15 sec

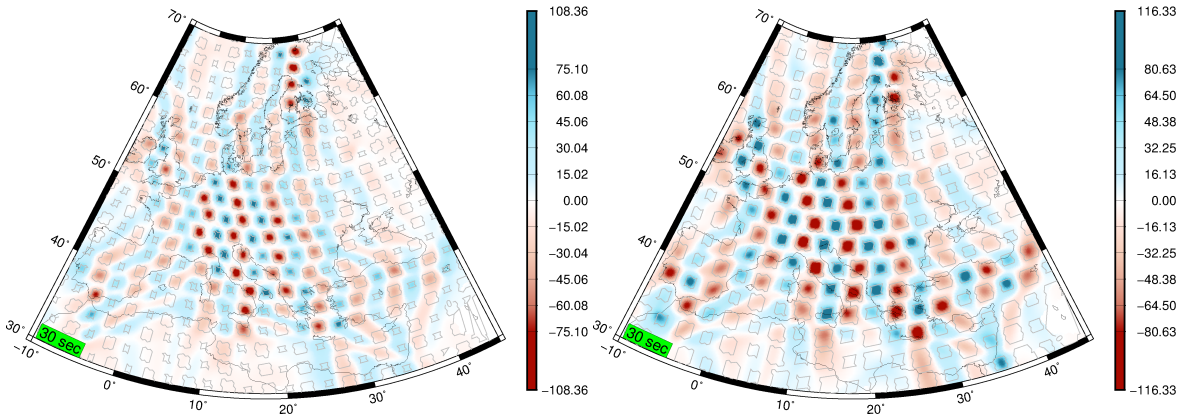

(e) Recovered model (100 km block size) at 30 sec (f) Recovered model (150 km block size) at 30 sec

Fig. 2.20 Checkerboard test for the Rayleigh phase-velocity maps with anomalies of approximately 100 km (left) and 150 km (right) size and 100m/s input amplitude. The top panel shows an input model fpr both (a) 100 km and (b) 150 km structure size. (c) and (d) show the recovered maps at 15 and 30 seconds for 100 km structure size. e and f) show the same maps for 150 km structure size.

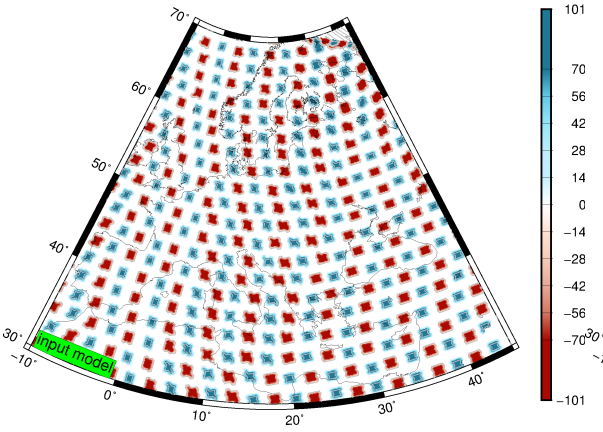

(a) Input model with 100 km blck size

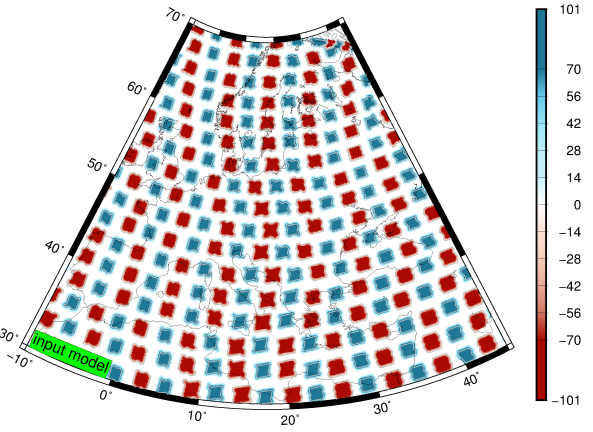

(b) Input model with 150 km block size

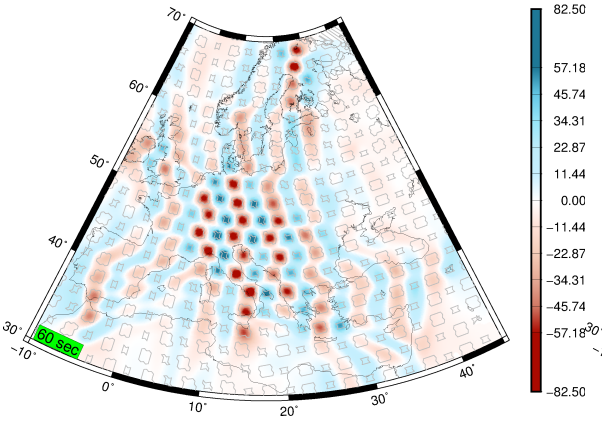

(c) Recovered model (100 km block size) at 06 sec

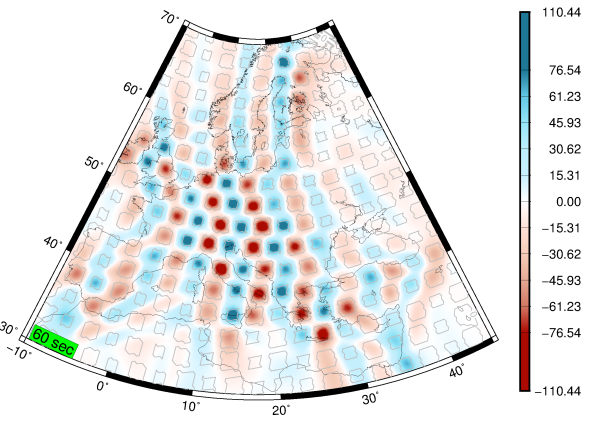

(d) Recovered model (150 km block size) at 60 sec

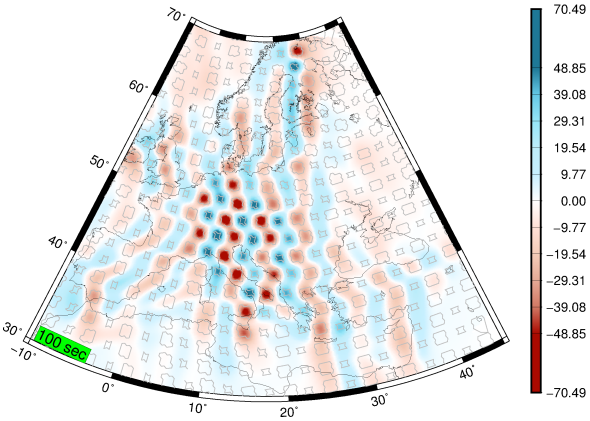

(e) Recovered model (100 km block size) at 100 sec

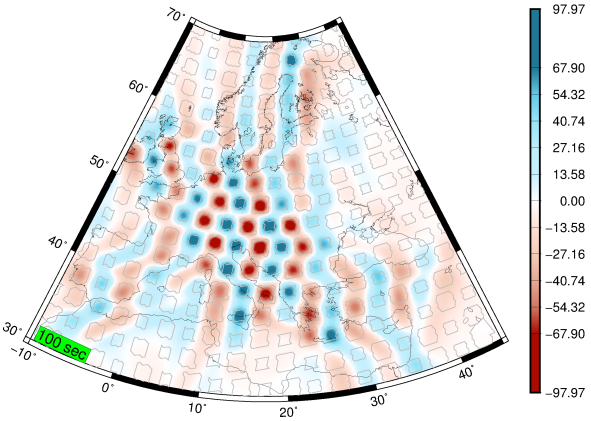

(f) Recovered model (150 km block size) at 100 sec

Fig. 2.21 The same as for figure 2.20 but at periods 60 and 100 seconds.

Depth sensitivity kernels allow the inversion of phase velocity anomalies into shear velocities as function of depth. The inversion of phase velocity maps for 3-D Vs structure of the upper mantle goes beyond the scope of this chapter. Here we can discuss the resulting tomographic maps from a qualitative point of view. In this study, more than 100 phase velocity maps were obtained from Rayleigh and Love surface wave tomographic inversions sampling the period range from 8 to 350 seconds. We investigated a quite large region located between -60° N and 80° N (latitudes) and -60° E and 100° E (longitudes). In the following we present the resulting isotropic and azimuthally anisotropic phase velocity maps for both Rayleigh and Love waves for some sub-regions including the North See and it's periphery, the Alps, central Europe and the greater Mediterranean.

2.6.1 Isotropic phase velocity maps

2.6.1.1 North Atlantic and it's periphery

The resulting phase velocity maps for the North Atlantic region and it's periphery are shown in figure (2.22). The distribution of the observed anomalies reflects the strong lateral heterogeneity of the Earth's structure of this region which changes from the mid oceanic ridge (MOR) system in the North Atlantic to thick sedimentary basins in the Barents Sea and old shields with continental crust on mainland Fennoscandia. Both 30 s Rayleigh (Fig. 2.22a) and Love (Fig. 2.22b) maps are characterized by widespread fast anomalies. Phase velocities in Norway are in agreement with the results presented in Köhler *et al.* (2012). However, toward the south in the Skagerrak region and in Denmark, we observe stronger negative velocity anomalies for Love waves than for Rayleigh. In Sweden, positive velocity anomalies and average values comparable to those in Norway are observed. Moreover, a higher velocity anomalies are observed beneath Greenland, Iceland and the Baltic Shield where the higher lithospheric velocities are associated with the Archean domain. Along the Fennoscandia, the northern part of the East European Craton (i.e., including the Archean Fennoscandian Shield and it's Proterozoic cover, the Precambian Fennoscandian southern continuation covered by sediments, and the Caledonides to the west), the Moho depth is anomalously deep as it varies between 40 and 60 km (Silvennoinen *et al.* 2014). Our phase velocity maps shows that the Archean and Proterozoic domains do not have significantly different velocities in the mantle lithosphere. The most pronounced feature at period of 60 s Rayleigh phase velocity map (Fig. 2.20c) is the sharp change in velocities along the mid Atlantic ridge. An elongated low velocity anomaly can be clearly seen beneath Iceland. The upper mantle low velocity anomaly associated with Iceland is of varying diameter and can be clearly traced at longer

periods than 100 s (Fig. 2.20e). It's lateral extent is large compared to the anomaly imaged with a smaller dataset (Pilidou *et al.* 2004). This low velocity anomaly is centred beneath Iceland and elongated along the direction of the mid atlantic ridge. The highest amplitude of this anomaly located to the southwest of Iceland.

2.6.1.2 Central Europe

Figure (2.23) shows the Rayleigh and Love wave phase velocity maps for central Europe region. At Rayleigh wave map of 30 s period (Fig. 2.23a) the most striking pattern is the clear separation between fast phase velocity anomalies in central and northern Europe from slower areas south of the Alpine Front (AF) and the convergence zone of Carpathian Arc and TTZ that is clearly visible at the 60 sec map. Such changes might be related to variations in crustal thickness. According to Meissner and Rabbel (1999), Moho depths north of the Alps show slight variations around 30 - 35 km which is expressed by relatively faster velocities in the phase velocity map due to their partial sensitivity to sub-Moho seismic velocities. This is consistent with the high shear wave velocities introduced previously in both global and regional tomographic studies (e.g. Bijwaard & Spakman, 2000; Karason & Van Der Hilst, 2000; Grand, 2002; Ritzwoller *et al.* 2002; Ritsema *et al.* 2004; Priestley & McKenzie, 2006; Lebedev & van der Hilst, 2008; Amaru *et al.* 2008; Boschi *et al.* 2009; Koulakov *et al.* 2009; Simmons *et al.* 2010; Schaefer *et al.* 2011; Legendre *et al.* 2012; Zhu *et al.* 2012; Soomro et. al. 2016; Meier *et al.* 2016). Towards the Carpathian-Pannonian system the observed low velocities indicates shallow asthenospheric flow beneath the Pannonian basin.

The 60 s Rayleigh phase velocity maps (Fig. 2.23c) is mainly sensitive to variations in the shear velocities at depth of the mantle lithosphere (80 - 120 km). The striking lineament of the Tornquist–Tesseyre Zone (TTZ), that is, the junction between the faster thicker East European Craton (EEC) and the slower thinner lithosphere of western Europe that runs from southern Scandinavia through Poland to the Black Sea. The TTZ has been imaged in previous group velocity studies of the region (Ritzwoller & Levshin 1998; Pasyanos 2005; Schivardi & Morelli 2009), but our dense ray coverage allows to delineate it with particular clarity and shows consistency with the other phase velocity studies of (Fry *et al.* 2008; Peter *et al.* 2008; Soomro *et al.* 2016). Low velocity anomalies indicate shallow asthenosphere in central Europe (CEA) including Eifel region as well as in Pannonian basin (PanB) have been detected. Interstingly, both 100 s phase velocity maps of Rayleigh (2.23e) and Love (2.23f) shows a sharp change in the velocity from high velocities beneath the very thick mantle lithosphere of the Precambrian East European Craton (EEC) to low velocities beneath

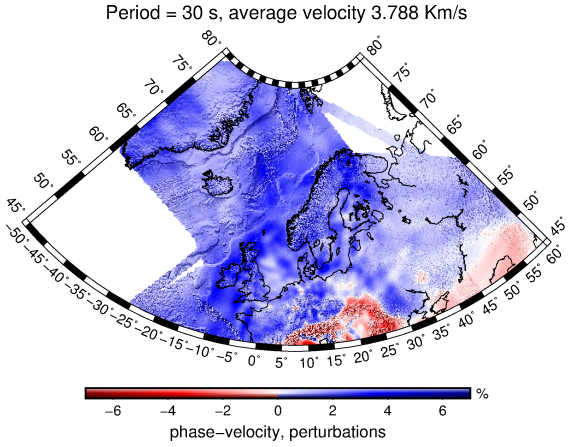

(a) Rayleigh (30 s)

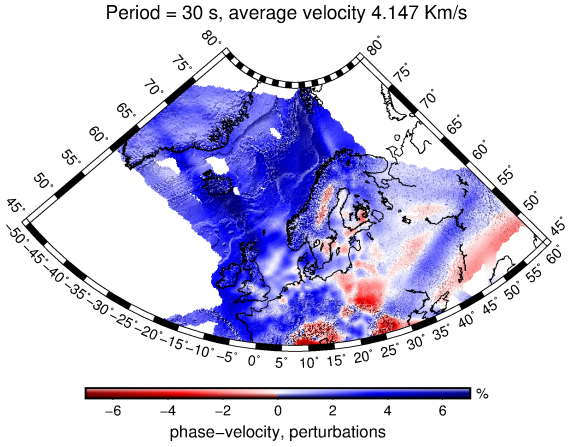

(b) Love (30 s)

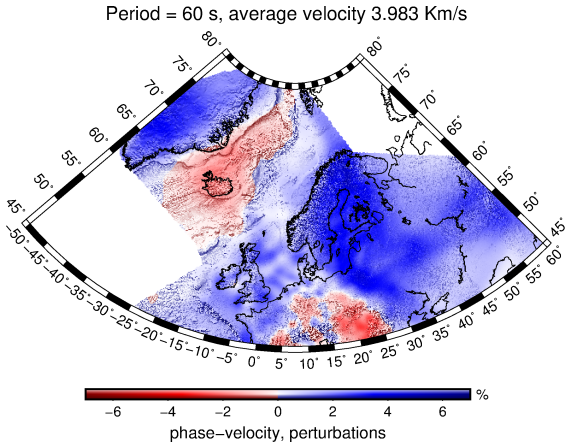

(c) Rayleigh (60 s)

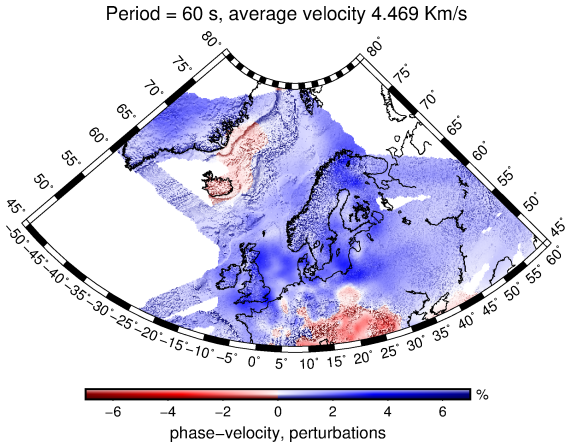

(d) Love (60 s)

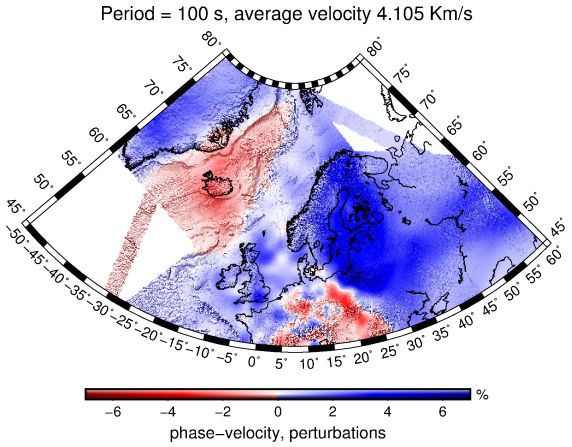

(e) Rayleigh (100 s)

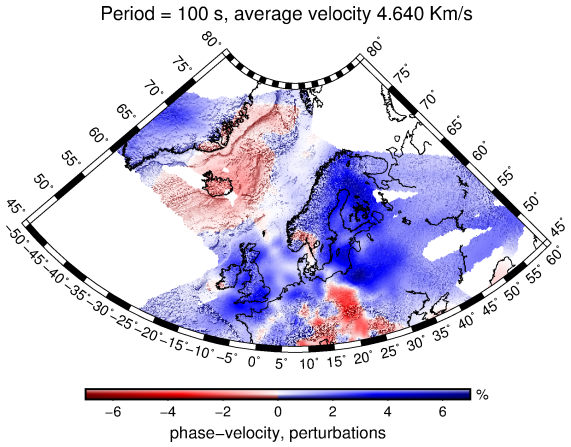

(f) Love (100 s)

Fig. 2.22 Isotropic Rayleigh and Love wave phase velocity maps for the North Sea and it's periphery.

the younger Phanerozoic Europe. It also show extended low velocity anomalies beneath the Panonian basin, central Europe and the Eifel hotspot.

2.6.1.3 The Alps

The 30 s Rayleigh phase velocity map (Fig. 2.24a) is characterized by anomalously low velocities at depths of deep crustal roots along the Alpine Arc, the Apennines and the Dinarides. The most pronounced feature on this map is the sharp change from higher phase velocities in central Europe to regions of lower velocities along of the Alpine Front (AF). This is largely correspond to variations in the crustal structure of the region. Moreover, another sharp contrast along the coastline of the Italian peninsula which reflects increasing the crustal thickness from the Tyrrhenian Sea towards the Apennines. This is consistent with the results shown by Greve *et al.* (2012). The observed high velocity anomaly beneath the Tyrrhenian indicates the shallow lithospheric structure in this area. Similar features are also detected on the 30 s Love wave phase velocity map (Fig. 2.24b). At longer periods, a clear distinction between regions of fast anomalies and those of slow velocity anomalies most importantly the Tyrrhenian sea, Ligurian basin and the Pannonian basin becomes evident in our maps. At 60 s Rayleigh wave map, the widespread fast anomalies are mainly due to cold continental lithosphere of Europe. Two spots of fast velocity anomalies along the Alpine arc have been detected. We interpret them as the SE-directed Eurasian subducted slab in the central Alps (CASl) and the NW-directed Adriatic subducted slab in the Eastern Alps (EASl). The subducting adriatic slab along the Dinarides emerges as a narrow belt of high velocity anomaly at the 60 seconds map. Slow velocities in the Liguria can be explained by its oceanic origin and young age. Handy *et al.* (2010) argued that a rollback subduction of the Ligurian oceanic plate along the Liguria-Adria plate boundary began 30 Ma ago and led to significant extension in the western Mediterranean. In the Pannonian basin, upwelling of the asthenosphere can explain the reduced velocities. The 60 s Love wave map (Fig. 2.24d) shows low velocities beneath the Apennines and the Dinarides. On the other hand, it shows high velocity anomalies beneath the Tyrrhenian sea, the wastern Alps and also western Europe. At 100 s maps which are sensitive to the depth range 120 -180 km, they both show a high velocities at the western Europe indicating thick continental mantle lithosphere. In the northern Apennines, a high velocity anomaly at the 100 s Rayleigh map (Fig. 2.24e) may be related to the subducted Apenninic slab. Beneath both central Apennines and the Dinarides, a low velocity anomalies show the Apenninic slab window and the Dinaridic slab gap. The same features have been imaged in previous studies (e.g., Lippitsch *et al.* 2003; Spakmann & Wortel 2004; Greve *et al.* 2012; Verbecke *et al.* 2012; Kästle *et al.* 2018).

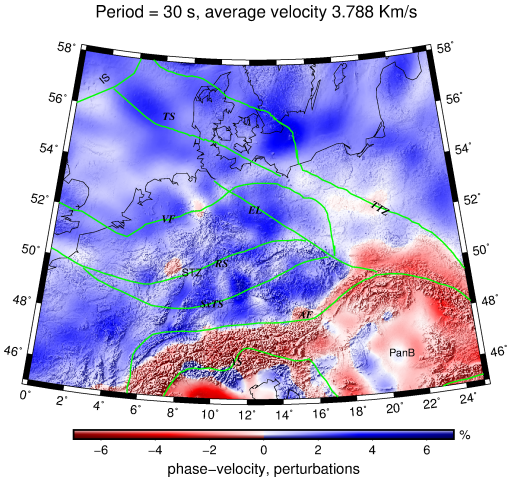

(a) Rayleigh (30 s)

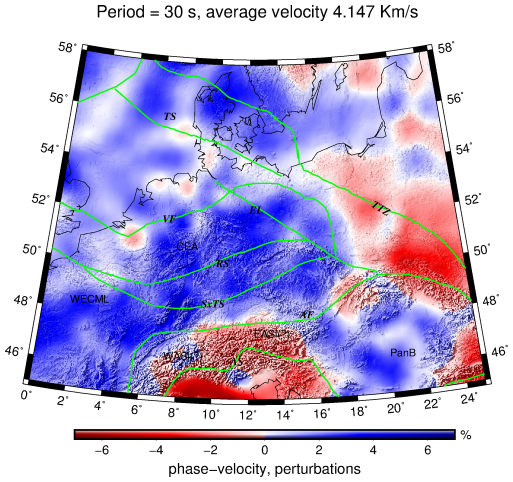

(b) Love (30 s)

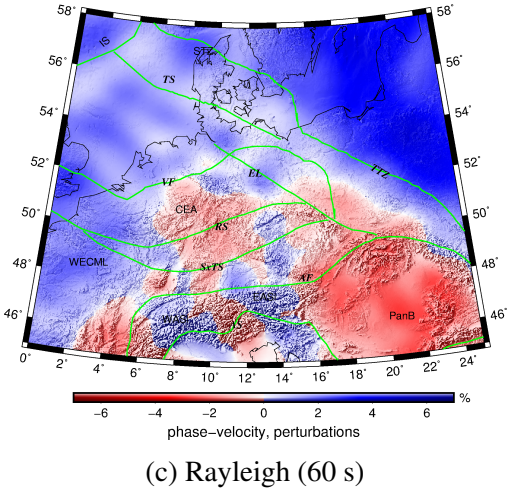

(c) Rayleigh (60 s)

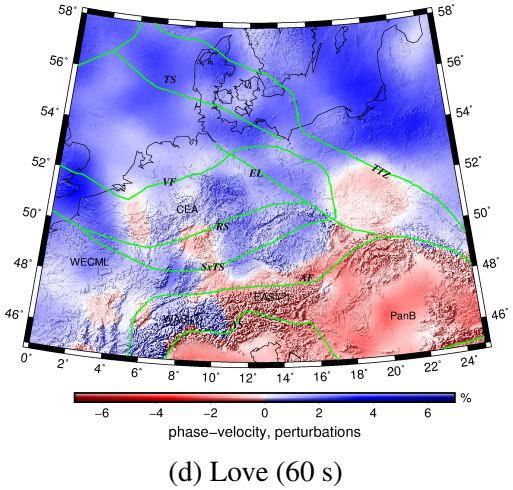

(d) Love (60 s)

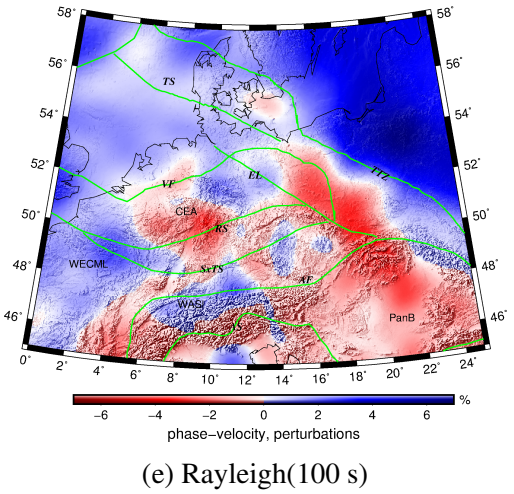

(e) Rayleigh(100 s)

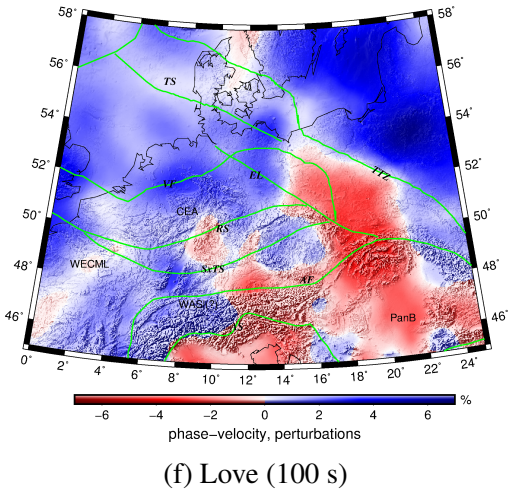

(f) Love (100 s)

Fig. 2.23 Isotropic Rayleigh and Love wave phase velocity maps for central Europe. The green lines indicate the main tectonic features. The abbreviations stand for Iapetus suture (IS), Thor suture (TS), Sorgenfrei-Tornquist Zone (STZ), Tornquist-Teisseyre Zone (TTZ), Variscan front (VF), Elbe line (EL), Rheic suture (RS), Saxothuringian suture (SxTS), Alpine front (AF) and Alpine suture (AS).

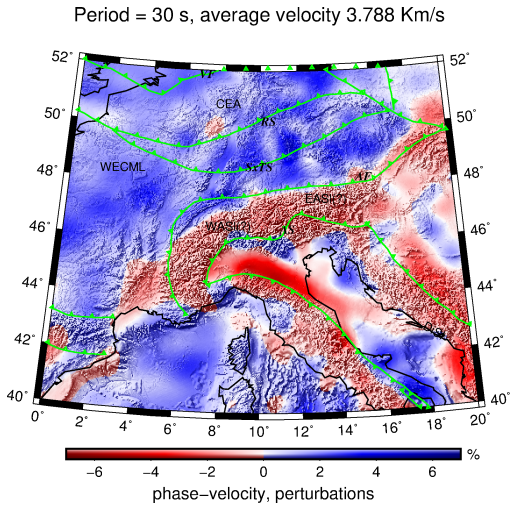

(a) Rayleigh (30 s)

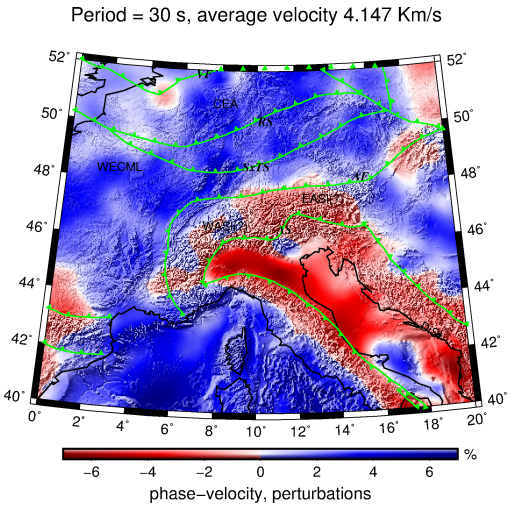

(b) Love (30 s)

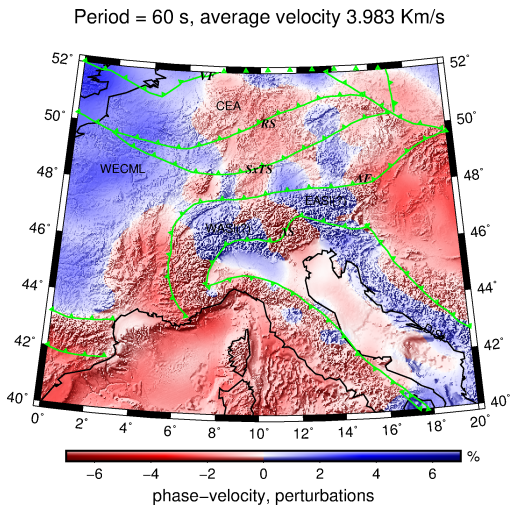

(c) Rayleigh (60 s)

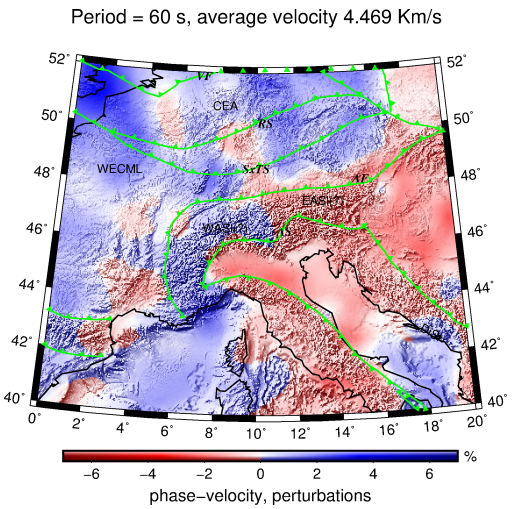

(d) Love (60 s)

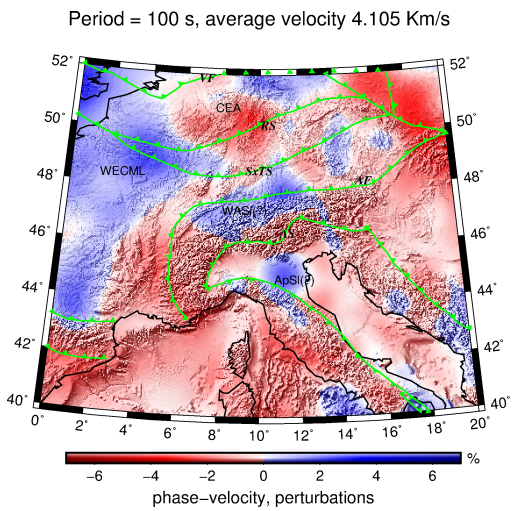

(e) Rayleigh (100 s)

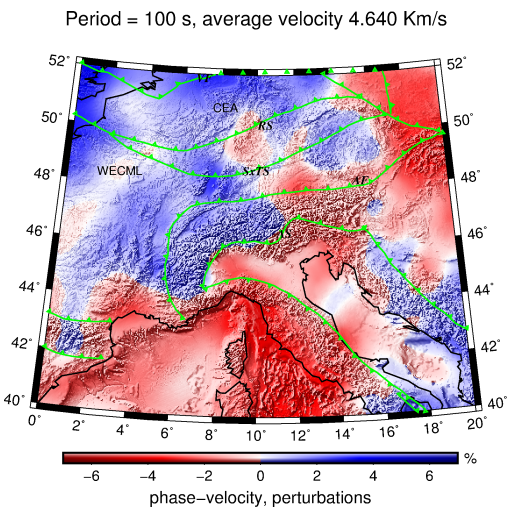

(f) Love (100 s)

Fig. 2.24 Isotropic Rayleigh and Love wave phase velocity maps for the Alps. Appreviations are the same as in figure 2.23.

2.6.1.4 The Alpine-Mediterranean Mobile Belt

Figures 2.25 and 2.26 show the isotropic phase velocity maps of the greater Mediterranean for both Rayleigh and Love waves, respectively. Numerous small- and large-scale features are coherently imaged at nearby periods showing robust and reliable structures. At 15 s Rayleigh phase velocity map (Fig. 2.25a), widespread low velocity anomalies are dominating the eastern Mediterranean, whereas the western Mediterranean is dominated by high phase velocity anomalies. This reflects that the rate of deformation in the eastern Mediterranean is much larger compared to the western part. The 15 s period is sensitive to a relatively shallow depth including the deepest part of the thicker sedimentary Basins. The most striking but small features on this this maps are the high amplitude low velocity anomalies, that are mostly associated with the Po Plain basin in the northern part of the central Mediterranean, the accretionary wedge beneath Calabria in southern Mediterranean and the marine Alboran basin in the western Mediterranean. The large scale high velocity anomaly beneath the Ligurian and the Tyrrhenian Sea indicates the oceanic nature of their crust. Another small but interesting feature, a sharp contrast in the velocity amplitudes along the straits of messina, east of Sicily. Figure (2.25b) shows the 30 s map which is sensitive to the Moho topography, the lower crustal velocities and velocities of the mantle lithosphere depending on the crustal thickness (Lippitsch *et al.* 2003; Panza & Raykova, 2008). The most striking feature on this map is somewhat continuous belt of low velocity anomaly starting from the marine Alboran basin in the western Mediterranean and continues beneath Atlas Mountains to Sicily, the Apennines, the Alpine chain, the Carpathian and the Dinarides till Anatolia in the eastern Mediterranean and Middle East. This indicates the deep crustal roots and the highly deformed regions within the Mediterranean. A narrow fast anomaly in 30 s Rayleigh map correlates very well with the Pannonian Basin area and which is consistent with recent images of a shallow Moho depth in this area (Raykova & Nikolova 2007). Beneath Anatolia, we observe a striking low velocity anomaly beneath central part which might be related to the distribution of the Cenozoic volcanism beneath that region.

Moreover, another extremely low velocity anomaly is also observed beneath the eastern Anatolia, a typical observation that is evident in areas of thick continental crustal structure and correlates very well with the high elevation plateau along the Eastern Anatolia Accretionary Complex (EAAC). Additionally, we also observed a wide spread fast anomalies beneath northern Africa. Along the Apennines and it's surroundings, the imaged features largely correspond to variations in the crustal structure of the region. Interestingly, the 30 s Love wave phase velocity map (Fig. 2.26b) shows the same features as the Rayleigh one except in few regions including the the Black Sea and the Pannonian Basin where a high Love

wave phase velocity anomalies were encountered. The 60 s Rayleigh phase velocity map (Fig. 2.25c) shows an extended upper mantle low-velocity anomaly occupying Anatolia, the Pannonian Basin, most of the Tyrrhenian Sea and the Ligurian Sea that is correlates very well to the magmatic nature of this area and showing the shallow asthenosphere. In contrast, the most pronounced feature is the continuous high velocity anomaly from southern Aegean Sea (Hellenic subduction) to western Greece and extend to the Ionian Sea. At period larger than 60 s, we also observed a high velocity anomaly north of Cyprus and we interpreted that as northward dipping African oceanic lithosphere subducted from the Cyprus trench. Along the Dinarides, Moreover, another high velocity anomaly can be traced clearly. The Eastern and the Central Alpine subducted slabs are seen as high anomalies separated by a low velocity anomaly. At 100 s map of Rayleigh wave (Fig. 2.25d), low velocities are extended beneath Anatolia, whereas a relatively high velocity anomalies have been encountered north of the NAF representing the thick continental mantle lithosphere of Eurasia. The African subducted lithosphere is still clearly seen as a dominant high velocity anomaly beneath the Hellenic Arc. The Ionian subducted slab beneath Calabria can be traced as a narrow belt trending SW-NE of high velocity anomaly that is highly correlated with the seismicity at those depths. The Intersting relative small features on this map include, the anomalously low velocity anomalies beneath central Apennines indicating it's slab window. In addition, the Dinaridic slab gap is also shown as low velocity anomaly beneath the Dinarides. Another moderately-sized high velocity anomaly in the northern Apennines indicates a remnant of the subducting northern Apenninic slab.

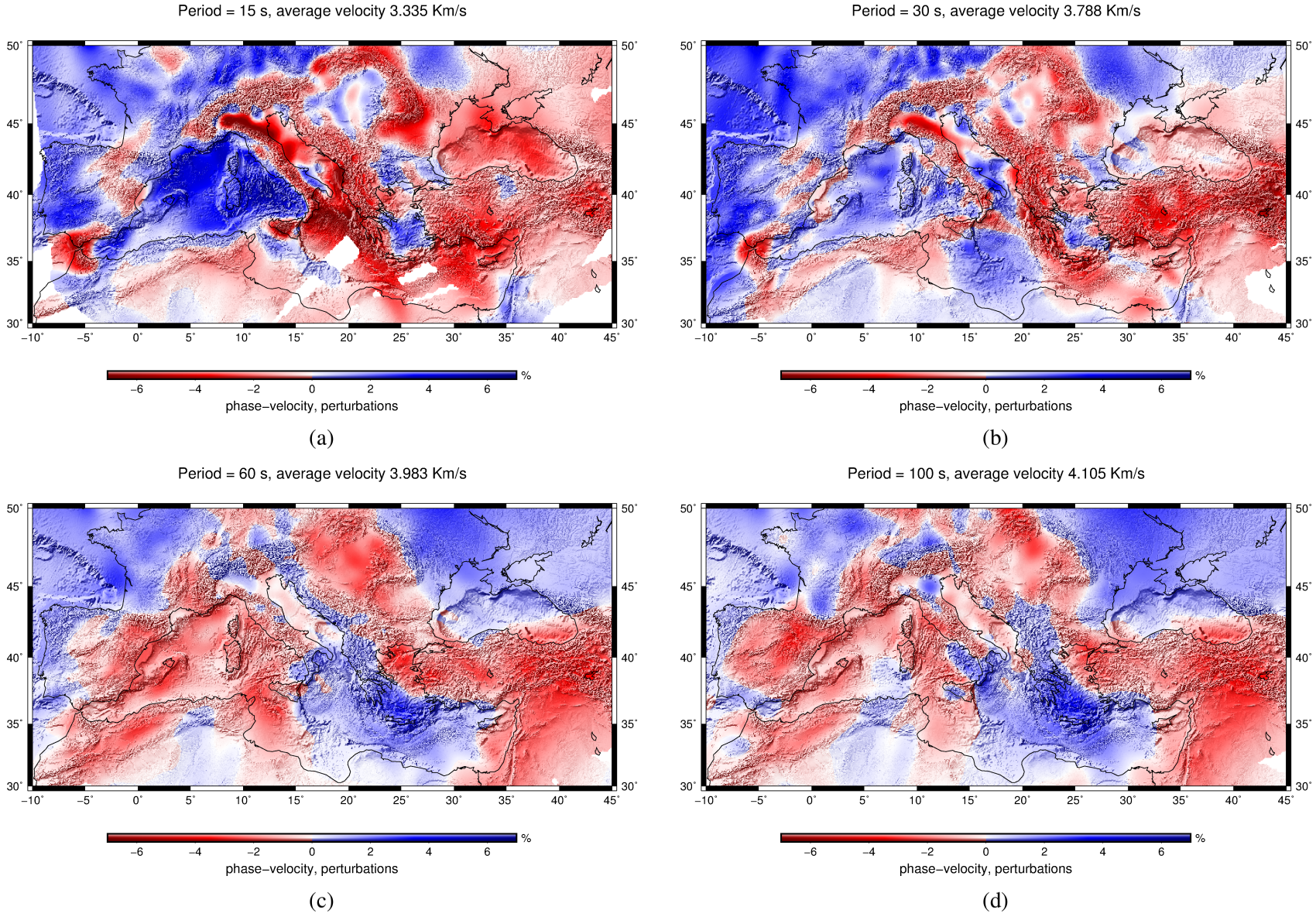

Fig. 2.25 Isotropic Rayleigh wave phase velocity maps for the Alpine-Mediterranean mobile belts at periods of 15 (a), 30 (b), 60 (c) and 100 (d) seconds.

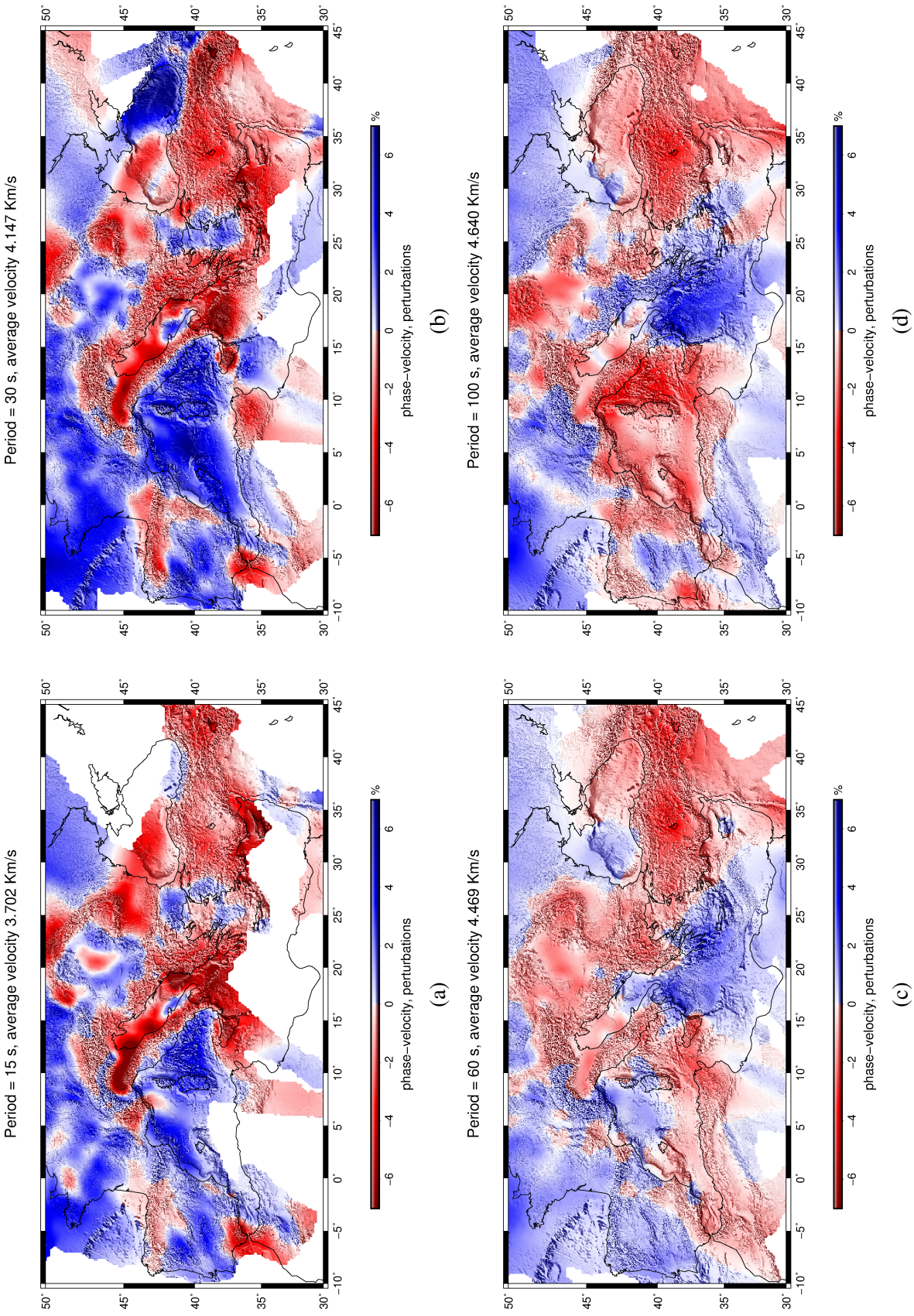

Fig. 2.26 Isotropic Love wave phase velocity maps for the Alpine-Mediterranean mobile belts at periods of 15 (a), 30 (b), 60 (c) and 100 (d) seconds.

2.6.2 Azimuthally anisotropic phase velocity maps

Azimuthal anisotropy can be defined as the directional dependence of seismic wave velocitites. According to Nicolas & Christensen (1987), the prescence of anisotrpy in the lithosphere and the asthenoshpere is largely due to the alignment of the anisotropic olivine crystals (lattice-preferred orientation, LPO) in mantle flow. Therefore, it can be used as indicator for the distribution and evolution of the upper mantle deformational regimes or as a measure of flow or velocity gradients in the mantle. McKenzie (1979) concluded that the presence of seismic anisotropy in the upper mantle can be associated with accumulated strain due to mantle convection. Anisotropy can also be shape preferred orientation (SPO). In SPO, the material aligns with distinct isotropic properties (heterogeneity) observable as for example cracks and melt pockets in the shallowest crust. Determination of the fast propagation direction of the anisotropy can give us hints of deformation in LPO. With the change in stress regime, the fast direction changes and erases the information of the previous deformation. Therefore, the measured anisotropy in the lithosphere always shows last significant deformation or thermal event. Wüstefeld *et al.* (2009) showed that the observed anisotropy may present in the form of frozen anisotropy after relaxation of thermal events. Mantle flow patterns can be understood from the anisotropy and deformation caused in the preferred orientation of the anisotropic material. This is because the fast axis of these minerals align with the direction of flow due to large tectonic deformations. Anisotropy in the asthenoshpere is related to present day flow pattern as mentioned by Debayle & Ricard (2013) whereas the anisotropy in lithosphere may be due to present or past deformation in mantle lithosphere (Silver, 1996; Silver & Chan, 1991).

Although the azimuthal anisotropy is beyond the scope of this chapter, our tomographic inversion is set in a way to simultaneously invert the phase velocity measurements for the spactial distribution of both the isotropic and azimuthally anisotropic phase velocity perturbations with respect to a regional phase velocity average at each period independently. Examples of the azimuthal anisotropic Rayleigh wave phase velocity maps at some selected periods for two different regions including central Europe and the Alps are shown in figure (2.27) and figure (2.28), respectively.

At 15 s phase velocity map (Fig. 2.27a), the fast propgation direction along the East European Craton is NW-SE directed, which is simialr to the 30 s map. At periods longer than 60 s (Fig. 2.27c), the anisotropic fast propagation direction shows slight variations as it changing from NE-SW to ∼N-S. At 150 s map (Fig. 2.27e), a NE-SW fast direction is observed. This might indicate a layering of anisotropy. Similarly, Yuan & Romanowicz (2010) at the north American Craton observed lithospheric layering in anisotropy. The 60 s

and 150 s phase velocity maps are roughly sensitive to depth range between 80 and 250 km. For an exact depth estimates, a depth inversion is required. Therefore, it is not clear from our phase velocity maps that the observed layering is within the mantle lithosphere or the asthenosphere. Along the TTZ, the fast propgation direction at all periods is NW-SE directed, except along it's northern part as it shows sligh variations. This might be due to sharp change from the Precambrian continental mantle lithosphere to the younger Phanerozoic Europe. Central Europe anisotropy at 15 s is following the Variscan front with the fast direction of NE-SW. This trend abruptly changes to SE-NW near Elbe line. At 60 s map, the anisotropy pattern follows the Variscan front (VF) and Elbe line (EL) near Bohemian massif. In the northwest part of the maps, at 15 s a nearly N-S oriented fast direction. At 30 s map low values of the anisotropic amplitudes are observed. At longer periods > 60 s the anisotropic pattern completely changes to NW-SW following the Thor suture (TS). In central Europe the fast direction of long periods follows the Rheic suture (RS) and Saxothuringian suture (SxTS).

The anisotropic fast propagation direction along the Alps (Fig. 2.28) is following the curvature of the Alpine arc parallel to the Alpine front (AF). It also shows more or less the same behaviour at 30 s map (Fig. 2.28b) as it changes to SE-NW beneath both the western Alps and the Ligurian Sea. At longer periods the amplitude and the direction are changing as well. Such anisotropic variations may be due to layering of the anisotropy. It is worth to mention that the azimuthally anisotropic phase velocity maps may contain artefacts. These artefacts arise from the leakage between isotropic and anisotropic coefficients or spurious anisotropy due to path bias (Darbyshire & Lebedev, 2009). In this regard a resolution tests are highly required to quantify the leakage between the isotropic and azimuthally anisotropic terms. Moreover, a depth inversion for a 3-D azimuthally anisotropic shear velocity model is also needed to estimate the change of anisotropy with depth.

2.7 Conclusion

Phase velocity measurements of the fundamental mode Rayleigh and Love surface waves for the Europe and the greater Mediterranean have been calculated in order to study, in greater detail, the crust, mantle lithosphere and asthenosphere of the region. An automated algorithm for inter-station phase velocity measurements (Soomro *et al.* 2016) is applied to very large and heterogeneous volumes of seismic database consists of more than 4000 seismic events in the time period from 1990 to 2016 and recorded by $\sim$ 4500 broadband stations of permanent and temporary deployments. The data have been collected from the European Integrated

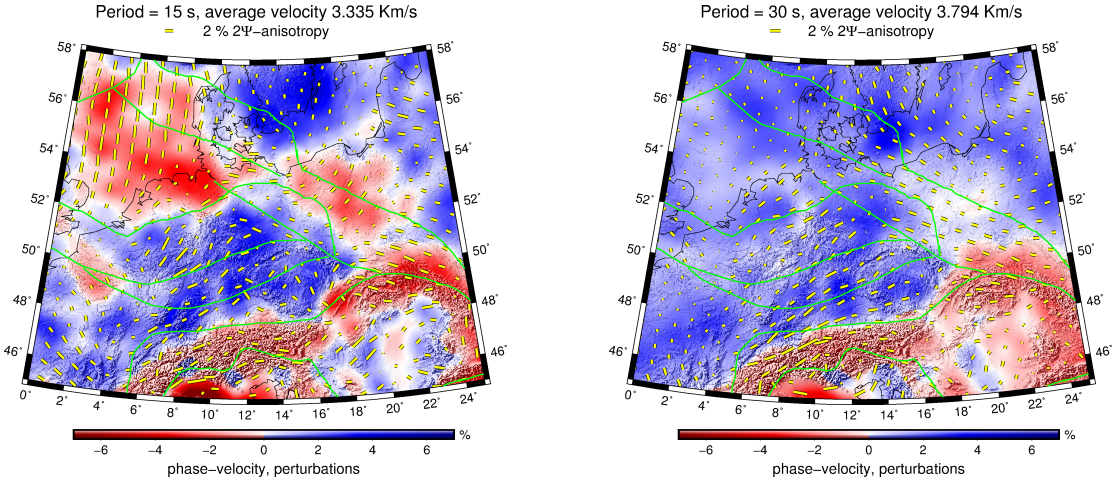

(a)

(b)

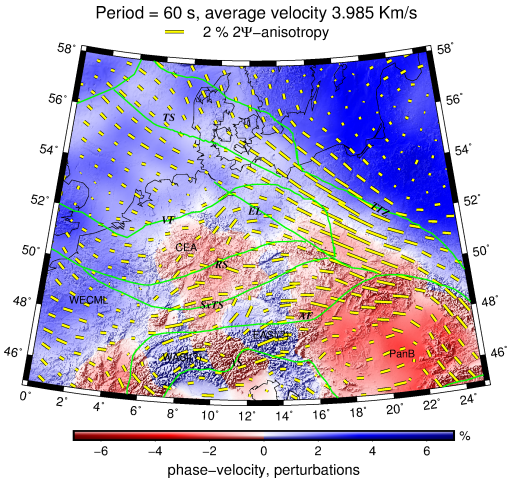

(c)

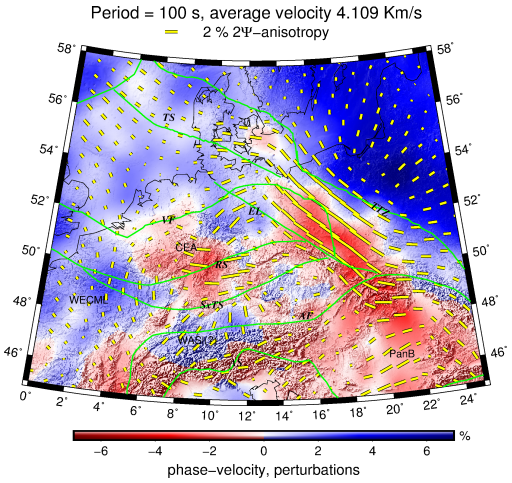

(d)

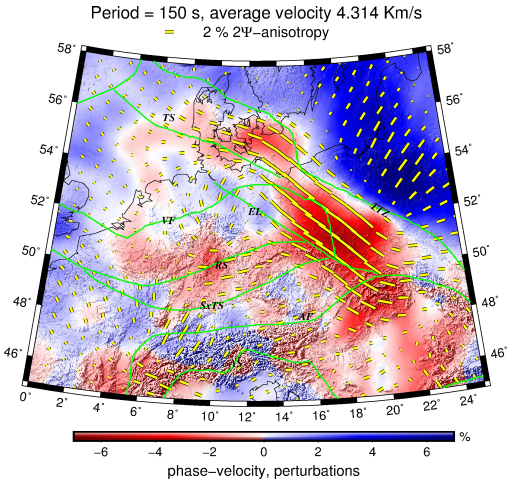

(e)

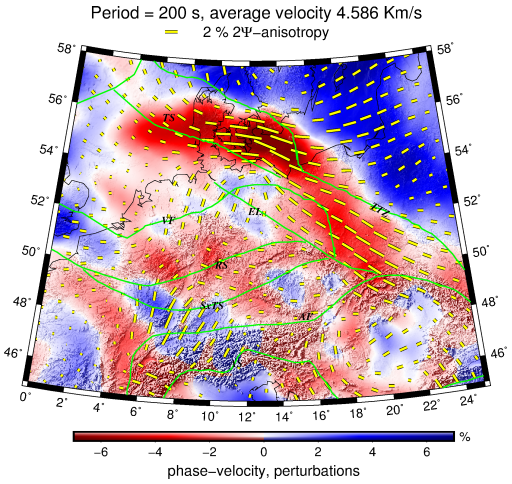

(f)

Fig. 2.27 Azimuthally anisotropic Rayleigh phase velocity maps for central Europe at different periods as indicated on the maps.

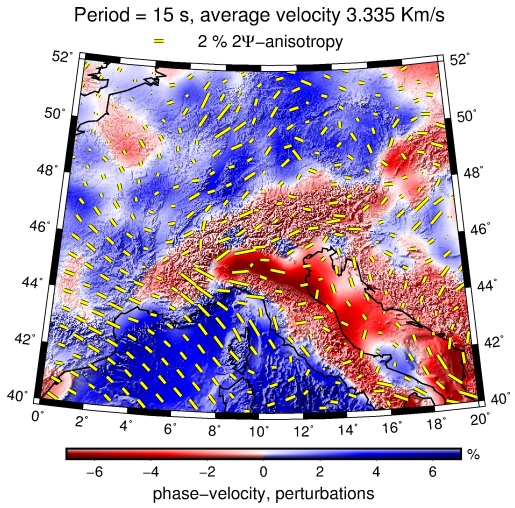

(a)

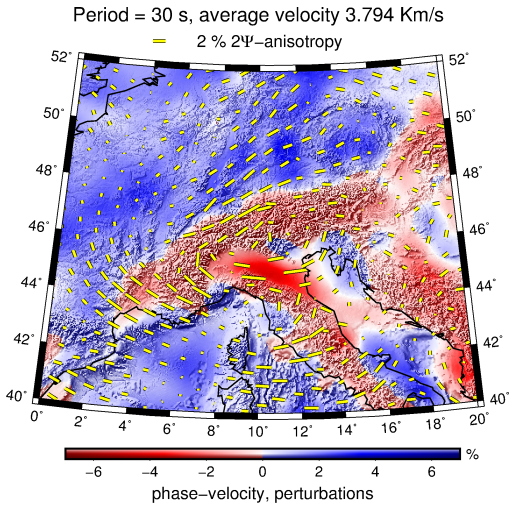

(b)

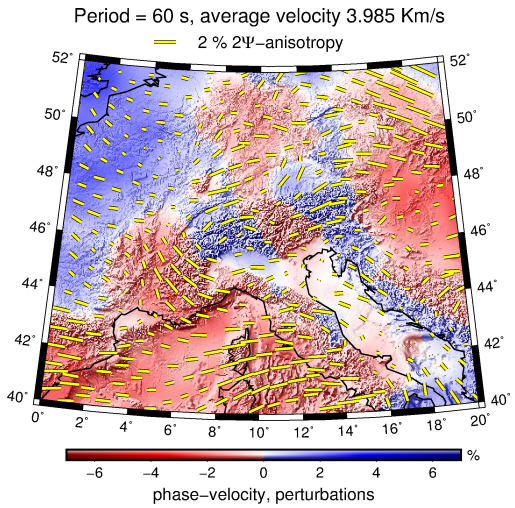

(c)

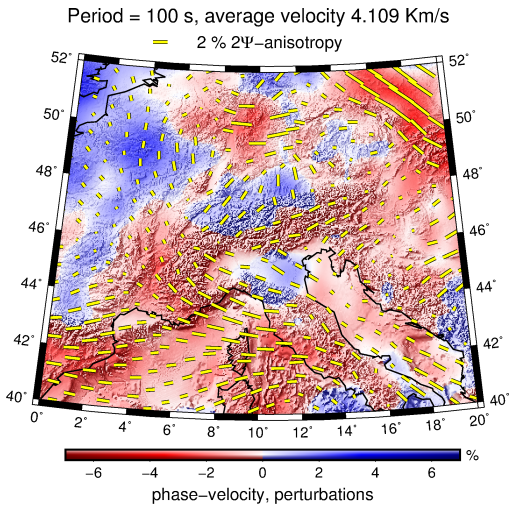

(d)

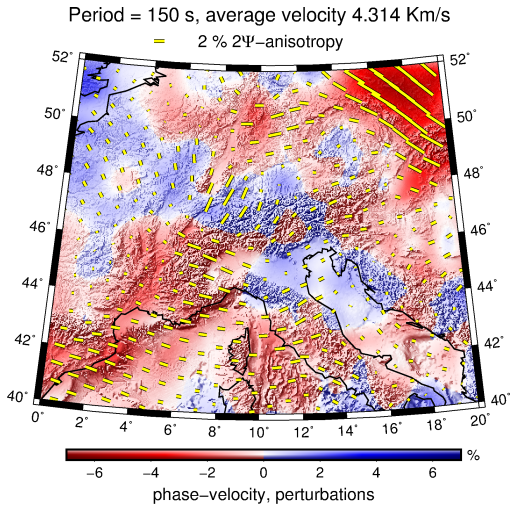

(e)

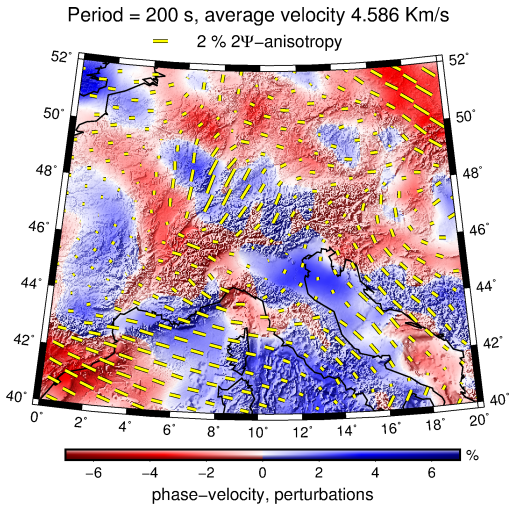

(f)

Fig. 2.28 Azimuthally anisotropic Rayleigh phase velocity maps for the Alps at different periods as indicated on the maps.

Data Archive (WebDc/EIDA) and IRIS, moreover for the first time, data from the Egyptian National Seismological Network (ENSN) recorded by $\sim$ 25 broad band seismic stations are also included in the analysis. For each station pair approxmately located on the same great-circle path, we cross correlated the waveform recorded by the considered two stations and the dispersion curve is calculated from the phase difference of the cross correlation functions weighted in the time-frequency plane. The selection of acceptable phase-velocity measurements for each event is performed in the frequency domain, based on a number of fine-tuned quality criteria. Path average dispersion curves were calculated by averaging a bundle of single-event measurements. Ranging between 20 and 2500 single-event dispersion measurements are averaged per inter-station path in order to obtain robust, broad-band path average dispersion curve with error estimate. This resulted in an unprecedented number of path average phase velocity measurements ($\sim$ 200,000 curves) in a very broad period range (8 - 350 seconds). A careful quality control of the resulting phase velocities is performed. The resulted inter-station phase velocities are then utilized in a surface wave tomographic inversion to construct both the 2-D isotropic and the azimuthally anisotropic phase-velocity maps for the entire region. The tomographic method described here uses the traditional ray representation of the interstation surface wave sensitivity; however, it was also possible to assign a frequency-dependant finite-path width to each inter-station path, to approximate a broad sensitivity area (kernel) in the inversion. For finite path widths extending to several hundred kilometres around the interstation ray path, although the tomographic inversion produces phase-velocity maps that are almost identical to those calculated using zero-width rays, there were some enhancements of the shape and amplitude of anomalies at some locations.

Moreover, various attempts to assess the reliabilty of the tomographic maps have been systematically performed. We investigated the effects of different regularization constraints on the shape and amplitude of the anomalies. We have shown that large-scale and most of the small-scale features of our model are generally robust and stable, whereas care must be taken in the interpretation of finer details. According to checkerboard tests, the lateral resolution in Europe and the Mediterranean is $\sim$ 150 km. From our phase velocity maps, We emphasize the following prominent features: Our phase-velocity maps show enhanced resolution with respect to previous local and regional surface wave studies and exhibit an excellent correlation with known tectonic features of the region. Particularly worth mentioning is the contrast between the slower central Europe and Western Mediterranean Basin and the higher velocity associated with the Eastern European Platform. These two different tectonic regimes are separated by a sharp contrast corresponding to the Tornquist–Tesseyre Zone, a consistent feature in our long period maps. The lateral resolution of the obtained phase velocity maps

for the European and Mediterranean region is mostly less than 100 km with is much better with respect to previous studies. We resolved in great detail both small scale and large scale features. Example of the small scale features include the sharp change in velocity across the strait of Messina at shprt and long periods where the transition from oceanic to continetal lithosphere is expected, moreover, the narrow fast anomalies of the Carpathian mountains, Central and Eastern Alpine slabs and Calabria subduction have also been imaged clearly. Large scale features include the widespread low velocity anomalies beneath Anatolia and the western Mediterranean and high velocity anomalies beneath the Cyprus Hellenic Arc, Herodutus basin, Ionian Sea and Dinarides.

References

Adam, J. M.-C. & Lebedev, S., 2012. Azimuthal anisotropy beneath southern Africa from very broad-band surface-wave dispersion measurements, Geophysical Journal International, 191(1), 155 - 174.

Alsina, D., & Snieder, R., 1993. A test of the great circle approximation in the analysis of surface waves. Geophys. Res. Lett., 20. 915 - 928.

Anderson, D. L., 1961. Elastic wave propagation in layered anisotropic media. Journal of Geophysical Research 66 (9), 2953 - 2963.

Barmin, M.P., Ritzwoller, M.H. & Levshin, A.L., 2001. A fast and reliable method for surface wave tomography, Pure appl. Geophys., 158, 1351 - 1375.

Beyreuther, M., Barsch, R., Krischer, L., Megies, T., Behr, Y., & Wassermann, J., 2010. ObsPy: A Python Toolbox for Seismology, Seismol. Res. Lett., 81, 530 - 533.

Bijwaard H and Spakman W (2000) Non-linear global P-wave tomography by iterated linearized inversion. Geophys. J. Int., 141. 71 - 82.

Boschi, L. & Ekström, G., 2002. New images of the Earth's upper mantle from measurements of surface wave phase velocity anomalies. Journal of Geophysical Research 107: B4 10.1029/2000JB000059.

Brilliant, R.M., E.-M., 1954. Dispersion of Rayleigh waves across the U.S., Bulletin of the Seismological Society of America., 44, 149 - 158.

Carannante, S. & Boschi, L., 2005. Databases of surface wave dispersion, Ann. Geophys., 48 (6), 945 - 955.

Chevrot, S. & Zhao, L., 2007. Multiscale finite-frequency Rayleigh wave tomography of the Kaapvaal craton, Geophys. J. Int., 169(1), 201–215.

Coste, J.-F., 1997. Approximate dispersion formulae for Rayleigh-like waves in a layered medium. Ultrasonics 35 (6), 431 - 440.

Cotte, N., Pedersen, H.A., Campillo, M., Farra, V. & Cansi, Y., 2000. Off-great-circle propagation of intermediate-period surface waves observed on a dense array in the French Alps, Geophys. J. Int., 142, 825 - 840.

Christensen, M. I. & Mooney, W. D., 1995. Seismic Velocity Structure and Composition of the Continental- Crust - a Global View. J. Geophys. Res. Earth 100, 9761 - 9788.

Christensen, N. I., 1996. Poisson's ratio and crustal seismology. J. Geophys. Res. Solid Earth 101, 3139 - 3156.

Darbyshire, F. A. & Lebedev, S., 2009. Rayleigh wave phase-velocity heterogeneity and multilayered azimuthal anisotropy of the Superior Craton, Ontario. Geophys. J. Int. 176, 215 - 234.

De Vos, D., Paulssen, H. & Fichtner, A., 2013. Finite-frequency sensitivity kernels for two-station surface wave measurements. Geophys. J. Int. 194, 1042 - 1049.

Deschamps, F., Lebedev, S., Meier, T. & Trampert, J., 2008. Stratified seismic anisotropy reveals past and present deformation beneath the East-central United States. Earth Planet. Sci. Lett. 274, 489 - 498.

Deschamps, F., Lebedev, S., Meier, T. & Trampert, J., 2008. Azimuthal anisotropy of Rayleigh-wave phase velocities in the east-central United States. Geophys. J. Int. 173, 827 - 843.

Dziewonski, A.M., 1984. Mapping the lower mantle: Determination of lateral heterogeneity in P velocity up to degree and order 6. J. Geophys. Res., 89, 5929 - 5952.

Dziewonski, A. & Anderson, D., 1981. Preliminary reference Earth model, Physics of the Earth and Planetary Interiors, 25, 297–356.

Dziewonski, A. M., & Woodhouse, J. H., 1987. Global images of the earth's interior. Science, 236, 37 - 48.

Dziewonski, A. M. and Romanowicz, B. A., 2007. Overview; in Romanowicz, B. A. and Dziewonski, A. M (eds.): Vol. 1 - Seismology and structure of the Earth; in Schubert, G. (ed.): Treatise on Geophysics, Elsevier, Amsterdam, pp 1–29.

Ekström, G., Tromp, J. & Larson, E. W. F., 1997. Measurements and global models of surface wave propagation. J. Geophys. Res. 102 (B4), 8137 - 8157.

Ekström, G., 2011. A global model of Love and Rayleigh surface wave dispersion and anisotropy, 25-250 s. Geophys. J. Int. 187, 1668-1686.

Endrun, B., Meier, T., Bischoff, M., & Harjes, H.-P., 2004. Lithospheric structure in the area of Crete constrained by receiver functions and dispersion analysis of Rayleigh phase velocities, Geophysical Journal International, 158(2), 592 - 608.

Endrun, B., Meier, T., Lebedev, S., Bohnhoff, M., Stavrakakis, G., & Harjes, H.-P., 2008. S velocity structure and radial anisotropy in the Aegean region from surface wave dispersion, Geophysical Journal International, 174(2), 593 - 616.

Endrun, B., Lebedev, S., Meier, T., Tirel, C., & Friederich,W., 2011. Complex layered deformation within the Aegean crust and mantle revealed by seismic anisotropy, Nature Geoscienes, 4(3), 203 - 207.

Engdahl, R. E., van der Hilst, R., & Buland, R., 1998. Global teleseismic earthquake relocation with improved travel times and procedures for depth determination, Bulletin of the Seismological Society of America, 88(3), 722 - 743.

Evernden, J.E., 1954. Direction of approach of Rayleigh waves and related problems, Part 11, Bull. seism. SOC. Am., 44, 159 - 184.

Forsyth, D.W., 1975. The early structural evolution and anisotropy of the oceanic upper mantle. Geophys. J. of the Royal Astronomical Society 43. 103-162.

Foster, A., Ekström, G., & Nettles, M., 2013. Surface wave phase velocities of the western United States from a two-station method, Geophysical J. Int.

Fry, B., L. Boschi, G. Ekstrom and D. Giardini, 2008. Europe-Mediterranean tomography: High correlation between new seismic data and independent geophysical observables, Geophysical Research Letters, 35: p. L04301.

Fu, C. Y., 1946. Studies on seismic waves: Ii. Rayleigh waves in a superficial layer. Geophysics 11 (1), 10 - 23.

Grand, S. P., 2002. Mantle shear–wave tomography and the fate of subducted slabs, Philosophical Transactions of the Royal Society of London A: Mathematical, Physical and Engineering Sciences, 360(1800), 2475 - 2491.

Haskell, N. A., 1953, January. The dispersion of surface waves on multilayered media. Bulletin of the Seismological Society of America 43 (1), 17–34.

Karagianni, E. E., Papazachos, C.B., Panagiotopoulos, D. G., Suhadolc, P., Vuan, A., & Panza, G. F., 2005. Shear velocity structure in the Aegean area obtained by inversion of Rayleigh waves. Geophys. J. Int., 160. 127 - 143.

Kästle, E., Soomro R., Weemstra C., Boschi L., Meier T., 2016. Two-receiver measurements of phase velocity: cross-validation of ambient-noise and earthquake-based observations. Geophysical Journal International, 207 (3), pp.1493 - 1512.

Kennett, B. L. N., 1976. The inversion of surface wave data: Pure and Applied Geophysics, v. 114, p 747-751.

Landisman, M., Dziewonski, A. & Sato, Y., 1969. Recent improvements in the analysis of surface wave observations, Geophys. J. R. astr. Soc., 17, 369–403.

Lay, T., & Wallace, T. C., 1995a. Modern global seismology, vol. 58, Academic press.

Lay, T. & Wallace, T. C., 1995b. Modern Global Seismology, vol. 58 of International Geophysics, Academic Press, 1st edn.

Lebedev, S., Adam, J. M. C. & Meier, T., 2013. Mapping the Moho with seismic surface waves: A review, resolution analysis, and recommended inversion strategies. Tectonophysics. 609, 377 - 394.

Lebedev, S., Meier, T. & van der Hilst, R. D., 2006. Asthenospheric flow and origin of volcanism in the Baikal Rift area. Earth Planet. Sci. Lett., 249, 415 - 424.

Lebedev, S., Boonen, J., & Trampert, J., 2009. Seismic structure of Precambrian lithosphere: New constraints from broad-band surface-wave dispersion, Lithos, 109, 96 - 111.

Legendre, C. P., Meier, T., Lebedev, S., Friederich, W., & Viereck-Götte, L., 2012. A shear wave velocity model of the European upper mantle from automated inversion of seismic shear and surface waveforms, Geophysical Journal International, 191, 282–304.

Levshin, A. L., Ritzwoller, M. H., & Ratnikova, L. I., 1994. The nature and cause of polarization anomalies of surface waves crossing northern and central Eurasia, Geophs. J. Int. 117, 577 - 590

Lippitsch, R., Kissling, E., & Ansorge, J., 2003. Upper mantle structure beneath the Alpine orogen from high-resolution teleseismic tomography. J. Geophys. Res. 108, 2376.

Liu, X. & Fan, Y., 2012, March. On the characteristics of high-frequency Rayleigh waves in stratified half-space. Geophysical Journal International 190 (2), 1041 - 1057.

Love, A. E. H., 1911. Some problems of geodynamics. Cambridge University Press.

McEvilly, T. V., 1964. Central U.S. crust-upper mantle structure from Love and Rayleigh wave phase velocity inversion, Bulletin of the Seismological Society of America, 54(6A), 1997 - 2015.

Meier, T., Dietrich, K., Stöckhert, B., & Harjes, H.-P., 2004. One-dimensional models of shear wave velocity for the eastern Mediterranean obtained from the inversion of Rayleigh wave phase velocities and tectonic implications, Geophysical Journal International, 156(1), 45 - 58.

Montagner, J.-P. & Tanimoto, T ., 1990. Global anisotropy in the upper mantle inferred from regionalization of phase velocities, J . geophys. Res., 95, 4797 - 4819.

Nakanishi, I. & Suetsugu, D. 1986. Resolution matrix calculated by a tomographic inversion method. Journal of Physics of the Earth 34, 95 - 99.

Nicolas, A. & Christensen, N. I., 1987. Formation of anisotropy in upper mantle peridotites: A review. In: Fuchs K and Froidevaux C (eds.) Composition, Structure and Dynamics of the Lithosphere-Asthenosphere System, pp. 111–123. Washington, DC: American Geophysical Union.

Nolet, G., (ed.), 1987. Seismic tomography, Kluwer, Dordrecht.

Paige, C.C. & Saunders, M.A., 1982. LSQR: an algorithm for sparse linear equations and sparse least squares, ACM Trans. Math. Softw., 8, 43 - 71.

Peter, D., C. Tape, L. Boschi, & J. H. Woodhouse, 2007. Surface wave tomography: Global membrane waves and adjoint methods, Geophys. J. Int., 171, 1098 - 1117.

Peter, D., L. Boschi, F. Deschamps, B. Fry, G. Ekström & D. Giardini, 2008. A new finite-frequency shear-velocity model of the European-Mediterranean region , Geophys. Res. Lett., 35, L16315, doi:10.1029/2008GL034769.

Priestley, K., & McKenzie, D., 2006. The thermal structure of the lithosphere from shear wave velocities. Earth and Planetary Science Letters 244: 285 - 301.

Prindle, K. & Tanimoto, T., 2006. Teleseismic surface wave study for S-wave velocity structure under an array: Southern California, Geophys. J. Int., 166(2), 601 - 621.

Rayleigh, J. W. S., 1885. On waves propagating along the plane surface of an elastic solid, Proc. London Math. Soc., 17, 4 - 11, citation from page 11. Reprinted in: Rayleigh, J. W. S., 1900: Scientific papers, Cambridge University Press, Vol. II. 1881 - 1887, 626 pp. Citation from page 447.

Ritsema, J., van Heijst, H. J., & Woodhouse, J. H., 2004. Global transition zone tomography. J. Geophys. Res., 109: B02302.

Ritzwoller, M. H., Barmin, M. P., Villasenor, A., Levshin, A. L., & Engdahl, E. R., 2002. Pn and Sn tomography across Eurasia to improve regional seismic event locations. Tectonophysics 358: 39–55.

Romanowicz, B. & Dziewonski, A., 2009. Seismology and Structure of the Earth. Treatise Geophys. 1, 872.

Rost, S. & Thomas, C., 2002. Array Seismology, Reviews of Geophysics.

Sato, Y., 1955. Analysis of Dispersed Surface Waves by means of Fourier Transform I. Bulletin of the Earthquake Research Institute 33, 33 - 47.

Shearer, P. M., 2009. Introduction to seismology, Cambridge University Press.

Sieminski, A., Leveque, J. J. & Debayle, E., 2004. Can finite-frequency effects be accounted for in ray theory surface wave tomography? Geophys. Res. Lett. 31, 1 - 4.

Silvennoinen, H., Kozlovskaya, E., Kissling, E., Kosarev, G., and POLENET/LAPNET working group, 2014. A new Moho boundary map for northern Fennoscandian shield based on combined controlled-source seismic and receiver function data, Geophys. Res. J., 19 - 32.

Simmons, N. A., Forte, A. M., Boschi, L., & Grand, S. P., 2010. GyPSuM: A joint tomographic model of mantle density and seismic wave speeds, J. Geophys. Res., Solid Earth, 115(B12).

Smith, M.L. & Dahlen, F.A., 1973. Azimuthal dependence of Love and Rayleigh wave propagation in a slightly anisotropic medium, J. geophys. Res., 78, 3321 - 3333.

Soomro, R., Weidle, C., Cristiano, L., Lebedev, S., Meier, T., & Group, P. W., 2016. Phase velocities of Rayleigh and Love waves in central and northern Europe from automated, broad-band, interstation measurements. Geophys. J. Int. 204, 517 - 534.

Spakman, W. & Nolet, G. 1988. Imaging algorithms: Accuracy and resolution in delay time tomography. In: Vlaar NJ, Nolet G, Wortel M, and Cloetingh S (eds.) Mathematical Geophysics: A Survey of Recent Developments in Seismology and Geodynamics, pp. 155–188. Dordrecht, The Netherlands: D Reidel.

Stoneley, R. 1932. The transmission of Rayleigh waves in a heterogeneous medium. Geophysical Supplements to the Monthly Notices of the Royal Astronomical Society 3, 222-232.

Thomson, W. T., 1950. Transmission of elastic waves through a stratified solid medium. Journal of Applied Physics 21 (2), 89 - 93.

Trampert, J. & Woodhouse, J.H., 1995. Global phase velocity maps of Love and Rayleigh waves between 40 and 150 s period, Geophys. J. Int., 122, 675 - 690.

Trampert J and Woodhouse JH (2003) Global anisotropic phase velocity maps for fundamental surface waves between 40 and 150s. Geophys. J. Int., 154, 154 - 167.

Wang, Z. & Dahlen, F. A., 1995. Validity of surface-wave ray theory on a laterally heterogeneous earth, Geophys. J. Int., 123(3), 757 - 773.

Weidle, C., Soomro, R. A., Cristiano, L. & Meier, T., 2013. Identification of response and timing issues at permanent European broadband stations from automated data analysis. Adv. Geosci. 36, 21 - 25.

Wielandt, E., 1993. Propagation and structural interpretation of non-plane waves, Geophysical Journal International, 113, 45 - 53.

van der Lee, S. & Nolet, G., 1997. Upper mantle S velocity structure of North America. J. Geophys. Res., 102, 22815 - 22838.

Vinh, P. C. & N. T. K. Linh, 2013. An approximate secular equation of generalized Rayleigh waves in pre-stressed compressible elastic solids. International Journal of Non-Linear Mechanics 50, 91–9

Yang, Y., Ritzwoller, M. H., Lin, F.-C., Moschetti, M., & Shapiro, N. M., 2008. Structure of the crust and uppermost mantle beneath the western United States revealed by

ambient noise and earthquake tomography, Journal of Geophysical Research: Solid Earth, 1978 - 2012, 113(B12).

Yanovskaya, T. B. & Ditmar, P. G., 1990. Smoothness criteria in surface wave tomography. Geophys. J. Int. 102, 63 - 72.

Yao, H., Van Der Hilst, R. D., & De Hoop, M. V., 2006. Surface-wave array tomography in SE Tibet from ambient seismic noise and two-station analysis i. phase velocity maps, Geophysical Journal International, 166(2), 732 - 744.

Yoshizawa, K. & Kennett, B. L. N., 2002. Determination of the in uence zone for surface wave paths. Earth 440 - 453.

Zhang, X., Paulssen, H., Lebedev, S., & Meier, T., 2007. Surface wave tomography of the Gulf of California, Geophys. Res. Lett., 34(15), L15305.

Zhu, H., Bozdag, E., Peter, D. & Tromp, J., 2012. Structure of the European upper mantle revealed by adjoint tomography. Nat. Geosci. 5, 493 - 498.

Chapter 3

Structure of the Crust and Mantle lithosphere of the Eastern Mediterranean from Surface Wave Tomography

3.1 Introduction

Since the early Mesozoic breakup of Gondwana, the Eastern Mediterranean witnessed an highly complicated tectonic history. The Cenozoic closure of the Tethys ocean and the following convergence between the relatively stable African and Eurasian plates, relatively small oceanic basins, in addition to the continent-continent collision between the northward-moving Arabian and Eurasian plates are shaping the present-day stress field and tectonic setting in that region (Taymaz *et al.* 2004; Faccenna *et al.* 2014). It represents a key region for investigating the fundamental tectonic processes, including continental rifting, passive margins, subduction, back-arc spreading, accretion, collision and post-collisional exhumation (Le Pichon & Angelier 1979; Jackson & Mckenzie 1984; Spakman *et al.* 1988; Westaway 1994; Barka & Reilinger 1997; Jolivet & Faccenna 2000; McClusky *et al.* 2000; Doglioni *et al.* 2002; Piromallo & Morelli 2003; Dilek 2006; Reilinger *et al.* 2006). The geological record of the eastern Mediterranean reveals the presence of variety of different tectonic units and comprises a zone of transition from the oceanic domain in Ionian sea to thinned or highly deformed continental domain in the Levant basin, known as the site of rifting (Garfunkel *et al.* 2006; Jolivet *et al.* 2009). Figure (3.1) shows a map of the Eastern Mediter-

ranean region with the age distribution of the oceanic lithospheric domains in the region (Müller *et al.* 2008). The black lines indicate the main tectonic lines in the area (Faccenna *et al.* 2014).

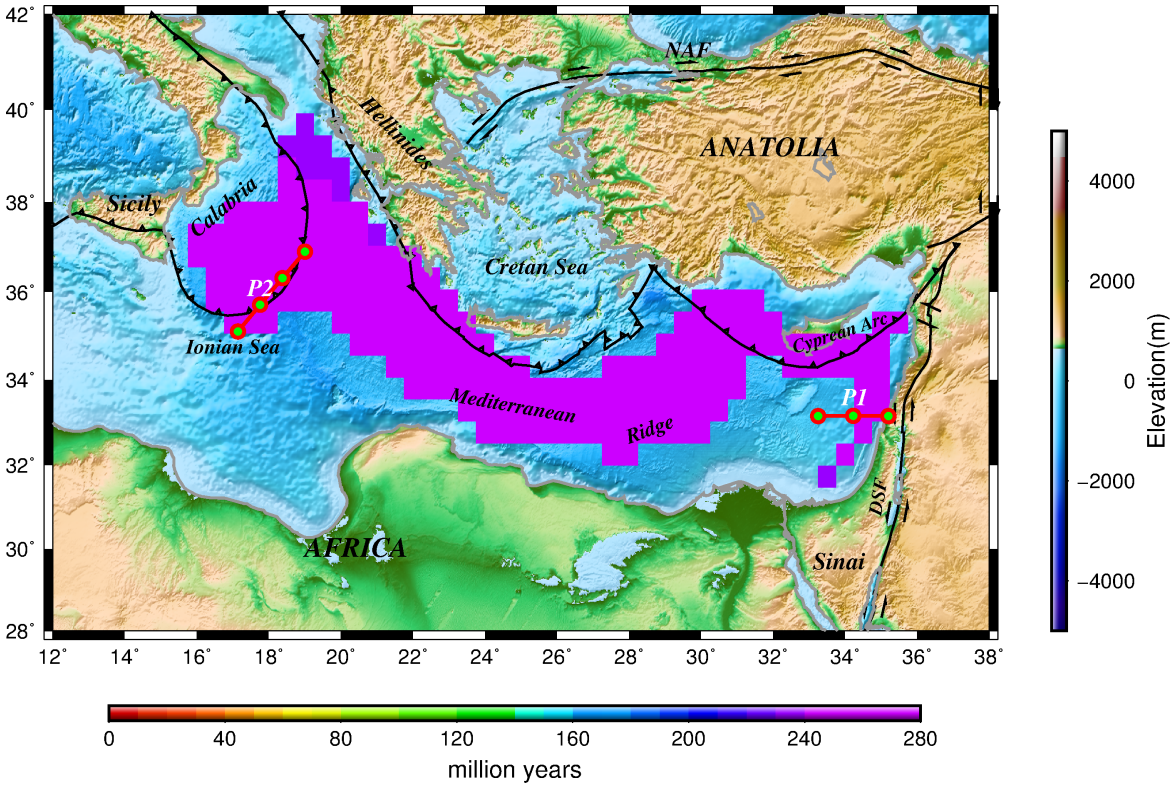

Fig. 3.1 Topographic and bathymetric map of the Eastern Mediterranean region with the age distribution of the oceanic lithosphere in the region after Müller *et al.* (2008). The black lines show the main tectonic lines in the area modified after Faccenna *et al.* 2014. The dotted red lines showing the location of two refraction profiles at the Ionian and the Levant basins.

According to Bigi *et al.* (1989), the Ionian sea is surrounded by a variety of geodynamic settings and separating two continenal blocks; the Apulian block towards the north and the Malta escarpment from the southwest (Boccaletti *et al.* 1984). The exact nature of the Ionian lithosphere has been the topic of much debate being interpreted either as a relic of oceanic crust (Biju-Duval *et al.* 1977; Vai 1994) or as thinned continental crust (Giese *et al.* 1982). Several geophysical studies on the Ionian sea have been performed during the last three decades (Hinz 1973; Panza & Müller 1979; Farrugia & Panza 1981; Makris 1981; Calcagnile *et al.* 1982; Finetti 1982, 1985; Makris *et al.* 1983, 1986; Morelli 1985; Leister *et al.* 1986; Ferrucci *et al.* 1991; de Voogd *et al.* 1992; Cernobori *et al.* 1996; Piromallo & Morelli 1997; Cataloni *et al.* 2001). Using surface wave dispersion measurements and heat flow, Farrugia and Panza (1981) suggested the Ionian sea is floored by a continental

crust relying on the overall estimated thickness of the crust (ca. 20 km). On contrary, and based on seismic refracation profiling, de Voogd *et al.* (1992) showed a relatively thin crust (8-11 km) underneath the Ionian sea overlain by a thick pile of sediments (up to 10 km), which contributed substantially to unravel the debated nature of the lower crust of the Eastern Mediterranean basins. The oceanic nature of the Ionian crust as well as its Permo-Triassic age has been suggested by Stampfli *et al.* (2001) based on seismostratigraphic results.

The Ionian lithosphere is subducting beneath the Calabrian arc to the northwest as a response to the Africa-Eurasia convergence in addition to a retreat of the Calabrian arc towards Africa (Finetti 1982; Cristofolini *et al.* 1985; Mele 1998; Chamot-Rooke *et al.* 2005; Minelli & Faccenna 2010). This invoked the formation of the associated accretionary wedge with its thick pile of sediments (Finetti 1982; Doglioni *et al.* 1999). The oceanic nature of the Ionian crust has been also proposed by seismic tomography (e.g. Di Luccio & Pasyanos 2007) and gravity modelling constrained by seismic data (Makris & Yegorova 2006).

On the other hand, the nature of the crust comprising the southeastern part of the eastern Mediterranean (Levant basin: fragment of crust between the Levant margin and the Eratosthenes seamount) has been also a subject of controversy over the last decades. One of the major uncertainties regarding the Levant basin concerns its deep crustal configuration and the nature of its crust despite the numerous studies that have been perfomed to deeply investigate this region. It has been proposed to be oceanic (Khair & Tsokas 1999; Ben-Avraham *et al.* 2002) or thin continental crust (Netzeband *et al.* 2006; Di Luccio & Pasyanos, 2007). As recently summarized by Ghalayini *et al.* (2014) the Levant Basin formed during the Late Paleozoic to Mesozoic in the course of the breakup of Gondwana (Ben-Avraham *et al.* 2002; Garfunkel & Derin 1984; Robertson 1998).The NW-SE directed extension caused several NE-SW striking Mesozoic normal faults perpendicular to the rift (Gardosh *et al.* 2010; Montadert *et al.* 2013). Most data based studies conclude on the presence of highly deformed continental crust in the central basin (Netzeband *et al.* 2006a; Longacre *et al.* 2007; Halstenberg 2014; among others).

During the Late Cretaceous, the northward drift of the African plate closed the Neo-Tethys ocean (Stampfli & Hochard 2009; Frizon de Lamotte *et al.* 2011), causing compression of the Levant basin and the passive margin. Recently, Gardosh and Druckman (2006) suggested an extended continental crust in the Levant basin, whereas Gallais *et al.* (2011) documented in detail the structure of the old oceanic crust in the Ionian sea. As a consequence of compression of the Levant basin, the Syrian Arc, an arcuate fold belt developed in Palmyra, Palestine, and Sinai during two main episodes by inverting Early Mesozoic extensional faults

(Druckman 1981; Hempton 1987; Best *et al.* 1993; Druckman *et al.* 1995; Moustafa & Khalil 1994; Eyal 1996; Walley 1998). Arabia separated from Africa in the Oligocene to early Miocene, resulting in the establishment of a new plate boundary along the Red sea and the Dead sea Transform (Le Pichon & Gaulier 1988).

The Dead sea Transform represents a 1000 km long, left-lateral transform system (Weber *et al.* 2004, and references there in). Among others, the basin fill deposits of the Levant Basin has been summarized by Garfunkel (1998), Breman (2006), Gardosh *et al.* (2008) and Steinberg *et al.* (2011). Above the basement, the depositional sequences are identified as Cretaceous-Jurassic, Paleogene-Neogene, Messinian, and Pliocene-Holocene (Aal *et al.* 2001). Ben-Avraham *et al.* (2002) have interpreted the Cretaceous-Jurassic unit above the basement as a carbonate sequence. During the Late Eocene, deposition of carbonates ceased and siliciclastic deposition started. A ca. 6 km thick sediment succession accumulated within 37 Ma. Late Miocene reduction in water exchange between the Atlantic Ocean and the Mediterranean sea initiated the Messinian Salinity Crisis at 5.96 Ma (Roveri *et al.* 2014)). During this period up to 2 km of evaporites were deposited in the Levant Basin, until the Messinian Salinity Crisis was terminated by a short period of rapid Early Pliocene reflooding at 5.33Ma (Krijgsman *et al.* 1999; Netzeband *et al.* 2006b).

Plenty of studies indicated that the eastern Mediterranean is of a Late Triassic or Early Jurassic opening (Garfunkel & Derin 1984; Sengor *et al.* 1984; Robertson *et al.* 1996). Rheological properties of the upper mantle play a role in the dynamics of the lithosphere and asthenosphere. The lithosphere is the mechanically hard and rigid outermost layer of the Earth that comprises the light, dry, chemically depleted, compositionally buoyant crust and the uppermost mantle layer. It represents the portion of the thermal boundary layer in which heat transfer is conductive, where as further down, convection currents are mainly driving the heat transfer within the hot, mechanically weak, hydrated, fertile asthenosphere (sublithospheric mantle).

Underneath the oceans, the thermal evolution of the lithosphere seems to be straightforward as it cools with continuous increase in thickness far away from the mid-oceanic ridges, as imaged clearly by different tomographic models (e.g., Schäffer & Lebedev 2013; Becker *et al.* 2014; Schäffer *et al.* 2016). There is no doupt that the low temperatures at shallow depth within the Earth are important for inceasing the lithospheric strength, which has the potential to soliciate initiating and developing different tectonic processes in addition to controlling the seismicity distribution.

The thickness of the oceanic lithosphere is a highly controversial issue in the sense whether it reaches a maximum thickness ($\sim 100km$) after 80 Ma as proposed by the thermal

plate cooling model or whether it thickens continuously with age according to the half-space cooling model (e.g., Davis & Lister 1974; McKenzie *et al.* 2005). Recent tomographic models show that the shear velocities of the oceanic lithosphere at depth evolve with the age of the seafloor following the half-space cooling models (Becker *et al.* 2014; Schäffer *et al.* 2016), however the flattening of the bathymetry of the old oceans as well as the heat flow reduction that depend on the age of the lithosphere (Levshin *et al.* 2001) are both arguments for the thermal plate cooling model (e.g., Stein & Stein, 1992, 2015).

The oldest ocean floor within the current major oceans is of Jurassic age and located in the western Pacific (around 180 Ma), whereas the oldest preserved in-situ oceanic crust may be a remnant of the Neotethys ocean beneath the Ionian sea, still only Triassic in age (230 - 270 Ma, Müller *et al.* 2008) and the east Mediterranean basin (340 Ma, Granot 2016). The nature, thickness and distribution of oceanic and continental crustal units in the eastern Mediterranean have been studied intensively and have major implications for the tectonic evolution of this region, however they are still far from being completely tacit. Determining whether the crust is continental or oceanic and properties of the mantle lithosphere are crucial for reconstruction of the Neo-Tethys opening and to understand the evolution of the Mediterranean dynamics. Investigating the crustal and upper mantle structure of the eastern Mediterranean including the Levant Basin and Ionian sea has been the purpose of numerous studies. Different geophysical techniques have been applied including seismic tomography to calculate the depth to the Moho and to map shear wave velocity in different locations in this region (e.g., Li *et al.* 2003; Marone *et al.* 2003; van der Mejide *et al.* 2003; Zor *et al.* 2003; Endrun *et al.* 2004; Hofstetter & Bock 2004; Meier *et al.* 2004; Tirel *et al.* 2004; Al-Damegh *et al.* 2005; Karagianni *et al.* 2005; Koulakov & Sobolev 2005; Makris & Yegorova 2005; Mohsen *et al.* 2005; Zhu *et al.* 2006; Luccio & Pasyanos 2007; Calo *et al.* 2012).

In this chapter, we present a high resolution surface wave tomography of the lithosphere and asthenospheric structure underneath the Ionian sea and the Levant basin. The dispersive properties of surface waves in a joint interpretation with local seismic refraction profiling are used to deduce the crustal thickness as well as the depth to lithosphere-asthenosphere boundary underneath both locations. The P-wave refraction profiles are used to constrain the inversion of the dispersion curves to 1-D velocity structure as function of depth. Then, the V_p/V_s ratio is utilized as a proxy to provide insights on the nature of the crust underlying the the eastern Mediterranean basin as well as thickness of its lithosphere.

3.2 Seismic refraction data

The nature of the crust underneath the Levant basin has been investigated and discussed since decades. A first refraction seismic experiment has been carried out in 1978 (Makris *et al.* 1983). The crustal model, interpreted and discussed in detail by Ginzburg and Ben-Avraham (1987) and Garfunkel (1998), showed a lower crust of 17 km thickness beneath Cyprus, thinning to 10 km towards Palestine. The upper crust is missing in the central Levant Basin, which has been taken as evidence for oceanic crust by these authors. Ben-Avraham *et al.* (2002) reported from another amphibian refraction experiment in 1989, which included one northern profile between the Eratosthenes seamount (ESM) and Palestine and one southern profile perpendicular to the southern Palestinian coast. The resulting crustal model refined the model by Makris *et al.* (1983) in some points, however, the basic model of an about 10 km thick oceanic crust overlain by 10-14 km of sediments was maintained. The last marine refraction/wide-angle experiment across the Levant Basin was carried out in 2002 (Hübscher *et al.* 2003). Two seismic refraction lines were acquired, approximately along the lines measured by Ben-Avraham *et al.* (2002). The data allowed a major refinement of the crustal structure. Modelling and inversion showed that the crystalline basement in the Levantine Basin consists of two layers with a P-wave velocity of 6.0 - 6.4 km/s in the upper and 6.5 - 6.9 km/s in the lower crust (Fig. 3.2a). Towards the center of the basin the Moho depth decreases from 27 to 22 km (Netzeband *et al.* 2006a).

On the other hand, plenty of seismic reflection and refraction studies have been performed to investigate the Ionian sea and the adjacent crystalline basement (Finetti 1982; Makris *et al.* 1986; de Voogd *et al.* 1992; Catalano *et al.* 2001; Chamot-Rooke *et al.* 2005). The model by de Voogd *et al.* (1992)suggested an oceanic crust of the Ionian sea with thickness of $\sim$ 8-9 km and $\sim$ 6-8 km of sedimentary cover of Mesozoic and Tertiary age. They concluded that the thickness of the entire crust is $\sim$ 17-19 km. Catalano *et al.* (2001) interpreted the top of the oceanic crust in their models at about 6.5-8.0 s two-way time. This was refined by a later wide-angle refraction seismic experiment in 2014 (Kopp *et al.* 2015), acquiring a seismic line above the Ionian Abyssal Plain (IAP) (Dannowski *et al.* in prep for JGR). The resulting velocity model (Fig. 3.2b) shows a 2.5 km thick upper crust with seismic velocities of 5.1 km/s to 6.4 km/s and a lower crust with velocities of 6.4 km/s to 7.2 km/s and a thickness of 4.5 km at the central part of the IAP. The crust is overlain by a 4 km thick pile of sediments.

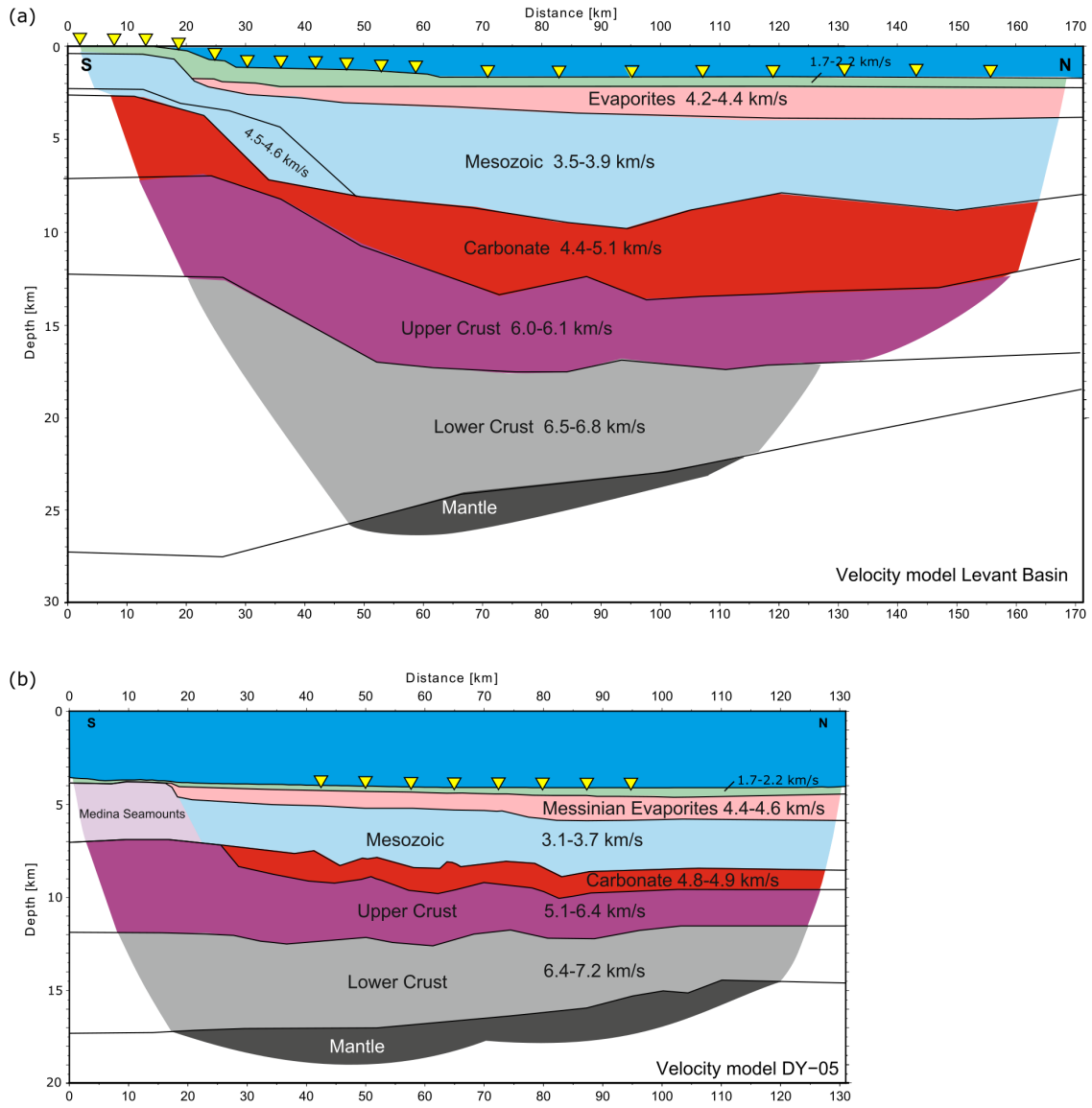

Fig. 3.2 P-wave velocity models of a) the Levant Basin and b) the Ionian sea. Velocities (in km/s) are indicated on the different color-coded layers. Thick black lines represent layer boundaries. Triangles mark positions of the recording hydrophones.

3.3 Surface wave tomography

Surface-wave tomography is based on the frequency-dependent surface wave velocities in a dispersive medium. High quality waveforms give us the possibility to retrieve such dispersion charcteristics (phase or group velocities) that can be inverted into the shear-wave seismic structure. Fundamental mode surface wave phase velocities are essential observables for the study of the Earth's lithosphere and sublithospheric mantle as they can be measured

with high accuracy over a broad period range which covers sensitivity from the shallow crust ($\leq$ 20 km, $\sim$ 10 s period) to asthenospheric depths ($\geq$ 300 km, $\sim$ 250 s period) and their particular sensitivity to vertical variations of shear wave velocity, and therfore largely avoiding vertical smearing effects often associated with body wave tomographic measurements. Recently, El-Sharkawy *et al.* (in prep.) have applied a newly elaborated algorithm for the automated inter-station phase velocity measurements to obtain Rayleigh fundamental mode phase velocities (Meier*et al.* 2004; Soomro *et al.* 2016). More than 3.5 millions of waveform in the time period from 1990 - 2015 recorded by $\sim$ 4500 broadband seismic stations within the Europe and the Mediterranean region are included in the anaylsis. Moreover, for the first time, data from the Egyptian National Seismological Network (ENSN), recorded by up to 25 broad band seismic stations, are also included in order to maximize the ray path coverage in the Eastern Mediterranean region. For each station pair, approximately located on the same great circle path, the recorded waveforms are cross correlated and the dispersion curves of fundamental modes are calculated from the phase difference of the cross correlation functions weighted in the time-frequency plane. After selection of smooth and reliable phase velocity curves with path-wise averaging we obtained a dataset of $\sim$ 200,000 inter-station Rayleigh wave phase velocity dispersion curves with an average standard error 0.5 % in a very broad period range (8 - 350 seconds). From these accurate measurements we calculated a new high resolution different period-dependent isotropic 2-D Rayleigh wave phase velocity maps across the Eastern Mediterranean in the period range between 8 and 350 s. Four examples of the phase velocity maps are shown in figure (3.3). All maps are represented as perturbations from the average reference phase velocity indicated on each map.

The 15 s Rayleigh phase velocity map is predominantly sensitive to the middle and lower crust, with an expected effect of the strong anomalies in the upper crust to overprint the maps, taking into account the sensitivity of surface wave to wide range of depths (Lebedev *et al.* 2013). This is clearly visible in figure (3.3a), where the deep sedimentary cover of the accretionary prism beneath Calabria and the Ionian sea is expressed by low seismic velocities. Generally a widespread low velocity anomalies are dominating the entire eastern Mediterranean at short periods. High velocity anomaly has been detected beneath the Aegean reflecting its shallow crustal thickness. A small but interesting features are sharp contrasts in the velocity amplitudes along the straits of messina, east of Sicily towards the Ionian sea and from the Levant basin towards the Eratothenes seamount. Figure (3.3b) shows the 30 s map which is sensitive to the Moho topography, the lower crustal velocities and velocities of the mantle lithosphere depending on the crustal thickness (Lippitsch *et al.* 2003; Panza & Raykova, 2008). Slow velocity anomalies underneath the Hellenides, Crete, Cyprus and

Anatolia. This indicates the deep crustal roots and the highly deformed regions within the Eastern Mediterranean. In western Anatolia recent receiver function measurements, showing an average crust ranging from 25 to 30 km (Karabulut *et al.* 2013; Vanacore *et al.* 2013). Moreover, another extremely low velocity anomaly is also observed beneath the eastern Anatolia, a typical observation that is evident in areas of thick continental crustal structure and correlates very well with the high elevation plateau along the Eastern Anatolia Accretionary Complex. Additionally, we also observed a wide spread fast anomalies beneath northern Africa and the Ionian sea.

In figure (3.3c) we present the 60 s phase velocity map which is dominantly sensitive to variations in shear wave velocity at mantle lithospheric depths (80 - 120 km) at which it is more heterogeneous at those depths. Continuous high velocity anomaly prevails from southern Aegean sea (Hellenic subduction) to western Greece that is highly consistent with the results obtained by Li *et al.* (2008), and is commonly interpreted as the subducted African lithosphere (Wortel & Spakman 2000). This high velocity anomaly extends towards the Ionian sea indicating the oceanic nature of its lithosphere. At period larger than 60 s, a high velocity anomaly north of Cyprus has been detected and interpreted as northward dipping African lithosphere subducted from the Cyprus trench. Away from the subduction zones, we also find an extended upper mantle low-velocity anomaly occupying Anatolia that is correlates very well with the distribution of the Cenozoic volcanism and the magmatic nature of this area reflecting its shallow asthenosphere as also shown in previous studies (Marone *et al.* 2003; Meier *et al.* 2004; Gok *et al.* 2006). At 100 s period map (Fig. 3.3d), low velocities are extended beneath Anatolia, whereas a relatively high velocity anomalies have been encountered north of the north anatolian fault representing the thick continental mantle lithosphere of Eurasia. The African subducted lithosphere is still clearly seen as a dominant high velocity anomaly beneath the Hellenic Arc. The Ionian subducted slab beneath Calabria can be traced as a narrow belt of high velocity anomaly trending SW-NE that is highly correlated with the seismicity at those depths (Zhu *et al.* 2012). A clear separation between lower phase velocities southern Sicily from higher phase velocities beneath the Ionian sea along the Malta escarpment, where a transition from continental lithosphere to oceanic lithosphere is expected. On contrary we observe a sharp change in the velocity from the Levant basin towards the west underneath the Eratothene seamount and the Herodoutus basin.

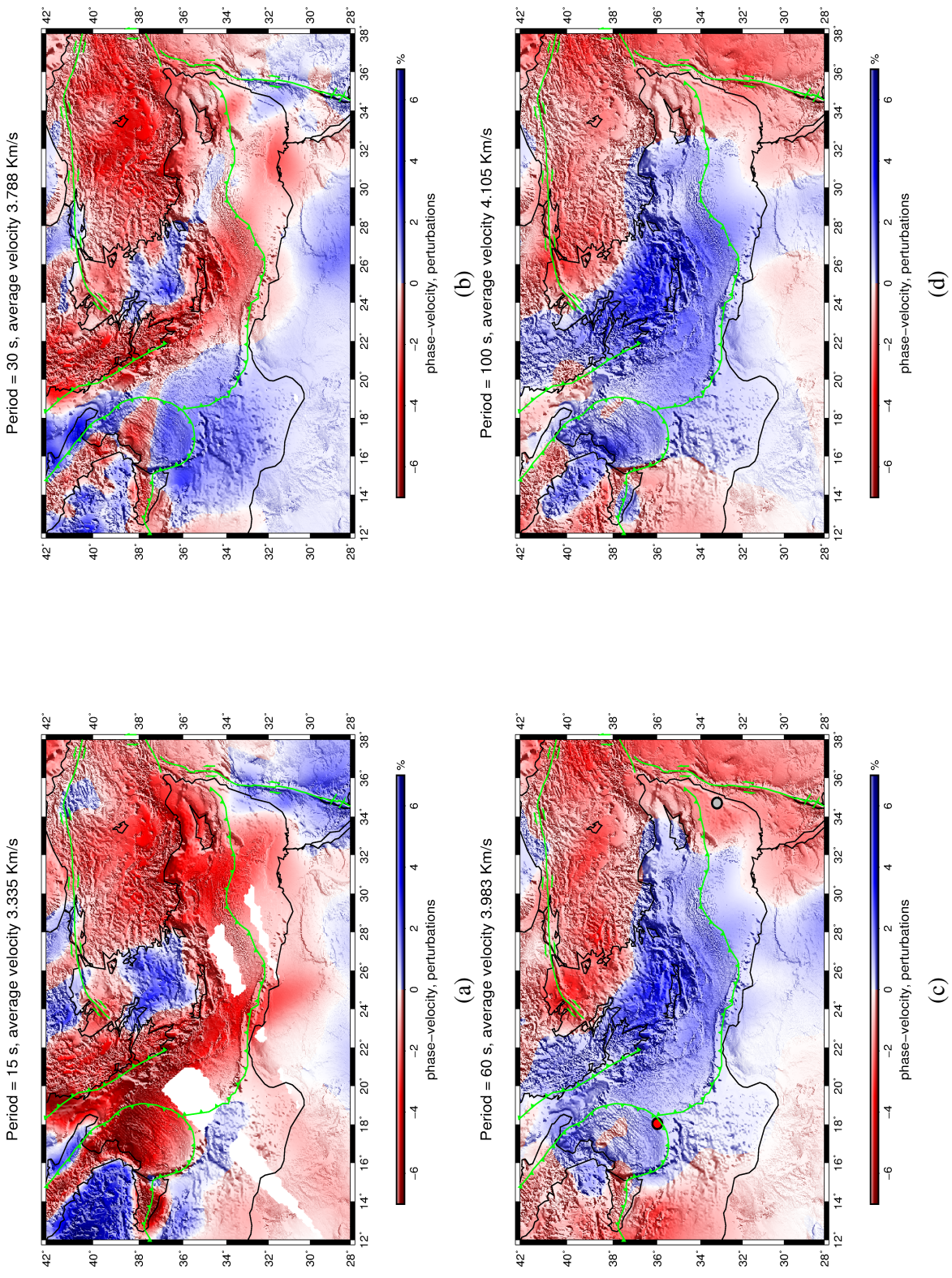

Fig. 3.3 Isotropic Rayleigh wave phase velocity maps underneath the Eastern Mediterranean at periods of (a) 15, (b) 30, (c) 60 and (d) 100 seconds. The red and gray circles show the location of the local dispersion curves at the Ionian and Levant basins, respectively.

3.4 Inversion for shear velocity structure as a function of depth

In order to relate the frequency-dependent phase velocities more quantitatively to shear-wave velocities at depth we invert the average local dispersion curves for 1-D velocity models as function of depth underneath the Ionian sea and the Levant basin. The local average phase-velocity dispersion curves are constructed from phase velocity maps at 100 different periods sampling the period range 8 - 350 s. Phase velocity measurements in such period ranges can resolve shear velocity structure from the lower crust down to the lithosphere and asthenosphere. The locations of the local dispersion curves are indicated as red (Ionian) and gray (Levant) circles on figure (3.3c). The constructed phase-velocity curves are plotted on top of each other (Fig. 3.4) in a comparison with a global reference model (PREM, Dziewonski & Anderson 1981). The strong variability in phase velocities at short periods below about 20 s is due to the influence of crustal properties on the dispersion curves.

At both locations, low phase velocities are caused by large thicknesses of the existing sedimentary basins. Between about 20 s and 200 s phase velocities are sensitive to properties of the mantle lithosphere and asthenosphere. Phase velocities of the Ionian sea (red) are anomalously higher than those in the Levant basin (gray) where it shows very low velocities in this frequency range. These two representative dispersion curves have been selected where data from seismic refraction measurements are available, in an effort to constrain the inversion of the dispersion measurements and minimizing the trade-offs between the different structural parameters by including accurate information about the crustal velocities and the Moho depth.

Shear velocities are sensitive to temperature and composition of the Earth's internal structure at depth. We invert Rayleigh wave dispersion curves for the vertically polarized shear wave velocity models. The relation between dispersion measurements of the surface waves and the velocity model of the Earth's interior is nonlinear (Levshin *et al.* 2001). There are two common ways to overcome the nonlinearity problem. Either to use waveform fitting by linearizing the relation between the velocity model and the recorded waveforms and iteratively the model is calculated (e.g. Snieder 1988; Nolet 1990) or by inverting the previously calculated measurements of surface wave dispersions individually for 1-D shear wave velocity model using diffferent approaches (Meier *et al.* 2004; Lebedev *et al.* 2006; Endrun *et al.* 2008). The second approach is followed here in which the Particle Swarm Optimization (PSO) algorithm is applied to invert the phase velocity curves to 1-D velocity models as function of depth.

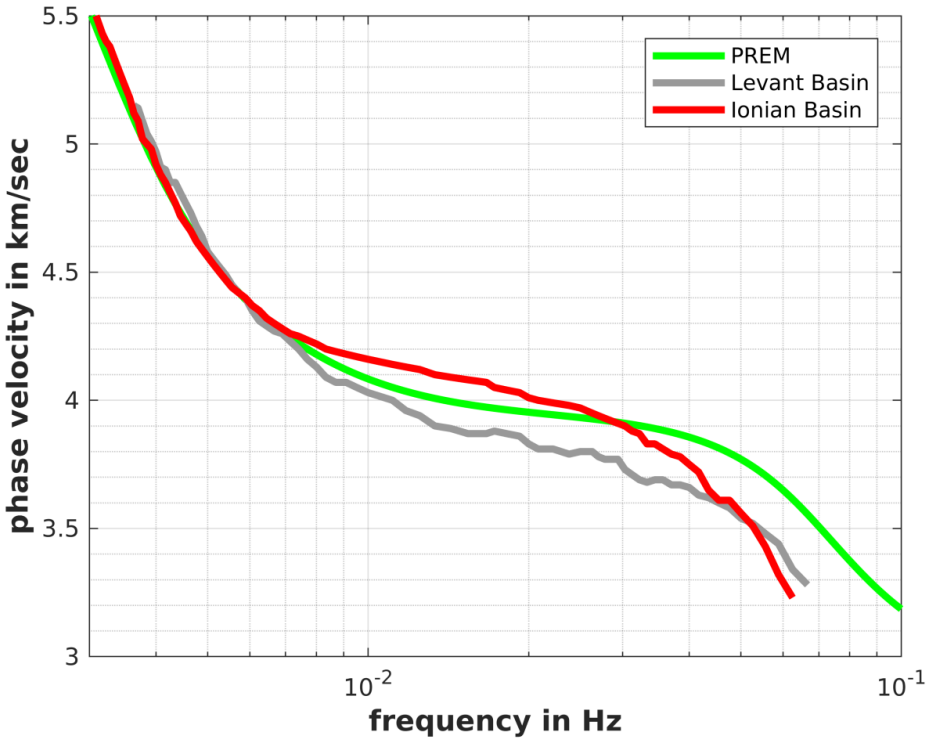

Fig. 3.4 Local dispersion curves assembled from phase velocity maps at several periods in comparison to a global average model. Red, gray and green curves represent the Ionian sea, the Levant Basin and PREM, respectively.

3.4.1 Particle Swarm Optimization algorithm

In 1995, Eberhart and Kennedy developed this algorithm which is a stochastic global optimization algorithm inspired by the social behavior of bird flocking or fish schooling (Kennedy & Eberhart 1995). Generally, a swarm is made up of multiple artificial members, each is called particle. These particles can exchange heuristic information in the form of local interaction. Such interaction, in addition to certain stochastic elements, generates the behavior of adaptive search, and finally leads to global optimization (Eberhart *et al.* 2001; Xie *et al.* 2002; Parsopoulos *et al.* 2004). The basis of this algorithm is a group of particles called a swarm, which are vectors in the parameter space. These particles are able to move within the boundaries of the parameter space in order to fully explore it. The particle movement has three components: cognitive, social and dynamic. They hold the main idea of a swarm behaviour. According to Engelbrecht *et al.* (2005), the movement of a particle is defined by adding a velocity vector to the particle current position. This velocity vector includes the three movement components: a *"cognitive"* component carries out the individual experience

of the particles, the *"social"* component bears shared information of the swarm's particles and the *"dynamic"* component holds information about the previous movement of the particles. The cognitive component means that each single particle remembers the position at which it has reached its best objective function value so far. The social component implies that all particles know the position where one of them has found the global best position so far. Each particle tries to move in these both directions, having its previous collected information, i.e. dynamic component (Wilken & Rabbel *et al.* 2012). In other words, each particle in the swarm adjusts its position in the search space based on the best position it has found so far as well as the position of the known best-fit particle of the entire swarm and finally converges to the global best position in the whole search space.

The search in the parameter space is done by employing a specific number of particles N called the swarm size. Assuming that the problem dimension D (where j = 1, 2,... D), each particle i (i = 1, 2, .., N) in the swarm is characterized by its current position X_i , current velocity V_i and local best position $Lbest$. The global best position that has been found in the search space since the start of the evolution is denoted by $Gbest$. During each of the iterations, the position and the velocity of every particle are updated according to these two parameters. This can be formulated as following:

$$V_{i,j}^{k+1} = \omega V_{i,j}^{k} + c_1 r_1 (Lbest_{i,j}^{k}) + c_2 r_2 (Gbest_{j}^{k} - X_{i,j}^{k}) \tag{3.1}$$

$$X_{i,j}^{k+1} = X_{i,j}^{k} + V_{i,j}^{k+1} \tag{3.2}$$

The c_1 and c_2 are non-negative constants representing the learning factors. The r_1 and r_2 are random uniformly distributed numbers in the interval (0, 1). The parameter ω is a constant used to balance the local and the global search in the parameter space. The term $(Lbest_{i,j}^{k})$ represents personal best j^{th} component of i^{th} particle, whereas $Gbest_{j}^{k}$ represents j^{th} component of the best particle of the entire population upto iteration k. The second term of eq. (3.1) is the cognitive component in the direction of the particle best position which is subjected to be modified if a better position is acheived (Engelbrecht 2005). This term together with the first term are responsible for triggering the exploration of the parameter space. On the other hand, the third term represents the social component providing a movement in the direction of the global best position of the entire swarm. This term enables the local convergence of the swarm. In general, the PSO is implemented as following:
(i) randomly initialize a population of particles and evaluate the misfit,
(ii) calculate the local best position of each particle for first iteration k = 0,
(iii) determine the global best position of the swarm,

(iv) adjust all particles according to eq. (3.1),
(v) perform the local search,
(vi) check stopping-criterion and go to step (ii).

The basic aspect of inverting the dispersion measurements to 1-D shear velocity models using the Particle Swarm Optimization (Eberhart & Kennedy 1995) is to select models randomly and to retain the subset of models that fit our selection criteria. Examples of these criteria are the fitting between the measured and the synthetic data (rms misfit) and *a priori* information that defines a reasonable parameter space to be searched and consequently it defines a plausible final model. The inversion results in abundle of acceptable models whose variability provides some information about model uncertainties. It is worthy mentinoning that the uncertainty estimates depend strongly on the model parameterization and also on the choice of the selection crieteria. On the other hand, this algorithm allows for over-parametrization of the model which may be useful to assess how the trade-offs between different model parameters that affect the range of the acceptable models.

3.4.2 Parameterization and *a priori* information

In general, inverting the fundamental mode dispersion curves does not provide a unique solution and the choice of the parameterization (number of layers, range of velocity perturbations, and thickness of layers, perturbation order) is of substantial significance for obtaining reliable results. In other words, the model parametrization highly affects the final model and it's uncertainties, which both depend on the width of the search space considered in the inversion (Shapiro & Ritzwoller 2002). For weakly constrained inversion, large number of the resulted models will fit the data and consequently large uncertainties will be obtained, whereas conservative constraints on the model space will result in overall reduction of the uncertainties, but the model will be sensitive to systematic errors of the data and noise. With intense testing, we developed a strategy to parametrize our inversion procedure by constraining each model parameter individually. For our inversion, we construct a range of possible models by defining the $(\pm)$ maximum perturbations of the shear wave velocity of the background model for each individual layer. The background model is only used as *a priori* information to define the boundaries of the parameter space. The inaccurate background model leads to large trade-offs between the crustal and upper mantle velocities.

Therefore, an accuarte background model will be highly useful for obtaining reliable measurements. In this regard, and more specifically in case of both the Ionian sea and Levant Basin, where seismic refraction data are available, we calculated specific and more

constrained 1-D background models of the crust and upper mantle that includes a water layer where appropriate, bathymetry, accurate Moho depth, variations in the V_s and vV_p in the sediments and crystalline crust from the refraction data (Netzband *et al.* 2006; Dannowiski *et al. in prep.*). Shear velocities in the mantle are taken from PREM (Dziewonski & Anderson 1981). Each model consists of a large number of fine layers representing the considered depth range for the inversion. Each i^{th} layer is characterized by the P-wave velocity, S-wave velocity, the density and the layer thickness. These models take into account the first order structural variations to which surface wave dispersion are strongly sensitive, primarily to Moho depth or the presence of sedimentary basins.

For both locations, we used a uniform inversion parametrization. The only difference between them is the number of layers in the crust. The definition of the crustal layers is based on the seismic refraction results. For the Ionian sea, three crustal layers are considered including a sedimentary layer, whereas five layers are considered for the Levant basin including also one sedimentary layer. The discontinuities in the crust are kept fixed with a constant velocity perturbation. The Moho depth is a parameter of the inversion. We constrain the depth of the Moho to be varied within $\pm$ 10 km of the initial model. In the upper mantle, a cubic perturbation in the shear wave velocity is considered from the Moho down to the 410 km discontinuity. A quadratic perturbation for the mantle transition zone followed by another linear perturbation below the 660 km discontinuity down to depth of 900 km. The 410 and 660 km discontinuities are kept fixed.

A graphical representation of the model parameterization of the Ionian's crust, the Levant's crust and the upper mantle structure for both are shown in figures (3.5a), (3.5b) and (3.5c), respectively. The dots show the depth nodes where fixed discontinuities are considered with variables velocities, whereas white horizontal bars show the locations of the depth nodes where the discontinuities are to be varied. Black line shows constant perturbations, green line represents linear gradient order of perturbations, red line shows the depth range where the velocity perturbation order is cubic, and blue line represent the depth range where quadratic variations of the velocity is considered. Tables (3.1) and (3.2) summerize the developed strategy for parameterizing the inversion of the dispersion curves using the particle swarm optimation algorithm at the Ionian sea and the Levant basin, respectively. The parametrization is given in terms of the following arrays; ***nodes:*** which contains the layer indices, each node is located at the top of the considered layers, ***pmax:*** defines the maximum perturbations in shear-wave velocity at each depth node in km/s, ***pdis:*** defined either the shear-wave velocity at the given node is continuous or not, ***pwvabs:*** defines the model regularization (model damping) applied to the absolute value of isotropic and anisotropic perturbations, ***pwvdiff:*** defines the model regularization (model damping) applied to differences of the shear

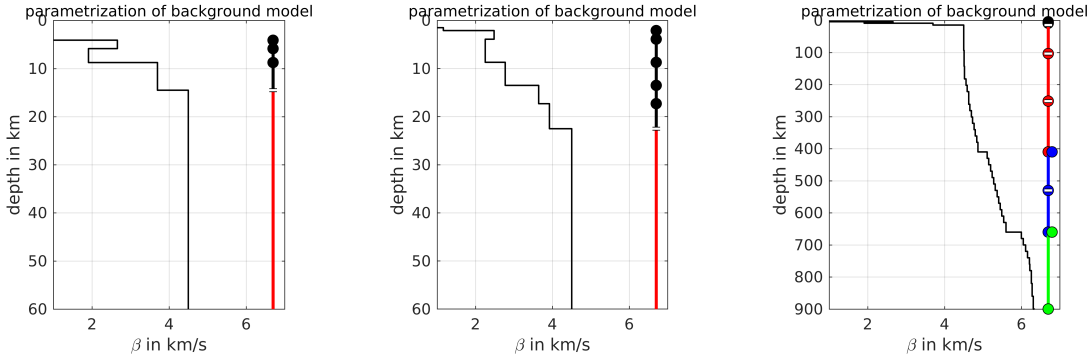

(a) Ionian's crust (b) Levant's crust (c) Upper mantle

Fig. 3.5 Graphical representation of the parameterization of the background model for the particle swarm inversion. The dots show the depth nodes where velocities are varied, whereas white horizontal bars show the node locations where depths of the discontinuities are varied. Black line shows constant perturbations, green line indicates the linear gradient perturbations, blue line represents the quadratic velocity variations and red line represnts the depth range of cubic velocity perturbations. particle swarm inversion. a) off-shore parameterization of the crust taking into account the bathymetery underneath the Ionian sea. b) the same as (a) but for the Levant basin. c) Full parameterization of the considered depth range including the crust, upper mantle and mantle transition zone down to 900 km.

velocity pertutbations at different nodes, ***pdepth:*** this define the maximum absolute value of perturbation in depth in km at a specific depth node if the node is not fixed, ***pwdabs:*** defines the model regularization (model damping) applied to the absolute value of the perturbations in depth, ***porder:*** defines the order of perturbations in shear-wave velocity between current and next deeper depth nodes. In which we allow for different types of the perturbation orders including *"constant"* perturbation until next deeper node, *"linear"* change until next deeper grid node, *"quadratic"* curvature between current and next two depth nodes and *"cubic"* curvature between current and next three grid nodes, ***paniso:*** with this parameter, we can allow for anisotropy of perturbations in shear-wave velocity between current and next deeper nodes (including radially and/or azimuthally anisotropic), and finally ***pcoup:*** this allows for coupling perturbations in V_p and ρ to perturbations in V_s. In general, the parameterization of all individual models including the perturbating the background model are defined for a continuous, specified depth range, from Earth's surface (0 km depth) down the uppermost lower mantle ($\sim$ 900 km). Topography and bathymetry is taken into account in the inversion of the phase-velocities including the presence of water layer.

The ratio between S- and P-wave velocity and the ratio between S-wave velocity and density are kept fixed during the inversion. This is because phase velocities of the fundamental

Table 3.1 Parameterization of the Ionian sea's background model.

nodes	pmax	pdis	pwvabs	pwvdiff	pdepth	pwdabs	porder	paniso	pcoup	comment
2	1.2	1	0.2	0.2	0	0	0	0	0	"sediments"
3	1.2	1	0.2	0.3	0	0	0	0	0	"u. crust"
5	1	1	0.7	0	0	0	0	0	0	"l. crust"
8	0.7	0	0.7	0.6	10	0.5	3	0	0	"Moho"
17	0.7	0	0.4	0.7	15	0.5	-3	0	0	"100 km"
32	0.7	0	0.4	2.5	25	0.5	-3	0	0	"250 km"
49	0.7	1	5.5	1	0	0.0	2	0	0	"410 km"
61	0.7	0	0.4	5.5	30	0.5	-2	0	0	"540 km"
66	0.7	1	5.5	1	0	0	1	0	0	"660 km"
75	0	1	0.4	0	0	0				"900 km"

Table 3.2 Parameterization of the Levant basin's background model.

nodes	pmax	pdis	pwvabs	pwvdiff	pdepth	pwdabs	porder	paniso	pcoup	comment
2	1.2	1	0.2	0.2	0	0	0	0	0	"sediments"
4	1.2	1	0.2	0.3	0	0	0	0	0	"u. crust"
7	1	1	0.2	0.5	0	0	0	0	0	"m1. crust"
10	1	1	0.2	0.5	0	0	0	0	0	"m2. crust"
13	1	1	0.7	0	0	0	0	0	0	"l. crust"
16	0.7	0	0.7	0.6	10	0.5	3	0	0	"Moho"
28	0.7	0	0.4	0.7	15	0.5	-3	0	0	"100 km"
40	0.7	0	0.4	2.5	25	0.5	-3	0	0	"250 km"
56	0.7	1	5.5	1	0	0.0	2	0	0	"410 km"
68	0.7	0	0.4	5.5	30	0.5	-2	0	0	"540 km"
74	0.7	1	5.5	1	0	0	1	0	0	"660 km"
85	0	1	0.4	0	0	0				"900 km"

Rayleigh mode are mainly sensitive to the S-wave velocity. Starting from this point, the model parameters are iteratively improved until a good fit between theoretical and measured dispersion curves is obtained. Theoretical phase velocities for an elastic, isotropic, 1-D model are calculated using Thomson-Haskell matrix formalism and an earth flattening approximation according to Schwab & Knopoff (1972) in which sphericity corrections are taken into account. The concept is to convert the spherical earth model into a flat earth model, compute the dispersion relation, and then adjust the dispersion from the flat earth model to make the spherical earth dispersion (Schwab & Knopoff 1972). The Thomson-Haskell technique synthesizes the surface wave dispersion functions by constructing layer matrices which relate the components of motion at one interface in a layered structure to those at the next. The product of these layer matrices then relates the components of motion at the deepest interface to those at the free surface, and this layer-matrix product is used to construct the synthetic dispersion curve and comparing it with the observed dispersion. The starting

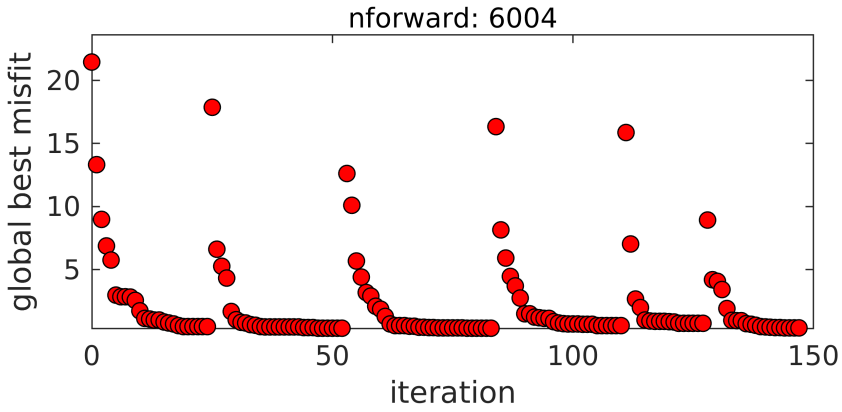

Fig. 3.6 Convergence rate of the particle swarm optimization algorithm towards the global best position after $\sim$ 6000 forward calculations. The global best misfit is plotted as function of number of iterations.

model is then iteratively refined until it fits the observations. On each iteration, repeated forward calculations ($\sim$ 6000 in both cases) are carried out to search for the global minimum. It's worthy mention that in the current implementation of the particle swarm optimization technique, we allowed for random local search in order to speed up the convergence of the entire swarm towards the global best position (Fig. 3.6). Moreover, a random excursion to best position of the other particles is also implemented in order to ensure the exploration of the entire model space. After small number of iterations, the inversion starts to converge to towards the global minimum. Figure (3.6) shows the convergence towards the global best misfit as a function of number of iterations. At the beginning, it shows fast convergence and with increasing iteration number, the global misfit is decreasing. If the search in the parameter space can not find a better model, it reaches the stagnation phase and then it randomly re-initiallizes the particles in the search space untill either the stopping criterion is statisfied or the maximum number of iteratios is reached.

3.4.3 Regularization

Regularization of the depth inversion procedure implies explicitly constraining the estimated model during the inversion in terms of the model amplitude, model rounghness and the magnitude of the perturbations from the background model. In other words, *a priori* information about the estimated model is taken into account to increase the inversion stability. The strength of regularization may vary in an adaptive way with information regarding the data quality and the reliability of the background model or any other *a priori* information. Here, we developed a regularization scheme of the model parameters which is adjusted to

the individual layers using three different parameters:
a) damping the absolute velocities at each node of the considered depth range (*pwvabs*),
b) damping the absolute depths at the nodes where they are of variable depths (*pwdabs*),
c) damping the differences in velocity perturbations at different depth nodes (*pwdiff*).

In order to quantify the effect of the regularization on the PSO inversion, we performed a series of systematic synthetic tests. The idea is to quantify the effect of each individual parameter on the inversion results. We tested each parameter using different values ranging from weakly regularized to strongly regularized inversion. It turns out that the most effective parameter is the differences of velocity perturbations at different nodes ***(pwdiff)***. Consequently, we conclude that a combination of all damping parameters is needed but with different weights. Figure (3.7) is an example of the best-fitting 1-D inversions and the corresponding dispersion curves for a synthetic model using different regularization scenarios where the phase velocity fit for Rayleigh waves is shown. We define a synthetic 1-D model and compute fundamental-mode phase velocities for it. Then we performed the particle swarm inversion using the developed strategy of parameterization as descriped in table (3.2). We introduced three different sets of regularization values including low damping, moderate damping and high damping. We checked the results and finally a regularization strategy has been developed as following:
1) Damping the perturbations differences *(pwdiff)* towards the background model with a linear gradient that increases with larger depths,
2) very strong damping of the perturbations differences *(pwdiff)* at the nodes which are located at the end of different perturbation orders to assure smooth final models and prevent kinks in the final model,
3) when fixing the Moho, the absolute velocities at the Moho node is damped strongly to minimize the tradeoff between the Moho depth and the crustal and upper mantle velocities,
4) when the Moho is variable, the perturbations differences at the node above the Moho should be undamped, in addition to damping the absolute velocities above and below the Moho while the Moho velocity is undapmed,
5) At the discontinuities of 410 and 660 km, both the absolute velocities and the differences in perturbations needs to be strongly regularized,
6) A slight damping the absolute depths at the nodes where the discontinuities are variables.

In the same figure the comparison between the final velocity model obtained from the inversion (coarse dashed line) and the initial model (white solid line) are shown. Weakly regularized inversion (3.7a) may introduce some artifacts due to noise or data errors and results in very rough model with some kinks at different depths where the perturbation order is changing. The resulting model is poorly recovered compared to the background model

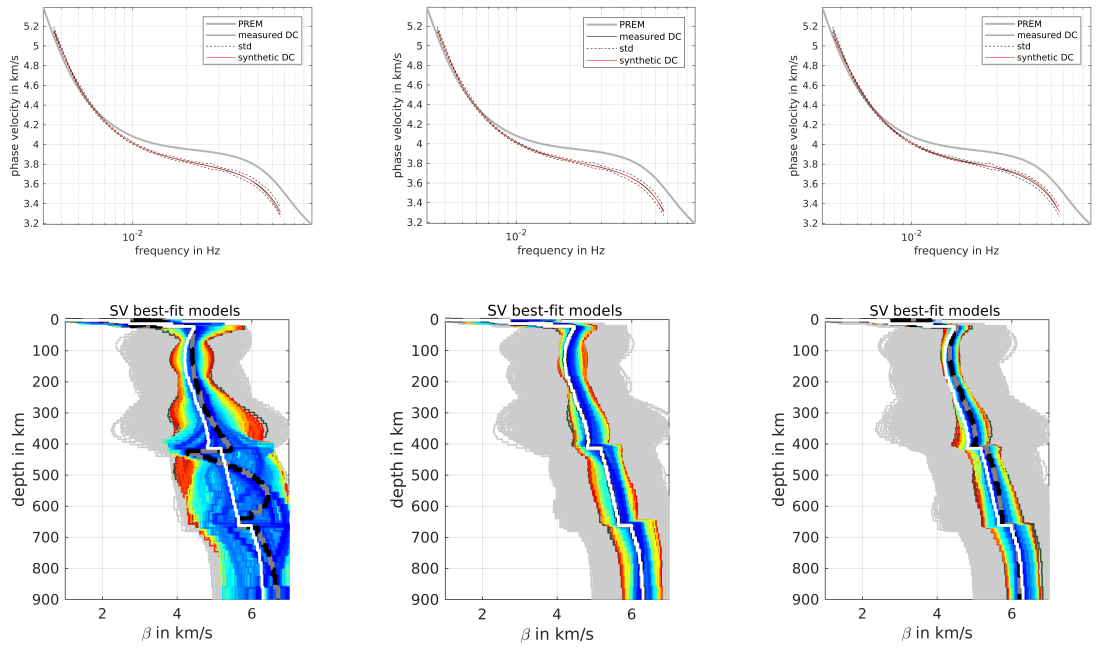

(a) Without damping (b) Optimal damping (c) High damping

Fig. 3.7 Regularization effect on the particle swarm inversion results. The dispersion curves and the corresponding 1-D depth models as function of depth are shown on the upper and lower panels, respectively. a) Without damping towards the background model, b) Optimal damping parameters, and c) High damping parameters. The coarse-dashed model shows the resulted best-fitting model, where as the white color indicates the initial model.

(white model), whereas the strongly regularized inversion results in very smooth model with low resolution and the results will be highly influenced by the background model (Fig. 3.7c). Note the good consistency between measured phase velocities and synthetic curves at intermediate frequencies, while it shows some deviations at higher and lower frequencies (figures 3.7a and c, on the top panel). Figure (3.7b) shows the best-fitting 1D model which resulted from the inversion using the developed regularization strategy. The recovered model is mostly fully covered by the initial model and overall good fitting between the dispersion curves has been obtained.

3.4.4 Uncertainity estimation of the Moho depth and crustal velocities

Inverting the surface wave dispersion measurements for the 1-D depth models suffers from the non-uniqueness solution (Meissner 1926; Nolet & Lebedev 2005; Bartzsch *et al.* 2011; Lebedev *et al.* 2013; Meier *et al.* 2016). Meissner (1926) introduced examples of different

1-D depth models that produced analogous dispersion curves. This is due to the trade-offs between the Moho depth and the shear wave velocities in the crust and the upper mantle. The trade-offs in isotropic average V_s have been investigated in a number of studies (e.g. Bodin *et al.* 2012; Lebedev *et al.* 2013). Furthermore, the Moho depth has its own signature on surface wave velocities as it shows a significant velocity perturbations from the lower crust to the upper mantle. This may result in velocity changes either in the lower crust or in the upper mantle similar to those at the Moho discontinuity itself (Lebedev *et al.* 2013).

Therefore, accurate measurements from dense networks as well as constrained *a priori* information on crust and its thickness help to reduce the trade-offs between the different structural parameters and enables resolving the Moho depth more accurately (Meissner 1926; Lebedev *et al.* 2013). Here, we constrained our dispersion inversions with accurate local P-wave initial models. The trade-offs between the parameters are quantified as shwon in figure (3.8). Each panel represents a two-parameter plane, which represent a slice through the resulted models and shows a color-coded dots according to the rms misfit value of the two considered parameters through all the models. The figure shows the Moho depth variation (in km) plotted as function of the shear velocity perturbations (km/s) in the lower crust and in the uppermost mantle for both the Ionian and the Levant basin, respectively. The blue dots represent the accepted models whereas the gray ones are rejected due to their higher misfit values. The outlined circle represents the best-fitting model with the lowest misfit value. For both locations, the Moho depth and shear wave velocities above and below the Moho show the expected constrained trade-offs: a misfit due to increasing or decreasing the Moho depth can be overcome by increasing or decreasing of the perturbations of the shear velocities above or below the Moho. This is intuitively occurs because surface wave are sensitive to broad depth range (Meissner 1926; Nolet & Lebedev 2005; Bartzsch *et al.* 2011; Lebedev *et al.* 2013).

To further investigate the uncertainties of the individual parameters, we plot the rms misfit values of all the resulted models as function of only one parameter. Figure (3.9) shows the estimated uncertainties of the Moho depth as well as of the crustal velocities at the two locations. Each panel represents a slice through the resulted models at a specific parameter. The rms misfit values of the considered parameter is shown as envelope. We empirically define the maximum allowed misfit value to be considered when defining the uncertainties. The uncertainties in the Moho depth estimation is $\sim \pm$ 2.5 km and $\sim \pm$ 1.0 km, whereas it is $\sim \pm$ 0.2 km/s and $\sim \pm$ 0.1 km/s in the crustal velocities for the Ionian sea and the Levant basin, respectively. All together, the joint analysis of surface wave dispersion measurements and seismic refraction data contribute significantly to reduce uncertainties further and facilitate Moho mapping.

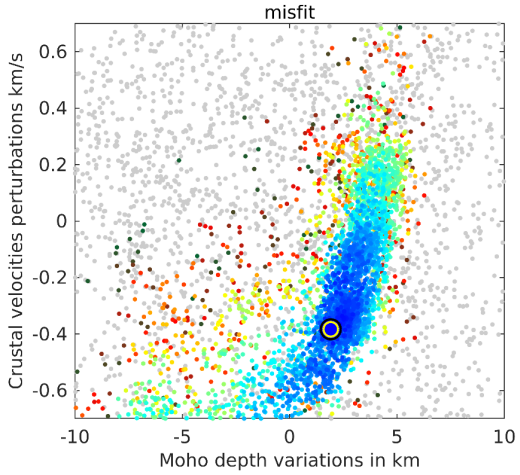

(a) Ionian's crust

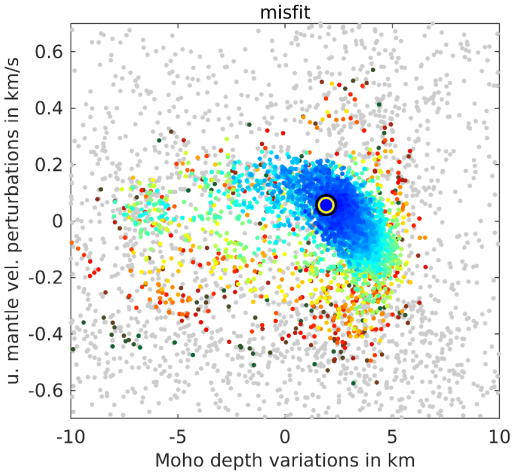

(b) Ionian's upper mantle

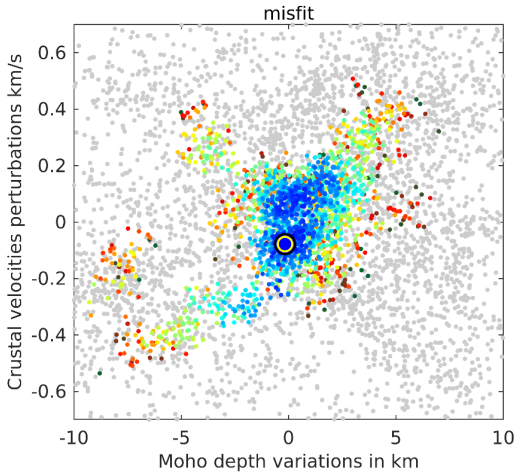

(c) Levant's crust

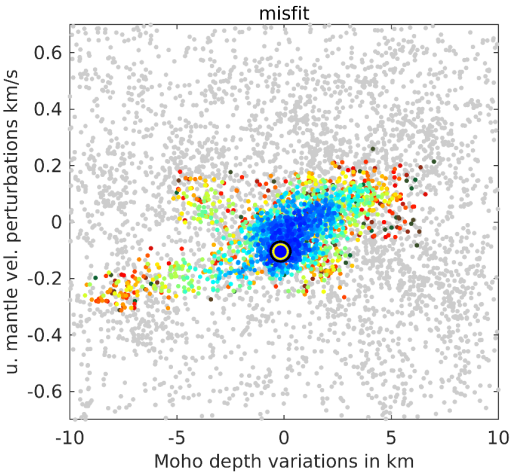

(d) Levant's upper mantle

Fig. 3.8 Trade-offs between the Moho depth variations and shear wave velocity perturbations in the lowermost crust and upper mantle at the Ionian sea (a and b), respectively. The same are shown for the Levant Basin (c and d). All the resulted models are plotted as small dots color-coded according to the misfit value. The blue dots represent the accepted models whereas the gray ones are rejected and of higher misfit values. The outlined circle represents the best-fitting model with the lowest misfit value.

3.5 Results and discussions

The resulting 1-D isotropic shear velocity models at the Ionian sea and Levant basin for the crust and upper mantle are shown in figures (3.10 - 3.12), respectively. For the crust we show the models down to 27 km, whereas for the upper mantle they are shown down to $\sim$ 300 km. The isotropic SV models are colour-coded according to the misfit values. While the

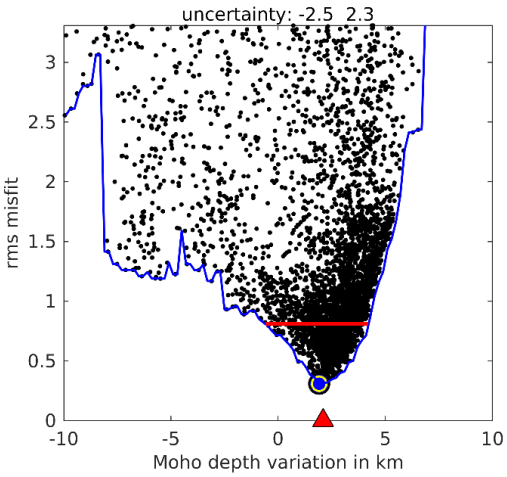

(a) Uncertainity of Ionian's Moho depth

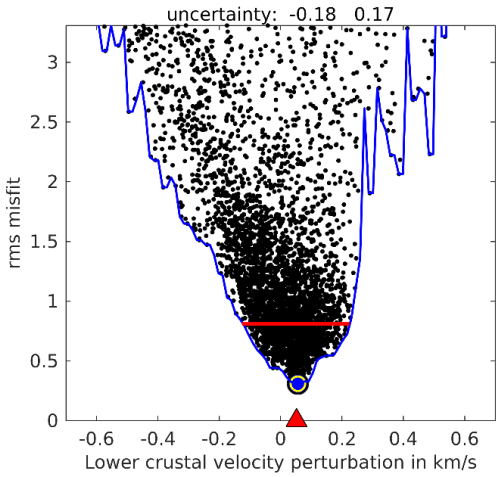

(b) Uncertainity of Ionian's crustal velocity

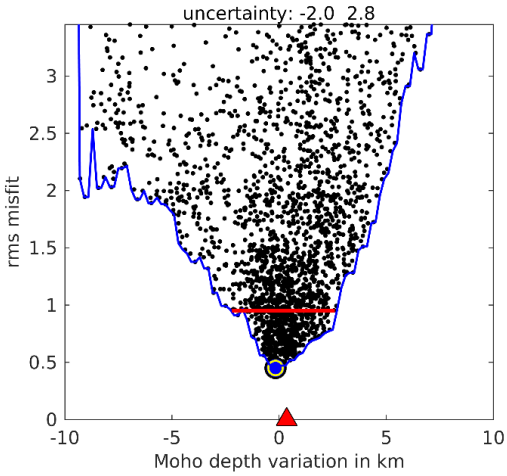

(c) Uncertainity of Levant's Moho depth

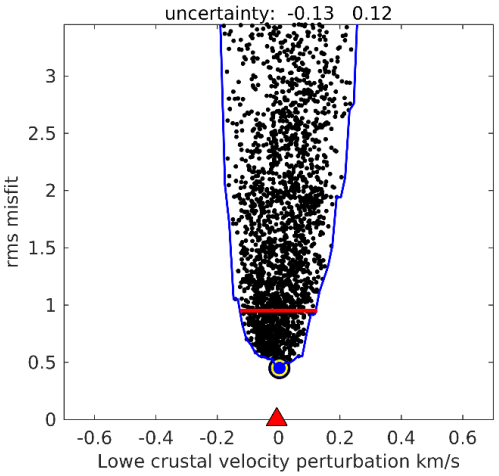

(d) Uncertainity of Levant's crustal velocity

Fig. 3.9 Uncertainties of the Moho depth estimation and crustal velocities. They are plotted as function of the rms misfit values at the Ionian sea (a and b) and the Levant basin (c and d), respectively. Each black dot represent a single model of the considered models. The blue line define the envelope which contain all the considered models. The outlined blue circle indicates the model with the lowest misfit. The red line defines the maximum allowed misfit for defining the model uncertainties.

blue bundle of the isotropic SV models represent the models with the lowest misfit values, the gray models represent the ones with the very large misfit values. The SV best-fitting model for the Ionian sea is indicated by coarse-dashed red line, whereas the SV best-fitting model for the Levant Basin is shown in coarse-dashed gray line. The blue bundle of models indicates the uncerainities in the inversion parameters(e.g., Moho depth, crustal velocities, upper mantle velocities, ...).

3.5.1 Crustal structure and Vp/Vs ratio

The 1-D velocity models representing the crustal structure underneath the Ionian sea and the Levant basin are shown in figure (3.8). On the top panel, the corresponding measured and best-fitting synthetic dispersion curves at both locations are presented in a comparison to a global reference model (PREM, Dziewonski & Anderson 1981). The measured dispersion curves and their standard deviations are shown in the same color as for the best-fitting 1-D models. Note the overall very good consistency between measured phase velocities and synthetic curves for the best-fitting models. The 1-D model for Ionian crust reveals a Moho depth of $\sim$ 16 km that is highly consistent with the results from the seismic refraction profile (Dannowiski *et al. in prep.*). The thickness of the crystalline crust is about 6 km overlain by a thick pile of sediments. The shear wave velocities in the crust range between 2.2 and 3.0 km/s.

de Voogd *et al.* (1992) highlighted that the Ionian sea has a thin oceanic crust ($\sim$ 7-9 km) that is formed during the early Cretaceous relying on a thick ($\sim$ 7 km) sedimentary cover of Mesozoic and Tertiary age (Sioni 1996; Cassinis *et al.* 2003). In their interpretation, the entire crust has a maximum thickness of 17 km. At depth of approximately 4.0 km underneath the Ionian sea, Gallais *et al.* (2011, 2012) and Polonia *et al.* (2011) imaged clearly a set of SW-NE faults from the analysis of seismic reflection profiling. These faults have been interprested as reverse faults formed during the late Miocene. It is worthy mention that, Gallais *et al.* speculated that these faults have been formed as a response of inverting the originally normal faults formed during seafloor spreading of the Ionian sea in Jurassic, counting on the oceanic nature of the Ionian crust as interpreted by de Voogd *et al.* (1992), which has interpreted as being early Jurassic of age (Finetti 1982). The potenial field data measured since the 1970s indicated that the Ionian sea reflected strong positive Bouguer anomalies of 130-270 mGal (Morelli *et al.* 1975; Catalano *et al.* 2001), that is highly consistent with the thin crustal thickness in this region. According to Della Vedova & Pellis (1989), the age of early Mesozoic (180$\pm$200 Ma) has been proposed for the oceanic crust of the Ionian sea based on the low heat flow values (30-40 mW/m²) at depth of about 4 km. The magnetic anomaly stripes typical for oceanic crust have been detected underneath Ionian sea by Speranza *et al.* (2012) suggesting the age of 220-230 Ma.

On the other hand, the recovered Moho depth underneath the Levant Basin is of $\sim$ 22 km which is compatible with the measurements of Netzeband *et al.* 2006. The thickness of the crystalline part of the Levant crust is about 10 km overlain by a thick sedimentary cover. Their crustal shear velocities range from 2.5 and 3.7 km/s. Ben-Avraham *et al.* (2002) showed that the crystalline basement in the Levantine Basin consists of two layers with a P-wave velocity

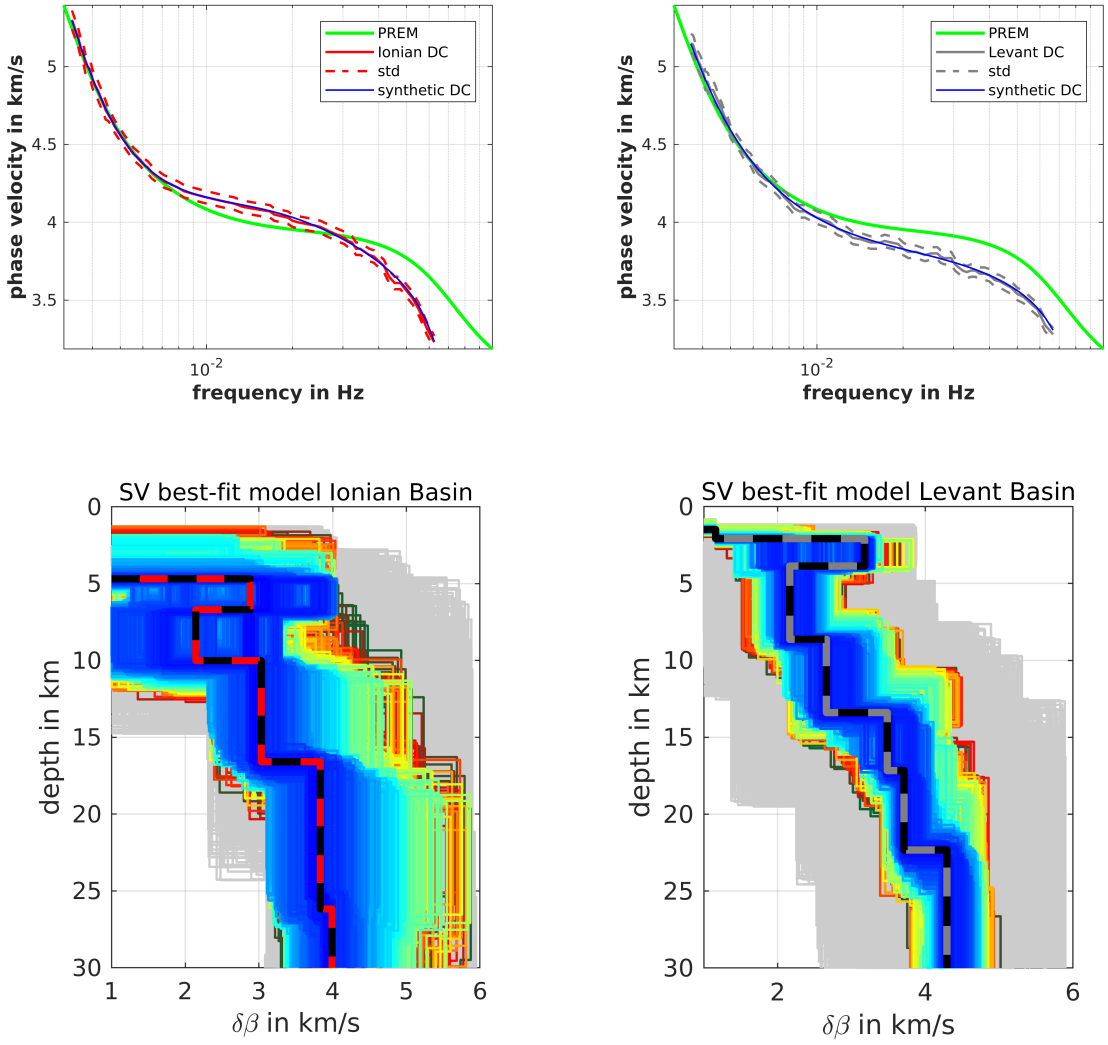

(a) (b)

Fig. 3.10 S-wave crustal models with uncertainties from inversion of dispersion curves at: a) the Ionian sea, and b) the Levant Basin. Gray shaded areas show all the sampled models space, the accepted range of models are in blue and the coarse-dashed line represents the best-fitting model. The top panel shows a comparison of the measured and best-fitting synthetic dispersion curves at both locations in a comparison to a global reference model, respectively.

of 6.0 - 6.4 km/s in the upper and 6.5 - 6.9 km/s in the lower crust. Towards the center of the basin the Moho depth decreases from 27 to 22 km (Netzeband *et al.* 2006a). The comparison with other seismic refraction studies in prolongation of Netzeband *et al.* (2006) profiles under Palestine and Jordan (Weber *et al.* 2004) and in the Mediterranean sea near Greece and Sardinia reveal similarities between the crust in the Levant Basin and thinned

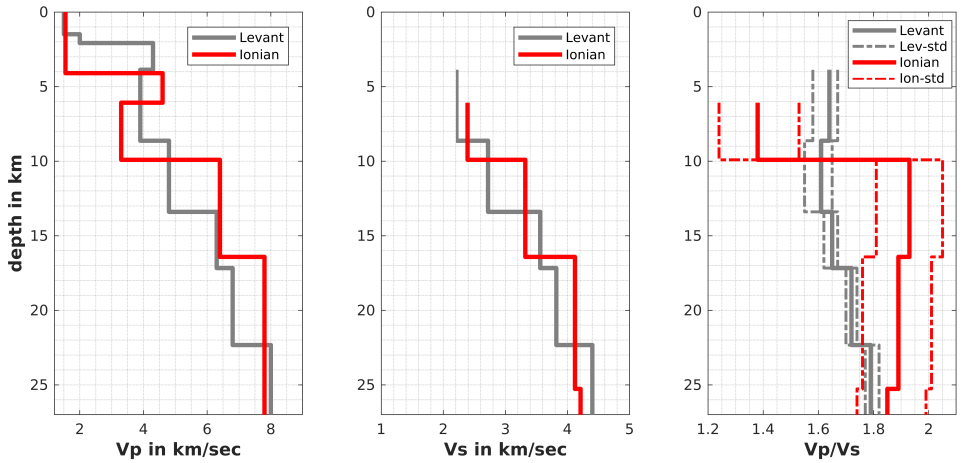

Fig. 3.11 Comparison between the crustal structure of the Ionian sea and Levant Basin. ***Left)*** The average V_p velocity profiles from refraction seismics, ***Middle)*** The average V_s strcuture from inverting the dispersion measurements, and ***Right)*** The V_p/V_s ratio underneath both locations and their uncertainties.

continental crust, which is found in that region. Netzeband *et al.* (2006a) concluded on the presence of thinned continental crust under the Levant Basin and estimated a streching factor (ß) of 2.3 - 3. These authors attributed local variations of the velocity gradient to previously postulated shear zones. Among others, Gardosh and Druckmann (2006) presented industrial seismic data from the Levant, showing that large scale horst and graben structures dominate the relief of the Levant crystalline basement. These obstacles were not taken into account into the ray-tracing models by Netzeband *et al.* (2006). Consequently, this might have enlarged the uncertainties of the crustal model by Netzeband *et al.* (2006). Welford *et al.* (2015 a, b) and Feld *et al.* (2017) presented crustal models of the Eratosthenes seamount based on an amphibian wide-angle reflection / refraction experiment carried out in 2010 (Hübscher *et al.* 2011). The continental nature of the Eratosthenes seamount is unchallenged and is well supported by numerous geophysical studies (Makris *et al.* 1983; Robertson 1998; Ben-Avraham *et al.* 2002; Welford *et al.* 2015). Moreover, there is a general consensus that Eratosthenes represent the seaward limit of streched continental crust underneath the Levant basin. Towards the north it is limited by an NNW-SSE oriented transform margin related to the Mesozoic Tethyan Ocean opening (Netzeband *et al.* 2006; Longacre *et al.* 2007; Frizon de Lamotte *et al.* 2011; Montadert *et al.* 2014; Welford *et al.* 2015).

The equivocality of potential field data modelling is expressed by various modelling results with different conclusions. Netzeband *et al.* (2006a) fostered their interpreted attenuated crustal model by gravity and magnetic modelling, yet, Ben-Avraham *et al.* (2002)

corroborated their oceanic crust model also by gravity and magnetic modelling. Rybakov and Segev (2004) compiled gravity and magnetic data from the Levant and computed the depth to basement. They suggested the presence of oceanic crust without showing evidence for that. Longacre *et al.* (2007) presented a continental crustal model of the Levant Basin with the continent-ocean boundary towards the Hecataeus Basin. Steinberg *et al.* (2018) used 3D gravity inversion and 3D-flexural backstripping techniques, concluding that stretching of the Levant continental crust did not progress to the formation of new oceanic crust. Halstenberg (2014) presented heat-flow data for three zones of shallow, intermediate and deep basin of 38.8 mW/m², 48.3 mW/m² and 41.2 mW/m², respectively. The author calibrated his models with vitrinite reflectance and temperature measurements in production well and concluded that the results promote thinned continental crust as the best option to underlie the basin, due to its higher heat production compared to oceanic crust. Sensitivity studies by Halstenberg identified crustal and lithospheric thicknesses as two paramount input parameters for tectonic heat flow models.

The univocal interpretations of the different seismic data played an important role in developing the ongoing debate on the nature of the crust underneath the Ionian sea and the Levant Basin. Here as a proxy, the V_p/V_s is used to shed light on the identification of the nature of the crust. According to Christensen (1996), the velocity ratios and the Poisson's ratios have the potential of providing valuable constraints on crustal composition and are highly helpful in distinguishing between the continental (Christensen & Fountain 1975; Zandt & Ammnon 1995). and oceanic nature of the crust (Christensen 1972; Spudich & Orcutt 1980). Christensen & Smewing (1981) and Christensen & Salisbury (1982) estimated the V_p/V_s and the Poissons's ratio for a typical oceanic crust, namely Samail Ophiolite in Oman and Bay of Islands Ophiolite in New foundland, respectively. In both cases they found the $V_p/V_s \geq 1.8$ and Poisson's ratio of ≥ 0.3. They attributed these relatively high averages ratios to the higher Poisson's ratios of the major lithologies constituting the oceanic crust (e.g., basalt, diabase, and gabbro) which are in reasonable agreement with a 0.32 Poisson's ratio obtained from the analysis of the converted phases recorded by ocean bottom seismometers at the East Pacific Rise (Bratt & Solomon 1984).

On the other hand, Christensen & Mooney (1995) estimated the average continental crustal velocity ratios and the average continental crustal Poisson's ratio. The velocities of the continental crust have been calculated from a world-wide compilation of plenty of seismic studies and then was compared with laboratory measurements of P-wave velocities for the different continental rocks. They concluded a value of $V_p/V_s \leq 1.8$ is charaterizing the continental crust (Miller & Christensen 1994; Christensen & Mooney 1995; Zandt & Ammnon 1995). Here we make use of the compressional velocities obtained from the seismic

refraction modelling and the shear velocities obtained from the inversion of surface wave dispersion measurements in order to calculate the V_p/V_s ratio for the crust underneath the Ionian and the Levant Basin. Figure (3.9) shows a comparison between the crustal structure of the Ionian sea (red) and Levant Basin (gray). On the left panel: the average V_p velocity profiles from seismic refraction analysis, on the middle panel: the average V_s strcuture obtained from inverting the dispersion measurements, and on the right: the V_p/V_s ratio underneath both locations and their uncertainties. Beneath the Levant basin, a V_p/V_s ratio of < 1.8 is obtained, whereas for the Ionian sea a value of > 1.8 is obtained. Our findings mainly support the idea of the oceanic nature of the crust underneath the Ionian sea while they are pointing out that the Levant basin is floored by a stretched continental crust.

3.5.2 Upper mantle structure and LAB depth

In a similar way, the 1-D shear velocity models representing the structure of the uppermost mantle underneath the Ionian sea and the Levant Basin are shown in figure (3.12a and b). They reveal strong variations in the shear wave velocities in the uppermost mantle. In figure (3.12c), the best-fitting 1-D models are plotted in a comparison to each other. The gray model represents the Levant Basin whereas the red model indicates the Ionian sea. Note the clear difference between the upper mantle structure beneath the two locations. The presence of the shallow asthenosphere beneath the Levant Basin is clearly indicated by a strong reduction in the shear wave velocity with depth as it shows slow upper mantle velocities lower than 4.5 km/s below the Moho (Fig. 3.12, middle). The low velocity anomalies under the Levant basin have been detected in previous models (Boschi *et al.* 2004). The depth to lithosphere-asthenosphere boundary (LAB) is difficult to be accurately estimated from the inversion of surface wave measurements because surface wave sensitivity kernels are too smooth (Bartzsch *et al.* 2011). However, it can be roughly defined in the middle of the zone where the reduction from higher velocities within the colder mantle lithosphere to lower velocities within the hotter asthenosphere occurs, as the occurrence of this reduction in general is well established (Brune *et al.* 1963; Dziewonski & Anderson 1981).

From the inversion results, the LAB depth underneath the Levant basin is about 70 ± 10 km. Clearly, no indications for fast oceanic mantle lithosphere are found beneath the Levant basin. This supports the hypothesis that the Levant basin is located above a thinned continental mantle lithosphere underlain by a shallow asthenosphere with low shear wave velocities. Based on our results, we argue that lithospheric thinning has to be taken into account when considering the evolution of the Levant basin. The relatively thin lithosphere beneath the Levant basin may imply that sublithospheric mantle could be responsible for and support the

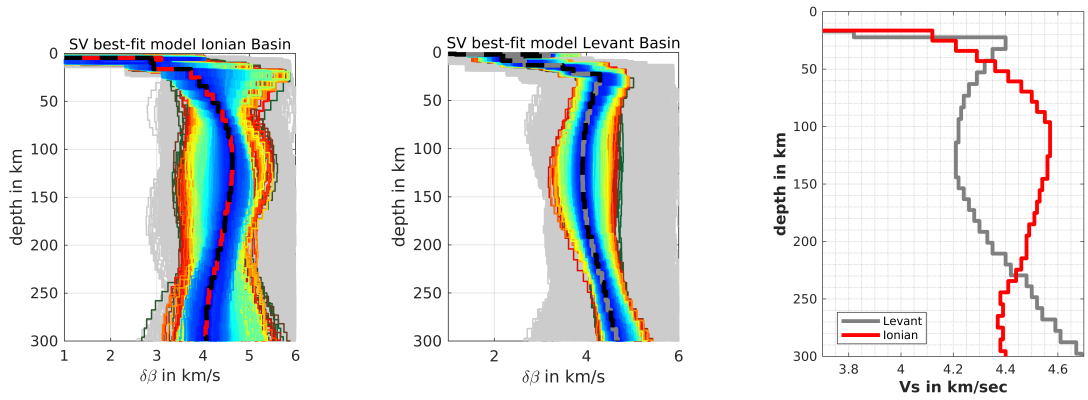

(a) (b) (c)

Fig. 3.12 1-D shear wave velocity models of the upper mantle beneath: a) the Ionian sea and b) the Levant Basin and their uncertainties. The blue models are accepted, the gray ones are rejected and the coarse-dashed lines represent the final best-fit models. c) Comparison between the best-fitting 1-D models at the two locations.

uplift of the Levant basin. Conversely beneath the Ionian sea, an anomalously high shear wave velocities have been detected (higher than 4.5 km/s) which indicate a very thick oceanic mantle lithosphere. Based on our model for the upper mantle of the Ionian sea we show that, on average, the Ionian oceanic lithosphere has continued to cool well beyond the 80 Ma age, in contrary to the "thermal plate cooling model" prediction, and is now extremely thick over 200 km. The LAB depth together with the general increase in shear wave velocities with depth show a consistency with the prediction from the half-space cooling model (Davis & Lister 1974; McKenzie *et al.* 2005), which predicts the systematic and continuous increase of the lithospheric thickness with cooling from mid-ocean ridges and increasing the plate age (230 - 270 Ma, Müller *et al.* 2008).

In order to verify our results and to see how reliable our average local dispersion measurements as well as the obtained velocity model underneath the Ionian sea, we considered the two scenarios for the cooling of the oceanic lithosphere. For each, a synthetic 1-D velocity model as function of depth with age-dependant lithospheric thickness has been constructed. In the first case, we proposed that the cooling of the oceanic lithosphere is following the thermal plate cooling model in which the lithspheric thickness reaches its maximum at 80 Ma with LAB depth of $\sim$ 100 km followed by pronounced asthenosphere downwards (Fig. 3.13a). In the second case, we constructed a 1-D model with lithospheric thickness that increases continuously with age (LAB depth of $\sim$ 200 km at 270 Ma). Synthetic dispersion curves have been calculated for each model though forward modelling (Schwap & Knopoff 1972) and then we compared the measured local disperion curve with the synthetic ones.

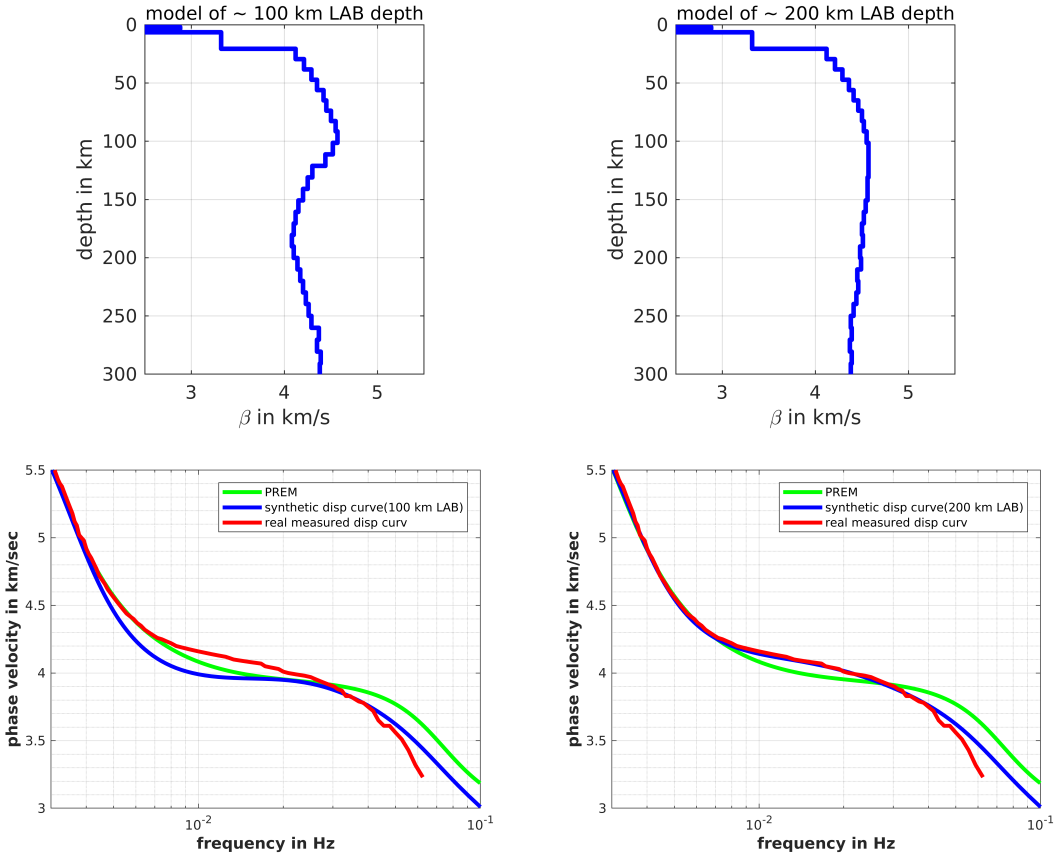

(a) (b)

Fig. 3.13 Predicted 1-D depth models with age-dependant lithospheric thicknesses, and the corresponding synthetic dispersion curves from each model (blue) in a comparison with the real measured dispersion curve at the Ionian sea (red) and PREM (green). a) The lithspheric thickness reaches it maximum at 80 m.y. with LAB depth of $\sim$ 100 km and pronounced asthenosphere downwards. b) Model with lithospheric thickness that increase continuously with age (LAB depth of $\sim$ 200 km).

The 1-D models and the corresponding synthetic dispersion curves (blue) from each model are plotted in a comparison with the real measured dispersion curve at the Ionian sea (red) and PREM (green). The results indicate the possible applicability of the half-space cooling model for the very old oceanic lithosphere underneath the Ionian sea.

3.6 Conclusions

Surface wave tomography has been performed to characterize the structure of the crust and the mantle lithosphere in the eastern Mediterranean. We calculated new high resolution Rayleigh wave phase velocity maps using an unprecedentedly large number (200.000) of fundamental mode inter-station automatically calculated phase velocity dispersion curves. For the first time, broad band waveform data from the Egyptian National Seismological Network (ENSN) have been combined with the available data from IRIS and EIDA in order to ensure a good path coverage especially for the southern part of the eastern Mediterranean. We constructed broad band local phase-velocity dispersion curves for the Levant Basin (deformed continental) and the Ionian sea (oceanic). Each local dispersion curve is inverted individually for 1-D shear wave velocity model as a function of depth. A newly implemented inversion algorithm called Particle Swarm Optimization (PSO) algorithm is used for the inversion. We developed a strategy to parametrize our inversion procedure by constraining each model parameter individually along the considered depth range. Moreover, a regularization scheme has been developed to increase the stability of the inversion process. We constrained our inversion with accurate local P-wave initial models. The P-wave velocity models have been calculated from two seismic refraction profiles recently recorded at Levant basin and the Ionian sea, where the local dispersion curves are available to minimize the trade-off between the crustal velocities, mantle velocities and the crustal thickness. The results indicate a Moho depth of about $\sim 22\pm2.5$ km and $\sim 16\pm2.$ km beneath the Levant and the Ionian Basin, respectively. The thickness of the crystalline part of the crust at the Levant basin is $\sim$ 10 km, whereas it is of $\sim$ 6 km beneath the Ionian sea, overlain by a thick pile of sediments at both locations. As a proxy, the Vp/Vs ratio is used to identify the nature of the crust. Beneath the Levant basin, a ratio of < 1.8 is obtained pointing to a continental crust, whereas the > 1.8 value at the Ionian sea indicates its oceanic nature. In the upper mantle, a shallow asthenosphere is highly pronounced beneath the Levant basin with $\sim 70\pm10$ km of LAB depth. On the other hand, anomalously higher shear-velocities beneath the Ionian sea indicates a very thick oceanic lithosphere. Based on our model for the upper mantle of the Ionian sea we show that, on average, the Ionian oceanic lithosphere has continued to cool well beyond the 80 Ma age, contrary to the "plate cooling model" prediction, and is now extremely thick, over 200 km. This may indicate the applicability of the half-space cooling model for the very old oceanic lithosphere underneath the Ionian sea.

References

Aal, A.A., A.E. Barkooky, M. Gerrits, H.-J. Meyer, M. Schwander and H. Zaki 2001. Tectonic evolution of the eastern Mediterranean basin and its significance for the hydrocarbon prospectivity of the Nile Delta deepwater areas. GeoArabia, v. 6, no. 3, p. 363-384.

Bartzsch, S., Lebedev, S., Meier, T., 2011. Resolving the lithosphere–asthenosphere boundary with seismic Rayleigh waves, Geophys. J. Int., Volume 186, Issue 3, Pages 1152-1164

Bayer, R., J.-L. Le Mouel & X. Le Pichon, 1973. Magnetic anomaly pattern in the western Mediterranean, Earth Planet. Sci. Lett. ,19, 168-176, doi:10.1016/0012-821X(73)90111-8

Becker, T. W., Schaeffer, A. J., Lebedev, S. & Conrad, C. P., 2015: Toward a generalized plate motion reference frame. Geophys. Res. Lett., 42, doi:10.1002/2015GL063695, 3188-3196, 2015.

Ben-Avraham, Z., A. Ginzburg, J. Makris and L. Eppel-baum, Crustal Structure of the Levant Basin, Eastern Mediterranean, Tectonophysics, Vol. 346, No. 1-2, 2002, pp. 23-43. doi:10.1016/S0040-1951(01)00226-8

Ben-Avraham, Z., Ginzburg, A., Makris, J. & Eppelbaum, L., 2002. Crustal structure of the Levant Basin, eastern Mediterranean, Tectonophysics, 346, 23–43.

Ben-Avraham, Z., Ginzburg, A., Makris, J. & Eppelbaum, L., 2002. Crustal structure of the Levant Basin, eastern Mediterranean. Tectonophysics, 346, 23-43.

Best, J. A., M. Barazangi, D. Al-Saad, T. Sawaf & A. Gebran (1993), Continental margin evolution of the Northern Arabian Platform in Syria, Am. Assoc. Pet. Geol. Bull., 77(2), 173–193.

Bigi, G., et al., 1989. Synthetic Structural±Kinematic Map of Italy, Scale 1:2 000 000, CNR, Progetto Finalizzato Geodinamica, Roma.

Bijwaard, H., Spakman, W. & Engdahl, R., 1998. Closing the gap between regional and global travel time tomography, J. geophys. Res., 103, 30055 - 30078.

Bratt, S. R. & S.C. Solomon, 1984. Compressional and shear wave structure of the East Pacific Rise at 11°20' N: Constraints from three-component ocean bottom seismometer data, J. Geophys. Res., 89, 6095-6110.

Breman, E. 2006. Oil and gas plays in the East Mediterranean. 5th Petroleum Exploration Society of Great Britain/Houston Geological Society, African Conference, London, (Expanded Abstract). Calabrian Arc, Tectonophysics, 84, 267±286.

Cassinis, R., S. Scarascia & A. Lozej, 2003. The deep crustal structure of Italy and surrounding areas from seismic refraction data. A new synthesis, Ital. J. Geosci., 122, 365-376

Catalano, R., C. Doglioni & S. Merlini, 2001. On the Mesozoic Ionian Basin, Geophys. J. Int., 144, 49-64.

Catalano, R., Doglioni, C., & Merlini, S. 2001. On the Mesozoic Ionian Basin, Geophys. J. Int. (2001) 144, 49±64.

Cernobori, L., Hirn, A., McBride, J.H., Nicolich, R., Petronio, L. & Romanelli, M., 1996. Crustal image of the Ionian basin and its Calabrian margins, Tectonophysics, 264, 175±189.

Christensen, N. I., 1972. The abundance of serpentinites in the oceanic crust, J. Geol., 80, 709-719.

Christensen, N. I., 1982. Seismic velocities, in Handbook of Physical Properties of Rocks, vol. 2, edited by R. S. Carmichael, pp. 1-228, CRC Press, Boca Raton, Fla.

Christensen, N. I., 1985. Measurements of dynamic properties of rock at elevated temperatures and pressures, in Measurement of Rock Properties at Elevated Pressures and Temperatures, edited by H. J. Pincus and E. R. Hoskins, pp. 93-107, Am. Soc. for Test. and Mater., Philadelphia, Pa.

Christensen, N. I. & D. M. Fountain, 1975. Constitution of the lower continental crust based on expertimental studies of seismic velocities in granulite, Geol.Soc. Am.Bull., 86, 227-236.

Christensen, N. I. & J. D. Smewing, 1981. Geology and seismic structure of the northern section of the Omanophiolite, J. Geophys. Res., 86, 2545-2555.

Christensen, N. I. & M. H. Salisbury, 1982. Lateralheterogeneity in the seismic structure of the ocean crust inferredfrom velocity studies in the Bay of Islandsophiolite, Newfoundland, Geophys. J. R. Astron. Soc., 68, 675-688.

Christensen, N. I. & W. D. Mooney, 1995. Seismic velocity structure and composition of the continental crust: A global view, J. Geophys. Res.,100, 9761-9788.

Christensen, N., 1996. Poisson's ratio and crustal seismology, J. Geophys. Res., Vol. 101, no. B2, 3139-3156.

Christensen, N.I., 1996. Poisson's ratio and crustal seismology, J. geophys. Res., 101(B2), 3139–3156.

Cristofolini, R., Ghisetti, F., Scarpa, R. & Vezzani, L., 1985. Character of the stress ®eld in the Calabrian arc and southern Apennines (Italy) as deduced by geological, seismological and volcanological information, Tectonophysics, 117, 39±58.

Davis, E.E., Lister, C.R.B., 1974. Fundamentals of ridge crest topography. Earth Planet. Sci.Lett. 21, 405 - 413.

Dannowski, A., H. Kopp, D. Klaeschen, F. Klingelhöfer, M.A. Gutscher, A. Krabbenhoeft, D. Dellong, M. Rovere, D. Grandorge, C. Papenberg, in prep. for JGR. Ionian Abyssal Plain: A window into the Tethys oceanic lithosphere.

De Vos, D., Paulssen, H., Fichtner, A., 2013: Finite-frequency sensitivity kernels for two-station surface wave measurements. Geophys. J. Int.194, 1042–1049.

Della Vedova, B. & G. Pellis, 1989. New heat flow density measurements in the Ionian sea, paper presented at VIII Convegno Nazionale, Gruppo Naz. di Geofis. Della Terra Solida, Rome

Dewey, J.F., Hempton, M.R., Kidd, W.S.F., Saroglu, F. & Sengör, A.M.C., 1986, Shortening of continental lithosphere: the neotectonics of Eastern Anatolia – a young collision zone, in Coward, M.P. & Ries, A.C., eds., Collision Zone Tectonics: Geological Society of London Special Publication 19, p. 3–36.

Dilek, Y., 2006, Collision tectonics of the Mediterranean region: causes and consequences

Dilek, Y. & Altunkaynak, S., 2007, Cenozoic crustal evolution and mantle dynamics of post-collisional magmatism in western Anatolia: International Geology Review, v. 49,

Dilek, Y. & Whitney, D.L., 2000, Cenozoic crustal evolution in central Anatolia: Extension, magmatism and landscape development, in Panayides, I., Xenophontos, C.

Doglioni, C., 1991. A proposal of kinematic modelling for W-dipping subductionsÐ-possible applications to the Tyrrhenian±Apennines system, Terra Nova, 3, 423±434.

Doglioni, C., Agostini, S., Crespi, M., Innocenti, F., Manetti, P., Riguzzi, F. & Savascin, Y., 2002, On the extension in western Anatolia and the Aegean sea, in Rosenbaum, G. & Lister, G.S., eds., Reconstruction of the evolution of the Alpine-Himalayan Orogen: Journal of the Virtual Explorer, v. 8, p. 169-183.

Doglioni, C., Innocenti, F. & Mariotti, G., 1998. On the geodynamic origin of Mt Etna, Atti 17u Gruppo Nazionale Geofisica Terra Solida, CNR, Roma.

Doglioni, C., Merlini, S. & Cantarella, G., 1999. Foredeep geometries at the front of the Apennines in the Ionian sea (central Mediterranean), Earth planet Sci. Lett., 168, 243-254.

Doglioni, C., Mongelli, F. & Pieri, P., 1994. The Puglia uplift (SE-Italy): an anomaly in the foreland of the Apenninic subduction due to buckling of a thick continental lithosphere, Tectonics, 13, 1309-1321.

Druckman, Y., 1981. Comments on the structural reversal model as a factor of the geological evolution of Israel, Isr. J. Earth Sci., 30, 44–48.

Druckman, Y., B. Buchbinder, G. M. Martinotti, R. Siman Tov & P. Aharon, 1995. The buried Afiq Canyon (eastern Mediterranean, Israel): A case study of a Tertiary submarine canyon exposed in Late Messinian times, Mar. Geol., 123, 167–185.

Eberhart, R. C., Y. Shi & J. Kennedy, Swarm Intelligence. Morgan Kaufmann, 2001.

Eyal, Y. (1996), Stress field fluctuations along the Dead sea rift since the Middle Miocene, Tectonics, 15(1), 157–170, doi:10.1029/95TC02619.

Faccenna, C., Jolivet, L., Piromelli, C. & Morallo, A., 2003, Subduction and the depth of convection in the Mediterranean mantle: Journal of Geophysical Research, v. 108, p. 2099, doi: 1029/2001JB001690.

Faccenna, C., Mattei, M., Funiciello, R. & Jolivet, L., 1997. Styles of back-arc extension in the Central Mediterranean, Terra Nova, 9, 126-130. Becker, T. W., Schäffer, A. J., Lebedev, S., & Conrad, C. P. ,2015. Toward a generalized plate motion reference frame. Geophys. Res. Lett., 42, doi:10.1002/2015GL063695, 3188-3196, 2015.

Faccenna, C., Becker, T. W., Auer, L., Billi, A., Boschi, L., Brun, J. P., Capitanio, F. A., Funiciello, F., Horvath, F., Jolivet, L., Piromallo, C., Royden, L., Rossetti, F., & Serpelloni, E., 2014. Mantle dynamics in the Mediterranean, Rev. Geophys., 52, 283 - 332, doi:10.1002/2013RG000444.

Farrugia, P. & Panza, G.F., 1981. Continental character of the lithosphere beneath the Ionian sea, in The Solution of the Inverse Problem in Geophysical Interpretation, pp. 327±334, ed. Cassinis, R., Plenum, New York.

Feld, C., Mechie, J., Hübscher, C., Hall, J., Nicolaides, S., Gurbuz, C., Bauer, K., Louden, K., Weber, M., 2017. Crustal structure of the Eratosthenes seamount, Cyprus and S. Turkey from an amphibian wide-angle seismic profile. Tectonophysics 700-701, 32-59.

Ferrucci, F., Gaudiosi, G., Hirn, A. & Nicolich, R., 1991. Ionian basin and Calabrian arc: some new elements from DSS Data, Tectonophysics, 195, 411-419.

Finetti, I. (1982), Structure, stratigraphy and evolution of central Mediterranean, Boll. Geofis. Teor. Appl., 24, 247-315

Finetti, I., 1982. Structure, stratigraphy and evolution of central Mediterranean, Boll. geo®s. Teor. Appl., 24, 247±315.

Finetti, I., 1985. Structure and evolution of the Central Mediterranean (Pelagian and Ionian seas), in Geological Evolution of the Mediterranean Basin, pp. 215±230, eds Stanley, D.J. & Wezel-Forese, C., Springer- Verlag, New York.

Finetti, I., Lentini, F., Carbone, S., Catalano, S. & Del Ben, A., 1996. Il sistema Appennino Meridionale-Arco Calabro-Sicilia nel Mediterraneo Centrale: studio geologico-geofisico, Boll. Soc. geol. It., 115, 529±559.

Frizon de Lamotte, D., C. Raulin, N. Mouchot, J. Christophe, W. Daveau, C. Blanpied & J. C. Ringenbach (2011), The southernmost margin of the Tethys realm during the Mesozoic and Cenozoic: Initial geometry and timing of the inversion processes, Tectonics, 30, 1–22, doi:10.1029/2010TC002691.

Gallais, F., Gutscher, M.A., Graindorge, D., Chamot-Rooke, N., Klaeschen, D., 2011. A Miocene tectonic inversion in the Ionian sea (central Mediterranean): evidence from multichannel seismic data. Journal of Geophysical Research—Solid Earth 116.

Gallais, F., M.-A. Gutscher, D. Graindorge, N. Chamot-Rooke, D. Klaeschen, 2011. A Miocene tectonic inversion in the Ionian sea (central Mediterranean): Evidence from multichannel seismic data, J. Geophys. Res. , 116, B12108, doi:10.1029/2011JB008505.

Gallais, F., M.-A. Gutscher, D. Klaeschen & D. Graindorge (2012), Two-stage growth of the Calabrian accretionary wedge in the Ionian sea (Central Mediterranean): Constraints from depth-migrated multichannel seismic data, Mar. Geol. ,326-328,28-45.

Gardosh, M. & Druckman, Y., 2006. Seismic stratigraphy, structure and tectonic evolution of the Levantine Basin, offshore Israel. In: Robertson, A. H. F. and Mountrakis, D. (eds.) Tectonic Development of the Eastern Mediterranean Region. Geol. Soc., London, Spec. Publ., 260:201-227.

Gardosh, M., Druckman, Y., Buchbinder, B. & Rybakov, M., 2008. The Levant Basin offshore Israel: Stratigraphy, structure, tectonic evolution and implications for hydrocarbon exploration: Geological Survey of Israel Report GSI/4/2008, 121 p.

Gardosh, M., Z. Garfunkel, Y. Druckman & B. Buchbinder, 2010. Tethyan rifting in the Levant Region and its role in Early Mesozoic crustal evolution, in: Evolution of the Levant Margin and Western Arabia Platform Since the Mesozoic, edited by C. Homberg and M. Bachmann, Geol. Soc. London Spec. Publ., 341, 9–36.

Garfunkel, Z., "Constrains on the Origin and History of the Eastern Mediterranean Basin," Tectonophysics, Vol. 298, No. 1-3, 1998, pp. 5-35. doi:10.1016/S0040-1951(98)00176-0

Garfunkel, Z., 1981. Internal structure of the Dead sea leaky transform (rift) in relation to plate kinematics, Tectonophysics, 80, 81–108.

Garfunkel, Z., 1998. Constrains on the origin and history of the Eastern Mediterranean basin, Tectonophys., 298, 5–35.

Garfunkel, Z., 1998. Constraints on the origin and history of the Eastern Mediterranean basin. Tectonophysics, 298, 5-35.

Garfunkel, Z. & B. Derin, 1984. Permian-early Mesozoic tectonism and continental margin formation in Israel and its implications for the history of the Eastern Mediterranean, in The Geological Evolution of the Eastern Mediterranean, edited by R. J. Dixon and A. H. F. Robertson, Geol. Soc. London Spec. Publ., 17, 187–201.

Ghalayini, R., J.-M. Daniel, C. Homberg, F. H. Nader & J. E. Comstock, 2014. Impact of Cenozoic strike-slip tectonics on the evolution of the northern Levant Basin (offshore Lebanon), Tectonics, 33, 2121–2142, doi:10.1002/2014TC003574.

Ginzburg, A. and Ben-Avraham, Z., 1987, The deep structure of the central and southern Levant continental margin. Ann.Tectonicae, 1, 105-115.

Granot, R., 2016. Palaeozoic oceanic crust preserved beneath the eastern Mediterranean. Nature Geosciences, DOI: 10.1038/NGEO2784

Halstenberg, D.B., 2014. Reconstruction of Tectonic Paleo-Heat Flow for the Levantine Basin (Eastern Mediterranean) - Implications for Basin and Petroleum System Modelling. MSc Thesis, RWTH Aachen, 85 p.

Hempton, M. R. (1987), Constraints on Arabian Plate motion and extensional history of the Red sea, Tectonics, 6(6), 687–705, doi:10.1029/TC006i006p00687.

Hinz, K., 1973. A low velocity layer in the upper crust of the Ionian sea, Geologie et Geophysique Marines. Rapports et Proces Verbaux Des ReunionsÐCommission Internationale Pour l'Exploration Scientifque de la Mer Mediterranee, 21, 865.

Hübscher, C., Pätzold, J., Arz, H.W., Ben-Avraham, Z., Berger, J., Dehghani, A., Dehning, K., Doormann, U., Ehrhardt, A., Farha, O., Gohl, K., Gradmann, S., Graumann, Grobys, J., Halaweh, S., Hall, J., Heinbockel, R., Hell, B., Kahl, G., Lazar, M., Meligy, M., Netzeband, G., Ochsenhirt, W., Seeberg-Elverfeldt, I., Sitko, R., Stöfen-Vosberg, B., Shattner, U., Thorwart, M., 2003. Black sea – Mediterranean – Red sea, Part 2. In: Pätzold, J., Bohrmann, G., Hübscher, C. (Eds.), 2003. Black sea – Mediterranean – Red sea, Cruise No. 52. Meteor-Berichte, Universität Hamburg, 178 pp.

Kennedy, J. & Eberhart, R., 1995: Particle Swarm Optimization, in Neural Networks. Proceedings, IEEE vol. 4 nov/dec 1995, pp. 1942-1948.

Kopp, H., Gutscher, M. A., Crozon, J., Dellong, D., Graindorge, D., Klaeschen, D., Klaucke, I., Klingelhöfer, F., Krabbenhoeft, A., Kurzawski, R., Matthiessen, T.,

Mögeltönder, J., Papenberg, C., Peyronnet, C., Prunier, C., Rovere, M., Schröder, H., Steffen, K. P., Wehner, D., Wieprich, M. und Wollatz-Vogt, M., 2015. Deep structure of the Ionian sea and Sicily Dionysus - Cruise No. M111, October 10 - November 1, 2014, Catania (Italy) – Catania (Italy). . METEOR-Berichte, M111 . DFG-Senatskommission für Ozeanographie, Bremen, Germany, 43 pp. DOI 10.2312/cr_m111.

Krijgsman, W., Hilgen, F.J., Raffi, I., Sierro, F.J., Wilson, D.S., 1999. Chronology, causes and progression of the Messinian salinity crisis. Nature 400, 652–655.

Le Pichon, X. & J.-M. Gaulier (1988), The rotation of Arabia and the Levant fault system, Tectonophysics, 153(1-4), 271–294, doi:10.1016/0040-1951(88)90020-0.

Leister, K., Makris, J., Nicolich, R. & Rancke, D., 1986. Crustal structure and crustal development in the Ionian sea, Condenses Des Travaux Presentes Lors Du Xxxe Congres-Assemblee Pleniere de la C.I.E.S.M., Commission Internationale Pour l'Exploration Scientifque de la Mer Mediterranee, Paris, 30, 84.

Longacre, M., Bentham, P., Hanbal, I., Cotton, J., Edwards, R., 2007. New Crustal Structure of the Eastern Mediterranean Basin: Detailed Integration and Modeling of Gravity, Magnetic, Seismic Refraction and Seismic Reflection Data. EGM 2007 International Workshop Innovation in EM, Grav and Mag Methods:a new Perspective for Exploration Capri, Italy, 4 p.

Makris, J., Ben-Avraham, Z., Behle, A., Ginzburg, A., Giese, P., Steinmetz, L. et al., 1983. Seismic reflection profiles between Cyprus and Israel and their interpretation. Geophys. J. R. Astron. Soc, 75, 575-591.

Makris, J., Ben-Avraham, Z., Behle, A., Ginzburg, A., Giese, P., Steinmetz, L., Whitmarsch, R.B. & Eleftheriou, S., 1983. Seismic refraction profiles between Cyprus and Israel and their interpretation, Geophys. J. R. astr. Soc., 75, 575–591.

Mcclusky, S., Balassanian, S., Barka, A., Demir, C., Ergintav, S., Georgiev, I., Gürkan, O., Hamburger, M., Hurst, K., Kahle, H., Kastens, K., Kekilidze, G., King, R., Kotzev, V., Lenk, O., Mahmoud, S., Mishin, A., Nadariya, M., Ozounis, A., Paradissis, D., Peter, Y., Prelipin, M., Reilinger, R., Sanli, I., Seeger, H., Tealeb, A., Toksöz, M.N. & Veis, G., 2000, Global Positioning System constraints on plate kinematics and dynamics in the eastern Mediterranean and Caucasus: Journal of Geophysical Research, v. 105, p. 5695–5719.

Mckenzie, D., Jackson, J.A., Priestley, K., 2005. Thermal structure of oceanic and continental lithosphere. Earth Planet. Sci. Lett. 233 (3–4), 337–349.

Meier, T., Dietrich, K., Stöckhert, B., & Harjes, H.-P., 2004. One-dimensional models of shear wave velocity for the eastern Mediterranean obtained from the inversion of Rayleigh wave phase velocities and tectonic implications, Geophysical Journal International, 156(1), 45 – 58.

Mele, G., 1998. High-frequency wave propagation from mantle earthquakes in the Tyrrhenian sea; new constraints for the geometry of the South Tyrrhenian subduction zone, Geophys. Res. Lett., 25, 2877-2880.

Miller, D. J. & N. I. Christensen, 1994. Seismic signature and geochemistry of an island arc:A multidisciplinary study of the Kohistan accreted terrane, northern Pakistan, d. Geophys. Res., 99, 11,623 - 11,642.

Montadert, L., S. Nicolaides, P. H. Semb & O. Lie (2013), Petroleum Systems offshore Cyprus, in Petroleum Systems of the Tethyan Region, edited by L. Marlow, C. Kendall & L. Yose, AAPG Spec. Publ., Tulsa, pp. 301–334.

Morelli, C., 1985. Geophysical contribution to knowledge of the Mediterranean crust, in Geological Evolution of the Mediterranean Basin, pp. 65±82, eds Stanley, D.J. & Wezel, F.C., Springer-Verlag, New York.

Morelli, C., M. Pisani & C. Gantar (1975), Bathymetry, gravity and magnetism in the Strait of Sicily and in the Ionian sea, Boll. Geofis. Teor. Appl. , 17, 39-58.

Moustafa, A. R. J. & M. H. Khalil (1994), Rejuvenation of the eastern Mediterranean passive continental margin in northern and central Sinai: New data from the Themed Fault, Geol. Mag., 131(4), 435–448.

Müller, R. D., M. Sdrolias, C. Gaina & W. R. Roest (2008), Age, spreading rates & spreading asymmetry of the world's ocean crust, Geochem. Geophys. Geosyst. ,9 , Q04006, doi:10.1029/2007GC001743.

Netzeband, G., Gohl, K., Hübscher, C., Ben-Avraham, Z., Dehghani, A., Gajewski, D., Liersch, P., 2006a. The Levantine Basin – crustal structure and origin. Tectonophysics 418, 178-188.

Netzeband, G.L., Hübscher, C.P., Gajewski, D., 2006b. The structural evolution of the Messinian evaporites in the Levantine Basin. Marine Geology 230, 249–273b.

Nicolosi, I., F. Speranza & M. Chiappini., 2006. Ultrafast oceanic spreading of the Marsili basin, southern Tyrrhenian sea: Evidence from magnetic anomaly analysis, Geology, 34 (9), 717-720 p. 431–453.

Panza, G. & Mueller, S., 1979. The plate boundary between Eurasia and Africa in the Alpine area, Mem. Soc. geol. It., 33, 43-50. Patacca, E. & Scandone, P., 1989. Post-Tortonian mountain building in

Parsopoulos, K.E. & Vrahatis, M.N., 2004. On the computation of all global minimizers through Particle Swarm Optimization, IEEE Trans. Evolut. Comput., 8(3), 211–224.

Pasyanos M.E., 2010. Lithospheric thickness modeled from long-period surface wave dispersion, Tectonophysics, 481, 38-50.

Piromallo, C. & Morelli, A., 2003. P wave tomography of the mantle under the Alpine-Mediterranean area, J. geophys. Res., 108(B2), 2065, doi:10.1029/2002JB001757.

Polonia, A., L. Torelli, P. Mussoni, L. Gasperini, A. Artoni & D. Klaeschen, 2011. The Calabrian Arc subduction complex in the Ionian sea: Regional architecture, active deformation and seismic hazard, Tectonics , 30, TC5018, doi:10.1029/2010TC002821.

Reilinger, R.E., Mcclusky, S.C. & Oral, M.B., 1997, Global positioning system measurements of present-day crustal movements in the Arabia-Africa-Eurasia plate collision zone: Journal of Geophysical Research, v. 102, p. 9983–9999.

Reilinger, R.E., Mcclusky, S.C., Vernant, P., Lawrence, S., Ergintav, S., Cakmak, R., Nadariya, M., Hahubia, G., Mahmoud, S., Sakr, K., Arrajehi, A., Paradissis, D., Al-Aydrus, A., Prilepin, M., Guseva, T., Evren, E., Dmitritsa, A., Filikov, S.V., Gomes, F., Al-Ghazzi, R. & Karam, G., 2006, GPS constraints on continental deformation in the Africa-Arabia-Eurasia continental collision zone and implications for the dynamics of plate interactions: Journal of Geophysical Research, v. 111, p. V05411, doi: 10.1029/ 2005JB004051.

Robertson, A. H. F., 1998. Mesozoic-Tertiary tectonic evolution of the Easternmost Mediterranean area: Integration of marine and land evidence, in Proceedings of the Ocean Drilling Program, Sci. Results, vol. 160, edited by A. H. F. Robertson et al., pp. 723–782, Ocean Drilling Program, College Station, Tex.

Robertson, A.H.F. & Dixon, J.E., 1984, Introduction: aspects of the geological evolution of the eastern Mediterranean, in Dixon, J.E. & Robertson, A.H.F., eds., The

Geological Evolution of the Eastern Mediterranean: Geological Society of London Special Publications, v. 17, p. 1–74.

Roveri, M., Flecker, R., Krijgsman, W., Lofi, J., Lugli, S., Manzi, V., Sierro, F.J., Bertini, A., Camerlenghi, A., De Lange, G., Govers, R., Hilgen, F.S., Hübscher, C., Meijer, P.Th., Stoica, M., 2014. The Messinian Salinity Crisis: past and future of a great challenge for marine sciences. Marine Geology, 352, 25-58.

Rybakov, M., Segev, A., 2004. Top of the crystalline basement in the Levant. Geomchemistry, Geophysics, Geosystems, 5(9), oi:10.1029/2004GC000690

Salisbury, M. H. & N. I. Christensen, 1987. The seismic velocitystruture of a traverse through the Bay of Islands ophiolite compleNewfoundland: An exposure of oceanic crustand upper mantld. Geophys. Res.,83, 805-817.

Schaeffer, A.J., Lebedev, S., 2013. Global shear-speed structure of the upper mantle and transition zone. Geophys. J. Int. 194, 417–449.

Schaeffer, A.J., Lebedev, S., 2015. Global heterogeneity of the lithosphere and underlying mantle: A seismological appraisal based on multimode surface-wave dispersion anal-

Schaeffer, A.J., Lebedev, S., Becker, T.W., 2016. Azimuthal seismic anisotropy in the Earth's upper mantle and the thickness of tectonic plates. Geophys. J. Int. 207, 901–933.

Schwab, F. and Knopoff, L., 1972: Fast surface wave and free mode computations, in Methods in Computational physics, Vol. 11, ed. Bolt, B.A., Academic Press, New York.

Sioni, S. (1996), Mer Ionienne et Apulie depuis l' ouverture de l' Ocean Alpin, PhD thesis, Univ. de Bretagne Occidentale, Brest, France.

Soomro, R.A., C. Weidle, L. Cristiano, S. Lebedev, T. Meier, 2016: Phase velocities of Rayleigh and Love waves in central and northern Europe from automated, broadband, inter-station measurements, Geophys. J. Int., 204, 517–534.

Spakman, W., Wortel, M.J.R. & Vlaar, N.J., 1988, The Hellenic subduction zone: a tomographic image and its geodynamic implications: Geophysical Research Letters, v. 15, p. 60–63.

Spudich, P., andJ. Orcutt, 1980. Petrology andporosity of an ocean crustal site: Results from wave form modeling of seismic refraction data, d. Geophys. Res.,85, 1409-1434.

Stampfli, G. M. & C. Hochard, 2009. Plate Tectonics of the Alpine Realm, in Ancient Orogens and Modern Analogues, edited by J. B. Murphy, J. D. Keppie & A. J. Hynes, Geol. Soc. London Spec. Publ., 327, 89–111.

Stein, C.A., Stein, S., 1992. A model for the global variation in oceanic depth and heat flow with lithospheric age. Nature 359 (6391), 123–129.

Stein, C.A., Stein, S., 2015. Are large oceanic depth anomalies caused by thermal perturbations? In: Foulger, G.R., Lustrino, M., King, S.D. (Eds.), The Interdisciplinary Earth: A Volume in Honor of Don L. Anderson: Geological Society of America Special Paper 514 and American Geophysical Union Special Publication. 71.

Steinberg, J., Gvirtzman, Z., Folkman, Y., Garfunkel, Z., 2011. Origin and nature of the rapid late Tertiary fi lling of the Levant Basin. Geology 39, 355-358

Taymaz, T., Westaway, R. & Reilinger, R. (Guest Eds.), 2004: Active faulting and crustal deformation in the eastern Mediterranean region, Special Issue of Tectonophysics 391, 1–4, 1–9, doi:10.1016/j.tecto.2004.07.005.

Van Hinsbergen, D.J.J., Hafkenscheid, E., Spakman, W., Meulenkamp, J.E. & Wortel, R., 2005, Nappe stacking resulting from subduction of oceanic and continental lithosphere below Greece: Geology, v. 33, p. 325–328.

Walley, C. D. (1998), Some outstanding issues in the geology of Lebanon and their importance in the tectonic evolution of the Levantine region, Tectonophysics, 298(1-3), 37–62, doi:10.1016/S0040-1951(98)00177-2.

Wang, Z. & Dahlen, F.A., 1995: Spherical-spline parameterization of 3-dimensional Earth models, Geophys. Res. Lett., 22, 3099–3102.

Weber, M., Abu-Ayyash, K., Abueladas, A., Agnon, A., Al-Amoush, H., Babeyko, A., Bartov, Y., Baumann, M., Ben-Avraham, Z., Bock, G., Bribach, J., El-Kelani, R., Förster, A., Förster, H.-J., Frieslander, U., Garfunkel, Z., Grunewald, S., Götze, H. J., Haak, V., Haberland, Ch., Hassouneh, M., Helwig, S., Hofstetter, A., Jäckel, K.-H., Kesten, D., Kind, R., Maercklin, N., Mechie, J., Mohsen, A., Neubauer, F. M., Oberhänsli, R., Qabbani, I., Ritter, O., Rümpker, G., Rybakov, M., Ryberg, T., Scherbaum, F., Schmidt, J., Schulze, A., Sobolev, S., Stiller, M., Thoss, H.,

Weckmann, U., Wylegalla, K., 2004, The crustal structure of the Dead sea Transform. Geophys. J. Int, 156, 655-681

Welford, K., Hall, J., Hübscher, C., Reiche, S., Louden, K., 2015a. Crustal seismic velocity structure from Eratosthenes seamount to Hecataeus Rise across the Cyprus Arc, eastern Mediterranean, Geophysical Journal International 200, 933-951.

Welford, K., Hall, J., Rahimi, A., Reiche, S., Hübscher, C., Louden, K., 2015b. Crustal structure from the Hecataeus Rise to the Levantine Basin, eastern Mediterranean, from seismic refraction and gravity modelling. Geophysical Journal International 203(3), 2055-2069

Westaway, B., 1994, Present-day kinematics of the Middle East and eastern Mediterranean: Journal of Geophysical Research, v. 99, p. 12071–12090.

Wilken, D., & Rabbel, W., 2012. On the application of Particle Swarm Optimization strategies on Scholte-wave inversion, Geophys. J. Int. (2012) 190, 580 – 594

Wortel, M. J. R. & W. Spakman (1992): Structure and dynamics of subducted lithosphere in the Mediterranean region, Proc. K. Ned. Akad. Wet., 95(3), 325–347.

Wortel, M. J. R. & W. Spakman 2000: Subduction and slab detachment in the Mediterranean-Carpathian region, Science, 290, 1910–1917.

Xie, X., Zhang, W. & Yang, Z., 2002. Adaptive Particle Swarm Optimization on individual level, in Proceedings of the Sixth International Conference on Signal Processing, Vol. 2, 1215–1218, IEEE, doi:10.1109/ICOSP.2002.1180009.

Zandt, G. & C. J. Ammon, 1995. Poisson's ratio of Earth's crust, Nature, 374, 152-155.

Chapter 4

High resolution 3-D shear wave velocity structure across the Alpine-Mediterranean mobile belt

4.1 Introduction

The Alpine-Mediterranean mobile belt, including north Africa and the Middle East, is characterized by a highly complicated and active tectonic setting. The closure of the Tethys ocean and the progressive subduction of its oceanic lithosphere as well as the opening of the Atlantic ocean played a substanial role in the evolution of the Mediterranean geology (Stampfli & Borel 2002; Carminati *et al.* 2004). As a result and since the Tertiary, a series of collisions between Gondwana-derived continental micro-continents and Eurasia have shaped the Mediterranean geology, which represents a prolonged interaction between the African-Arabian and Eurasian plates and provides a present-day geodynamic analog for the final stages of a continent-continent orogenic collision. The Mediterranean can be divided into three main basins: western, central, and eastern basins including the Pannonian-Carpathian system due to its tectonic affinity (Carminati *et al.* 2004; Faccenna *et al.* 2014). The western Mediterranean is younger (late Oligocene to present $\sim$ 25 Ma) than the central Mediterranean and eastern Mediterranean, which have been assumed to be relics of the Mesozoic to possibly Cenozoic Tethys ocean based on the low heat flow values (30-40 mW/m^2) and the 4-8 km of sedimentary cover of the Ionian Sea (Della Vedova & Pellis 1989; Carminati *et al.* 2004).

The African plate is converging towards the European plate since the last 84 Ma (Stampfli & Borel 2002; Faccenna *et al.* 2003). This convergence forced micro-plates and fragements

of continental and oceanic lithosphere to interact (Schmid *et al.* 2004; Boschi *et al.* 2010), which in turn invoked the coexistence of many different tectonic units: the progressive subduction of the Tethys oceanic lithosphere underneath the Calabrian and Hellenic Arc, whereas extension is currently occuring in the Tyrrhenian and Aegean back-arc basins; continental collision and the formation of the orogenic belts underneath the Alps, the Pyrenees, the Apennines, the Dinarides and the Carpathians (Dercourt *et al.* 1986; Dewey *et al.* 1989; Platt *et al.* 1989; Jolivet *et al.* 2009; Faccenna *et al.* 2014). The originally existing oceanic lithosphere between these converging plates have been subducted and partially obducted (ophiolitic terranes), except for the Ionian sea and the southeastern Mediterranean (Carminati *et al.* 1998; Stampfli & Borel 2002; Taymaz *et al.* 2004; Jolivet *et al.* 2009; Faccena *et al.* 2014; Garnot 2016). According to Dewey *et al.* (1986), the Arabia-Eurasia continental collision took place during the Late Eocene along the Bitlis-Zagros fold and thrust belt. This has been accomodated by a counter-clockwise rotation and westward motion of Anatolia along the right-lateral North Anatolian Fault (NAF) and the left-lateral East Anatolian Fault (EAF) (McKenzie 1972; Burke & Sengör 1986; McClusky 2000).

Figure (4.1) shows a topographic/bathymetric map of the entire Mediterranean with the age distribution of the oceanic lithosphere throughout the region after Müller *et al.* (2008). The age of the oceanic lithosphere in the Mediterranean is highly variable. The oldest oceanic lithosphere preserved in-situ is located underneath the Ionian sea (230-280 Ma, Müller *et al.* 2008) and the Herodutus Basin (340 Ma, Garnot 2016), whereas a recently formed oceanic lithosphere is located beneath the Tyrrhenian sea and the the Ligurian sea (Malinverno & Ryan 1986; Faccenna *et al.* 2004; Müller *et al.* 2008). On the other hand, extended continental lithosphere is found in the Alboran sea, Valencia Trough and Aegean sea, whereas a thick continental lithosphere is found underneath Adria.

Investigating the lithopshere-asthenosphere system across the Alpine-Mediterranean mobile belt is of fundamental importance to improve our uderstanding of its complexities and the geodynamic evolution. This has been the subject of plenty of tomographic studies with different scales, which might be subdivided into three major categories: body-wave models based on inversion of compressional or shear wave travel time perturbations (e.g., Spakmann 1986, 1991; Spakmann *et al.* 1993; Piromallo & Morelli 2003; Spakman & Wortel 2004; Amaru 2007; Li *et al.* 2008; Koulakov *et al.* 2009; Giacomuzzi *et al.* 2011); surface-wave models based on inversion of Love- and Rayleigh wave dispersion measurements (e.g., Snieder 1988; Marquering & Snieder 1996; Villasenor *et al.* 2001; Pasyanos & Walter 2002; Boschi *et al.* 2004; Schivardi & Morelli 2009; Nita *et al.* 2016) and full wave form inversion (Fichtner *et al.* 2013a,b; Zhu *et al.* 2012, 2016; Fichtner & Villasenor 2015). Down to the mantle transition zone underneath the Mediterranean, the tomographic images indicate the

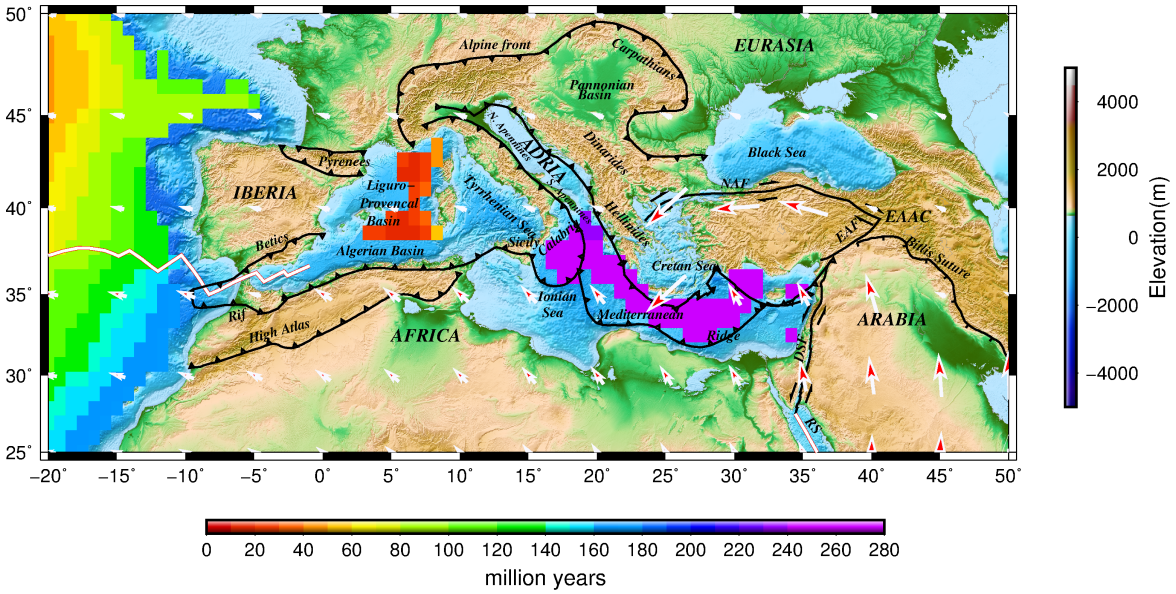

Fig. 4.1 Topographic and bathymetric map of the Alpine-Mediterranean mobile belt with the age distribution of the oceanic lithosphere in the region after Müller *et al.* (2008). The white arrows shows the absolute plate motion after Becker *et al.* (2015). Tectonic lines from Faccenna *et al.* (2014).

presence of several high velocity anomalies interpreted as subducted slabs (Piromallo & Morelli 2003; Spakman & Wortel 2004; Li *et al.* 2008; Koulakov *et al.* 2009; Giacomuzzi *et al.* 2011). Lippitsch *et al.* (2003) calculated a high resolution local-scale model using P-wave travel-time tomography with careful crustal corrections specifically for the Alps. They show in the western-central Alps high velocity anomaly which has been attributed to the southeast subducting Eurasian slab, whereas in the eastern Alps a northeast dipping Adriatic slab has been imaged down to ∼250 km.

For the Mediterranean basin, seismic tomography has dramatically constringed the range of the possible scenarios for the capturing the kinematics and geodynamic evolution of lithosphere-asthenosphere system underneath the area. However, there are still many controversial issues that are considered far from being unambiguously imaged such as the switches in the subduction polarities, the geometry of the subducting slabs, the forethoughted N-S subduction beneath Anatolia, subduction of Adria and Eurasia beneath the Alps, the opening of the slab gaps beneath the Alps, Apennines and Dinarides and the continuity of the Alboran subduction. Indeed, the existing tomographic models are highly variable in the sense of either they are of high lateral resolution but covering a limited areas (e.g., Lippitsch *et al.* 2003; Mitterbauer *et al.* 2011) or are regional models of low resolution and consequently can not resolove the small-scale features of the upper mantle structure

(Schivardi & Morelli 2009). On the other hand, the P-wave models have clearly imaged the deep structure of the Mediterranean mantle, but suffer from the poor depth sensitivity of the lithosphere and asthenosphere due to the uneven ray path coverage that is highly depending on the stations and sources distribution (Spakman *et al.* 1993; Piromallo & Morelli 2003; Wortel & Spakmann 2004).

Surface waves, due to their high sensitivity to the isotropic as well as the anisotropic 3D shear velocity variations with depth, are well suited to study properties of the lithosphere-asthenosphere system underneath the Mediterranean allowing especially to illuminate the structure of the regions characterized by low seismicity and sparse distribution of seismic stations. In this chapter, we use information extracted from dispersive nature of the fundamental mode Rayleigh wave phase velocities in a very borad period range (8-300 seconds) in order to construct a high-resolution 3-D shear wave velocity model in order to investigate the lithosphere-asthenosphere system underneath the entire Mediterranean including the Alps and the adjacent regions.

4.2 Local dispersion curves

Surface wave tomography has been utilized to estimate with a high lateral resolution (< 100 km) 2-D period-dependent phase velocity maps spanning a very broad period range (8 - 350 s), showing the spatial distribution and strength of the isotropic and azimuthally anisotropic phase velocity perturbations. These maps provide the local phase velocity dispersion curves at each geographical grid node on the map. With 30 km inter-grid spacing, the local dispersion curves have been constructed. Phase velocity measurements in this period range show particular sensitivity to the vertical variations of the shear wave velocities in broad depth intervals including the crust, mantle lithosphere and asthenosphere with the advantage of avoiding, to large extent, the vertical smearing effects often associate with body wave measurements ((e.g. Ekström *et al.* 1997; Ritzwoller & Levshin 1998; Adam & Lebedev 2012; Lebedev *et al.* 2013; Meier *et al.* 2016). Their depth sensitivity is period-dependent: the longer the periods penetrate and sample the Earth deeper and are sensitive to mantle lithosphere and athenosphere ($\geq$ 250 km, $\sim$200 s period) whereas short periods are of particular sensitivity to shallow crust ($\leq$ 15-20 km, $\sim$10 s period).

The accuracy of the phase velocity measurements $C(\omega)$ might be biased by noise, complexities in the crustal wavefield and presence of strong lateral hetereogeneities (de Vos *et al.* 2013). Such perturbations render the dispersion curves to be a bit rough, at least at the higher frequencies. Therefore, the roughness of each dispersion curve is evaluated and the

rough parts of each curve are excluded. This evaluation is done by calculating the first partial derivative of measured phase velocity $C'(\omega)$ with respect to frequency and comparing it with the corresponding value of the background model $C'_o(\omega)$. For this purpose, a point-wise 1-D background models have been extracted through a 3-D reference model composed of CRUST1.0 (Laske *et al.* 2013) and PREM (Dziewonski & Anderson 1981). These models take into account the first order structural informations to which surface wave dispersion are highly sensitive, primarily the presence of sedimentary basins or Moho depth. Then a summation of the absolute values of the first derivative deviation from the background model is performed in the frequency domain over a moving window. The absolute value is taken so that positive as well as negative deviations are treated in the same way. The frequency range of the summation is increasing linearly towards the lower frequencies, to account for the greater first derivative of the phase velocities at lower frequencies. The evaulated roughness of each local dispersion curve is used to define the uncertainties of the phase velocities at each frequency. Furthermore, we cut the higher frequencies part of the local disersion curve at which their standard deviation values exceeds a certain threshold, which is in turn an empirically defined frequency-dependent value (in this case (th_S = 0.075). This can be formulated as:

$$S(\omega_i) = \sum_{\omega_i=\omega_i-d(\omega_i)}^{\omega_i+d(\omega_i)} \left|\frac{C'(\omega_j) - C'_o(\omega_j)}{C_o(\omega_j)}\right| \times \Delta f < th_S, \tag{4.1}$$

where, Δf represents the sampling rate in the frequency domain. Figure (4.2) illustrates the criterion for measuring the roughness of the local phase velocity curves at two different cases. The smoothed first derivatives (standard deviations) of the phase velocities are plotted as a function of frequency. The gray dashed line represents the empirically-defined constant threshold (maximum standard deviation) at all frequencies. On the left panel, a smooth curve where the overall standard deviations are below the threshold, therefore the entire curve will be considered without rejecting any of the higher frequencies. On the right panel, another example where we reject some of the rough samples at higher frequencies which their standard deviations exceed the threshold.

The constructed local dispersion curves plotted on top of each other in a comparison to PREM are shown in figure (4.3). The phase velocities as well as the newly defined standard deviation values plotted as function of frequencies are shown on the left panel and the right panels, respectively. Red and blue colors represent the standard deviation-based rejected and accepted parts of the dispersion curves, respectively. Figure (4.4) shows the color-coded minimum (top) and maximum (bottom) considered periods for each dispersion

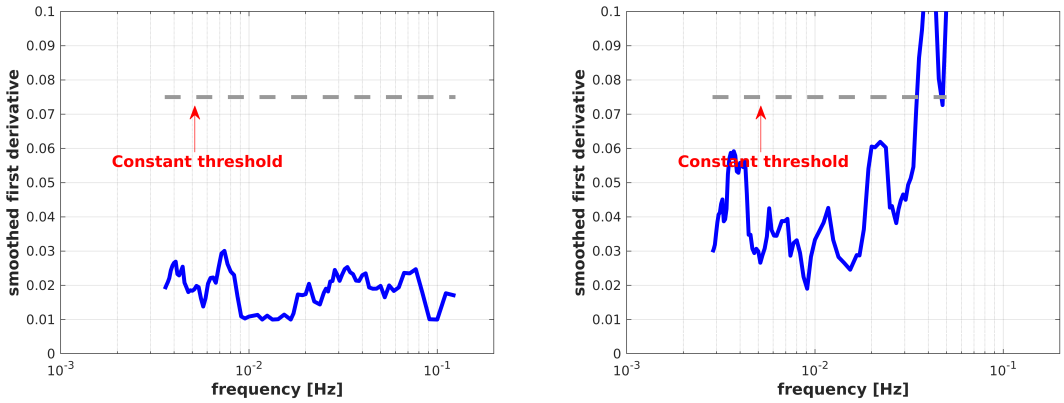

Fig. 4.2 Illustration of the criterion for automated cutting of the higher frequencies; the smoothed first derivatives (standard deviation) of the phase velocities are plotted as function of frequency. The gray dashed line represents a constant threshold (0.075) (a) A smooth curve where the overall standard deviations are below the threshold. (b) Another example where cutting is done for higher frequencies, at which the standard deviation exceeds the threshold.

curve after excluding the rough high frequency parts of the curves. The majority of the local dispersion curves exploit a wide range of frequecies starting from 8.0 - 10.0 sec to 350 sec reflecting the smoothness of the constructed dispersion curves at the continental areas. On the other hand at oceanic areas, the minimum considered periods ranging from 15 - 20 sec. This is clearly indicating the effect of presence of thick sedimentary basins on the propagation of surface waves and their dispersion at higher frequencies due to complexities of the wavefield that include multiple scattering, amplification, the formation of secondary wavefronts, and subsequent healing of the wavefronts. This may introduce systematic bias to the dispersion measurements at short periods (Feng & Ritzwoller 2017). This phenomenon has been discussed deeply in plenty of studies (e.g., Aki & Larner 1970; Kawase 1996; Rawlinson & Sambridge 2004; Day *et al.* 2012; Feng & Ritzwoller 2017). This can also be traced on figure (4.5) which shows the average standard deviation at each grid node at periods shorter than 25 s (top) and the overall average standard deviation (bottom). At short periods, the highest standard deviation values are associated with the presence of sedimentary basins.

Examples of the final local dispersion curves are shown in figure (4.6). Their locations are indicated on the 60 s period phase velocity map (top), and the corresponding individual phase velocity curves are plotted on top of each other in a comparison to PREM (bottom). The strong variability in the phase velocities at short periods below about 25 s is due to the influence of crustal properties on the dispersion measurements. Low phase velocities in the Hellenic Arc and the Ionian sea are caused by large sedimentary thicknesses, whereas the

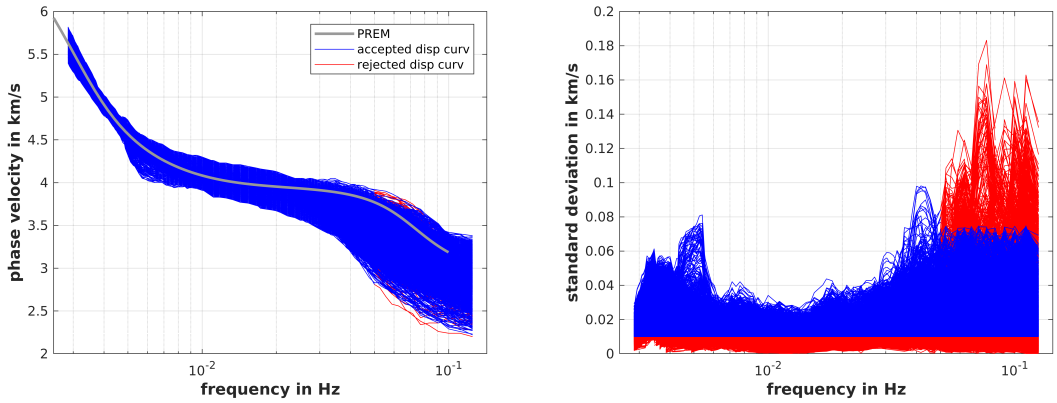

Fig. 4.3 **Left:** Local Rayleigh wave phase velocity curves constructed from the dispersion maps in broad period range are plotted on top of each other; phase velocities as function of frequencies. The accepted measurements (blue) and the rejected parts of the curves (red) after cutting of the higher frequencies. **Right:** Newly defined standard deviations are shown as function of frequencies for all curves. Red and blue represent the standard deviation-based rejected and accepted parts of the curves, respectively.

thick crustal thickness underneath Anatolia and eastern Alps lowers the phase velocities in this period range. Between about 20 s and 200 s phase velocities are sensitive to properties of the mantle lithosphere and asthenosphere. Phase velocities in the Hellenic arc and the Ionian sea are significantly larger than in the Anatolia, Tyrrhenian sea and Liguria but also larger than the global average obtained from PREM.

4.3 Inversion for 1-D Shear velocity models

A promising newly elaborated stochastic global optimization algorithm, the particle swarm optimization (PSO) is utilized to invert the local Rayleigh dispersion curves to 1-D shear wave velocities as function of depth (Eberhart & Kennedy 1995; Wilken & Rabbel 2012; El-Sharkawy *et al.* in preparation). This algorithm is developed by imitating the social behavior of bird flocking or fish schooling (Kennedy & Eberhart 1995). A swarm is made up of an employed number of particles (i.e., vectors in the parameter space), each is considered a solution for the problem and are able to move within the boundaries of the parameter space in order to fully explore it. In the PSO, these particles can exchange heuristic information in the form of local interaction to enable generating the behavior of adaptive search so that each particle in the swarm adjusts its position in the search space based on the best position it has found so far as well as the position of the known best-fit particle of the entire swarm and finally converges to the global best position of the whole search space (Eberhart *et al.* 2001;

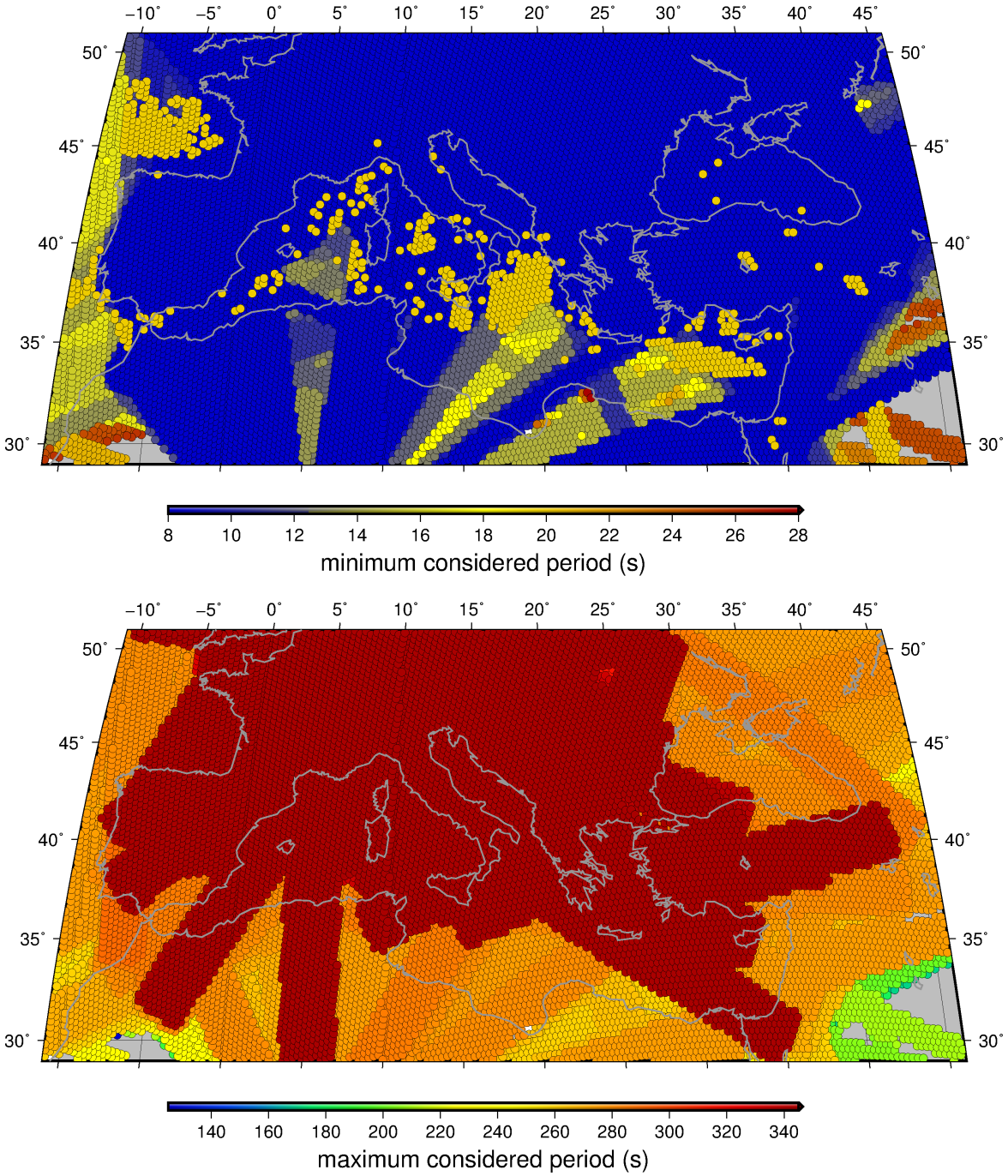

Fig. 4.4 The minimum (top) and the maximum (bottom) considered period at each local dispersion curves are shown at the nodes locations.

Xie *et al.* 2002; Parsopoulos *et al.* 2004). The current application of the particle swarm optimization allow for random local search in order to speed up the convergence of the entire swarm towards the global best position. In addition, a random excursion to best position of

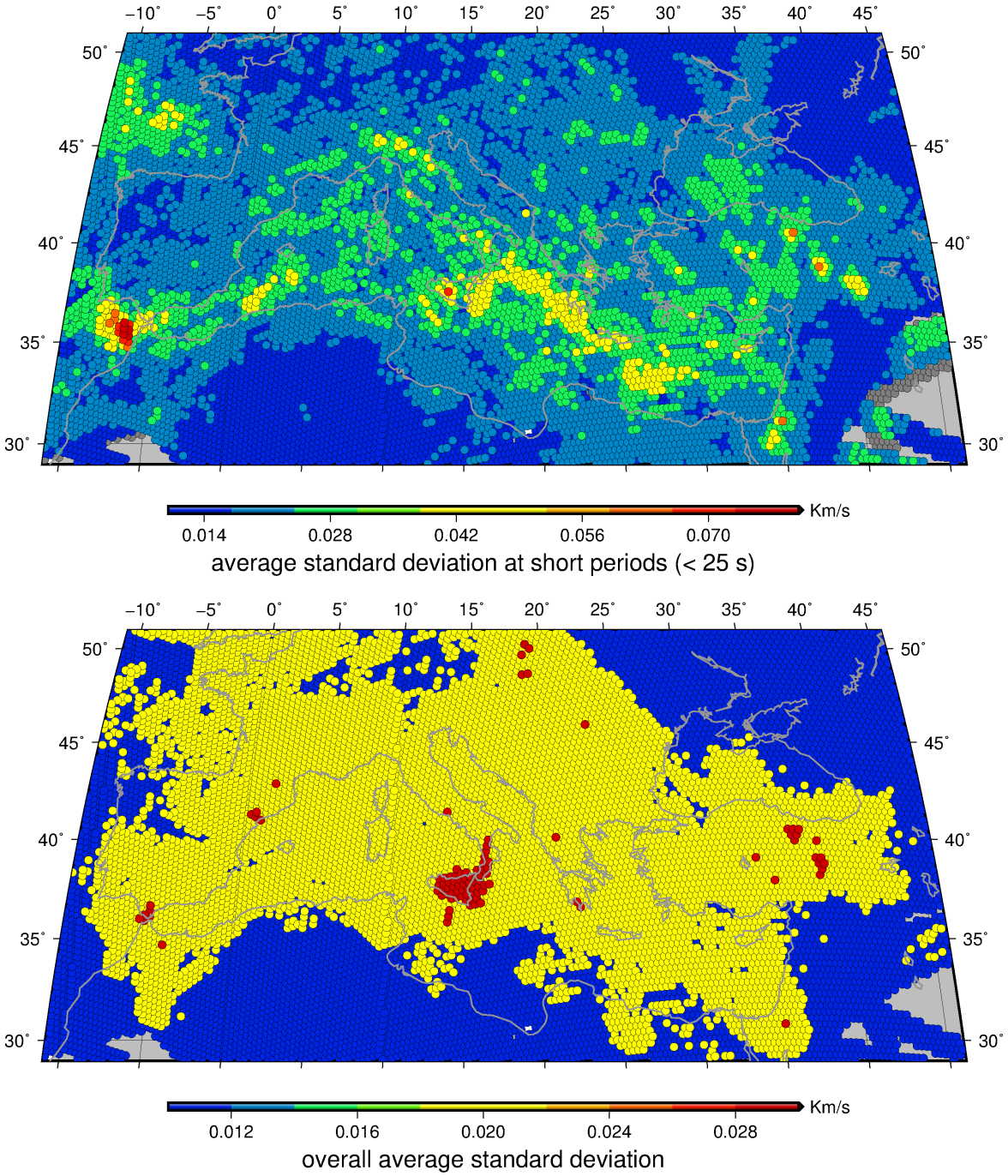

Fig. 4.5 Average standard deviation at each grid node. a) Overall average standard deviation at periods shorter than 25 s. b) Overall average standard deviation at all periods.

the other particles is perfomed in order to ensure the exploration of the entire model space (El-Sharkawy *et al.* in preparation).

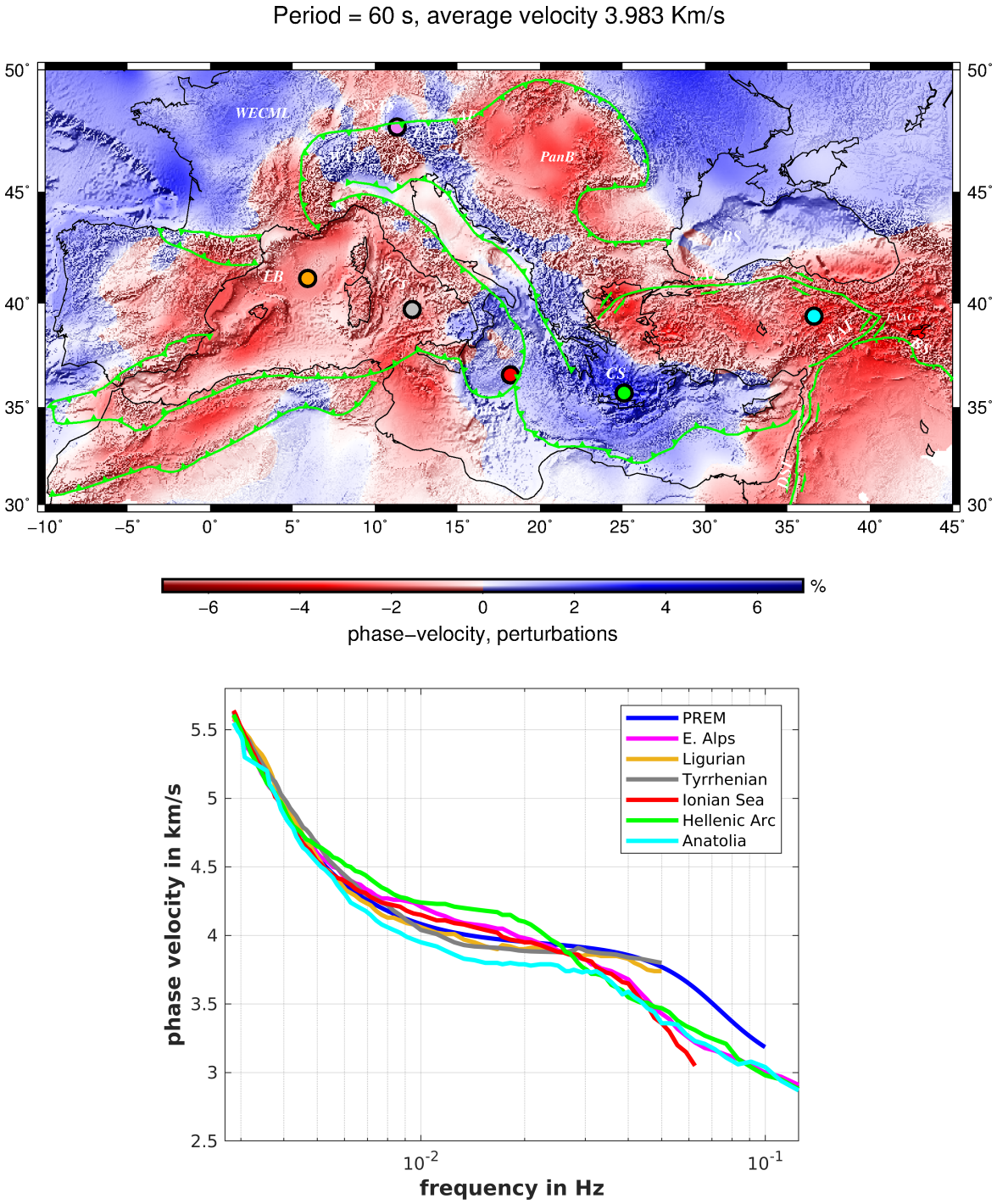

Fig. 4.6 Examples of the local dispersion curves as constructed from the phase velocity maps. Their locations are indicated by circles on the 60 s period phase velociy map.

For the inversion, we construct a range of possible models by defining the (±) maximum perturbations of the shear wave velocity of the background model for each individual layer.

The background model consists of a large number of fine layers representing the considered depth range for the inversion and is only used as *a priori* information to define the boundaries of the parameter space. The poorly constrained background model often leads to large trade-offs between the crustal and upper mantle velocities. Therefore, a 3-D reference model composed of CRUST1.0 (Laske *et al.* 2013) and PREM (Dziewonski & Anderson 1981) is used to calculate more specifically point-wise 1-D background models of the crust and upper mantle that includes a water layer where appropriate, topography of the sea bottom and the Moho as well as 3D variations in the V_s and V_p in the sediments and crystalline crust. Shear velocities in the mantle are taken from PREM (Dziewonski & Anderson 1981). Each 1-D model consists of a large number of fine layers representing the considered depth range for the inversion. Each i^{th} layer is characterized by the P-wave velocity, S-wave velocity, the density and the thickness. These models take into account the first order structural variations to which surface wave dispersion are strongly sensitive, primarily to Moho depth or the presence of sedimentary basins.

The model parameterization is highly flexible, as we allow for different perturbation orders of the background model and they are defined for a continuous, specified depth range, from Earth's surface down to 900 km. The parametrization is given in terms of arrays defining the maximum perturbations in shear-wave velocity (km/s) at each depth node as well as the perturbation in depth of the different discontinuities in km. Seven parameters describe the model in the crust with a constant velocity changes. Furthermore, the perturbation of the Moho depth is a parameter of the inversion. In the upper mantle, a cubic perturbation in the shear wave velocity is considered from the Moho down to the 410 km discontinuity. A quadratic perturbation is applied to the mantle transition zone followed by another linear perturbation below the 660 km discontinuity is considered down to 900 km. The 410 and 660 km discontinuities are kept fixed. This is generally a uniform parametrization that can be applied over the whole stduy area. However, we included the water layer in the background model in case of oceanic domains.

A graphical representation of the model parameterization for the crust (at both on-shore and of-shore domain) as well as for the upper mantle are shown in figure (4.7). The dots represent the depth nodes where they are fixed discontinuities and their velocities are to be varied, whereas white horizontal bars indicate the node locations where the discontinuities are to be varied. Black line shows constant perturbations of the shear velocity of the background model, green line indicates the linear gradient perturbations, blue line represents the quadratic velocity variations, while the red line represnts the depth range of cubic velocity perturbations. Tables (4.1) and (4.2) summerize the developed strategy for parameterizing the inversion of the dispersion curves using the particle swarm optimization algorithm at continental and

oceanic domains, respectively. The regularization of the model parameters is adjusted to the individual layers including the damping of differences between the shear wave velocity perturbations at the different depth nodes in order to ensure the smoothness of the final model (El-Sharkawy *et al.* in preparation).

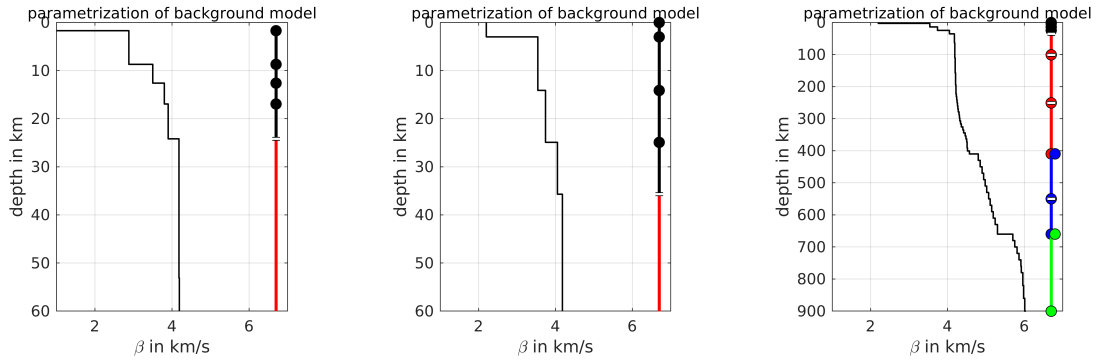

(a) With water layer on top (b) Without water layer on top (c) Full parameterization

Fig. 4.7 Graphical representation of the parameterization of the background model for the particle swarm inversion. a) Off-shore parameterization of the crust taking into account the bathymetery. b) On-shore parameterization of the crust. c) Full parameterization of the considered depth range including the crust, upper mantle and mantle transition zone down to 900 km. The dots show the depth nodes where they are fixed discontinuities and their velocities are varied, whereas white horizontal bars show the node locations where the discontinuities are to be varied. Black line shows constant perturbations of the shear velocity of the background model, green line indicates the linear gradient perturbations, blue line represents the quadratic velocity variations, while the red line represnts the depth range of cubic velocity perturbations.

Table 4.1 PSO parameterization of the background model at on-shore domains.

nodes	**pmax**	**pdis**	**pwvabs**	**pwvdiff**	**pdepth**	**pwdabs**	**porder**	**paniso**	**pcoup**	**comment**
1	1.2	1	0.2	0.2	0	0	0	0	0	"sediments"
2	1.2	1	0.2	0.3	0	0	0	0	0	"u. crust"
4	1	1	0.2	0.5	0	0	0	0	0	"m. crust"
6	1	1	0.7	0	0	0	0	0	0	"l. crust"
8	0.7	0	0.7	0.6	10	0.5	3	0	0	"Moho"
16	0.7	0	0.4	0.7	15	0.5	-3	0	0	"100 km"
31	0.7	0	0.4	2.5	25	0.5	-3	0	0	"250 km"
48	0.7	1	5.5	1	0	0.0	2	0	0	"410 km"
60	0.7	0	0.4	5.5	30	0.5	-2	0	0	"540 km"
65	0.7	1	5.5	1	0	0	1	0	0	"660 km"
74	0	1	0.4	0	0	0				"900 km"

Table 4.2 PSO parameterization of the background model at off-shore domains.

nodes	pmax	pdis	pwvabs	pwvdiff	pdepth	pwdabs	porder	paniso	pcoup	comment
2	1.2	1	0.2	0.2	0	0	0	0	0	"sediments"
3	1.2	1	0.2	0.3	0	0	0	0	0	"u. crust"
5	1	1	0.2	0.5	0	0	0	0	0	"m. crust"
7	1	1	0.7	0	0	0	0	0	0	"l. crust"
9	0.7	0	0.7	0.6	10	0.5	3	0	0	"Moho"
17	0.7	0	0.4	0.7	15	0.5	-3	0	0	"100 km"
32	0.7	0	0.4	2.5	25	0.5	-3	0	0	"250 km"
49	0.7	1	5.5	1	0	0.0	2	0	0	"410 km"
61	0.7	0	0.4	5.5	30	0.5	-2	0	0	"540 km"
66	0.7	1	5.5	1	0	0	1	0	0	"660 km"
75	0	1	0.4	0	0	0				"900 km"

During the inversion, the ratio between S- and P-wave velocities and the ratio between S-wave velocity and density are kept fixed. The model parameters are iteratively improved until a good fit between theoritical and measured dispersion curves is obtained. Theoretical phase velocities for elastic, isotropic, 1-D model are calculated using the Knopoff method which is based on Thomson-Haskell matrix formalism and an earth flattening approximation (Knopoff 1964; Schwab & Knopoff 1972). With this method, the sphericity corrections are taken into account. The Thomson-Haskell algorithm synthesizes the surface wave dispersion functions by constructing layer matrices which relate the components of motion at one interface in a layered structure to those at the next. The product of these layer matrices is then relating the components of motion at the deepest interface to those at the free surface. This layer-matrix product is used to construct the synthetic dispersion curve and comparing it with the observed dispersion. The initial model is then iteratively refined until it fits the observations. Iterations are controlled to avoid artefacts like spurious low velocity zones. On each iteration, repeated forward calculations ($\sim$ 8000) are carried out to search for the global minimum. With this algorithm we aim to select models randomly and to retain the subset of models that fit our selection criteria. Consequently, the inversion results in abundle of acceptable models whose variability provides some information about model uncertainties.

Figures 4.8 and 4.9 depict the isotropic 1-D shear velocity models resulted from inverting some selected dispersion curves (see Fig. 4.6) using the particle swarm optimization approach. Generally, bundles of isotropic SV models of all inversions at each region are plotted colour-coded according to the misfit values. While the blue bundle of the models represent the models with the lowest misfit values, the gray ones represent the models with the highest misfit values. The coarse-dashed line indicates the SV model with the lowest misfit value (best-fitting model) at each location. The models exhibit considerable lateral heterogeneities

throughout the region and are interpreted with respect to average shear wave properties of the deeper crust and of the upper mantle down to a depth of approximately 300 km. On the top panel, the corresponding measured and best-fitting synthetic dispersion curves are presented in a comparison to a global reference model (PREM, Dziewonski & Anderson 1981). Note the overall very good consistency between measured phase velocities and synthetic curves for the best-fitting models. The models exhibit considerable lateral heterogeneities throughout the region and are interpreted with regard to average shear wave properties of the deeper crust and of the upper mantle down to a depth of approximately 300 km.

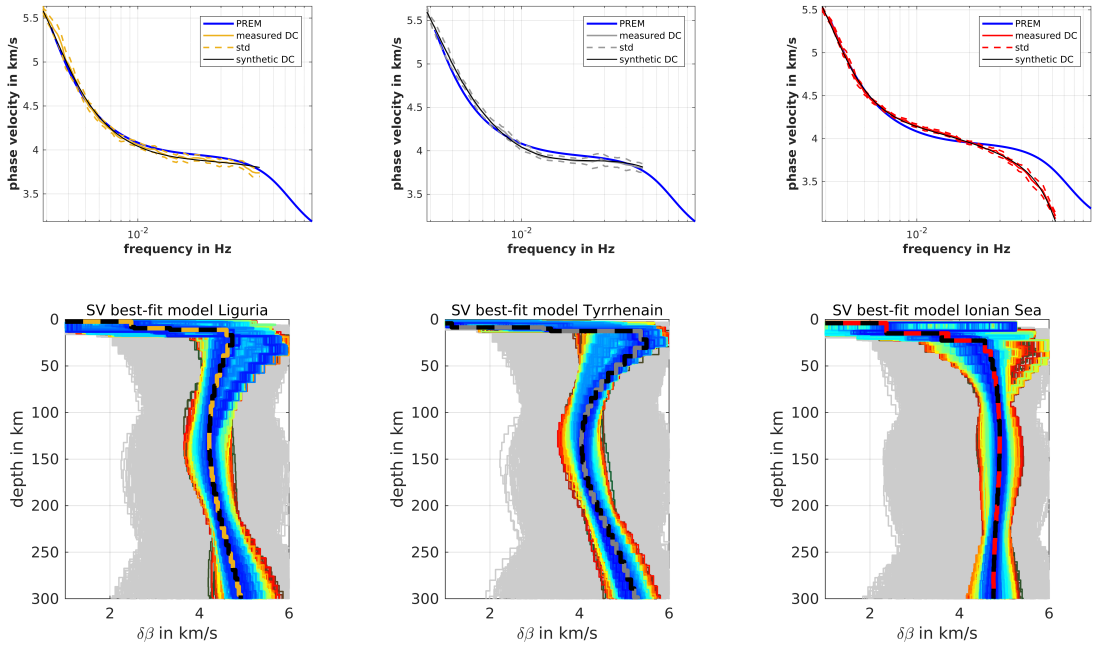

(a) Ligurian Sea (b) Tyrrhenian Sea (c) Ionian Sea

Fig. 4.8 The 1-D shear-velocity models resulting from the model search and their corresponding misfit between the measured and the best-fitting synthetic dispersion curves at: a) Ligurian Sea, b) Tyrrhenian Sea and c) Ionian Sea. The preferred model (coarse-dashed) is the best-fitting with lowest misfit. The corresponding dispersion curves on the top of each panel.

The 1-D models show the overall structure of the crust and lithosphere, respectively, at different locations over the Mediterranean region. Thin crustal thickness has been detected underneath oceanic domains including Liguria, Tyrrhenian Sea and Ionina Sea (figures 4.8a, b and c, respectively). The crustal thickness is getting thicker underneath the orogenic belts as in the eastern Alps and Anatolia (4.9a and b, respectively). On the other hand, the lithospheric thickness is thin in Liguria and Tyrrhenian Sea representing a recently formed oceanic domains (Quaternary of age, ∼20 - 25 Ma, Müller *et al.* 2003), whereas the

lithospheric thickness underneath the much older Ionian ocean have a thicker lithosphere associated with a pronounced high shear velocities down to a depth $\sim 200km$. The 1-D model underneath the Ligurian Sea (Fig. 4.8a) shows low shear wave velocities over a depth range from roughly 50 to 180 km, whereas underneath the Tyrrhenian sea (Fig. 4.8b) a much pronounced decrease in the shear wave velocities is observed in the depth range from 70 - 200 km which is highly consistent with the results shown in different tomographic images (e.g., Piromallo & Morelli 2003). Greve *et al.* (2012), indicated that the northern Tyrrhenian Sea shows a shallow asthenosphere around 70 km depth. Figure 4.9a reveals a pronounced high shear velocity down to a depth of approximately 250 km. This might be related to the subducted slab in the Eastern Alps. According to Koulakov *et al.* (2009), a continuous high-velocity zone is observed under the eastern Alpine chain at a depth of 300 km which is in agreement with previous studies (e.g. Lippitsch *et al.* 2003, Mitterbauer *et al.* 2011; Zhao *et al.* 2016; Kästle *et al.* 2018). There is ongoing debate regarding this fast anomaly as it is complicated and not clear either it is related to a continuous European subducted slab or deep Adriatic one or a combination of both European and Adriatic subductions in the uppermost mantle underneath the Eastern Alps. Interestingly, an anomalously thin

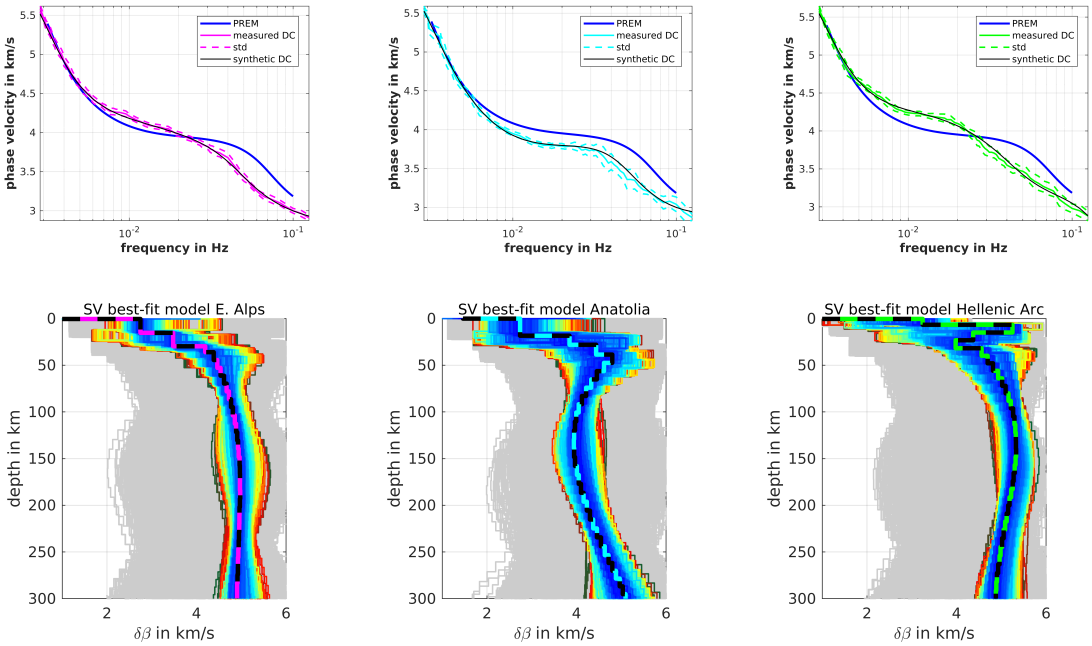

(a) Eastern Alps (b) Anatolia (c) Hellenic arc

Fig. 4.9 The same as figure 4.9 but at different locations. a) Underneath the a) The Eastern Alps, b) Anatolia and c) Hellenic arc.

lithospheric thickness has been detected underneath eastern Anatolia (Fig. 4.9b) overlying a

shallow asthenospheric materials as indicated by a strong decrease in the shear velocities from a depth of approximately 70 km and downwards. P- and S-receiver function studies proved the presence of a hot and partially molten asthenospheric materials underlying thin lithosphere in that region (Zor *et al.* 2003; Özacar *et al.* 2008; Vanacore *et al.* 2013). The decrease in the seismic shear velocities has been attributed to upwelling of the asthenospheric materials that followed the detachment of the northward subducting Arabian lithosphere (Faccenna 2003; Biryol *et al.* 2011; Fichtner *et al.* 2013a,b). This is highly supporting the high elevation of Eastern Anatolia (Biryol *et al.* 2011; Fichtner *et al.* 2013a). Along the Hellenic arc, the obtained 1-D model shows significantly increased shear velocities in the upper mantle. This is highy consitent with previous results obtained from inverting two-station phase velocity dispersion measurements (Meier *et al.* 2004) and also in tomographic images (e.g, Li *et al.* 2008). Wortel and Spakman (2000) related this high velocity anomaly to the subducted African oceanic lithosphere underneath the Hellenic arc.

4.4 3-D isotropic Rayleigh wave velocity model

The 3-D shear wave velocity model down to depth of approximately 300 km is constructed as juxtaposition of the obtained 1-D phase velocity inversions at each grid node. Figures (4.10 - 4.15) illustrate the obtained model as map views and vertical depth slices. The shear velocity variations are shown with respect to a depth-depedent regional-average velocity as indicated on each map. In the color code, red represents slower velocities than the average, whereas blue is faster. Due to the strong sensitivity of upper mantle velocities to variations in the temperatures, velocity anomalies are interpreted in terms of temperature anomalies (Goes *et al.* 2000; Nolet *et al.* 2007). The clear distinction between regions of significantly high shear velocities and regions of reduced velocities is characterizing the derived 3-D shear velocity structure, which in turn displays significant variations across the region both laterally and vertically showing high correlation with the major tectonic features. Moreover, it provides new insights on the structural evolution of the Mediterranean by providing information on the subducted lithosphere in the upper mantle asthenosphere especially at the aseismic parts of the subducting slabs. The increased strength of heterogeneities is most likely due to the unprecedented high resolution (< 100 km), i.e. less spatial and vertical smearing.

4.4.1 The Mediterranean's lithosphere-asthenosphere system

In order to unravel the controversial issues regarding the the Alpine-Mediterranean mobile belt and its complicated history of subduction and continental colissions, a clear images of the the lithosphere-asthenosphere system are fundamentally required. Figure (4.10 - 4.11) shows selected map views of the obtained 3-D shear wave velocity variations at depths of 100, 150, 200, and 230 km depth, respectively. They show structural features which were also detected in many earlier tomographic models. The main characteristics of the model at 100 km is the presence of widespread high velocity large-scale feature underneath the cold and thick continental mantle lithosphere in western Europe (WECML).

The very old lithosphere beneath eastern Europe is dominated by high velocities reflecting its cratonic nature (Precambrian East European Craton, EEC) which extends down to depths larger than 230 km (Fig. 4.11). The Alboran slab (AlbS) in the west appears from beneath the Moho and downwards as a curved feature following the geometry of the Gibraltar arc. It continues as separate entity down to depths of > 210 km, then a detached part of the Alboran basin appears from depths of 230 km and downwards from underneath the Betics to the Valencia Trough. Moreover, a pronounced high velocity anomaly occupies the southeastern Mediterranean which is associated with the subduction of African lithosphere underneath the Hellenic arc (HeS), north of Crete. It can be traced down to larger depths with shift towards the north as a function of increasing depth. The general strike of this anomaly is roughly NW-SE on the Aegean side. On the other hand, the distribution of the oceanic lithosphere in the Eastern Mediterranean (EMOL) is clearly imaged underneath the Ionian Sea and the Herodotus basin reaching the Eratosthene Seaamount in the East and extends down to depths of approximately 210 km. Figure (4.12) shows a vertical cross section through this oceanic lithosphere, which crosses the Arabian plate from the East, towards the Levant basin, Herodotus basin, Ionian Sea and ends at the Tyrrhenian sea. Clearly, there is a sharp contrast from slow to fast shear velocities which indicates a clear transition from the shallow asthenosphere (MeA) beneath the Middle East and the continental Levant basin to the thick oceanic lithosphere beneath the Herodotus basin and westwards. The thickness of the oceanic lithosphere is about $\sim$ 200 - 230 km. Directly below the Calabrian arc, the subducting slab (CalS) is imaged clearly as a continuous high-velocity anomaly which broadens with depth especially below 200 km, where it starts to underlie the eastern part of the Tyrrhenian sea.

Significant feature of the model at 100 km and downward is the widespread distribution of low velocity anomalies underneath the extensional basins (e.g., the Tyrhhenian, the Agean and the Pannoinan basins). A corridor of low velocities starts from beneath northwestern Africa (Morocco) and northward connecting the western Mediterranean as-

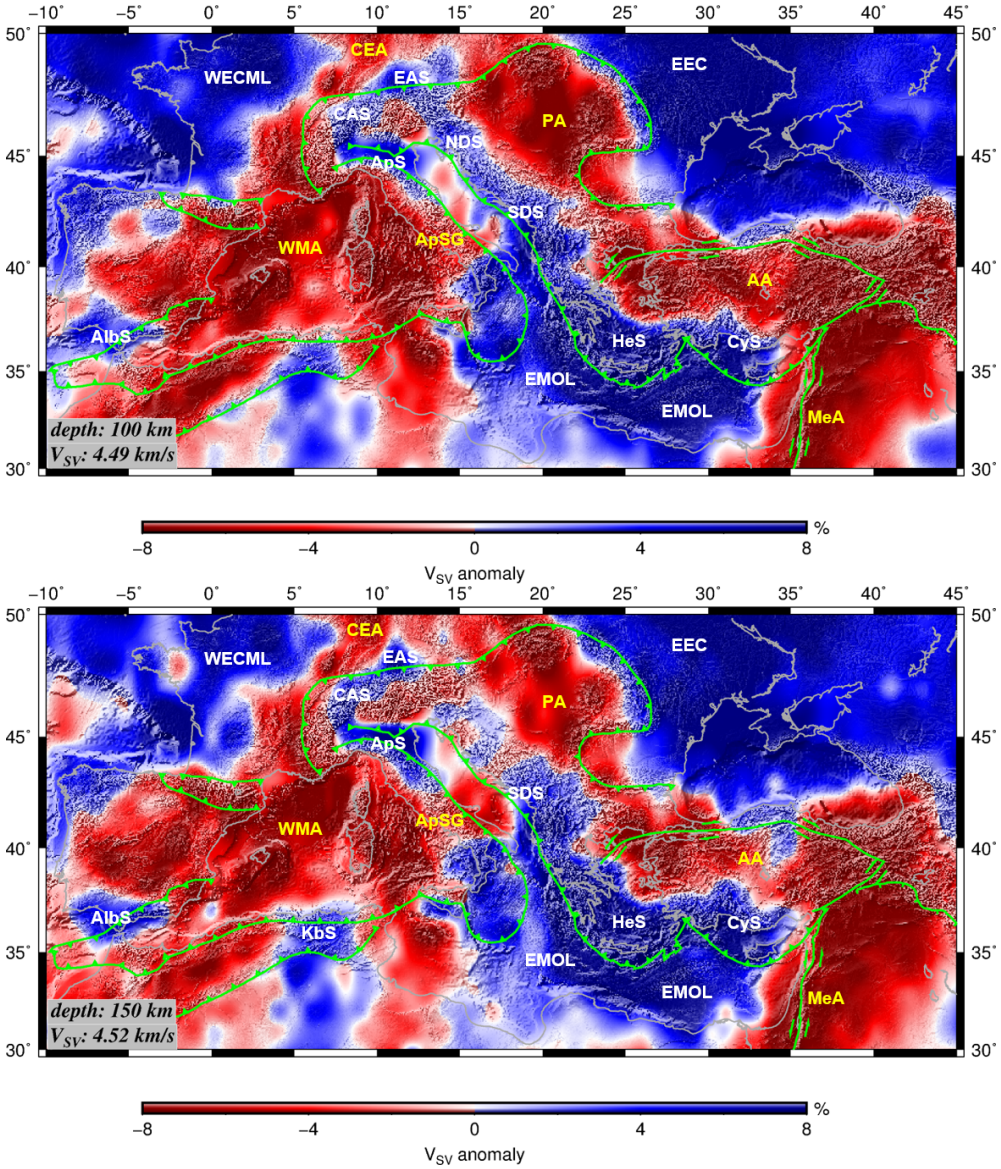

Fig. 4.10 Horizontal slices through the 3-D shear wave velocity model at depths of 100 (top) and 150 km (bottom) as indicated on each map. Shear wave velocity perturbations are shown with respect to a depth-dependent average velocity value as indicated on the map. The green lines indicate the major tectonic lines. AA: Anatolia Asthenosphere, AlbS: Alboran Slab, ApS: Apenninic Slab, ApSG: Apenninic Slab Gap, AS: Anatolian slab, CalS: Calabrian Slab, CEA: Central European Asthenosphere, CyS: Cyprus Slab, EMOL: Eastern Mediterranean Oceanic Lithosphere, CAS: Central Alpine Slab, EAS: East Alpine slab, EEC: East European Craton, HeS: Hellenic Slab, MeA: Middle East Asthenosphere, NDS: Northern Dinaridic Slab, NDSG: Northern Dinaridic Slab Gap, PA: Pannonian Asthenosphere, SDS: Southern Dinaridic Slab, WECML: Western European Contintal Mantle Lithosphere, WMA: Western Mediterranean Asthenosphere.

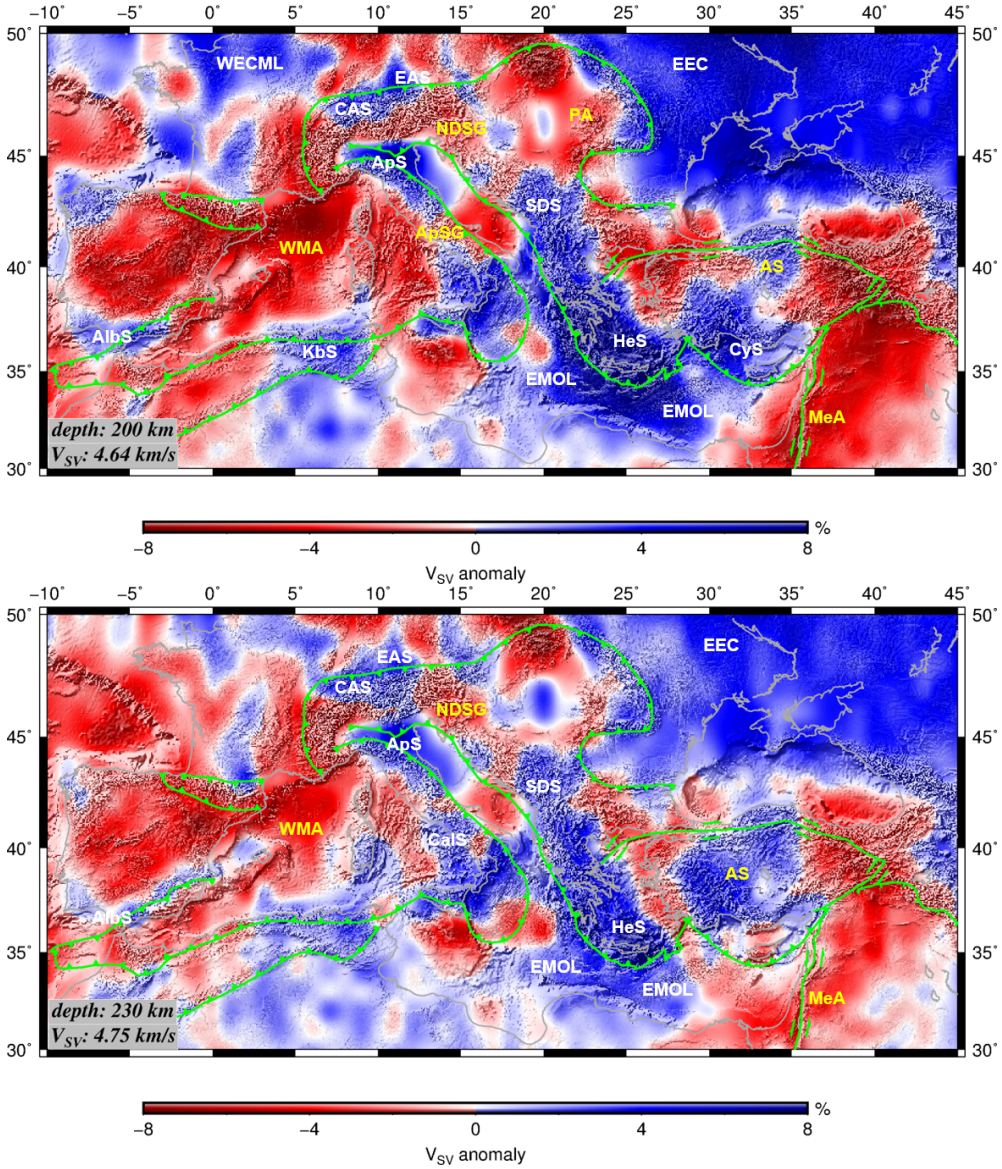

Fig. 4.11 Horizontal slices through the 3-D shear wave velocity model at depths of 200 (top) and 230 km (bottom) as indicated on each map. Shear wave velocity perturbations are shown with respect to a depth-dependent average velocity value as indicated on the map. The green lines indicate the major tectonic lines. AA: Anatolia Asthenosphere, AlbS: Alboran Slab, ApS: Apenninic Slab, ApSG: Apenninic Slab Gap, AS: Anatolian slab, CalS: Calabrian Slab, CEA: Central European Asthenosphere, CyS: Cyprus Slab, EMOL: Eastern Mediterranean Oceanic Lithosphere, CAS: Central Alpine Slab, EAS: East Alpine slab, EEC: East European Craton, HeS: Hellenic Slab, MeA: Middle East Asthenosphere, NDS: Northern Dinaridic Slab, NDSG: Northern Dinaridic Slab Gap, PA: Pannonian Asthenosphere, SDS: Southern Dinaridic Slab, WECML: Western European Contintal Mantle Lithosphere, WMA: Western Mediterranean Asthenosphere.

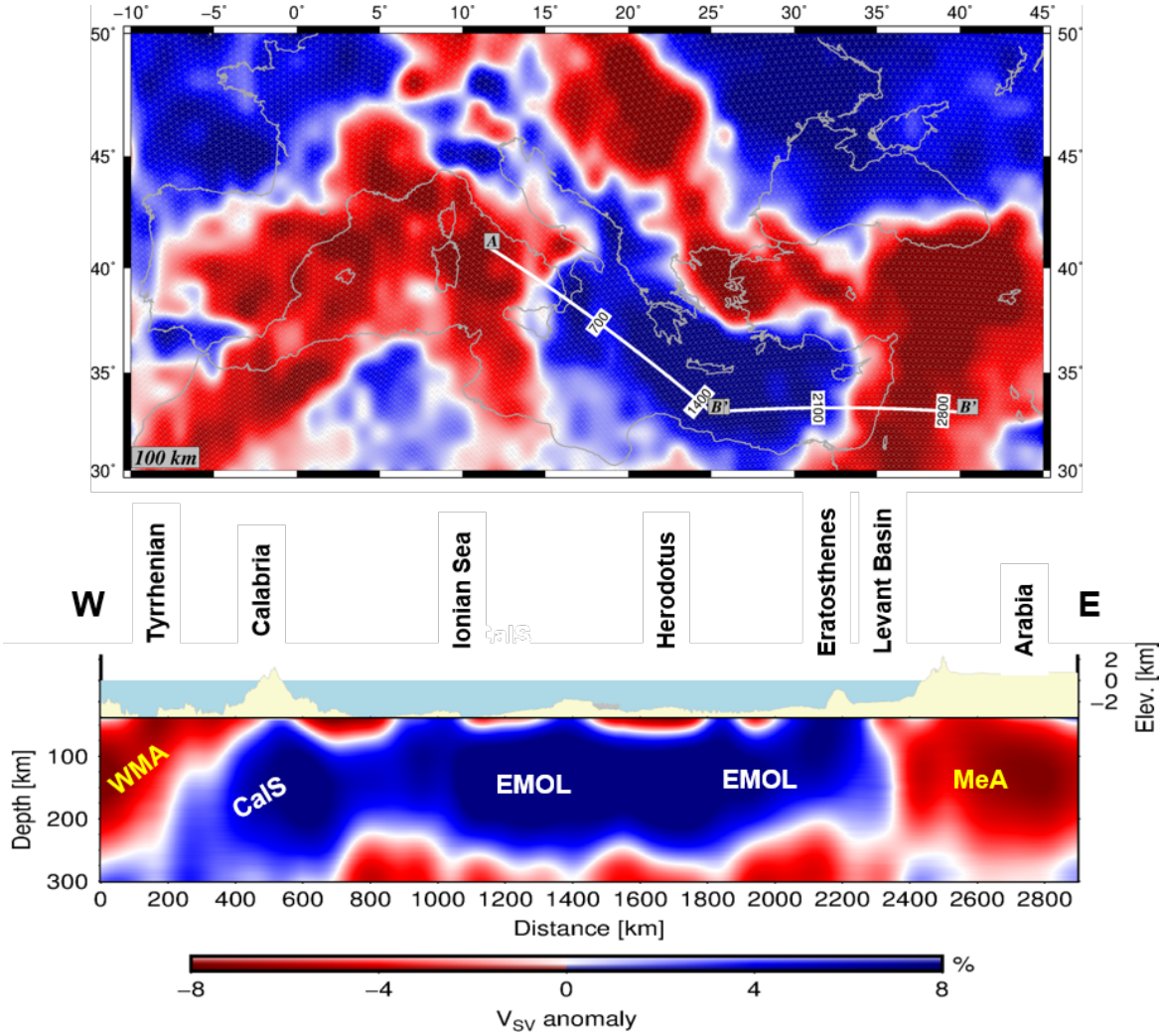

Fig. 4.12 Vertical cross section through the Eastern Mediteranean Oceanic Lithosphere. The location of the profile is showm 100 km depth map (top). CalS: Calabrian Slab, EMOL: Eastern Mediterranean Oceanic Lithosphere, MeA: Middle East Asthenosphere, WMA: Western Mediterranean Asthenosphere.

thenosphere (WMA) with central Europe Rift System through Rhöne strike, the Bohemian Massif and the Massif Central that extends to include the Pannonian basin, Aegean, Anatolia and Middle East regions. These pronounced low velocities are widespread beneath centres of volcanic activity include the Massif Central and the Valencia Trough. The pronounced slow shear velocities underneath the Ligurian sea can be explained by the presence of a recently-formed (Neogene), thin oceanic lithosphere (Handy *et al.* 2010), whereas in the Pannonian basin can be attributed to the shallow asthenosphere that is formed due to the asthenospheric upwellings after the break-off of the eastward subducting Adriatic slab since $\sim$ 35 Ma (Handy *et al.* 2015). Underneath the entire Anatolia, a widespread pattern of high

amplitude low velocity anomalies are imaged clearly from depths shallower than 80 km and downwards, which correlates very well with the distribution of the Cenozoic volcanism in this region (Ozgenc & Ilbeyli 2008). The presence of the upwelling of asthenospheric materials underneath Anatolia explains the 2.0 km high topography that might be afftected by uplifting after the detechment of the subducted Arabian lithosphere. Below 180 km depth, the model underneath Anatolia is characterized by the presence anomalous high velocities which we interpert as the detached Anatolian slab (AS), with typical Vs values of 4.7-4.8 km/s, reaching more than 5 km/s at depths > 250 km.

Embedded in this low velocity anomalies is a continuous, complicated, small-scale structure of high velocity anomalies underneath the northern Appennines, the Alps and the Dinarides. At depth of 100 km and deeper, a well developed high velocity anomaly along the northern Appennines and the Po plain basin that might be related to the subduction of the Adriatic plate. While there is no indications for high velocities along the central and the southern part of the the Appennines, a reduced shear wave velocities have been imaged in the central Appennines which we attributed to a slab gap (ApSG). In Central Alps, the 100 km depth map shows a band of high velocity anomaly that seems to be continuous and steep with increasing depth as it does not show a significant horizontal changes through the different map views (Figs. 4.10 and 4.11). This anomaly can be attributed to the Eurasian subducting slab where it can be traced down to depths larger than 270 km (CAS) and partly down to 300 km. On the other hand, the situation in the eastern Alps is much more complicated than in the central part, however the model shows a high velocity anomaly that can be traced down to depth of approximately > 280 km (EAS). The map view of 200 km depth (Fig. 4.11) indicates that the high velocities underneath both the Central and Eastern Alpine slabs are getting closer to each other, whereas it shows a separated high velocity block underneath the Po plain.

Furthermore, a slow shear velocities are imaged underneath the western Alps representing a shallow asthenosphere, which might be taken as an evidence for horizontal slab tearing. A narrow belt of high velocity anomaly embbeded in the low velocities is representing the deep lithospheric structure along the Dinarides from depths shallower than 100 km. This can be attributed to the subducted Adriatic slab along the Dinarides. There is a clear difference in the structure of the subducting slab between the northern and southern Dinarides. While the high velocity anomalies underneath the southern Dinarides (SDS) can be traced down to depths larger than 250 km, a slow shear velocity anomalies are clearly imaged underneath the northern part, from depths of 150 km and downwards showing a gap in the northern Dinarides (NDSG).

4.4.2 Subducted slabs in the Mediterranean

Probing the plate boundaries along the uppermost part of a subduction zone is still an evasive task in seismic tomography (Kissling & Lahr 1991; Spakmann *et al.* 1993). The subduction system in the Alpine-Mediterranean mobile belt is clearly imaged by our 3D shear wave velocity model and presented here in vertical depth slices (Figs. 4.13 - 4.15). They are visible in the form of high shear velocity anomalies embedded in the surrounding low velocities. In western Mediterranean, pronounced low velocity anomalies appear beneath the Ligurian basin, the Massif Central, but also beneath southern Iberia. The tomographic cross section (Fig. 4.13, profile $A-A^{'}$) crosses the Betics and Iberian Massif in the south towards the western Europe and Massif Central. It shows the Alboran subducted slab (AlbS) as a E-W dipping high velocity anomaly down to depth of appoximately > 200 km. On the other hand a thick continental mantle lithosphere can be traced down to 200 km underneath western Europe (WECML). The Alboran slab is also shown on the profile $B-B^{'}$ (Fig. 4.13), which extends NW-SE from the Betics towards the Ligurain sea. It also shows a rather broad asthenospheric upwelling associated with the relatively thin lithosphere beneath the Ligurian sea (WMA). The shallow asthenosphere is associated with high topography that could be formed due to the uplifting and upwelling of the asthenospheric materials. The profile $C-C^{'}$ (Fig. 4.13), shows clearly the N-S subducted African lithosphere underneath the Kabylides mountains and northward underneath Corsica island, which we interpret at the Kabylides slab (KbS).

The complexity of the subdction system through the Alpine region is shown in figure (4.14). The cross-section ($A-A^{'}$) shows a south-north directed section of the model that starts from Sardinia and extends to cross the Apennines, Po plain basin and central Alps and ends at the nothern foreland. It shows a shallow asthenosphere characterized by velocity reductions underneath the western Mediterranean (WMA) and central Europe (CEA). Moreover, a 100-150 km thick, nearly vertical high velocity anomaly which we attribute to the Eurasian subducting slab in central Alps (CAS) and penetrate deeper in to the asthenosphere. In the proximity of CAS, another deep seated, $\sim$ 200 km thick, high velocity anomaly underneath the Po plain basin and northern Appennines is imaged clearly. We interpret this anomaly as the Adriatic lithosphere is subdcuting underneath the northern Apennines (ApS). The Apenninic slab is well illuminated along the cross section ($B-B^{'}$), where it is west-east directed normal of the strike of the Apenninic slab. It looks steeply dipping and very close to the western Alps. This cross section extends to the northern Dinarides where it shows a high velocity anomaly down to depth of 150 km indicating a shallow subduction of Adria beneath northern Dinarides followed by a slab gap from 150 km and downwards.

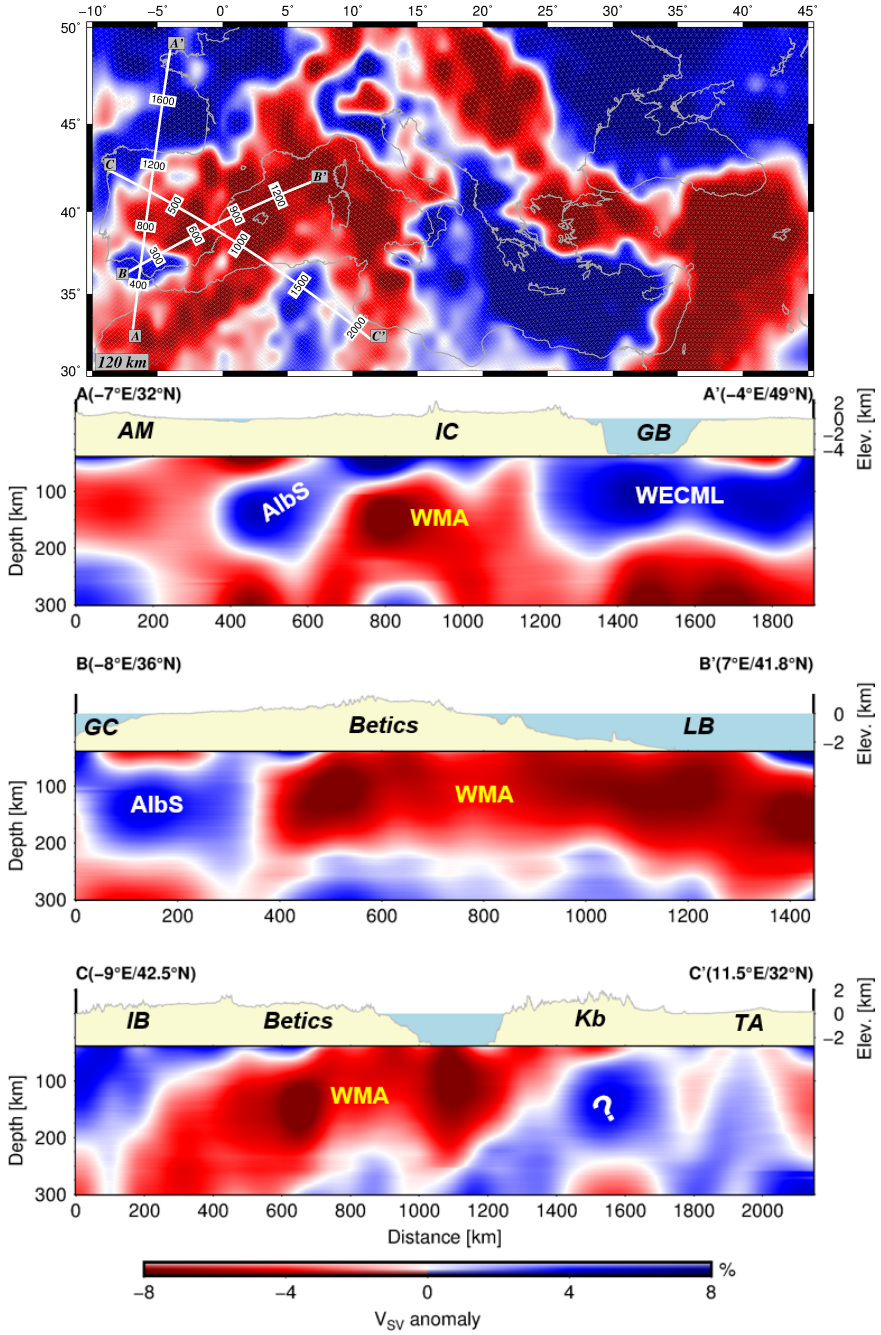

Fig. 4.13 Vertical slices through the 3D model in the western Mediterranean. In depth range from 40 - 300 km, variations in absolute velocities with respect to the regionally averaged 1-D model are shown. The topography along each profile is plotted on top of the vertical velocity cross sections. AlbS: Alboran slab, AM: Atlas mountains, IB: Iberia basin, GC: Gulf of Biscay, GC: Gulf ofCadiz, Kb: Kabylies mountains, TA: Tunisian atlas, WECML: western Europe continental mantle lithosphere, WMA: western Mediterranean asthenosphere. The location of the profiles are shown on the map view of 120 km.

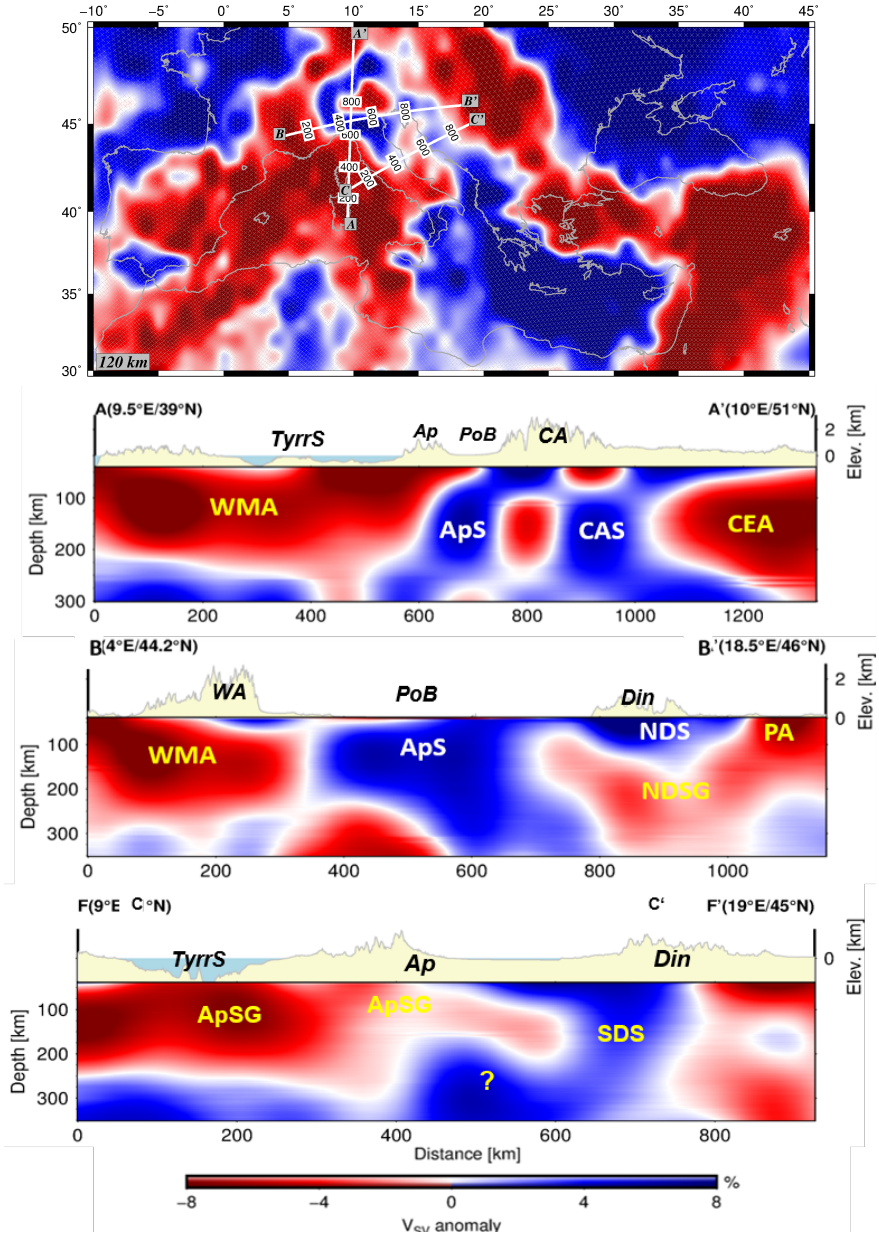

Fig. 4.14 Vertical slices through the 3D model in the Alps. In depth range from 40 - 300 km, variations in absolute velocities with respect to the regionally averaged 1-D model are shown. The topography along each profile is plotted on top of the vertical velocity cross sections. Ap: Apennines, ApS: Apenninic slab, ApSG: Apenninic slab gap, CA: Central Alps, CAS: central ALpine slab, CEA: central Europe asthenosphere, Din: Dinarides, NDS: north Dinaridic slab, NDSG: north Dinaridic slab gap, PA: Panonnian asthenosphere, PB: Panonnian basin, SDS: south Dinaridic slab, TyrrS: Tyrrhenian Sea, WA: Western Alps, WMA: western Mediterranean asthenosphere. The location of the profiles are shown on the map view of 120 km.

Beneath the western Alps, we propose a slab break-off of the Eurasian slab as we observe a reduced seismic velocities indicating its shallow astheosphere. The profile ($C-C^{'}$, Fig. 4.14) is SW-NE oriented which extends from the Tyrrhenian sea passing through the central Apennines towards southern Dinarides. It depicts a slow shear velocities representing shallow asthenosphere beneath Central Apennines which we interpret as a slab gap (ApSG). This indicates that a slab tear in the Apenninic is propagating towards the south and is connected to the shallow asthenosphere underneath the Tyrrhenian sea (WMA) and are associated with high topography. At depths larger than 250 km, a widespread high velocity anomaly underneath the Tyrrhenan sea and as well as the Central Apennines is detected. Along the southern Dinarides towards the Hellinides, a high velocity anomaly down to depth of > 300 km indicating a progressive subduction of Adria in the southern Dinarides.

The profile ($A-A^{'}$, Fig. 4.15) is SW-NE oriented and extends from Corsica towards the Central Apennines, northern Dinarides and passing through the Pannonian basin reaching the East European Craton (EEC). It shows a high velocity anomaly down to 150 km which we interpret as the Adriatic plate is subducting underneath the northern Dinarides. On the other hand a continuous belt of reduced shear velocities connecting the shallow asthenosphere beneath the Tyrrhenian extensional basin (WMA), Central Apennines (ApSG) and the Pannonian basin (PA). The end of the profile crosses a thick high velocity anomaly that can be traced down to a depth of 250 km and has been interprested as the East European Craton. The very thick lithosphere of the East European Craton is well illuminated along the N-S directed profile ($B-B^{'}$, Fig. 4.15) which extends southward to the Middle East. It shows a clear transition from the high velocity anomalies that have been encountered north of the north Antolian fault (NAF)indicating the thick continental mantle lithosphere of Eurasia and the EEC to the low velocities underneath Anatolia. This extremely low velocity anomalies observed beneath Anatolia (AA) and middle East (MeA), a typical observation that is evident in areas of thick continental crustal structure and correlates very well with the high elevation plateau along the region, have been attributed to its thin lithospheric thickness and the progressive upwelling of the asthenospheric materials that is correlates well with the distribution of the Cenozoic volcanism in this region. A high velocity anomaly north of Cyprus (CyS) is clearly imaged and interpreted as northward dipping African oceanic lithosphere subducted from the Cyprus trench. This is clear along the SW-NE directed profile ($C-C^{'}$, Fig. 4.15) which extends from the Herodotus basin towards Cyprus, Anatolia and ends at the EEC. Additionally, a robust well-developed N-S dipping fast anomaly is noted underneath Anatolia (AS) that is approaching the Cyprus slab (CyS) at depth of approximately 200 km.

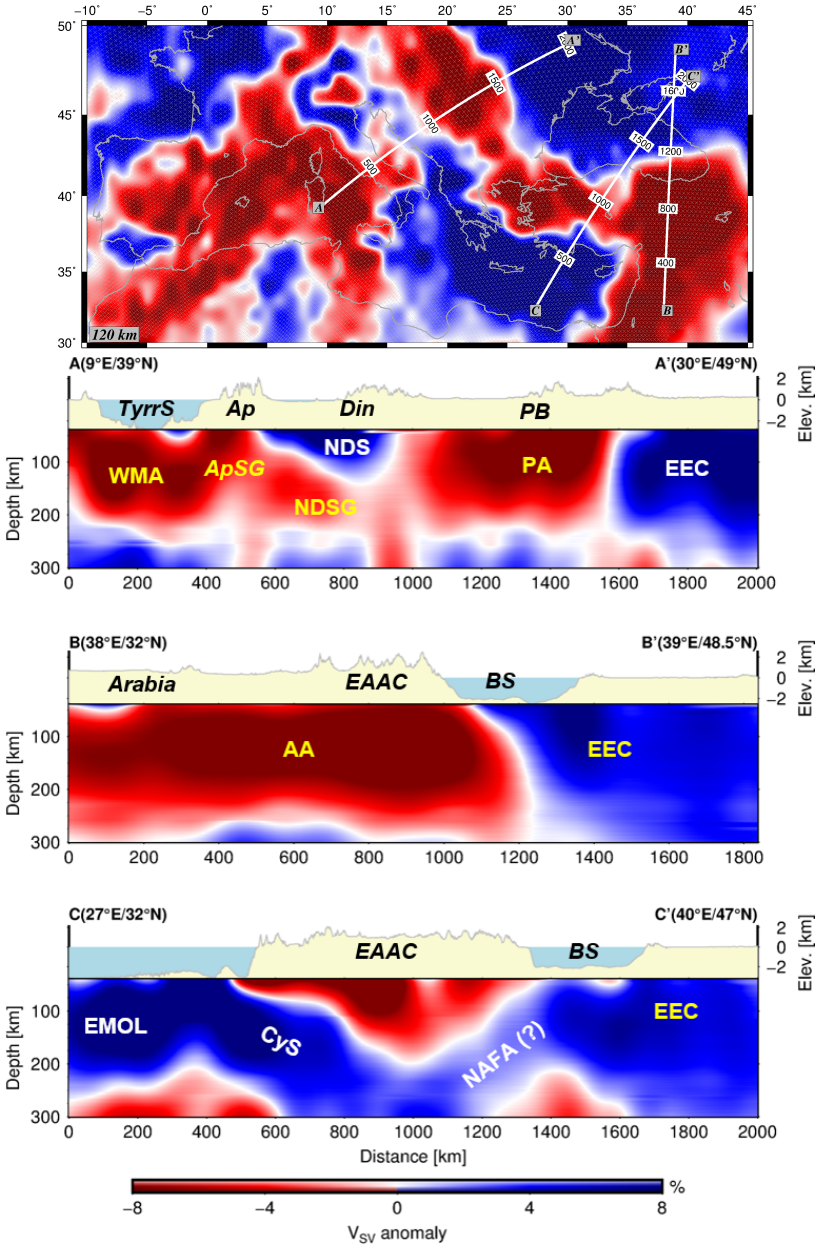

Fig. 4.15 Vertical slices through the 3D model in the Eastern Mediterranean. The topography along each profile is plotted on top of the vertical velocity cross sections. AA: Anatolia asthenosphere, Ap: Apennines, ApSG: Apenninic slab gap, AS: Anatolian slab, BS: Black Sea, CEA: central Europe asthenosphere, CyS: Cyprus slab, Din: Dinarides, EAAC: East Anatolian Accretionary complex, EEC: East European craton, EMOL: eastern Mediterranean oceanic lithosphere, NDS: north Dinaridic slab, NDSG: north Dinaridic slab gap, PA: Panonnian asthenosphere, PB: Panonnian basin, TyrrS: Tyrrhenian Sea, WMA: western Mediterranean asthenosphere. The location of the profiles are shown on the map view of 120 km.

4.5 Discussions

The aforementioned patterns of both high and low shear wave velocities are broadly consistent with previous tomographic models obtained either from inverting body wave travel time measurements from regional and teleseismic earthquakes (Spakman 1986, 1991; Spakman *et al.* 1993; Piromallo & Morelli 2003; Spakman & Wortel 2004; Li *et al.* 2008; Koulakov *et al.* 2009; Giacomuzzi *et al.* 2011) or from inverting fundamental mode Love and Rayleigh dispersion measurements (e.g., Schivardi & Morelli 2009; Palomeras *et al.* 2014; Nita *et al.* 2016). Nevertheless, finer details of the detected anomalies still show some inconsistencies that can not be ignored especially among the recent models. This can be attributed to several factors include the data selection, ray path coverage, parameterization, inversion's regularization and tomographic techniques. Vertical smearing and limited depth resolution are common features of teleseismic traveltime tomography due to the insufficient coverage in the upper mantle where all incoming P-waves travel nearly vertically over most of the upper matle and are sensitive to deeper structures with less focus on the lithosphere-asthenosphere system. On the other hand, surface wave data (fundamental and higher modes) which are primarily sensitive to shear velocity, are strongly affected by the uppermost mantle structure can minimize the vertical smearing effects and enhance vertical resolution in the depth range of the lithosphere-asthenosphere system. In the following we provide a discussion of specific structural features in our model especially the subduction of the lithosphere, associated with a qualitative comparison with previously published models.

In the western Mediterranean region, especially undernearth the Betic-Rif and Alboran basin a high velocity anomaly dipping to the East has been imaged clearly from P-wave tomographic models which extends from shallow depths down to the mantle transition zone (Spakman & Wortel 2004). Spakman *et al.* (1993) imaged this anomaly from 200 km and downwards whereas it has been imaged from the base of the crust and downward by Bijwaard *et al.* (1993). Piromallo and Morelli (2003) found abit larger positive anomaly below northern Morocco to the Betics that extends to deeper levels. This anomaly has been interpreted as the Alboran subducting slab. A recently constructed model by Palomeras *et al.* (2014) for the crust and upper mantle of the western Mediterranean from Rayleigh wave fundamental mode in the period range of 20-167 s indicates the Alboran slab as a nearly circular feature down to appoximately 200 km depth. Our results indicate the Alboran slab (AlbS) as a bit larger high velocity anomaly shifted a bit towards the north and elongated along the Betics from depths as shallow as 60-70 km and downwards through the upper Mantle down to larger depths (figures 4.10, 4.11). Therefore, we argue that the Alboran slab is either still attached to the crust, is currently detaching from the crust, or has detached from the bottom of the crust.

In the depth range of 200-300 km, our model shows the extension of this anomaly more in the NE as elongated high velocity anomaly belt following the strike of the Betics and ends underneath the Valencia Trough, which we attribute to the detached part of the Alboran slab in this depth range. Several models e.g., Bijwaard & Spakman 2000; Piromallo & Morelli 2003; Sakman & Wortel 2004; Amaru 2007; van der Meer *et al.* 2010) show the deeper part of the eastward dipping Alboran slab reaches the 660 km and is captured in the Mantle transition zone. Fichnter *et al.* 2015 observed an approximately E-W trending Alboran slab around 200-300 km depth from the full-waveform inversion that is bit different from our model, but this may result from the absence of body waves that would contribute more lateral resolution, in addition to the fact that the fundamental mode are of limited vertical resolution. Towards the north, a homogenous pattern of low velocity anomalies is observed below the Iberian Massif from depths as shallower as 60 km and downwards through the upper mantle, which we attribute to the presence of a shallow asthenosphere and associated with a high topographic plateau that correlates very well with the distribtion of the Cenozoic volcanism in the region (Lustrino *et al.* 2000).

Below the Alboran sea, the upper mantle is characterized by low shear velocities from depths shallower than 80 km and downwards, which we attribute to upwelling of asthenospheric materials and the presence of high temperatures at this depth range relying on the heat flow data provided by Polyak *et al.* 1996. They indicated that the average values decreases from the east ($\sim$124 mWm^{-2}) to the west ($\sim$70 mWm^{-2}) of the Alboran sea which in turns imply that high temperatures encompasses the eastern Alboran. Moreover, this can be partly attributed to the partial melting due to the presence of the Miocene magmatism on the Alboran seafloor which erupts as a response to back-arc extension associated with slab rollback (Duggen *et al.* 2004). The same feature has been captured by previous tomographic models (Bijwaard & Spakman 2000; Piromallo & Morelli 2003; Sakman & Wortel 2004; Amaru 2007; Palomeras *et al.* 2014). Along north Africa, our model detected a high velocity anomaly indicating the subducted African lithosphere underneath the Kabylides (Kabylides slab, KbS) which broadens at larger depths and shows a northward dipping (profile $C-C^{'}$, Fig. 4.13) down to depths of 250 km below Corsica and Sardinia. This contradicts the earlier findings by Spakman and Wortel (2004) and Amaru (2007) that there is no continuous northward dipping slab still attached to Africa. The model of Piromallo and Morelli (2003), also shows a local high velocity anomaly in this area. Our results coincides with the suggestion of Faccenna *et al.* (2004) and Jolivet *et al.* (2009) that a largely continuous northward dipping slab is present below north Africa between the Rif and Kabylides which supports a predominantly N-S extension during southward rollback of the African slab. Recent tectonic reconstructions proposed that the subducted African lithosphere beneath the Kabylides (KbS)

might be remnants of the slab that caused the opening of the Ligurian sea by rollback and the opening of back-arc basin (Faccenna *et al.* 2014).

Along the Alps, our model shows a nearly vertical, continuous, nearly vertical, high velocity anomaly underneath the central Alps (CAS) which indicates the European suducted slab. It extends from below the Moho down to depths of approximately 230 km. This is mostly coinciding with a recently published model by Kästle *et al.* 2018 of the crust and upper mantle of the Alps obtained from inverting fundamental mode phase velocities from ambient noise and earthquake measurements. On the other hand, both local and regional body-wave models show a continuous European slab under the central Alps (e.g., Lippitsch *et al.* 2003; Koulakov *et al.* 2009; Mitterbauer *et al.* 2011; Zhao *et al.* 2016; Hua *et al.* 2017). The vertical termination of the slab around 230 km depth indicates $\sim$150 km slab length that is roughly coinciding with the convergence rate since 35 Ma (Schmid *et al.* 2004). In contrast to the central Alps, our model shows a low velocity anomaly underneath the western Alps suggesting the presence of a shallow European slab break-off, which has been suggested by the model of Beller *et al.* (2017), obtained from full-waveform inversion. Kästle *et al.* (2018) indicated a high velocity anomaly under the western Alps down to depths of approximately 90 - 120 km with a support to shallow slab break-off as has been proposed by Lippitsch *et al.* (2003) at lithospheric depths. However, regional body wave models indicate a continuity between the deeper anomaly and the lithosphere (Koulakov *et al.* 2009; Zhao *et al.* 2016). In the eastern Alps, the relationship between the European and Adriatic plates is still a matter of debate. The 3-D model shows a complicated wedge structure of the fast anomalies underneath the Eastern Alps that are limited by the Pannonian Basin towards the east. Lippitsch *et al.* (2003) imaged a northward dipping slab down to 250 km depth and interpreted it as the Adriatic subducted slab beneath the eastern Alps, whereas other models (e.g. Koulakov *et al.* 2009; Dando *et al.* 2011; Zhao *et al.* 2016; Hua *et al.* 2017) show a nearly vertical slab. The model by Dando *et al.* indicates that the slab beneath the eastern Alps may be continuous and coonected vertically to a deep anomaly beneath the Pannonian Basin.

In the Pannonian basin, the model reveals a deep seated high velocity anomaly approximately at depth of 200 km and downward. Wortel and Spakman (2000) detected a similar feature below the Pannonian basin which they interpreted as remnants of deep subduction. Considering the robustness of this feature in our model, we suggest that this anomaly is a detached part of the Eurasian slab that can be explained by the continuous convergence between the European plate and the Alps-Carpathian-Pannoinan system after the slab break-off (Zeyen *et al.* 2002). Beneath the northern Apennines, our model shows a broad high velocity anomaly that shifts to the southwest with increasing depths indicating the subduction of

the Adriatic lithosphere down to depths of 250 km below the Po plain basin, which is separated by a sharp contrast from the low velocity anomalies across the western Mediterranean shallow asthenosphere. Consequently, we argue that the Po plain basin is considered the surface expression of the subducted slab beneath the Apennines. Our results also indicate the proximity of Eurasian slab in the central Alps and Adriatic slab in the northern Apennines. The regional P-wave model of Piromallo & Morelli (2003) exhibits evidences for a local continuous slab in northern Apennines, whereas the model of Bijwaard & Spakman (2000) shows a continuous high velocity anomaly in the upper 200 km. Towards the south, our model does not detect high velocities underneath both the central and southern Apennines, rather it shows a pronounced low velocity feature that is entirely encompasses the depth range from below the Moho down to 250 km depth, that is consistent with the findings of the previous regional and global models (Spakman *et al.* 1993; Bijwaard & Spakman 2000; Piromallo & Morelli 2003). We attribute the presence of the low anomalies in the Central Apennines to a slab detachment of the Adriatic lithosphere in addition to the upwelling of asthenospheric materials to fill this gap. It has been suggested that a lateral slab tear may have propagated from the northern Apennines towards the southeast (Wortel & Spakman 2004; Faccenna *et al.* 2005).

Wortel and Spakman (2004) revealed the absence of subcrustal seismicity underneath the southern Apennines as well as low velocities in the upper mantle down to 200 km. However, a continuous pattern of seismicity directly underneath the Calabrian in addition to a broad, continuous high velocity anomaly down to the mantle transition zone indicating the subducted slab underneath Calabria has been imaged through the majority of the regional and global tomographic models (e.g., Spakman *et al.* 1993; Bijwaard & Spakman 2000; Piromallo & Morelli 2003; Koulakov *et al.* 2009; Zhao *et al.* 2016; Hua *et al.* 2017). The sharp contrast of the subduction process between the respective regions has been related to the lateral heterogeneities across the lithosphere that is continental in southern Apennines and oceanic in the Ionian sea towards Calabria. Our results reveal the Calabrian subduction as a NW-SE dipping high velocity anomaly. The imaged anomaly broadens with depth, in particular at 200 km, underneath the Tyrrhenian sea which in turn is characterized by low shear wave velocity anomalies. We relate these low velocities as thermal anomalies in the Tyrrhenian mantle due to the slab retreat and the subsequent rising of the asthenosphere in the Tyrrhenian Basin, that is consistent with the presence of Quaternary volcanism and the associated high heat flow rates (Marani & Trua 2002; Zito *et al.* 2003). Gvirtzman and Nur (2001) revealed that the Tyrrhenian sea is characterized by high residual topography and shows a sharp transition towards very low residual topography over the edge of the subducting lithosphere beneath Calabria. Therefore, they argued on the absence of mantle lithosphere, associated with a

rapid slab rollback and upwelling of the asthenospheric materials. On top of the high velocity of the Calabrian slab, low velocity anomaly has been detected (Fig. 4.12) which might be attributed to the presence of subducting crustal material. Therefore, we support the idea of the undetached subducted slab below Calabrian arc at least down to 300 km. However, the model by Zhu *et al.* (2012) supported the existence of slab detachment proposed by Wortel and Spakman (2000) as they found a clear gap between shallow lithosphere and deep seated high velocity anomalies.

In a general agreement with the previous models, our model shows that the Ionian and Kabylides slabs are isolated from each other due to the eastward retreat of the Calabrian slab along a subduction transform edge propagator (STEP) fault (Carminati *et al.* 1998; Faccenna *et al.* 2004; Spakman & Wortel, 2004; Jolivet *et al.* 2009). To the southwest of Calabria subduction, below the northwest of Sicily, we image a low shear velocity anomaly down to depths of approximately 200 km, as has been imaged previously (Piromallo & Morelli 2003; Wortel & Spakman 2004). Montuori *et al.* (2007) indicated the lack of subcrustal seismicity in this region. A lateral slab tear propagating towards east from the northern Africa has been suggested for this region (Faccenna *et al.* 2005).

The 3-D shear velocity strucure reveals a high velocity anomaly encompasses the entire Dinarides representing the subduction of Adriatic lithosphere beneath it. This anomaly shows a steep dipping towards the northeast and indicates Adria's downwelling underneath the Dinarides and the Pannonian basin (Fig. 4.11). In the northern Dinarides, this anomaly extends from beneath the Moho down to depth of appoximately 150 km, whereas the southern Dinarides seems to be continuous and much deeper and is connected to the northeast downgoing high velocity anomaly beneath the Hellenides. Previous tomographic models (Bijwaard & Spakman 2000; Piromallo & Morelli 2003; Koulakov *et al.* 2009) show high velocity anomaly beneath the southern Dinarides. It has been attributed to underthrusting of the Adriatic lithosphere beneath the Dinarides (Schmid *et al.* 2008; Handy *et al.* 2015). Beneath the northern Dinarides, a large low shear velocity anomaly separates the Eastern Alpine slab from the slab anomaly beneath the southern Dinarides has been detected in the depth range of approximately 150 - 250 km, that is in a general agreement with previous tomographic studies (e.g., Bijwaard & Spakman 2000; Wortel & Spakman 2000; Piromallo & Morelli 2003; Koulakov *et al.* 2009). We attribute this low velocity anomaly to a slab gap beneath the northern Dinarides due to the rollback of the subducted Adriatic lithosphere along the Dinaric-Hellenic front in addition to the Pannonian extension associated with the presence of shallow asthenosphere ($\sim$25 Ma, Handy *et al.* 2015). According to Handy *et al.* 2015, a break-off of the Adriatic slab has initiated the continental collison ($\sim$35 Ma ago) which invoked the upwelling of asthenospheric material.

In the eastern Mediterranean, the imaged high shear velocities correlates with the northward dipping subducting African oceanic lithosphere underneath Hellenic arcs. Results from teleseismic body wave tomography have detected the Hellenic subducting slab in the upper mantle (e.g., Bijwaard and Spakman 2000; Piromallo & Morelli 2003; Spakman & Wortel 2004; Zhu *et al.* 2012), that may penetrate deeper down to the lower mantle (Spakman *et al.* 1993; van der Meer *et al.* 2017), suggesting a significant aseismic deeper part of the slab. At depths as shallower as 60 km depth, our model reveals another high velocity anomaly located to the east of the Hellenic arc and shift towards the north east with depth, between the Cyprus and Anatolia (profile $C - C^{'}$, Fig. 4.15). This anomaly correlates with the subducted African lithosphere underneath the Cyprus arc (Zhu *et al.* 2012). At the map of 200 km depth (Fig. 4.11), the high velocity anomalies beneath the southern Aegean and southern Anatolia are clearly separated by a zone of low velocity anomaly. We relate this low velocity anomaly to the presence of a slab tear between the western edge of the Cyprus slab and the eastern edge of the Hellenic slab, which invoked the upwelling of the asthenospheric materials.

To the south of the Hellenic subduction system, the coexistence of very old oceanic lithosphere in the Eastern Mediterranean has been suggested between Sicily and west of Cyprus (270-230 Ma, Müller *et al.* 2008; 340 Ma in the Herodotus basin, Granot 2016; 220-230 Ma in the Ionian sea, Speranza *et al.* 2012). Our results reflect the distribution of the oceanic lithosphere in the Eastern Mediterranean as high amplitude fast shear wave anomalies. Figure (4.12) shows a vertical cross section through the Eastern Mediterranean oceanic lithosphere which reveals a rather uniform structure along the profile with approximately a uniform very thick oceanic lithosphere ($\sim$ 200 km). This means that the oceanic lithosphere has continued to thicken well beyond the 80 Ma age, in contrary to the "thermal plate cooling model" prediction, and is now extremely thick over 200 km. The LAB depth together with the general increase in shear wave velocities with depth show a consistency with the prediction from the half-space cooling model (Davis & Lister 1974; McKenzie *et al.* 2005), which predicts the systematic and continuous increase of the lithospheric thickness with cooling from mid-ocean ridges and increasing the plate age (230 - 270 Ma, Müller *et al.* 2008). Previous tomographic images have suggested the presence of the Eastern Mediterranean oceanic lithosphere (e.g., Boschi *et al.* 2009; Legendre *et al.* 2012).

Along the North Anatolian Fault, a clear transition from high to low shear wave velocity anomalies has been imaged. To the north of the fault system, the high velocities can be explained by the presence of the East European Craton and the stable Eurasian lithosphere which is much thicker than the lithosphere beneath the Aegean (e.g. Schivardi & Morelli 2011). To the south, an extended upper mantle low shear velocity anomalies occupying Anatolia and the middle East and correlates very well with the distribution of the Cenozoic

volcanism and the magmatic nature of this area reflecting its shallow asthenosphere as has been shown in previous studies (Marone *et al.* 2003; Meier *et al.* 2004; Gok *et al.* 2006). This prominent slow anomaly extends down to depths of approximately 160 -170 km and overlays a large volume of high velocity anomalies, located to the northeast of the Cyprus slab. These high velocity anomalies (AS) can be identified on the map views at depths larger than 170 km (Fig. 4.11). In a well-oriented depth profile profile ($C-C^{'}$, Fig. 4.15), these anomalies appear as dipping, continuous bodies, which are approximately 150 km thick, which we interpret as the Anatolian slab (AS). The tomographic model by Zhu *et al.* (2012) has imaged a localized high velocity features at larger depths underneath central Anatolia and has been interpreted as remnants of ancient oceanic lithosphere related to the collision between the Anatolian and African/Arabian plates. A similar transition from low to high velocities located at slightly different depths (approximately 150 and 230 km depth, respectively) have been detected in previous tomographic models (Spakman *et al.* 1993 Piromallo & Morelli 2003).

In the following, we summarize our findings regarding the subducting slabs in the Mediterranean realm. Surface traces of the subducted lithospheric mantle are plotted on a topographic map (Fig. 4.16). The red and bue colors indicate Africa/Adria and Europe mantle lithosphere, respectively. We identified three categories of the subducting slabs: attached (solid), detached (stippled) and shallow (disparated) slabs based on the depth continuity of the high velocity anomalies through our 3-D shear velocity model. The approximate depth of the shallow slabs as well as the top of the detached slabs are shown on the map as values in km. The imaged attached slab structures include the E-W directed Alboran slab (AlbS) beneath the Betic-Alboran sea, the N-S dipping Kabylides slab beneath northern Africa (KbS), the nearly vertical slab in the central Alps (CAS), the northern Apenninic slab (ApS), the NW-dipping Calabrian slab (CalS), the NE-dipping southern Dinaridic slab (SDS) and the NE-dipping African lithosphere undernearth both the Hellenic arc (HeS) and the Cyprus arc (CyS). On the other hand, the detached parts of the slabs are found at larger depths. They include an extension of the the Alboran slab deceted from depth of 230 km as NE-directed slab from undernearth the strike of the Betics to the Valencia Trough. The detached part of the Kabylides Slab has been detected at depth of 220 km dipping towards the north underneath Sardinia. To the southwest of the attached Calabrian slab, below the north of Sicily, we imagd a high shear velocity anomaly at 130 km depth. At 250 km, high velocity anomalies have been detected underneath the Central Apennines which might be related to the the detached part of Adria underneath the the Apennines. At the same depth to the northeast, another high velocity anomlay has been detected undeneath the Adriatic sea, which we interpret as the detached Eurasian slab underneath Adria. Remnant of deep

subduction beneath the Pannonian basin have been detected at depth of 200 km. Along the eastern Carpathian arc, a continuous high velocity anomaly from depth of 60 km and downwards has been detected. To the southeast of the Carpathian, a very localized high velocity anomaly indicating the Vrancea slab (VrS) has been detected and correlates well with the seismicity down to about 180 km depth. At 230 km depth, we detected an aseismic extension of the high velocity anomaly of the Vrancea slab underneath southern Carpathians. We interpret the Vrancea slab either as attached slab or it is much thinner to be resolved by the resolution of our tomographic imaging in the depth range from 180 km to 230 km. Underneath Anatolia, a N-S dipping deep-seated high velocity anomaly has been detected at depth of 160 km and downward. Shallow slabs have been detected underneath the northern Dinarides (NDS) and eastern Alps (EAS) down to depths of approximately 150 and 250 km, respectively.

4.6 Conclusions

A 3-D Rayleigh wave velocity structure for the lithosphere-asthenosphere system beneath the Mediterranean including the Alps and the adjacent regions has been constructed from surface wave tomography. The tomographic images have been calculated with unprecedented high lateral resolution (> 100 km) in a very broad period range (8-350 seconds). Due to trade-offs between crustal structure and uppermost mantle velocities, we consider the model resolved between 50 and 300 km depth. The velocity distributions through our 3-D model confirms the previous findings of the Mediterranean's lithosphere-asthenosphere system, and provides new information about the areas with none or poor studies at this resolution level. High velocity anomalies have been detected underneath western Europe indicating its thick continental mantle lithosphere as well as below the East European Craton and the relatively stable lithosphere of Eurasia. The eastern Mediterranean from the Herodotus basin in the East towards the Ionian sea in the west is dominated by rather high velocity anomaly indicating the thick oceanic mantle lithosphere that is subducting beneath Calabria and the southern Aegean. Both the Hellenic and Cyprus arcs are clearly imaged with a complicated transition from the Hellenic arc towards the Hellenides and the Dinarides. A vertical slab tear has been imaged between the eastern part of the Hellenic and western Cyprus arcs.

Slab structures are found below the Betic-Alboran region, Alps, Apenneines, Dinarides, Calabrian arc, the Hellenic and Cyprus arcs. In the western Mediterranean, the Betic-Alboran slab is imaged clearly, whereas the Calabrian slab is the dominant feature in the central Mediterranean. Remnants of deep subduction below the Pannonian basin have been detected.

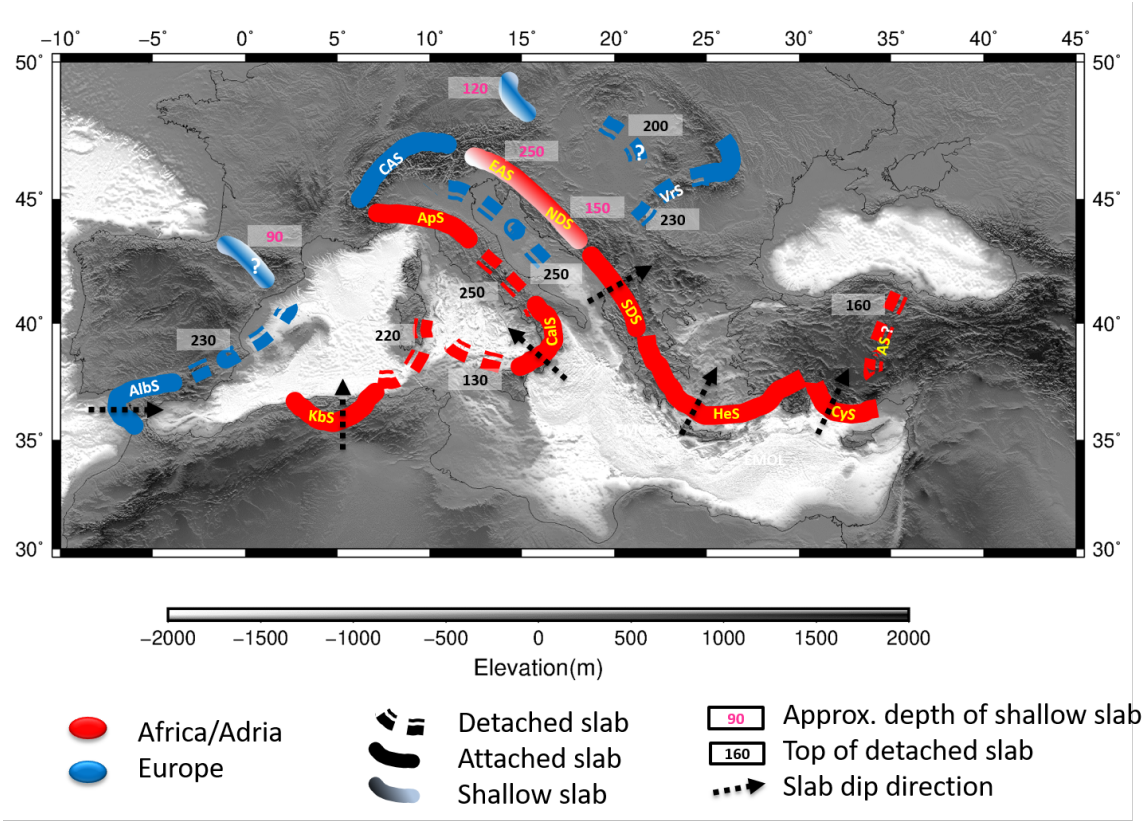

Fig. 4.16 Topographic map of the Alpine-Mediterranean mobile belt overlain by surface traces of the subducted slabs beneath the entire Mediterranean. Red and blue lines indicate the subducted lithosphere of Africa/Adria and Europe projected to the surface, respectively. AlbS: Alboran slab, ApS: Apenninic slab, ApSG: Apenninic slab gap, AS: Anatolian slab, CalS: Calabrian slab, CAS: central Alpine slab, CyS: Cyprus slab, EAS: eastern Alpine slab, HeS: Hellenic slab, KbS: Kabylides slab, NDS: north Dinaridic slab, SDS: southern Dinaridic slab.

We support the idea of slab break-off in the Western Alps. In the central Alps, the European subducted slab appears as nearly vertical high velocity anomaly, whereas a very complicated wedge structure in the Eastern Alps has been imaged. The northern Apenninic slab is imaged below the Po plain basin. Slab gaps have been detected in the northern Dinarides at depth of about 150 km and downwards as well as beneath the central Apennines but at much shallower depths. Slow shear velocities have been imaged below the western Mediterranean especially beneath the extensional basins that is connected to the central European shallow asthenosphere through the Rhöne asthenosphere and the Massif Central towards the Pannonian Basin.

In addition, the imaged slow velocities beneath Anatolia favours that the lithosphere beneath the area is overall thin. An anomalously hot uppermost mantle could also explain the presence of a relatively high plateau and surface uplift in Anatolia and correlates very well with the distribution of the Cenozoic volcanism in this area. In central Anatolia, from 160 km and downward a N-S trending dipping high velocity anomaly in the upper mantle is detected. Based on our results, surface wave tomography can contribute significantly to the imaging of the complex slab geometries and slab segmentations in the Mediterranean, moreover we emphasize that surface wave tomography has not reached the resolution limit yet.

References

Adam, J. M.-C. & Sergei Lebedev, S., 2012: Azimuthal anisotropy beneath southern Africa from very broad-band surface-wave. Geophys. J. Int. (2012) 191, 155-174, doi: 10.1111/j.1365-246X.2012.05583.x dispersion measurements

Aki, K. & Larner, K. L., 1970. Surface motion of a layered medium having an irregular interface due to incident plane SH waves. Journal of geophysical research , 75 (5), pp.933-954. Amaru, M. L., 2007. Global travel time tomography with 3-D reference models, Geol. Ultraiectina, 274, 174 pp.

Beller, S., Monteiller, V., Operto, S., Nolet, G., Paul, A., and Zhao, L. (2017). Lithospheric architecture of the South-Western Alps revealed by multiparameter teleseismic full-waveform inversion. Geophysical Journal International, 212(2):1369-1388.

Bijwaard, H., Spakman, W. & Engdahl, R., 1998. Closing the gap between regional and global travel time tomography, J. geophys. Res., 103, 30055 - 30078.

Biryol, C. B., Beck, S. L., Zandt, G., & Özacar, A. A., 2011. Segmented African lithosphere beneath the Anatolian region inferred from teleseismic P-wave tomography, Geophys. J. Int., 184, 1037-1057.

Boschi, L., C. Faccenna, & T. W. Becker, 2010. Mantle structure and dynamic topography in the Mediterranean Basin, Geophys. Res. Lett., 37, L20303, doi:10.1029/2010GL045001.

Burke, K., & Sengör, A.M.C., 1986. Tectonic escape in the evolution of the continental crust, in Reflection Seismology: The Continental Crust, pp. 41-53, eds Barazangi, M., Brown, L., Am. Geophys. Union, Geodyn. Ser. 14, Washigton, DC: Am. Geophys. Union.

Calo, M., Dorbath, C., Luzio, D., Rotolo S. G., & D'Anna G., 2012. Seismic velocity structures of southern Italy from tomographic imaging of the Ionian slab and petrological inferences, Geophysical Journal International, 191, 2, (751-764).

Carminati, E., Wortel, M.J.R., Spakman, W., & Sabadini, R., 1998. The role of slab detachment processes in the opening of the western-central Mediterranean basins: some geological and geophysical evidence. Earth and Planetary Science Letters 160: 651-665.

Dando, B., Stuart, G., Houseman, G., Hegedüs, E., Brückl, E., and Radovanovic, S., 2011. Teleseismic tomography of the mantle in the Carpathian-Pannonian region of central Europe. Geophysical Journal International, 186(1):11-31.

Day, S.M., Roten, D. and Olsen, K.B., 2012. Adjoint analysis of the source and path sensitivities of basin-guided waves. Geophys. J. Int., 189 (2), pp.1103-1124.

De Vos, D., Paulssen, H. & Fichtner, A., 2013. Finite-frequency sensitivity kernels for two-station surface wave measurements, Geophys. J. Int., 194(2), 1042-1049.

Dewey, J.F., Hempton, M.R., Kidd, W.S.F., Saroglu, F. & Sengör, A.M.C., 1986. Shortening of continental lithosphere: the neotectonics of Eastern Anatolia-a young collision zone, in Collision Tectonics, pp. 3-36, eds Coward M. P., Ries, A.C., Geol. Soc. London, London.

Duggen, S., Hoernle K., van den Bogaard P., & Harris, C., 2004. Magmatic evolution of the Alboran region: The role of subduction in forming the western Mediterranean and causing the Messinian Salinity Crisis, Earth Planet. Sci. Lett., 218 (1-2), 91-108, doi:10.1016/S0012-821X(03)006 32-0

Eberhart, R. C., Y. Shi, and J. Kennedy, Swarm Intelligence. Morgan Kaufmann, 2001. Ekstrom, G., Tromp, J. & Larson, E.W.F., 1997. Measurements global models of surface wave propagation, J.Geophys. Res.-Solid Earth, 102(B4), 8137-8157, 62 AMER GEOPHYSICAL UNION.

Faccenna, C., Becker, T. W., Auer, L., Billi, A., Boschi, L., Brun, J. P., Capitanio, F. A., Funiciello, F., Horvath, F., Jolivet, L., Piromallo, C., Royden, L., Rossetti, F., & Serpelloni, E., 2014. Mantle dynamics in the Mediterranean, Rev. Geophys., 52, 283-332, doi:10.1002/2013RG000444.

Faccenna, C., Bellier, O., Martinod, J., Piromallo, C., & Regard, V., 2006. Slab detachment beneath eastern Anatolia: a possible cause for the formation of the North Anatolian Fault, Earth Planet. Sc. Lett., 242, 85-97, doi:10.1016/j.epsl.2005.11.046.

Faccenna, C., C. Piromallo, A. Crespo-Blanc, & L. Jolivet, 2004, Lateral slab deformation and the origin of the western Mediterranean arcs, Tectonics, 23, TC1012, doi:10.1029/2002TC001488.

Faccenna, C., F. Funiciello, D. Giardini, & P. Lucente, 2001a. Episodic back-arc extension during restricted mantle convection in the central Mediterranean, Earth Planet. Sci. Lett., 187(1-2), 105-116.

Faccenna, C., F. Funiciello, L. Civetta, M. D'Antonio, M. Moroni & C. Piromallo, 2007. Slab disruption, mantle circulation, and the opening of the Tyrrhenian basins, in Cenozoic Volcanism in the Mediterranean Area, edited by L. Beccaluva, G. Bianchini, and M. Wilson, Geological Society of America Special Paper 41, pp. 153-169, AGU, Washington, D. C., doi:10.1130/2007.2418(08).

Faccenna, C., Jolivet, L., Piromallo, C., & Morelli, A., 2003. Subduction and the depth of convection in the Mediterranean mantle, J. Geophys. Res., 108, 2099, doi:10.1029/2001JB001690.

Faccenna, C., L. Civetta, M. D'Antonio, F. Funiciello, L. Margheriti, & C. Piromallo, 2005. Constraints on mantle circulation around the deforming Calabrian slab, Geophys. Res. Lett., 32, L06311, doi:10.1029/2004GL021874.

Faccenna, C., L. Jolivet, C. Piromallo, & A. Morelli, 2003. Subduction and the depth of convection in the Mediterranean mantle, J. Geophys. Res., 108(B2), 2099, doi:10.1029/2001JB001690.

Faccenna, C., O. Bellier, J. Martinod, C. Piromallo, & V. Regard, 2006. Slab detachment beneath eastern Anatolia: A possible cause for the formation of the North Anatolian fault, Earth Planet. Sci. Lett., 242(1), 85-97.

Faccenna, C., P. Molin, B. Orecchio, V. Olivetti, O. Bellier, F. Funiciello, L. Minelli, C. Piromallo, & A. Billi, 2011. Topography of the Calabria subduction zone (southern Italy): Clues for the origin of Mt. Etna, Tectonics, 30, TC1003, doi:10.1029/2010TC002694.

Faccenna, C., T. W. Becker, F. P. Lucente, L. Jolivet, & F. Rossetti, 2001b. History of subduction and back-arc extension in the central Mediterranean, Geophys. J. Int., 145, 809-820.

Feng, L., & Ritzwoller, M., 2017. The Effect of Sedimentary Basins on Surface Waves That Pass Through Them, Geophys. J. Int., 1-47.

Fichtner, A., Saygin, E., Taymaz, T., Cupillard, P., Capdeville, Y., & Trampert, J., 2013a. The deep structure of the North Anatolian Fault Zone, Earth Planet. Sc. Lett., 373, 109-117.

Fichtner, A., Trampert, J., Cupillard, P., Saygin, E., Taymaz, T., Capdeville, Y., & Villasenor, A., 2013b. Multiscale full waveform inversion, Geophys. J. Int., 194, 534-556.

Garfunkel, Z., 1981. Internal structure of the Dead Sea leaky transform (rift) in relation to plate kinematics, Tectonophysics, 80, 81-108.

Garfunkel, Z., 1998. Constrains on the origin and history of the Eastern Mediterranean basin, Tectonophys., 298, 5-35.

Goes, S., Govers R., & Vacher P., 2000. Shallow mantle temperatures under Europe from P and S wave tomography, J. Geophys. Res., 105, 11,153-11,169, doi:10.1029/1999JB900300.

Granot, R., 2016. Palaeozoic Oceanic Crust Preserved Beneath the Eastern Mediterranean. Nature Geoscience, 9, 701-705. https://doi.org/10.1038/ngeo2784

Gvirtzman, Z., & Nur, A., 2001. Residual topography, lithospheric structure and sunken slabs in the central Mediterranean, Earth Planet. Sci. Lett., 187, 117-130.

Handy, M. R., Schmid, S. M., Bousquet, R., Kissling, E., & Bernoulli, D., 2010. Reconciling plate-tectonic reconstructions of Alpine Tethys with the geological-geophysical record of spreading and subduction in the Alps. Earth-Science Reviews, 102(3):121-158.

Handy, M. R., Ustaszewski, K., & Kissling, E., 2015. Reconstructing the Alps-Carpathians-Dinarides as a key to understanding switches in subduction polarity, slab gaps and surface motion. International Journal of Earth Sciences, 104(1):1-26.

Hua, Y., Zhao, D., and Xu, Y., 2017. P-wave anisotropic tomography of the Alps. Journal of Geophysical Research: Solid Earth.

Jolivet, L., C. Faccenna, & C. Piromallo, 2009. From mantle to crust: Stretching the Mediterranean, Earth Planet. Sci. Lett 285(1-2), 198-209, doi:10.1016/j.epsl.2009.06.017.

Kästle, E. D., El-Sharkawy, A., Boschi, L., Meier, T., Rosenberg, C., Bellahsen, N., Weidle, C., 2018. Surface wave tomography of the Alps using ambient-noise and earthquake phase velocity measurements. Journal of Geophysical Research: Solid Earth, 123, 1770-1792. https://doi.org/10.1002/2017JB014698

Kennett, B.L.N., Engdahl, E.R. & Buland, R., 1995. Constraints on seismic velocities in the Earth from traveltimes. Geophys. J. Int., 122 (1), pp.108-124.

Kissling E., & Lahr J.-C., 1991. Tomographic image of the Pacific slab under southern Alaska. Echgae geol. Helv. 84, 297-315.

Kissling E., 1988. Geotomography with local earthquake data. Reu. Geophys. 26,659-698.

Kissling E., 1993. Deep structure of the Alps-what do we really know? Phys. Earth Plan. Int. 79. 87-112.

Knopoff, L., 1964. A matrix method for elastic wave problems. Bull. Seismol. Soc. Am. 54, 431 - 438.

Knopoff, L., 1972. Observation and inversion of surface wave dispersion. Tectonophysics 13, 497 - 519.

Koulakov, I., Kaban, M. K., Tesauro, M., & Cloetingh, S., 2009. P-and S-velocity anomalies in the upper mantle beneath Europe from tomographic inversion of ISC data, Geophys. J. Int., (2009) 179, 345-366, doi: 10.1111/j.1365-246X.2009.04279.x

Koulakov, I., Kaban, M., Tesauro, M., and Cloetingh, S., 2009. P-and s-velocity anomalies in the upper mantle beneath europe from tomographic inversion of isc data. Geophysical Journal International, 179(1):345-366.

Lebedev, S., Adam, J. M.-C. & Meier, T., 2013. Mapping the Moho with seismic surface waves: a review, resolution analysis, and recommended inversion strategies, Tectonophysics, 609, 377-394.

Legendre, C., T. Meier, S. Lebedev, W. Friederich, and L. Viereck-Götte, 2012. A shear wave velocity model of the European upper mantle from automated inversion of seismic shear and surface waveforms, Geophys. J. Int., 191(1), 282-304.

Levshin, A.L. & Ritzwoller, M.H., 2001. Automated detection, extraction, and measurement of regional surface waves, Pure appl. Geophys., 158(8), 1531-1545.

Li, C., R. D. van der Hilst, E. R. Engdahl, & S. Burdick, 2008. A new global model for P wave speed variations in Earth's mantle, Geochem. Geophys. Geosyst., 9, Q05018, doi:10.1029/2007GC001806.

Lippitsch, R., Kissling, E. & Ansorge, J., 2003. Upper mantle structure beneath the Alpine orogen from high-resolution teleseismic tomography. J. Geophys. Res. 108, B82376.

Müller, R. D., M. Sdrolias, C. Gaina, & W. R. Roest, 2008. Age, spreading rates, and spreading asymmetry of the world's ocean crust, Geochem. Geophys. Geosyst. ,9 , Q04006, doi:10.1029/2007GC001743.

Marani, M. P., and T. Trua (2002), Thermal constriction and slab tearing at the origin of a superinflated spreading ridge: Marsili volcano (Tyrrhenian Sea), J. Geophys. Res., 107(B9), 2188, doi:10.1029/2001JB000285.

McClusky, S., 2000. Global Positioning System constraints on plate kinematics and dynamics in the eastern Mediterranean and Caucasus, J. Geophys. Res., 105, 5695-5719.

Mckenzie, D., Jackson, J.A., & Priestley, K., 2005. Thermal structure of oceanic and continental lithosphere. Earth Planet. Sci. Lett. 233 (3-4), 337-349.

McKenzie, D.P., 1972. Active tectonics of the Mediterranean region, Geophy. J. Roy. Astr. Soc., 30, 109-185.

Meier, T., Dietrich, K., Stöckhert, B., & Harjes, H.-P., 2004. One-dimensional models of shear wave velocity for the eastern Mediterranean obtained from the inversion of Rayleigh wave phase velocities and tectonic implications, Geophysical Journal International, 156(1), 45 - 58.

Meier, T., Soomro, R., Viereck, L., Lebedev S., Behrmann, L.C., Weidle, C., Cristiano, L., & Hanemann, R., 2016. Mesozoic and Cenozoic evolution of the Central European lithosphere, Tectonophysics (2016), http://dx.doi.org/10.1016/j.tecto.2016.09.016

Mitterbauer, U., Behm, M., Brückl, E., Lippitsch, R., Guterch, A., Keller, G. R., Koslovskaya, E., Rumpfhuber, E.-M., & Sumanovac, F., 2011. Shape and origin of

the east-alpine slab constrained by the alpass teleseismic model. Tectonophysics, 510(1):195-206.

Montuori, C., Cimini, G. B., Favali, P., 2007. Teleseismic tomography of the southern Tyrrhenian subduction zone: New results from seafloor and land recordings, Journal of Geophysical Research: Solid Earth, 112, B03311.

Nita, B., S. Maurya, & J.-P. Montagner, 2016. Anisotropic tomography of the European lithospheric structure from surface wave studies, Geochem. Geophys. Geosyst., 17, doi:10.1002/2015GC006243.

Nolet, G. and Dahlen, F.A., 2000. Wave front healing and the evolution of seismic delay times. Journal of Geophysical Research: Solid Earth, 105 (B8), pp.19043-19054.

Ozgenc, I., & Ibeyli, N., 2008. Petrogenesis of the Late Cenozoic Egrigöz Pluton in Western Anatolia, Turkey: Implications for Magma Genesis and Crustal Processes. International Geology Review, Vol. 50, 2008, p. 375–391. DOI: 10.2747/0020-6814.50.4.375

Özacar, A. A., Gilbert, H., & Zandt, G., 2008. Upper mantle discontinuity structure beneath East Anatolian Plateau (Turkey) from receiver functions, Earth Planet. Sc. Lett., 269, 427-435, doi:10.1016/j.epsl.2008.02.036.

Palomeras, I., Thurner, S., Levander, A., Liu, K., Nor, A.V., Carbonell, R., Harnafi,M., 2014. Finite-frequency Rayleigh wave tomography of the western Mediterranean: mapping its lithosphere structure. Geochem. Geophys. Geosyst. 15. http://dx.doi.org/10.1002/2013GC004861.

Parsopoulos, K.E. & Vrahatis, M.N., 2004. On the computation of all global minimizers through Particle Swarm Optimization, IEEE Trans. Evolut. Comput., 8(3), 211-224.

Piromallo, C., & A. Morelli, 2003. P wave tomography of the mantle under the Alpine-Mediterranean area, J. Geophys. Res., 108(B2), 2065, doi:10.1029/2002JB001757.

Ravenna M., & Lebedev, S., 2018. Bayesian inversion of surface-wave data for radial and azimuthal shear-wave anisotropy, with applications to central Mongolia and west-central Italy, Geophys. J. Int. (2018) 213,278-300, doi: 10.1093/gji/ggx497

Rawlinson, N. & Sambridge, M., 2004. Wave front evolution in strongly heterogeneous layered media using the fast marching method. Geophys. J. Int., 156 (3), pp.631-647.

Schivardi ,R.,& Morelli, A., 2009. Surface wave tomography in the European and Mediterranean region, Geophys. J. Int. (2009) 177, 1050-1066. doi: 10.1111/j.1365-246X 2009.04100.x

Schivardi, R. & Moreli, A., 2013. EPmantle: A 3-D transversely isotropic model of the upper mantle under the European Plate. Geophys. J. Int. 185, 469-484.

Schmid, C., S. van der Lee, & D. Giardini, 2004. Delay times and shear wave splitting in the Mediterranean region, Geophys. J. Int., 159(1), 275-290, doi:10.1111/j.1365-246X.2004.02381.x.

Schmid, C., van der Lee, S., VanDecar, J., Engdahl, E. & Giardini, D., 2009. Three-dimensional S velocity of the mantle in the Africa-Eurasia plate boundary region from phase arrival times and regional waveforms. J. Geophys. Res. 113, B03306.

Schmid, S. M., Fügenschuh, B., Kissling, E., & Schuster, R., 2004. Tectonic map and overall architecture of the Alpine orogen. Eclogae Geologicae Helvetiae, 97(1):93-117.

Schmid, S. M., Fügenschuh, B., Kissling, E., and Schuster, R., 2004. Tectonic map and overall architecture of the Alpine orogen. Eclogae Geologicae Helvetiae, 97(1):93-117.

Schwab, F. and Knopoff, L., 1972: Fast surface wave and free mode computations, in Methods in Computational physics, Vol. 11, ed. Bolt, B.A., Academic Press, New York.

Spakman, W., S. van der Lee, and R. van der Hilst (1993), Travel-time tomography of the European-Mediterranean mantle down to 1400 km, Phys. Earth planet. Inter., 79, 3 - 74, 10.1016/0031-9201(93)90142-V.

Speranza, F., and M. Chiappini (2002), Thick-skinned tectonics in the external Apennines, Italy: New evidence from magnetic anomaly analysis, J. Geophys. Res., 107(B11), 2290, doi:10.1029/2000JB000027.

Stampfli G.M., & Borel, G.D., 2002. A plate tectonic model for the Paleozoic and Mesozoic constrained by dynamic plate boundaries and restored synthetic oceanic isochrons, Earth and Planetary Science Letters, 196, 17-33.

Stampfli, G., and G. Borel (2002), A plate tectonic model for the Paleozoic and Mesozoic constrained by dynamic plate boundaries and restored synthetic oceanic isochrons, Earth Planet. Sci. Lett., 196, 17 - 33.

van der Meer, D. G., W. Spakman, D. J. J. van Hinsbergen, M. L. Amaru, & T. H. Torsvik, 2010. Toward absolute plate motions constrained by lower mantle slab remnants, Nat. Geosci., 3, 36-40.

Vanacore, E. A., Taymaz, T., & Saygin, E., 2013. Moho structure of the Anatolian Plate from receiver function analysis, Geophys. J. Int., 193, 329-337.

Wortel, M. J. R & Spakman, W., 2000. Subduction and slab detachment in the Mediterranean-Carpathian region. Science 290, 1910-1917.

Wortel, M. J. R. & Spakman, W., 2000. Subduction and slab detachment in the Mediterranean-Carpathian region, Science, 290, 1910-1917, doi:10.1126/science.290.5498.1910

Xie, X., Zhang, W. & Yang, Z., 2002. Adaptive Particle Swarm Optimization on individual level, in Proceedings of the Sixth International Conference on Signal Processing, Vol. 2, 1215-1218, IEEE, doi:10.1109/ICOSP.2002.1180009.

Zeyen H., Dererova, J., & Bielik, M., 2002. Determination of the continental lithospheric thermal structure in the Western Carpathians: integrated modeling of surface heat flow, gravity anomalies and topography. Physics of the Earth and Planetary Interiors, 134: 89-104.

Zhao, L., Paul, A., Malusa, M. G., Xu, X., Zheng, T., Solarino, S., Guillot, S., Schwartz, S., Dumont, ., Salimbeni, S., 2016. Continuity of the Alpine slab unraveled by high-resolution P wave tomography. Journal of Geophysical Research: Solid Earth.

Zhao, L., Paul, A., Malusa, M. G., Xu, X., Zheng, T., Solarino, S., Guillot, S., Schwartz, S., Dumont, T., & Salimbeni, S., 2016. Continuity of the Alpine slab unraveled by high-resolution P wave tomography. Journal of Geophysical Research: Solid Earth.

Zhu, H., Bozdag, E., Peter, D., & Tromp, J., 2012. Structure of the European upper mantle revealed by adjoint tomography, NATURE GEOSCIENCE, VOL 5, 493-498.

Zito, G., F. Mongelli, S. de Lorenzo, and C. Doglioni (2003), Heat flow and geodynamics in the Tyrrhenian Sea, Terra Nova, 15, 425 - 432, doi:10.1046/j.1365-3121.2003.00507.x.

Zor, E., Sandvol, E., Gurbuz, C., Turkelli, N., Seber, D., & Barazangi, M., 2003. The crustal structure of the East Anatolian Plateau (Turkey) from receiver functions, Geophys. Res. Lett., 30, 8044, doi:10.1029/2003GL018192.

Chapter 5

Summary and outlook

5.1 Summary

Surface wave phase velocities are well suited for imaging the lithosphere-asthenosphere system. With a high accuracy they can be measured over a broad period band which is sensitive to shear wave velocities at different depths, from the crust (including sedimentary basins down to the Moho), the mantle lithosphere to the asthenosphere. Due to their particular sensitivity to the vertical velocity variations, they enable to avoid, to a large extent, the vertical smearing effects often present in investigations with body wave data. A newly elaborated algorithm for the automated measurement of the inter-station phase velocities from earthquake-based surface waves is well suited for large, and hetereogeous permanent and temporary networks. It enables performing the measurements in a very broad period ranges. We applied the method to very large volumes of seismic data consisting of more than 4000 seismic events in the time period from 1990 to 2016 and recorded by $\sim$4500 broadband stations of permanent and temporary deployments, in a combination, for the first time, with data from the Egyptian National Seismological Network (ENSN). Rayleigh and Love path average inter-station phase velocity dispersion curves were calculated by averaging single-event measurements in order to obtain robust, broad-band dispersion measurements with error estimates. This resulted in an unprecedentd number of path-averaged phase velocity curves ($\sim$ 200,000) in a very broad period range (8 - 350 seconds). A careful quality control of the resulting phase velocities is performed. Surface-wave tomography exploited the resulting inter-station phase velocities to construct both isotropic and azimuthally anisotropic 2-D phase-velocity maps at more than 100 different periods sampling the period range 8-350 s.

The obtained lateral resolution in Europe and the northern Mediterranean is better than 100 km, otherwise it is 150 km.

Furthermore, we investigate the variability of the lithsopheric structure in the eastern Mediterranean. From the phase velocity maps, we constructed broad band local phase-velocity curves at the Levant Basin (deformed continental) and the Ionian sea (oceanic). Each local dispersion curve is inverted individually for 1-D shear wave velocity model as a function of depth using the Particle Swarm Optimization (PSO) algorithm, a newly elaborated inversion algorithm. This algorithm allows for the investigation of the whole parameter space and for estimating the uncertainities. We developed a parameterization strategy to allow constraining each model parameter individually along the considered depth range from the earth's surface down to the upper part of the lower mantle (900 km), which take into account the presence of the water, bathymetry or topography. Moreover, a regularization scheme has been developed to increase the stability of the inversion process. The inversion of the dispersion curves has been constrained using accurate local P-wave initial models. The P-wave velocity models have been calculated from two seismic refraction profiles recently recorded at Levant Basin and the Ionian Sea, where the local dispersion curves are available, in an efforts to minimize the trade-off between the crustal velocities, mantle velocities and the crustal thickness. The results indicate a Moho depth of about $\sim$ 22 km and $\sim$ 16 km beneath the Levant and the Ionian Basin, respectively. The thickness of the crystalline part of the crust at the Levant basin is $\sim$ 10 km, whereas it is of $\sim$ 6 km beneath the Ionian Sea, overlain by a thick pile of sediments at both locations. As a proxy, the Vp/Vs ratio is used to identify the nature of the crust. Beneath the Levant basin, a ratio of $<$ 1.8 is obtained pointing to a stretched continental crust, whereas the $>$ 1.8 value at the Ionian sea indicates its oceanic nature. In the upper mantle, a shallow asthenosphere is highly pronounced beneath the Levant Basin with $\sim$ 70 km of LAB depth. On the other hand, anomalously higher shear-velocities beneath the Ionian Sea indicates a very thick oceanic lithosphere. Consequently, we propose that, on average, the Ionian oceanic lithosphere has continued to cool well beyond the 80 Ma age, contrary to the "plate cooling model" prediction, and is now extremely thick, over 200 km. This may indicate the applicability of the half-space cooling model for the very old oceanic lithosphere underneath the Ionian sea.

Moreover, a high resolution 3-D Rayleigh wave velocity model for the lithosphere-asthenosphere system underneath the Alpine-Mediterranean mobile belt has been constructed. The main features through the model are the imaged high velocity anomalies underneath western Europe indicating the thick continental mantle lithosphere and the East European Craton and the relatively stable lithosphere of Eurasia. In addition to a large scale feature of high velocities encomapsses the eastern Mediterranean from the Herodotus basin in the East

reaching the Ionian Sea in the west indicating the thick oceanic lithosphere that is subducting beneath Calabria and in the southern Aegean. Slab-like structures are found below the Alboran sea, the Eastern and Central Alps, northern Apenneines, Dinarides, Calabrian arc, the Hellenic and Cyprus arcs. Remnants of deep subduction below the Pannonian basin have been detected. Furthermore, we support the idea of slab break-off in the Western Alps. Slab gaps have been detected in the Northern Dinarides at depth of about 150 km and downwards, whereas beneath the slab gab beneath the central Apennines is detected from beneath the Moho. Low shear velocities have been imaged below the western Mediterranean especially beneath the extensional basins that is connected to the central European shallow asthenosphere through the Rhöne channel and the Massif Central towards the Pannonian basin and southern Aegean reaching the Anatolia and the middle East. The imaged slow velocities beneath Anatolia favours that lithosphere beneath the area is overall thin. An anomalously hot uppermost mantle could also explain the presence of a relatively high plateau and surface uplift in Anatolia and correlates very well with the distribution of the Cenozoic volcanism in this area. In central northern Anatolia, from 160 km and downward a N-S trending dipping high velocity anomaly in the upper mantle is detected.

All together, surface wave tomography can contribute significantly to the imaging of the complex slab geometries, gaps and slab segmentations.

5.2 Outlook

Based on the resulting 3-D velocity model, the geometry and orientation of the subducted slabs across the Mediterranean realm can be defined which are essential for the geodynamic modelling. Using gravity gradients together with the thermal and compositional properties of the slabs, we can determine the contribution of the slabs to the overall gravity field. Mapping the Moho topography as well as the variations of lithosphere-asthenosphere boundary are among our priorities. Moreover, predictions of the mantle models from reconstructions of the evolution of the Mediterranean region correlate with major features in the tomographic images. From our model results we aim to verify processes represented in different tectonic scenarios with the seismologically determined velocity structure.

The long term prespective that we have is that we continue working on the inversion algorithm in order to allow for calculating the 3-D anisotropic shear velocity structure both azimuthally and radially as well as allowing for variable crustal layers. Moreover, inferring the crustal structure from ambient noise tomography and combining them with the phase velocities obtained from earthquakes measurements. Due to automated procedure, the method

can be applied to other regions e.g. Indonesia and North America. Furthermore, the joint inversion with different data sets including the receiver functions and gravity measurements may provide better constraints on the lithospheric structure. In addition to the application of the Array methods, we may wish to analyze the propagation of the fundamental mode surface wavefield. The application of the Helmholtz tomography for structural phase velocity where the curvature and amplitude variations of the wavefront are taken into account.